Cooling of Advanced Gas-cooled Reactor Fuel Pin Bundles – Flow Physics and Engineering Predictions

Kenneth Chinembiri

A thesis submitted in partial fulfilment of the requirements for the degree of Doctor of Philosophy

Department of Mechanical Engineering

Faculty of Engineering

The University of Sheffield

March 2021

Acknowledgements

First and foremost, I owe a great debt of gratitude to my supervisors Prof. Shuisheng He and Dr. Jiankang Li. Thank you for the initial invaluable offer to undertake the supervision of this Ph.D. study and the patience you have shown these past years. Without your continued guidance, encouragement, and help, I would have not made it this far.

I would also like to thank and acknowledge the technical support provided by the EDF Manchester team (particularly Dr. Juan Uribe and Mr. Jacopo De Amicis), Dr. Charles Moulinec, and the *Code_Saturne* development team. Your advice and suggestions have been of great help throughout this project. I am also grateful for the financial support that has been provided by EDF Energy through a Ph.D. studentship.

It would be remiss of me not to mention and thank the members of the DFDHG (Dropped Fuel Discipline Health Group) whose technical expertise has helped me gain a deeper understanding of the background and current thermal assessment approaches for dropped fuel scenarios.

To my colleagues and friends in the Heat, Flow, and Turbulence Research Group, thank you all for the support, help, and encouragement you have shown to me. It has been my great pleasure to work alongside everyone and experience the moments we have shared as a group. I would also like to especially thank and acknowledge Dr. Cosimo Trinca whose support and knowledge were invaluable.

Last but certainly not least, I am grateful to my family and friends outside the group for their constant encouragement and understanding these past years.

Abstract

This thesis studies the cooling of rod bundles within the Advanced Gas-cooled Reactor (AGR) fuel route at non-design conditions using a variety of methods. The aims of the thesis are listed below:

(i) to contribute to the general understanding of the detailed flow, heat transfer, and turbulence phenomena in AGR rod bundles.

(ii) to develop a 3-D porous model software package for the thermal-hydraulics analysis of the fuel route. Of primary concern to this project are scenarios where the fuel bundle is distorted as a result of being dropped or damaged during refuelling operations. The model developed herein will complement the current 1-D thermal codes in use at EDF Energy. This is particularly for the cases where the latter would be excessively pessimistic or inaccurate due to their inability to capture the 3-D characteristics of the flow.

The open-source, co-located, and segregated Computational Fluid Dynamics (CFD) solver *Code_Saturne* developed by EDF has been used throughout this thesis. For the first aim, three studies have been carried out, that is, (a) Large Eddy Simulation (LES) study of natural circulation in a short 0.25 m enclosed bundle (b) Large Eddy Simulation study of natural circulation in a 1 m tall enclosed bundle and (c) Reynolds Averaged Navier Stokes (RANS) study of forced convection in a damaged bundle. In a short bundle, (a) the flow is largely laminar and constrained to the thin boundary layers around the fuel rods and containment wall. Away from the walls, in the core, the flow is stagnant. The vertical temperature distribution is heavily stratified. The natural circulation flow in the 1 m domain is heavily influenced by a vertically developing boundary layer on the containment surface, which is initially laminar but transitions to turbulence at about a quarter of the height from the top. The Nusselt number on the containment wall can be correlated using a well established expression over a vertical plate in a free space. Laminar boundary layers observed in both the long and short domains compare very well with similarity solutions, though for those over the fuel rods, the curvature needs to be considered. Forced convection in a damaged *WheatSheaf* bundle shows the flow to swirl around the rods as it is diverted to regions of less resistance through the rod gaps. Hot spots on the fuel at any axial location are found on the leeward side of the cross-flow.

To fulfil the requirements of the second aim a thermal-hydraulics code for the fuel route, named *FREEDOM* has been developed. FREEDOM aims to predict AGR fuel component temperatures under potential fault conditions while the fuel is being handled or stored within the AGR fuel route. *FREEDOM* has two modes, one for intact and another for damaged fuel. The main focus of this thesis is on damaged fuel. The model comprises of two domains, the fluid domain computed using *Code_Saturne* and the solid domain computed using *Syrthes*. In the fluid domain, the porous media representation is used to simplify the mesh generation and lessen computation cost. Thermal conduction and radiation are associated with the solid domain. The two domains are coupled together through the exchange of temperatures and heat transfer coefficients. In addition, oxidation due to the fuel and carbon deposit have been modelled considering both diffusion and reaction dynamics controlled conditions. The code is validated by performing experimental and code-to-code comparisons for a variety of flow conditions and idealised geometries. Forced convection comparisons were in good agreement and natural convection comparisons ranged from good to acceptable. The validated *FREEDOM* has then been successfully used to support a safety case argument by taking into account the three-dimensional effects for the flow, radiation, and solid conduction.

Contents

Appendices

List of Figures

List of Acronyms

AGR Advanced Gas-cooled Reactor . . . 2

BFRM Bare Fuel Rate Multiplier . . . 170

CANDU Canada Deuterium Uranium . . . 18

CDS Central Differencing Scheme . . . 54

CFD Computational Fluid Dynamics . . . 3

CGCFD Coarse Grid CFD . . . 38

DNS Direct Numerical Simulation . . . 44

EDF Électricité de France . . . 2

EVM Eddy Viscosity Model . . . 20

FEA Finite Element Analysis . . . 43

GCF Graphite Compaction Factor 268

GUI Graphical User Interface 61

HRN High Reynolds Number 21

LES Large Eddy Simulation 2

LRN Low Reynolds Number 21

IAEA International Atomic Energy Agency 19

IEA International Energy Agency 1

IFDF Irradiated Fuel Dismantling Facility 154

NIST National Institute of Standards and Technology 157

PCPV Prestressed Concrete Pressure Vessel 6

PWR Pressurised Water Reactor 2

RANS Reynolds Averaged Navier Stokes 3

REV Relative Elementary Volume 35

RSM Reynolds Stress Model 20

SCWR Super Critical Water Reactor 38

SGDH Simplified Gradient Diffusion Hypothesis 46

SIMPLEC Semi-Implicit Method for Pressure Linked Equations Consistent 58

SOLU Second Order Linear Upwind 54

SubChCFD Sub-Channel CFD 39

SSG Speziale-Sarkar-Gatski 46

SST Shear Stress Transport 46

URANS Unsteady RANS 20

WALE Wall Adapting Local Eddy-viscosity 51

Nomenclature

$*$	Quantity normalised using bulk values (unless indicated otherwise)

Greek letters

α	Thermal diffusivity, $\lambda/\rho\mathrm{Cp}\ \left[m^2/s\right]$
α_v	Volumetric porosity
α_{ij}	Anisotropic porosity
β	Thermal expansion coefficient, $1/(T+273.15)\ \left[1/^\circ\mathrm{C}\right]$
$\Delta x^+, \Delta y^+, \Delta z^+$	Grid spacing
Δ	Pitch (unless indicated otherwise)
δ_{ij}	Kronecker delta
ϵ	Dissipation term
λ	Thermal conductivity (unless stated otherwise), [W/m°C]
μ	Molecular viscosity,[Pa s]
Ω	Pitch correction (unless indicated otherwise)
ω	Specific dissipation rate
$\Omega_{ij,\mathrm{rot}}$	Rotation tensor
ϕ	Generic variable (unless indicated otherwise)

Ψ	Relative angle between bundle axis and coolant velocity (unless indicated otherwise)
ρ	Density, $\left[kg/m^3\right]$
Θ	Angle between bundle axis and horizontal plane (unless indicated otherwise)

Roman Letters

A	Aspect ratio, H/L
Cf	Fanning friction factor, $\tau_w/\rho\left(\overline{w}^2/2\right)$
Cp	Specific heat capacity, [J/kg°C]
Fuel pin	Also referred to as fuel rod in some of the text
$\mathrm{Gr}_{\Delta T}$	Grashof number, $g\beta\left(T_w - T\right)L^3/(v^2)$
$\mathrm{Gr}_{q''}$	Grashof number, $g\beta q'' L^4/(v^2\lambda)$
H	Height,[m]
No	Oxygen rate, [kg/s]
Nu	Nusselt number, hL/λ
Pr	Prandtl number, μCp/λ
Ra	Rayleigh number, GrPr
Re	Reynolds number, $\left(\rho uL\right)/\mu$
Sc	Schmidt number, $\mu/\left(\rho D_{O-A}\right)$
Sh	Sherwood number, $\left(h_m L\right)/D_{O-A}$
SPH	Equivalent spherical diameter, [m]
St	Stanton number, Nu/ (RePr)
C_F	Far-field concentration, $\left[\mathrm{kg/m^3}\right]$
C_S	Surface concentration, $\left[\mathrm{kg/m^3}\right]$

ci	Coefficient (Can vary as a function of flow condition and/or voidage)
D	Diameter (unless stated otherwise), [m]
D_{O-A}	Binary mass diffusion, $\left[\mathrm{m}^2/s\right]$
Dh	Hydraulic diameter, [m]
ds	Length along pin bundle surface
e	Rib height
e^+	Dimensionless rib height
Eu	Euler number
$Eu^{'}$	Combined Euler number
F	Analogy factor
f	Friction factor
F_{ij}	Boundary Face
g	Gravity, $\left[m/s^2\right]$
h	Heat transfer coefficient, $\left[\mathrm{W}/\left(\mathrm{m}^2\,{}^{\circ}\mathrm{C}\right)\right]$
h_m	Mass transfer coefficient, [m/s]
J	Radiosity
k	Turbulent kinetic energy, $\left[m^2/s^2\right]$
L	Length scale, [m]
L_{GD}	Length of graphite debris bed
P/D	Pitch-to-diameter ratio
Q	Source energy equation
q''	Heat flux, $\left[\mathrm{W}/\mathrm{m}^2\right]$
Q_j	Jacobian

R	Radius, [m]
r	Radial distance,[m]
$S_{ij,\text{strain}}$	Strain tensor
S_{ij}	Normal vector between cell i and cell j
S_v, S_ϕ, S	Source term
T	Temperature,[°C]
t	Time, [s]
T^*	Non-dimensional temperature
T^+	Non-dimensional temperature normalised using friction temperature
Te	Tensor
Tr	Transpose
U	Normalised velocity
u, v, w	Velocity components,[m/s]
u^+, v^+, w^+	Non-dimensional velocity normalised using friction velocity
u_τ	Friction velocity, $\sqrt{\tau_w/\rho}$ [m/s]
V	Volume, $\left[\text{m}^3\right]$
v	Kinematic viscosity,μ/ρ $\left[\text{m}^2/\text{s}\right]$
$V_{\text{max,z}}, V_{\text{n},\Delta T}$	Reference velocity, $\left[\text{m/s}\right]$
W	Mass flow (unless used as unit), [kg/s]
x, y, z	Spatial distances, [m]
y^+	Non-dimensional distance in viscous units, $y^+ = y\overline{w}_\tau/v$
Z^*	Non-dimensional height

Subscripts

$'$	Temporal fluctuation (unless stated otherwise)
GD	Graphite Debris
${}^{i}\phi$	Spatial deviation of variable ϕ
b	Branch
c	Cold surface
crs	Cross flow
f	Fluid
h	Hot surface
i, j, k	Directional terms
max	Maximum velocity
$n1$	Exponent (Can vary as a function of flow condition and/or voidage)
$num - diff$	Numerical diffusion
s	Solid
s/v	Surface and/or Volume
sgs	Subgrid scale
w	Wall

Symbols

$\langle\rangle$	Spatial average/filter
$\langle\rangle^{a}$	Filter area average of variable passed from solid domain
$\langle\rangle^{i}$	Intrinsic average
$\overline{\phi}$	Reynolds average of the variable ϕ

Chapter 1

Introduction

The world population has grown to unprecedented a level and so is its affluence. This in terms of energy entails an ever-increasing demand for the foreseeable future[20]. To meet these predicted demands not only is increased energy production required but in particular low carbon sources are needed to tackle the associated climate change.

Nuclear energy is a low carbon generation method that can offer a stable baseload supply to the grid and provide the required energy security demanded by modern economies. In conjunction with renewable sources, nuclear energy can grant energy security and have a positive impact on the amount of greenhouse gases and pollutants being released into the atmosphere. A scenario by the International Energy Agency (IEA) for capping global temperature increase to below 2 °C and improving our energy security, envisions a strong role for nuclear energy. To meet this scenario, global nuclear energy generation would have to more than double by 2050[21].

The growth of nuclear energy has not been without opposition or obstacles. Safety concerns are a major point of contention and well-publicised incidents such as the Three-Mile Island accident, the Chernobyl disaster, and the much more recent Fukushima Daiichi accident are usually brought up as examples of what can go wrong. Such incidents have had a significant impact on the perception of nuclear energy. For example, after the Fukushima Daiichi accident, the Japanese government responded by changing its energy policy with a view of reducing dependency on nuclear energy[22]. Some countries also similarly adapted their policies. Immediately after the incident, Germany closed some of its nuclear power stations and put in motion a plan to shut down all reactors within the country by 2022[23].

Although some countries have taken the approach to curb their dependence on nuclear energy, others still see it as an important contributor in their energy policy. China intends to generate 139 GW from nuclear by 2040[20]. Within the UK the government has given the go-ahead to build two new reactors at Hinckley point C each with a generation capacity of 1600 MW[24]. Currently, in the UK, there are fifteen Électricité de France (EDF) Energy owned reactors in operation, of these one is a Pressurised Water Reactor (PWR), and fourteen reactors are AGR's. While the PWR is a common light-water reactor design found in a variety of countries, the AGR is a gas-cooled reactor design that is unique to the UK.

At EDF Energy, nuclear safety is of paramount importance and as part of safety requirements, the company has to demonstrate that the plant is safe during routine operations and fault conditions. Of particular note and relevance to this project are the activities performed within the fuel route, where the irradiated fuel assembly is extensively handled as it is moved from the reactor, to the decay storage tube, and Irradiated Fuel Dismantling Facility. During fuel handling activities, there is the possibility of dropping/damaging the fuel assembly or a loss of forced cooling (i.e. as a result of blockages post drop or extractor failure). In such scenarios, part of fulfilling safety requirements involves ensuring staff have the tools to analyse faults and prevent further fault escalation.

Currently, at EDF Energy thermal-hydraulics analysis of the fuel route is performed using 1-D codes. Such codes have a long history in nuclear safety applications, are typically bounding due to their inherent pessimisms, and are trusted by regulators. However, in certain scenarios, 1-D codes can be markedly pessimistic. An example is when natural circulation is prevalent. Additionally, over time as the AGR's age, the operational conditions within the fuel route change such that the safety cases need to be revisited. This typically requires a new or better understanding of the physics along with a best-estimate 3-D model to better capture the flow phenomena.

This research project is concerned with the thermal hydraulics analysis of AGR fuel bundles under non-design scenarios. The thesis can be broadly split into two distinct aims, which constitute the two parts of the thesis:

- Part-1: Study of the detailed flow phenomena and physics for Advanced Gas-cooled Reactor (AGR) rod bundles using Large Eddy Simulation (LES) and

Reynolds Averaged Navier Stokes (RANS) at natural circulation and forced flow conditions, respectively. The solver used is Code_Saturne an open-source, finite volume, co-located and single-phase Computational Fluid Dynamics (CFD) solver developed by EDF[12].

- Part-2: Development, validation, and safety case application of an industrial 3-D porous model named *FREEDOM* for the thermal-hydraulics analysis of the fuel route. *FREEDOM* uses *Code_Saturne*[12] and the solid thermal conduction and radiation software *Syrthes*[25]. The model is developed starting from the intact fuel model *POSTR* by Trinca[26]. The modifications and additions made as part of this Ph.D. project extend the capabilities such that dropped or damaged fuel can now be considered. These include the addition of an automatic mesh generation and computation of geometric parameters stage (e.g. volumetric or anisotropic porosity, etc.) for damaged rod bundles. Computation stages for *FREEDOM* are then heavily modified by mainly introducing correlations for damaged rod bundles and graphite particulates. Methods for computing additional heat generation from fuel and carbon oxidation are further included, along with a method to simulate transients lasting several hours. Lastly, a postprocessing stage is also developed.

1.1 Thesis structure

The structure of the thesis is as listed below:

- Chapter 2: Provides background information on AGR reactors, facilities in the fuel route and dropped fuel scenarios.
- Chapter 3: Contains the literature survey and is split into two-parts based on the two aforementioned aims.
- Chapter 4: Discusses turbulent flow modelling and numerical methods used in the CFD solver *Code_Saturne*. This chapter particularly focuses on the methods and approaches used for the first aim of the thesis.
- Chapter 5: In this chapter, the study of natural circulation in a small aspect ratio (cavity height of 0.25 m) enclosed rod bundle is presented.

- Chapter 6: Results are presented for natural circulation in a large aspect ratio (cavity height of 1.0 m) enclosed rod bundle.

- Chapter 7: Presents and discusses the results of the RANS study for flow and heat transfer in a distorted *WheatSheaf* bundle.

- Chapter 8: The methodology of the 3-D porous model *FREEDOM* is discussed in this chapter.

- Chapter 9: The *FREEDOM* code is validated against a variety of flow conditions and damage configurations using both experimental data and code-to-code comparisons.

- Chapter 10: A high carbonaceous deposit safety case scenario is modelled using *FREEDOM.*

- Chapter 11: Overall conclusions to thesis and recommendations for future work are given in this chapter.

Chapter 2

AGR reactor, fuel route and current thermal codes

2.1 AGR and the fuel route

AGR's are a British thermal reactor design developed from the earlier Magnox reactor. Currently, there are 14 AGR reactors in the UK that are owned and operated by EDF Energy. AGRs use CO_2 as coolant and graphite as the moderator. The reactor core is typically just above a pressure of 4 MPa and the core outlet temperature is 650 °C, which is much higher than that of light water reactors. This results in the efficiency of AGRs being much higher, at about 42 % than most other commercial reactors.

2.1.1 Reactor characteristics

There are eight nuclear power stations in the UK and seven are of the AGR type. Each AGR power station has two reactor units, with each unit being housed in a pre-stressed concrete pressure vessel (PCPV). The reactor core comprises of graphite bricks of two types, a large round/polygonal brick and a smaller square or octagonal interstitial brick. The large graphite bricks house the fuel channels. The bricks are piled up and locked together using graphite keys. A number of the interstitial bricks are bored to form control-rod channels or used as graphite monitoring locations for flux scanning and neutron scanning. Figure 2.1 shows a portion of the reactor core. Surrounding the core are reflectors that prevent neutrons from escaping and help to maintain the chain reaction. Outside the reflectors, there is a shield comprising of

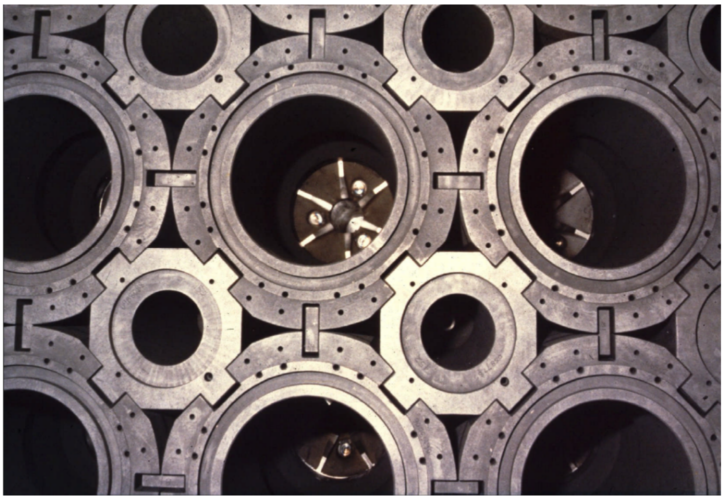

Figure 2.1: Image showing a portion of the reactor core[1]. Note that the circular graphite bricks can be locked directly together or through the graphite keys (square blocks)

graphite and steel. Most AGRs have the boilers embedded within the Prestressed Concrete Pressure Vessel (PCPV). There is a steel gas baffle in-between the boilers and the shield. The gas baffle separates the hot gas exiting from gas outlet ports of the fuel assembly and the re-entrant flow used to cool the graphite bricks. At the bottom of the core, there are support plates which rest upon a steel structure termed the diagrid. In turn, the diagrid is supported by steel struts which are bolted on to the PCPV.

Gas circulators, eight in each reactor, are located at the bottom and pump carbon dioxide at approximately 300 °C into the lower plenum where the flow then goes through two routes[3]. In the first route, the flow goes underneath the diagrid into the fuel channels where it is heated as it is forced over the fuel pins and is constrained by the graphite sleeve. The hot gas exits from the gas outlet ports, into the hotbox. From the hotbox, the flow then goes down to the boilers, where heat is transferred to the secondary circuit. A schematic of the flow route is shown in Figure 2.2.

The second route forces the gas upwards through an annuli passage outside the core and exits underneath the gas baffle. The flow is then directed to the annular spaces in-between the main bricks and fuel sleeve thus cooling the graphite bricks. This flow is termed re-entrant flow. At the bottom, the re-entrant flow joins the first route being directed upward through the fuel channels (see Figure 2.2).

At the top of the PCPV, there are penetrations called standpipes and each penetration is aligned with either a fuel or control-rod channel. During refuelling, the fuel assembly is inserted through the appropriate standpipe by a fuel handling machine. In

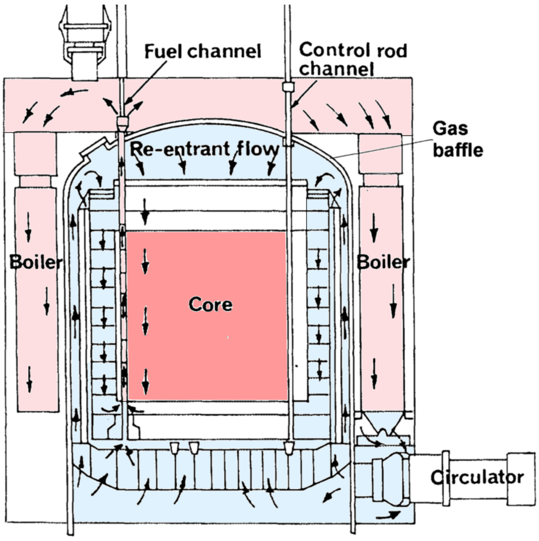

Figure 2.2: Schematic showing the flow-routes within the AGR reactor. Image adapted from Nonbel[2]

the plant a single fuel handling machine serves both reactors.

2.1.2 Fuel assembly

The AGR fuel assembly is 23 m long and comprises two main parts, namely the fuel stringer and fuel plug unit, in Figure 2.3 these are coloured in maroon and green, respectively.

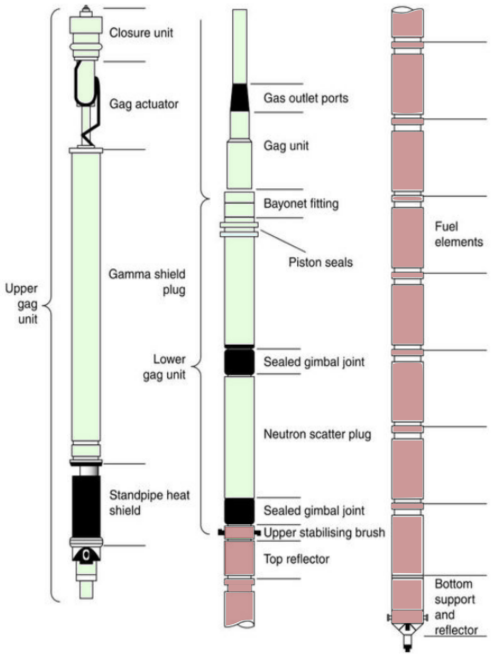

Figure 2.3: Illustration showing the fuel assembly modified from [3]

The fuel plug unit comprises multiple components, which will not be described in-depth instead, an overview is given. At the top, there is a closure unit that seals the fuel standpipe or the decay storage tube thus maintaining the pressure boundary[3]. Shields and reflectors are the next components, which are there to prevent neutrons and radiation from escaping through the fuel standpipe, while the flow through the gas ports into the hotbox is controlled through a gag unit. Next is a neutron scatter plug unit, which protects the upper section of the plug unit from excessive irradiation.

A fuel stringer comprises of eight fuel bundles[i], each about a meter long and held together by a centrally located cobalt steel tie bar with a diameter of 1 cm. The tie bar is anchored to the gag unit and supports the weight of the fuel stringer. This component is under considerable stress and non-redundant, thereby making the tie bar a critical component as failure would result in the fuel stringer being dropped. The tie bar, although non-redundant, has a large factor of safety and is designed to have an extremely low probability of failure.

Each fuel bundle comprises 36 fuel pins which are ribbed to promote heat transfer to the carbon dioxide coolant. The cladding material for the fuel pins is stainless steel and each fuel pin contains stacked uranium dioxide pellets enriched to various levels depending on fuel stages. The fuel pins are arranged in concentric annuli of 6, 12, and 18 from the center moving outwards. The pins are supported by a combination of grids and braces, at the bottom there is a support grid, while at the top and middle there are support braces. The whole bundle is surrounded by a graphite sleeve. The sleeve separates the re-entrant downward flow and the upward flow in the stringer. In addition, the graphite sleeve helps to increase the life span of the graphite bricks as it absorbs a portion of the gamma and neutron radiation.

2.1.3 Refuelling

During the lifetime of the station, new fuel assemblies must be brought online, while depleted fuel assemblies should be removed from the reactor, safely stored until dismantled and finally safely transported off-site. The stages that encompass the aforementioned are termed the fuel route. Events that occur within the fuel route are safety-sensitive as the stringer throughout the entire process is extensively handled.

---

[i] Dungeness uses seven fuel bundles

Moreover, associated risks increase significantly if irradiated fuel is being handled. Of particular importance to this project are the stages where irradiated fuel is handled.

New fuel is loaded into the reactor and depleted fuel is unloaded by the fuel machine. Depending on the station, the fuelling machine might have a single chamber or multiple chambers, but in general can be described as a hoist, which is shielded and pressurised. During the discharge of the fuel assembly from the reactor, a pressure boundary is maintained by seals between the standpipe and fuelling machine.

Compared to reactor pressure, the pressure level in the fuelling machine is higher. The pressure differential is necessary as it prevents hot gas from the reactor entering into the fuelling machine. AGR reactors were initially designed to be capable of online refuelling but due to an accident at Windscale where a fuel stringer was damaged during a test, refuelling has been restricted to 30 - 40 % of load[2].

During the lift, the fuel stringer passes through distinct stages where the behaviour of the coolant varies[27]. These stages vary from station to station but in general, the following can be stated. When the fuel stringer is still within the reactor core, cooling is provided by gas circulators. Once the bottom of the stringer is within the standpipe, depending on the station, either the FMCS (Fuel Machine Cooling System) provides the cooling flow or cooling is by natural recirculation. Finally, when the fuel assembly is completely contained in the fuelling machine cooling is maintained by natural recirculation.

Subsequently, the fuelling machine traverses the charge hall and deposits the spent assembly into the buffer store. This is a concrete vault that is used to store both new and irradiated fuel. The facility contains banks of tubes which are either pressurised or unpressurised. New fuel is stored in unpressurised tubes while irradiated fuel is stored in a pressurised CO_2 environment. Within the decay storage tubes, heat is transferred by natural convection from the fuel bundles to the tube walls. The decay storage tube walls are in turn cooled by a water jacket. At high gas pressures natural convection is dominant but if a sudden de-pressurisation of the tubes occurs then heat transfer by radiation becomes more important/dominant.

Irradiated fuel assemblies are stored in the decay storage tubes up until the residual heat is low enough to allow dismantling. After the requisite residual heat levels have been achieved, the fuel assembly is extracted by the fuelling machine and sent to the irradiated fuel disposal cell.

The irradiated fuel disposal cell is a tall concrete vault at approximately atmospheric pressure. Forced convection provided by suction pumps is the main method of heat removal during disassembly in an isolated tube within the cell. The fuel plug unit and stringer are separated remotely, the stringer is further split into individual fuel bundles by cutting the tie bar. In turn, the fuel plug unit is dismantled into lower and upper sections, with both sections being sent for refurbishment. If any fuel plug components are worn beyond repair, they are sent to the debris vault along with pieces of the tie bar and other irradiated ancillary components. The fuel bundles are sent to the cooling ponds where they are cooled and stored until radioactivity has decreased to levels permissible to allow transportation off-site to Sellafield. Figure 2.4, shows all the pertinent stages of the fuel route.

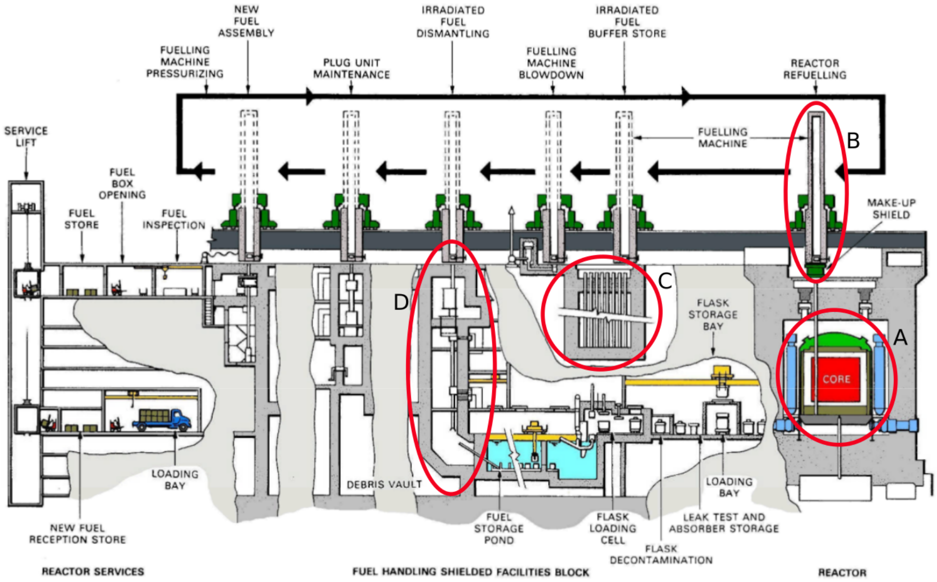

Figure 2.4: Schematic of the various stages within the fuel route. (A) Reactor core, (B) Fuelling machine, (C) Decay storage tube and (D) IFDF. Image adapted from EDF presentation material.

2.2 Dropped Fuel

Dropping or damaging the fuel assembly, although highly unlikely due to the safety measures put in place, is still considered a credible event thus EDF Energy must demonstrate capabilities are in place to prevent fault escalation and to protect employees and local communities from radiological release. A fuel drop can occur at any stage of the fuel route, stages of particular concern are those that involve the handling of irradiated fuel assemblies.

As the assembly is being transported there is a risk of the following types of drops occurring at the different facilities[28]:

1. Fuel stringer drop or dropping individual bundles: Can occur due to tie bar failure or at IFD cell during dismantling.
2. Partial assembly drop: Can occur due to fuel plug unit failure.
3. Full assembly drop: Can occur due to grab failure
4. Full assembly plus the grab: Can arise due to hoist failure.

In the types of drops mentioned above, significant impact energies can arise due to the masses of the components involved. The fuel stringer alone weighs approximately 765kg while the whole assembly is close to 2.5 tonnes[28]. Once a fuel drop has occurred an assessment with the following stages of analysis is carried out[15].

1. Impact velocity of the fuel is calculated
2. Assessment of fuel damage and post drop morphology
3. Calculation of debris temperature
4. Calculation of radiological consequences

2.2.1 Impact of dropped components/assembly

Impact force is dependent upon the drop height, the mass of the missile (dropped component/s) and frictional forces dissipating the kinetic energy of the missile.

2.2.2 Assessment of fuel damage and post drop morphology

Initial damage is calculated whether the drop is contiguous or non-contiguous. In a contiguous drop, the missile falls as one unit (i.e the fuel bundles are in contact with each other). Conversely, for a non-contiguous drop, the bundles separate and impact each other sequentially[29]. To calculate damage progression it is assumed that progression follows the weak link theory. From experimental and theoretical work, the amount of energy absorbed and failure loads of each damage mechanism or component can be obtained. Weak link theory is then used, where the mechanism with the lowest failure load succumbs first and absorbs a certain portion of the total impact energy. Damage progression continues until all the energy is accounted for.

Energy absorption varies due to component irradiation and the type of fuel[ii][28]. Irradiation effects are obtained from correlations of fuel burn up. The failure load of all damage mechanisms barring fuel pin buckling and graphite sleeve crumbling are independent of the facility[28]. Fuel pin buckling and crumbling energies are dependent upon the diameter at the drop location. In ascending order the facility diameters increase from reactor to decay storage tube and finally the irradiated fuel disposal cell. Once the damage progression and the number of damaged bundles have been calculated, the post drop morphologies are then calculated for the thermal assessment.

2.2.3 Thermal assessment

A thermal assessment is required on two fronts, the first is due to its role in the assessment of the radiological consequences and secondly, once a drop has occurred, the temperature distribution of key components such as fuel claddings and the graphite sleeve needs to be known.

Currently, 1-D thermal hydraulic codes are used for conducting thermal assessments. The aim is to have a three-dimensional code assisting current modelling methodology's and this is especially pertinent as neglecting the three-dimensional effects can give overly pessimistic or optimistic results.

Thermal assessment codes internally used at EDF Energy:

CoolFuel 1-D, developed by NNC in the 1990's, is a thermal hydraulic code based on the flow resistance network code SheepDip[30]. The code is capable of predicting debris temperatures for prescribed damage geometries at various conditions and can account for all the modes of heat transfer.

To predict temperatures and coolant velocities, the code bases the calculation on a flow network with nodal points and connecting branches. Coolant nodes are linked

---

[ii] Over the years, the design of fuel pins has evolved thus data sources for the correct fuel type (stage 1, stage 2, stage 3, robust fuel) have to be used

by flow resistance branches, where the pressure drop between the two connected nodes is calculated based on the hydrostatic pressure difference and branch resistance (computed from correlations). Equation 2.1 is used to calculate pressure between two connected nodes. P_1 and P_2 are the nodes connected by branch L. Inlet and outlet pressures are used to prescribe boundary conditions on the flow network.

$$P_2 - P_1 = \rho_L g(h_1 - h_2) - \frac{R_L}{\rho_L^{upwind}} w_L |w_L| \tag{2.1}$$

With regards to the energy equation, energy is conserved at the nodes. Branches linking the nodes account for the conductances and the heat transfer coefficients. A single sink node is used to define the boundary condition. To solve the network branch resistance, heat transfer coefficient and branch conductances must be modelled.

In conducting the simulation, the same number of nodes is used for both the coolant flow and solid nodes. Radially, it is recommended the domain have a maximum of 5 nodes, or a minimum of three nodes[30]. Axially there is no such limitation. To simplify the calculation, damage geometries are considered axisymmetric and network is represented as independent flow loops, which when summed together satisfy continuity[30]

Pressure boundary conditions, when the fuel assembly is in the reactor can be obtained from MACE[15]. MACE is a system code which models the thermal hydraulic transient behaviour of the whole reactor[iii]. In MACE all the reactor channels are lumped together and results for a single averaged channel are returned, these include predicted pressures and temperatures at the hotbox, lower plenum, top and bottom headers are returned[27].

Besides *CoolFuel* 1-D, *HOTDROP* is another one dimensional code which can be used predict to fuel debris temperatures after a drop within the reactor and other stages mentioned in Section 2.2. *HOTDROP* is a network code, but is much simpler than *CoolFuel* 1-D in that, the code assumes the fuel bundle and graphite sleeve are regions where no flow can pass through. In the interstitial spaces, for example the annuli region, between the graphite and pin bundle convective heat transfer is modelled[31]. Another code *FOXDROP* is largely based on *HOTDROP* but takes into account fuel and carbon oxidation.

The codes mentioned above are the current modelling methodologies in use at EDF Energy. Another code *CoolFuel* 3-D developed by NNC could model the 3-D effects of

---

[iii] includes boilers and gas recirculators

the flow. The code was based on a finite volume code (PHOENICS CFD). Currently this code is no longer supported or available for use at EDF Energy.

CoolFuel 3-D could model non-axisymmetric geometries of damaged fuel, unlike *CoolFuel* 1-D. The code was based on the finite volume approach and used the porous media approach to model solid-fluid interactions[17]. The solver (PHONECIS) would receive the porosity field, geometrical information and other data from a satellite file, which are a collection of subroutines written in Fortran[17]. A staggered grid was used, with the scalar variables located at the center and vectors located at cell interfaces. Interpolation for the convective terms was limited to a first order upwind scheme[17]. Correlations similar to those used for *CoolFuel* 1-D were used to model heat transfer and resistance due to the solid components. Turbulence was modelled using a zero equation turbulence model similar to that described in Chapter 8. *CoolFuel* 3-D represented the geometry as a cylindrical flow domain, subdivided into segments. The maximum number of radial and azimuthal divisions was limited to 12 and 18 respectively. Typically, the simulations were run using a coarser grid with 6 azimuthal and 12 radial divisions. Axial refinement of the flow domain was based on the damage geometry being modelled. The last step in the post drop analysis involves the calculation of radiological consequences.

Chapter 3

Literature review

3.1 Flow studies in rod bundles and simple geometries

3.1.1 Experimental studies for forced convection in rod bundles

Rod bundles consist of multiple heating rods arranged into a geometric array where the interstices of the rods, which are termed sub-channels are locations of fluid flow and these are illustrated in Figure 3.1. As will be shown later much effort has not just been devoted to understanding the overall bundle flow behaviour, but in particular to understanding how these sub-channels interact with one another. The influence of the sub-channel shape and gap spacing are also considered. Correlations for pressure loss and heat transfer have also been considered for the different sub-channel types.

Skinner et al.[32], conducted an experimental study aimed at investigating the rate of heat transfer between sub-channels of an AGR fuel bundle. The experiment used a six-rod cluster, containing either roughened or smooth rods. Results from both sets of rod clusters returned mixing rates between the sub-channels that were higher than that which sole turbulent diffusion theory predicted.

Trupp and Azad[4] carried out a study of turbulent flow in triangular arrays at P/D ratios of 1.2, 1.35, and 1.5 with the aim of investigating flow structures in rod bundles. In their results, they were not able to directly measure secondary velocities, but they were able to infer characterisations of their effect on the flow. Figure 3.2

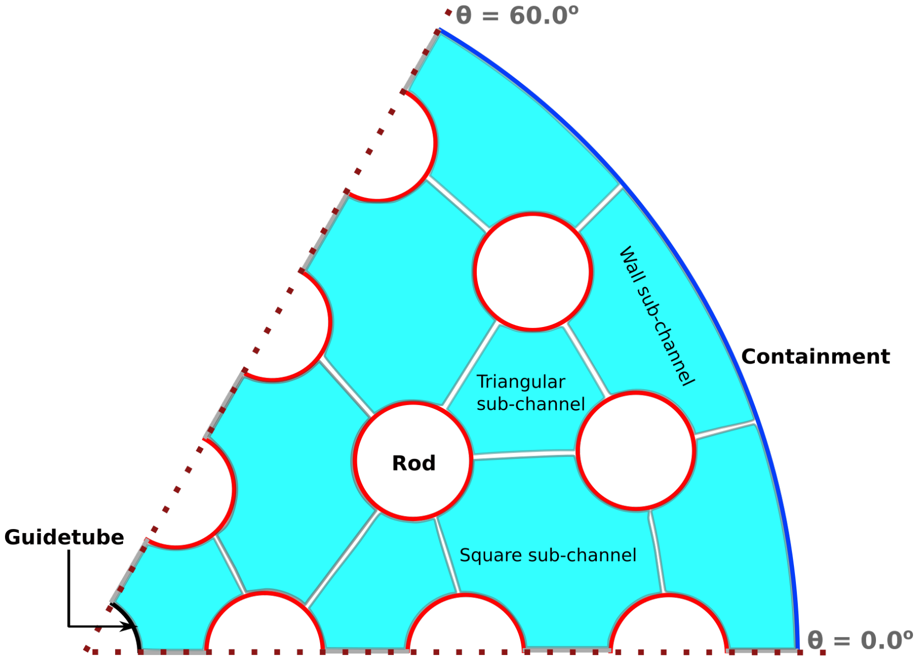

Figure 3.1: Sub-channels types commonly found in rod bundles. This particular rod arrangement is for an AGR fuel bundle.

shows a schematic of their test rig and the inferred secondary flows at a P/D ratio of 1.35. Their results also showed the “bulging” of velocity towards the gap regions and this was in agreement with earlier work by Kjellstroem[33].

Kjellstroem[33] had earlier conducted experimental investigations on a triangular array with a constant P/D ratio of 1.22. In the paper, it was shown that the radial turbulent stress was comparable to that of circular ducts, but the azimuthal turbulent viscosity was greater by a factor of 1.5 to 10, depending on the wall proximity[33].

Seale[34] conducted experimental studies on turbulent mixing and secondary flows using smooth rod bundles. A range of Reynolds numbers were used along with three different P/D ratios of 1.1, 1.375, and 1.833. His results confirmed the increased sub-channel mixing observed by Skinner et al.[32]. However, from the work presented in the paper, Seale inferred that the secondary velocities were not the cause of increased sub-channel mixing.

Based on the works above and further works by Vonka[35], Carajilescov and Toderas[36], and Rehme[37], the following is revealed about secondary flows in rod bundles. Secondary flows are a flow pattern perpendicular to the predominant flow direction and arise due to the anisotropy of Reynolds stress. Secondary flows recirculate within the gap region, thus could not be the main contributor to increased sub-channel mixing as

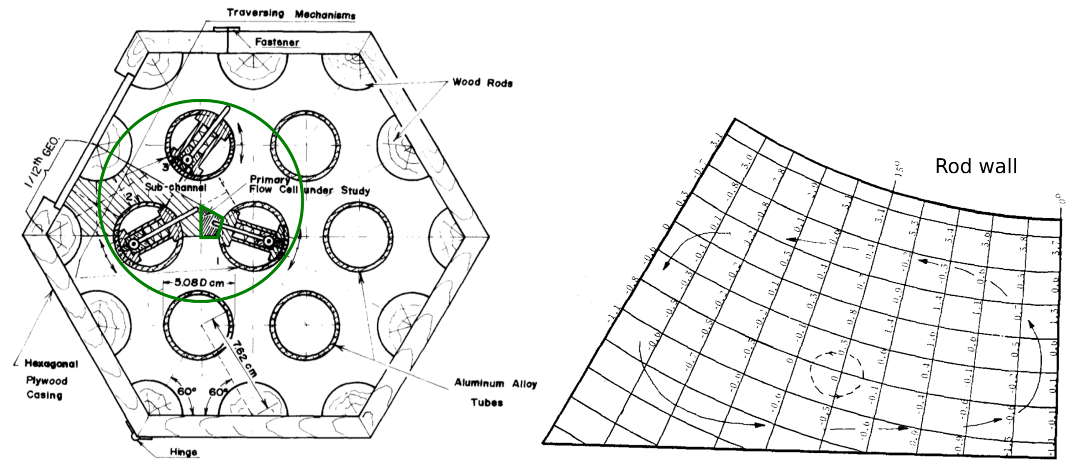

(a) Test rig (b) Secondary flow

Figure 3.2: Sketch of the test rig used by Trupp and Azad[4] and the deduced secondary flows from the experimental run at a P/D ratio of 1.35. The sub-channel under consideration is encircled and the secondary flow sketch in subfigure (b) is extracted from the highlighted quadrilateral.

initially hypothesised by Skinner et al.[32].

Rowe et al.[38] conducted forced convection experiments using water for high Reynolds number flows (5×10^4 - 2×10^5) through rod bundle arrays at P/D ratios of 1.125 and 1.25. The experimental results revealed that the region in-between the gap and sub-channel centre contained macroscopic flow pulsations. From his investigations Rowe further concluded that changes in the P/D ratio significantly affected this flow structure.

Enhanced mixing between the sub-channels was a result of the azimuthal periodic flow pulsation first noticed by Rowe[38] and later confirmed by Rehme and Hooper[39] instead of the secondary flow as initially postulated by Skinner et al.[32].

Hooper and Rehme[39] confirmed that the azimuthal turbulent-velocity component dominates heat transfer between sub-channels. The authors attributed the component to parallel channel instabilities. It is generally agreed that these instabilities arise due to quasi-periodic vortex pairs forming in adjacent gap regions [5, 40, 41, 42, 43].

Krauss and Meyer[5] conducted an experiment using a 37-rod bundle test rig comprising of triangular arrays. Two P/D ratios of 1.06 and 1.12 were considered. Peak temperatures were shown to occur at the narrow gaps and there was a wider azimuthal wall shear stress variation at a P/D ratio of 1.06. Turbulence intensities were observed to be similar to those for pipes away from the rod gaps. However, at or close to the rod gaps the intensities were higher as a result of the pseudo-periodic vortices and this was particularly so for the smaller P/D case. Figure 3.3(a) shows the recordings of temperature and velocity components from the experiment, which highlight the periodic nature of the flow across the gaps. Figure 3.3(b) shows a schematic of the flow structure across the gap region. As seen there are large scale counter-rotating vortices either side of the gap, which move upwards in the streamwise flow direction.

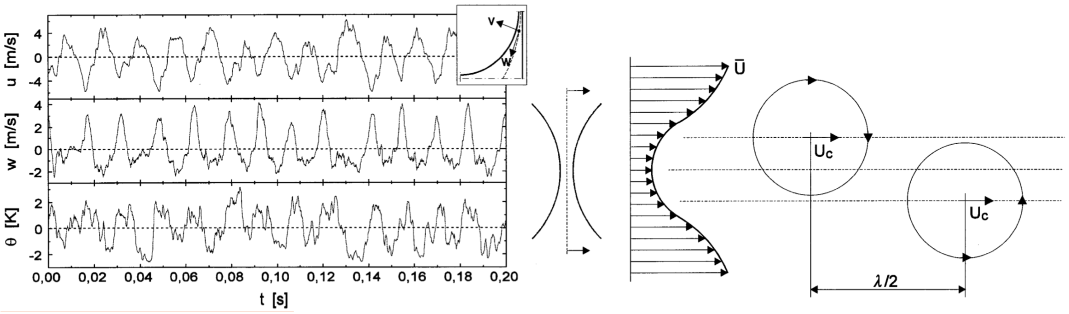

(a) Low pass filtered fluctuating variables (b) Sketch of main flow and vortices at the gap region

Figure 3.3: Fluctuating data from the experiment and schematic of the flow at the gap region by Krauss and Meyer[5].

Ouma and Tavoularis[44] carried out experiments at design and non-design conditions using a five-rod sector of a 37-rod Canada Deuterium Uranium (CANDU) bundle consisting of triangular and wall sub-channels. The rods in a CANDU bundle are arranged in concentric ranks and the sector selected comprised of rods in the last two-ranks. The middle outer rod of the rig could be displaced either inwards to the rods or outwards to the wall. Isothermal conditions were considered and the working fluid was air. Results for the wall shear stress showed that as the central rod was moved closer to the wall, there was a reduction in shear stress at the narrow gap. Conversely, wall shear stress at the open regions increased. At a wall-to-diameter ratio of less than 1.05, wall shear stress showed a significant decrease in the narrow region. Similar to Trupp[4] and Kjellstroem[33] bulging of the velocity towards the gap regions was observed. Secondary velocities in the sub-channel were noted at levels less than 1 % of bulk velocity, and as the rod was moved closer to the wall the intensity of the secondary flows was observed to increase.

Heina et al.[45] performed isothermal investigations for undamaged and damaged rod bundles. The aforementioned paper is in Russian but a synopsis is given in an

International Atomic Energy Agency (IAEA) report [46]. Their results showed a decrease in mass flow in the reduced sub-channel, which in turn led to increased temperatures in the respective sub-channels.

3.1.2 Numerical studies for forced convection in rod bundles

Rock and Lightstone[47] conducted a study on the use of the isotropic k - ϵ model to predict sub-channel mixing. In the study, steady-state calculations were performed with Reynolds number values between 3×10^4 and 3×10^5. Three different P/D ratios of 1.1, 1.375, and 1.833 were investigated. Their simulation results were compared to those obtained from Seale's[48] experiment. The k - ϵ model was found to under-predict the azimuthal turbulent velocity component thus resulting in sub-channel mixing being under-predicted. However, as noted in the paper the predictions improved as the P/D ratio increased. At the smaller gap spacing, the pseudo-periodic pulsation increases in strength, and unsteady methods are required. The RANS method as will be highlighted in some of the forthcoming literature sources becomes inaccurate at smaller rod spacings.

Rapley and Gosman[49] performed steady-state simulations for developed flows in triangular arrays with P/D ratios of 1.06, 1.123 and 1.2. A particular focus of their study was the modelling of secondary flows, which as discussed earlier arise due to the anisotropy of the Reynolds stresses. To model this they used an algebraic stress model, developed by Launder and Ying[50]. Production and dissipation terms within the algebraic stress model were obtained through coupling with the k - ϵ model. Experimental comparisons for wall shear stress and velocity profiles showed that in general, there was fair agreement. At a P/D of 1.2, the maximum secondary velocity was found to be 0.6 % of the average axial velocity, while at lower P/D ratios it was 2 %. A particularly interesting result was a comparison of the azimuthal distribution of shear stress at all P/D ratios, where simulation results with and without the presence of secondary flows were compared. From the comparison, secondary flows were numerically shown to have the effect of reducing wall shear stress variation thus making it uniform.

Sofi et al.[51] compared RANS simulation results obtained using a variety of turbulence models, against experimental data for differing rod bundle arrays. Their comparisons showed the non-linear k-ϵ and RSM models returned improved predictions compared to the standard k-ϵ model. The predictions were also better for the larger P/D ratios (i.e. P/D > 1.06).

Baglietto and Ninokata[52] used observations from linear Eddy Viscosity Model (EVM), non-linear EVM and experimental secondary flow measurements by Vonka [35] to develop a new set of coefficients for the quadratic k-ϵ model by Zhu and Lumley[53]. RANS simulations were used and the geometry simulated was a sixth of a triangular sub-channel with a given P/D ratio of 1.17. Before altering the coefficients it was shown that the standard models linear k-ϵ, k-ω, k-ω SST and quadratic k-ϵ had a qualitative agreement with the distribution of wall shear stress obtained from experimental investigations, with the unmodified quadratic k-ϵ models offering better qualitative agreement. Results for the axial velocity showed the EVM models and unmodified quadratic k-ϵ gave good quantitative agreement, with the unmodified quadratic k-ϵ returning closer results. An in-depth look at the quadratic k-ϵ equation revealed that it under-predicted the flattening of the shear stress. To achieve better predictions, the authors altered the coefficient within the quadratic k-ϵ associated with the product of strain and vorticity. Conducting simulations at Reynolds numbers ranging from 23 760 to 109 000 and comparing against experimental results, it was shown that at the higher Reynolds numbers there was good agreement, but at 23 760 only the qualitative trend could be caught.

Chang and Tavoularis[54] applied Unsteady RANS (URANS) along with a Reynolds Stress Model (RSM) model to simulate axial flow in a rectangular channel containing a single cylindrical rod. From the results, it was found that the quasi-periodic structures can account for up to 60 % of the total kinetic energy in the gap region.

Chang and Tavoularis[40] used the URANS method with a Reynolds stress model to simulate fully developed flow in a 60° sector of CANDU fuel bundle. Validation was mainly performed by comparing against the experimental data from Ouma and Tavoularis[44]. Velocity and shear stress distributions were found to be in good agreement with experimental data. Observations of the coherent flow structure showed the vortices on either side of the gap were strongly correlated and this is in agreement with the findings of Krauss and Meyer[5].

Baglietto[55] showed that for a relatively large P/D ratio, the RANS method in conjunction with an anisotropic turbulence model was sufficient to get good comparisons against experimental data. However, if the P/D ratio was < 1.1 the URANS method had to be used to capture the pseudo-periodic flow structure identified by earlier investigators such as Rowe et al.[38].

Yan et al.[56] modelled fully developed axial flow in a tight lattice using URANS and a RSM. In their paper, they studied the coherent flow structure and the effect changes in the P/D ratio had on mixing. To make the model less computationally expensive three pairs of periodic boundary conditions were employed. It was shown that when the P/D ratio was 1.03, the coherent structure was stronger and easily discernible. At P/D ratios less than 1.01 the strength of the coherent structure was greatly reduced, thus in turn impairing sub-channel mixing.

To finish off this part of the literature review, papers focusing on the flow and heat transfer characteristics for roughened rod surfaces and/or rod bundles at non-design scenarios are now discussed.

Keshmiri[57] investigated rib-roughened passages using both 2-D and 3-D simulations at a bulk Reynolds number of 3×10^4. The investigation had a direct application to AGR reactors as the modelled geometry was a simplified representation of rib roughened AGR rod bundles. Two Low Reynolds Number (LRN) turbulence models $k - \epsilon$ and Durbins $v^2 - f$ model were used. These two models were also compared against a high Reynolds $k - \epsilon$ model with a further view of evaluating the applicability of using standard wall functions for rib-roughened surfaces. From an earlier paper[58], Keshmiri had already established that the $v^2 - f$ returns more accurate results. The comparison between the use of a high Reynolds $k - \epsilon$ with a standard wall function against LRN models revealed that the first approach returned inadequate results. Turbulent kinetic energy at the ribs, wall-normal velocity, and recirculation region after the rib were under-predicted by the High Reynolds Number (HRN) $k - \epsilon$ model.

Triangular sub-channel asymmetry was numerically investigated by Hofmann[59] using a network code. The coolant was sodium and to simulate asymmetry the central rod could be radially or azimuthally displaced. It was found that moderate degrees of asymmetry led to considerable velocity and temperature changes in the coolant.

Ooi et al.[60] compared experimental data for flow and heat transfer in rib-roughened passages against predictions obtained from $v^2 - f$, SpalartAllmaras. and $k - \epsilon$ turbulence models. Results showed that in terms of heat transfer the $v^2 - f$ model agreed well with experimental data while the remaining two models returned considerably under-predicted values. $k-\epsilon$ results in particular predicted half the heat transfer rate compared to the experimental results.

Davari et al.[61] simulated flow channel blockage in a Tehran research reactor. The blockage could arise due to buckling as a consequence of material defects, swelling, or hydraulic instabilities. Obstruction levels of 0 % to 70 % were simulated. If the plate is buckled, the affected channel has a reduction in flow area while conversely, the neighbouring channel has an increase in flow area. To simulate flow in such a domain, the authors used a realisable $k-\epsilon$ model with advanced wall functions. Simulation results showed that flow in the constricted channel was reduced due to increased resistance, while flow in the adjacent channel had increased. A look at the temperature results revealed that temperature in the reduced channel increased as the obstruction levels increased. At above 50 % the integrity of the cladding was predicted to be compromised and at 70 % nucleate boiling predicted.

Salama and El-Morshedy[62] similarly simulated blocked flow in a geometry akin to that used by Davari et al.[61]. Flow blockages of up to 90 % were simulated using the realisable $k-\epsilon$ model. Their results show coolant redirection from the constricted channel. As to be expected, cladding temperatures in the damaged channel were higher and heat transfer was impaired. In the adjacent channels, due to increased heat transfer, the temperature distributions were altered compared to the 0 % blockage case.

Chauhan et al.[63] conducted a numerical simulation where they investigated the effect of eccentricity on the thermal hydraulics. A $k-\omega$ SST turbulence model was selected to close the RANS equations. Their geometry was a fuel bundle containing 19 fuel rods. In their study, they varied eccentricity by translating the whole bundle towards the pressure tube wall. Various degrees of eccentricity were investigated, and as it increased there was a reduction in the flow area of the bottom peripheral sub-channel (constricted sub-channel). Turbulent kinetic energy at the maximum eccentricity was found to reduce by as much as 63 % in the narrow gap, while a temperature increase of over 200 % was noted.

3.1.3 Numerical and experimental studies for buoyant flow on vertical surfaces and in channels

The natural convection boundary layer for an isolated vertical plate surface was experimentally studied by Tsuji and Nagano[64]. Contrary to forced convection flows they showed the y^+ range for the viscous sublayer was much smaller. However, the profile for T^+ against y^+, showed that the non-dimensional temperature had a linear relation up to $y^+ \leq 5$. This is similar to forced convection flows. In their measurements, the mean heat transfer rate remained constant with height, while the wall shear stress increased.

Versteegh and Nieuwstadt[65] used DNS to simulate natural convection in an infinite differentially heated rectangular vertical channel. Temperature and velocity profiles showed that they could be split into two regions; one (near the wall) where the viscous effects are dominant and the second region in-between the velocity maxima and core where the turbulence effects dominate. Turbulence budgets showed that transport due to advection was of importance only near the velocity maximum. In the near-wall region, it was shown that the turbulent shear stress at higher Rayleigh numbers tended to become negative. Paolucci[66] simulated a rectangular cavity using DNS and also showed that the turbulent shear stress was negative near the wall.

Nakao et al.[67] numerically investigated natural convection boundary layer development on a heated vertical wall. In their study, the LES method with a modified Smagorinsky model was used. Numerical results obtained compared well against experimental data for the laminar and turbulent regions. However, the onset and duration of the transition regime differed with viscosity and the streamwise grid resolution. Profiles for the Reynolds stresses were shown to peak on the outer layer.

Goodrich and Marcum[68] experimentally studied the radius of curvature effect on flow transition and heat transfer. Five cylindrical heating rods with diameters ranging from 0.0064 m to 0.025 m were considered by the authors. Results showed that at large values of Ra_D the influence of curvature was nearly negligible with the heat transfer being approximated by flat plate correlations. Transition to turbulence was noted to occur at lower values of Ra with a wider span for the smaller cylindrical diameter cases.

The interior sub-channels in a rod bundle are likely to act as a symmetrically heated channel or heat pipe. This part of the literature review draws from the relevant literature sources tackling these specific geometries.

Natural convection in an open-ended pipe was one of the test configurations experimentally investigated by Eckert and Diaguila [69]. The length of the heated pipe section was 2.5 m with an internal diameter of 0.6 m. High Grashof numbers, based on the length, up to 10^{13} were considered in the experiment. Thin boundary layers existed on the heated pipe walls. Heat transfer in the turbulent region was well correlated to that for an isolated flat vertical surface. However, in the laminar region heat transfer was over predicted. Large diameter pipes were also investigated by Yan and Lin[70], using both experimental and numerical methods. Similarly, they showed that the heat transfer phenomena was akin to an isolated vertical plate in a large free space.

Ohk and Chung[71] experimentally and numerically investigated the influence of length, diameter, and Prandtl number on natural convective flow through an open-ended pipe. The pipe length ranged from 0.2 m to 1 m, with the pipe diameter ranging from 0.003 m to 0.03 m. For the large diameter pipes, the observations were consistent with the studies cited in the preceding paragraph [69, 70]. Decreases in the pipe diameter and/or Prandtl number led to the thermal boundary layers merging and velocity peaks occurring near the centre, which is a deviation from the typical natural convection flow profile. Instead, this is now a mixed convection pipe flow. As the pipe length was increased it was shown that the heat flux progressively reduced as the thermal boundary layer developed along the pipe length.

Inagaki and Maruyama[72] investigated laminar, transitional, and turbulent natural convection between two uniformly heated vertical plates open at four sides. The effect of various gap spacings and channel lengths were additional parameters under investigation. The working fluid was water and the peak Rayleigh number (based on height) was 10^{15}. In the laminar region, the heat transfer increased with a decrease in gap spacing. This behaviour was attributed to the chimney effect. However, in the turbulent region with a decrease in gap spacing heat transfer deterioration occurred at Rayleigh numbers greater than 10^{14}. The authors stated this behaviour and the physical mechanisms underlying it was similar to heat transfer deterioration in vertical forced flow channels as a result of buoyancy.

Lewandowski et al.[73] experimentally investigated the effect of gap spacing on the computed Nusselt number for a symmetrically heated vertical channel. The working fluid was air with a given Prandtl number of 0.71 and a peak Rayleigh number (based on height) of up to 10^9. Gap spacing was shown to have a significant effect on the heat transfer rate. At a gap spacing of approximately zero, the heat transfer was via conduction. As the gap spacing increased, convection became dominant past a critical Rayleigh number. With a further increase in spacing leading to the formation of the chimney effect, which greatly aided the heat transfer. A peak heat transfer enhancement of 69 % compared against that for an isolated vertical plate was recorded as a result of these effects. However, further increases in gap spacing led to a weakening of the chimney effect up until the increase in gap space was such that the two convective boundary layers no longer interacted and the predicted heat transfer coefficient approximated to that of a flat vertical plate.

3.1.4 Experimental investigations for natural convection in enclosures

Laminar natural convection in rectangular and annular cavities was experimentally studied by Elder[74]. Two of the opposite facing walls had different but constant temperature boundary conditions. The top horizontal surface was left open to the ambient air while the bottom surface was insulated. The aspect ratios of the cavities ranged from 1 - 60 and the Rayleigh number was limited to 10^6 with fluids (Silicone oil and medicinal paraffin) of Prandtl number 1000. At low Rayleigh numbers $\left(\mathrm{Ra}_L < 10^3\right)$, the heat transfer was dominated by conduction across the cavity. Flow circulation did occur but it was weak with a unicellular motion. A further increase of the Ra_L number up to 10^5 led to the formation of three distinguishable regions. The wall region noted to be a region of large horizontal temperature gradients, while the interior region was a region of a uniform vertical temperature gradient. The end region, which was heavily influenced by the boundary conditions as the top and bottom were not insulated and in particular, the top of the cavity was open to the surroundings. The velocity profiles at half-height were shown to be antisymmetric, but with an increase in Ra_L the inflexion point was drawn closer to the heating/cooling walls (vertical flow constrained to the boundary layers) while the interior core increasingly became a stagnant region. Furthermore, this leads to the formation of additional "primary circulation vortices" at $\mathrm{Ra}_L = 10^5$. A further increase of Ra_L generates even more vortices and at $\mathrm{Ra}_L = 10^6$, tertiary flows were shown to occur. These were defined as counter-rotating vortices between the newly generated primary circulation vortices. Elder[74] concluded that these are formed due to the shear layer between them increasing in strength.

Macgregor and Emery[6] noted several flow regimes from their numerical and experimental data for natural circulation in rectangular cavities. The fluids investigated had a Prandtl number range of 1 to 2×10^4, while the cavity aspect ratios were $1 \leq \mathrm{H/L} \leq 40$. The regimes were defined using Ra_L. The conduction regime is for $\mathrm{Ra}_L \leq 10^3$, which was characterised by a linear temperature profile across the cavity. In $10^3 < \mathrm{Ra}_L < 10^4$, both conduction and convection contributed to heat transfer and the regime is referred to as asymptotic flow. The flow would then transition to a "laminar boundary layer flow" regime for $10^4 < \mathrm{Ra}_L < 10^6$, where convection dominates with the flow constrained to the wall layers. The interior core is quiescent and of uniform temperature. At Rayleigh numbers between $10^6 < \mathrm{Ra}_L < 10^7$ the flow is considered transitional. After $\mathrm{Ra}_L = 10^7$ the flow would then transition to the turbulent boundary layer flow regime. These regimes and transition to turbulence are further illustrated in Figure 3.4. Correlations for the Nusselt data highlighted a dependence on the Prandtl number and aspect ratio in the laminar flow regime, while for the turbulent regime the effects of both parameters were negligible.

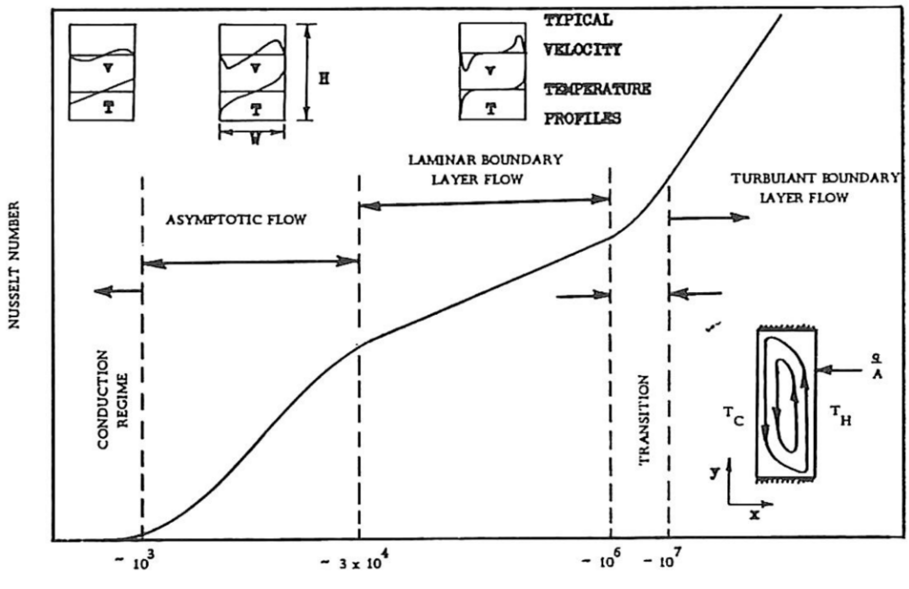

Figure 3.4: Diagram of flow regimes in enclosed vertical cavities[6].

Yin et al.[75] carried out an experimental study for natural convection in a rectangular air-filled cavity. Aspect ratios considered ranged from 4.9 - 78.7 and the Grashof number range was from $1.5 \times 10^3 \leq \mathrm{Gr}_L \leq 7.0 \times 10^6$. Isothermal boundary conditions were imposed on the opposing vertical surfaces. In some of their experimental runs, a temperature inversion of the profiles occurred. They postulated these inversions were tied to the secondary flows observed in Elder's[74] study and arise as a result of the strong tangential convection relative to the vertical heat transfer. Temperature profiles were also noted to be relatively independent of the temperature difference between the isothermal walls.

Elder[7] in a continuation of his earlier laminar study investigated turbulent natural convection in rectangular cavities. Nearly all the reported measurements were for water with a given Prandtl number of 7. The cavity aspect ratios ranged from 10 to 30 and the Rayleigh numbers were $\mathrm{Ra}_L > 10^6$. An increase of the Rayleigh number led to the formation and growth of travelling wave fronts on both the hot and cold surface. Elder[7] found that the onset of transition or the formation of the travelling-waves occurs for a Rayleigh number greater than;

$$\mathrm{Ra}_{ts,L} = \frac{\left(8 \times 10^8\right) \cdot \sqrt{\mathrm{Pr}}}{\mathrm{A}^3} \tag{3.1}$$

The critical Rayleigh number is dependent on the aspect ratio, and this is in agreement with data from Yin et al.[75] and MacGregor and Emery[6] who both concluded the aspect ratio had a strong influence on the turbulence transition. Elder also suggests a dependence on the Prandtl number based on data from a silicone oil run. Figure 3.5 from Elder[7] illustrated the growth of wall waves and eventual transition to turbulence. Temperature profiles across the cavity in turbulent flow showed large temperature gradients near the walls with a uniform temperature core. The turbulent interior was stated to extend to the ends with a further increase of Rayleigh number.

Transitional and turbulent natural circulation in an annular enclosure was experimentally investigated by Weidman and Mehrdadtehranfar[76] for water-glycerol mixtures. The Prandtl number was between 15 to 150, with Ra_L ranging from 10^4 to 10^6. Aspect and radius ratios were given as 64 and 0.62, respectively. Their data showed a Prandtl number dependence to the onset of transition similar to Elder[7]. The critical Rayleigh number for the onset of transition were defined as follows for the hot and cold

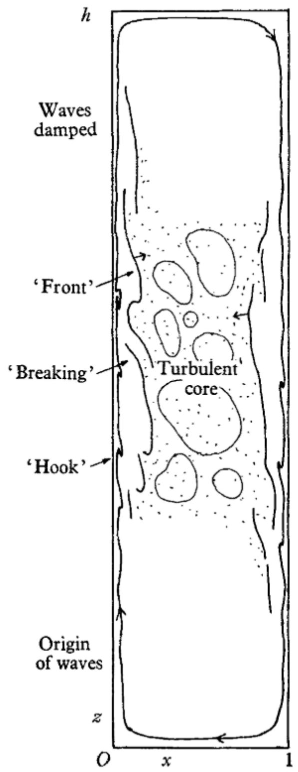

Figure 3.5: Illustration of the formation of wall-waves and transition to turbulence in vertical cavity[7].

wall, respectively ;

$$\mathrm{Ra}_{ts,L} = \frac{\left(1.5 \times 10^{7}\right) \cdot \sqrt{\mathrm{Pr}}}{\mathrm{A}^{3/2}} \tag{3.2a}$$

$$\mathrm{Ra}_{ts,L} = \frac{\left(2.5 \times 10^{7}\right) \cdot \sqrt{\mathrm{Pr}}}{\mathrm{A}^{3/2}} \tag{3.2b}$$

At the onset of transition, horizontal travelling ring waves were noted on both interior and exterior cylindrical surfaces with a largely stagnant core. These rings travelled in the direction of fluid before merging at the ends. Increasing the Rayleigh number beyond the critical value led to a turbulent transition with a turbulent core forming. It should be noted, the authors admittedly point out their data had relatively large uncertainties for the Rayleigh numbers due to difficulties in surface temperature measurements.

Betts and Bokhari[77] performed experimental measurements for natural convection of air in a vertical enclosure. The aspect ratio of the cavity was 28.6 at Rayleigh numbers $\mathrm{Ra}_{ts,L}$ of 0.86×10^{6} to 1.43×10^{6}. The experiments performed by Betts and Bokhari used a modified test rig from Dafa'Alla and Betts[78]. Earlier experiments by Dafa'Alla[78] had struggles implementing well-defined boundary conditions in-particular at the junction between the adiabatic top and bottom walls with the heating vertical wall. Betts and Bokhari[77] modified the test rig to ensure well-defined boundary conditions; isothermal boundary conditions were imposed on the hot and cold wall, with a partially conducting top and bottom surface. In the turbulent region, the hot and cold boundary layers strongly interacted with each other leading to peak velocity fluctuations occurring in the core of the cavity. As a result, profiles for the velocity and temperature had a linear gradient across the core, this is contrary to the distributions observed for low aspect ratio cavities. Cheesewright[10] studied a cavity with an aspect ratio of 5 and at the core, the flow was quiescent with uniform temperature. Other investigators have made similar observations for low aspect ratio cavities[6, 79, 80].

Experimental studies for natural convection in rod bundles are rarely reported in the literature. The few that have been found are reviewed below.

Natural circulation in square rod bundle arrays was experimentally investigated by Keyhani et al.[81]. The test configurations studied consisted of a 3 x 3 and a 5 x 5 rod bundle, with pitch-to-diameter ratios of 3.08 and 2.25, respectively. The characteristic length used was that of the containment diameter (D). For the 3 x 3 bundle, the resulting aspect ratio was $H/D = 10.62$ and the Rayleigh number range was $1.95 \times 10^4 \leq \mathrm{Ra}_D \leq 4.5 \times 10^7$. The aspect ratio for the 5 x 5 case was $H/D = 5.79$ and the Rayleigh number range was $2.6 \times 10^5 \leq \mathrm{Ra}_D \leq 1.06 \times 10^9$. Three fluids which are helium, air, and water were considered for the 3 x 3 bundle. Their overall Nusselt number correlations for the boundary layer flow regime stated are $0.072\mathrm{Ra}_D^{0.332}$ for helium/air and $0.151\mathrm{Ra}_D^{0.274}$ for water. However, for the 5 x 5 bundle only helium was studied and the Nusselt number correlation is $0.095\mathrm{Ra}_D^{0.323}$. A flow visualisation study was also carried out for the 3 x 3 bundle. The containment was switched to one made of acrylic giving an aspect ratio $\big(H/D\big)$ of 11.81 and the flow was visualised using suspended aluminium powder in ethylene glycol. The Rayleigh number of the study was $\mathrm{Ra}_D = 2.92 \times 10^7$ and the Prandtl number was 46.4. The flow observations showed that there was a boundary layer on the rod surfaces. At the sub-channel centres, between the rods, there was no flow interaction. Interestingly, the authors noted that there was a low magnitude downward flow here. At the end-regions cross flow was observed.

McEligot et al.[82] studied natural convection in an air-filled rod bundle consisting of three cooling rods arranged in a triangular array with a central heating slender rod. An acrylic shroud surrounded the rods and the whole assembly was encased using a top and a bottom plate, with adiabatic and uniform temperature boundary conditions, respectively. Rayleigh numbers based on the rod diameter were 2.9×10^4 to 4.6×10^5. The Nusselt number correlation for the heating rod surface was $\mathrm{Nu}_D \left(T_h/T_c\right) = 0.156\mathrm{Ra}_D^{1/3}$.

3.1.5 Numerical and analytical studies for natural convective flow in enclosures

Batchelor[83] analytically investigated natural convection in air-filled rectangular cavities intending to determine the Rayleigh numbers and aspect ratios at which the flow regimes occur. Aspect ratios considered ranged from 5 to 200. At small Rayleigh numbers, giving a limit of $\mathrm{Ra}_L = 10^3$, he concluded that the heat transfer would be dominated by conduction. Fixing the aspect ratio and increasing the Rayleigh number, Batchelor[83] predicted steep temperature and velocity gradients only near the wall, with a core of uniform temperature. The suggested isothermal core was wrong as seen for example by Elder's[74] experimental investigations.

Natural convection in rectangular cavities was analytically and numerically investigated by Kimura and Bejan[84]. On the heating and cooling walls, a constant heat flux boundary condition was applied, and the wall separation distance varied such that the aspect ratio ranged from 1 to 3. Water with a given Prandtl number of 7 was the fluid under consideration and the Rayleigh number based on the cavity heightRa_H ranged from 3.5×10^5 to 2.835×10^8. A stratified stagnant core with a vertical linear temperature gradient similar to that at the wall was predicted. Flow at the boundary was predicted to be of constant boundary layer thickness.

Turbulent natural convection in rectangular cavities was numerically studied by Ince and Launder[8]. A modified low-Reynolds-number $\kappa - \epsilon$ turbulence model by Jones and Launder[85] was used. The authors altered the turbulence model by introducing the general gradient diffusion hypothesis by Daly and Harlow[86] to solve the turbulent flux. Temperature predictions against data from Dafa'Alla[9] for a tall cavity and the low-aspect-ratio data from Cheesewright[10] were good. Velocity profiles for the high-aspect-ratio and low-aspect-ratio cases are shown in Figure 3.6, which also serves an example of the difference in flow profiles between the high and low-aspect-ratio cavities.

Kumar and Kalam[87] numerically investigated laminar flow in annular enclosures with a hot inner wall and cooling outer wall. Rayleigh (Ra_L) numbers considered in their simulation ranged from 10 to 10^6. Radius and aspect ratios were 1 to 15 and 0.3 to 10, respectively. At $\mathrm{Ra}_L = 2 \times 10^5$ and aspect ratio of 1, it was shown increasing the diameter ratio led to lower core temperatures, steeper temperature gradients on the hot inner-surface, with shallower temperature gradients on the cold exterior surface. Temperature inversions were also noted at the lower diameter ratios.

The physical mechanisms for the temporal and spatial onset of transition in rectangular cavities were investigated using DNS simulations by Paolucci and Chenoweth[88]. At the critical Rayleigh number, turbulence transition was a result of instabilities in the vertical boundary layer. However, at aspect ratios $0.5 < \mathrm{A} < 3$, internal waves near the departing corners led to transition. Departing corners were defined as where the flow is ejected to the interior cavity from the side wall boundary layers. At significant Rayleigh numbers (much larger than the critical value) both transition instabilities could be present.

Hsieh and Lien[89] compared numerical predictions obtained using variants of the $\kappa - \epsilon$ low-Reynolds-number model by Lien and Leschziner[90]. Comparisons were made against experimental data from the tall cavity case of Betts and Bokhari[77], and the square cavity data from Tian and Karayiannis[91]. In the tall cavity case, the Lien and Leschziner[90] model predicted reasonable temperature and velocity fields. It was found Nusselt number predictions were further improved by incorporating the non-linear relation by Shih et al.[92]. The square cavity case required the use of URANS due to the transitional nature of the flow. Furthermore, low levels of turbulence meant, the $\kappa - \epsilon$ models tended to relaminarize the flow. To improve the flow predictions, the model by Lien and Leschziner[90] was modified using the non-linear stress-strain relation by Speziale[93]. The authors concluded that further improvements to the ϵ equation were needed to improve the Nusselt number predictions.

Ammour et al.[94] used several turbulence models implemented in the CFD solver *Code_Saturne* to simulate free convection in vertical and inclined cavities. The vertical cavity comparisons were against data from the Betts and Bokhari case study[77]. In

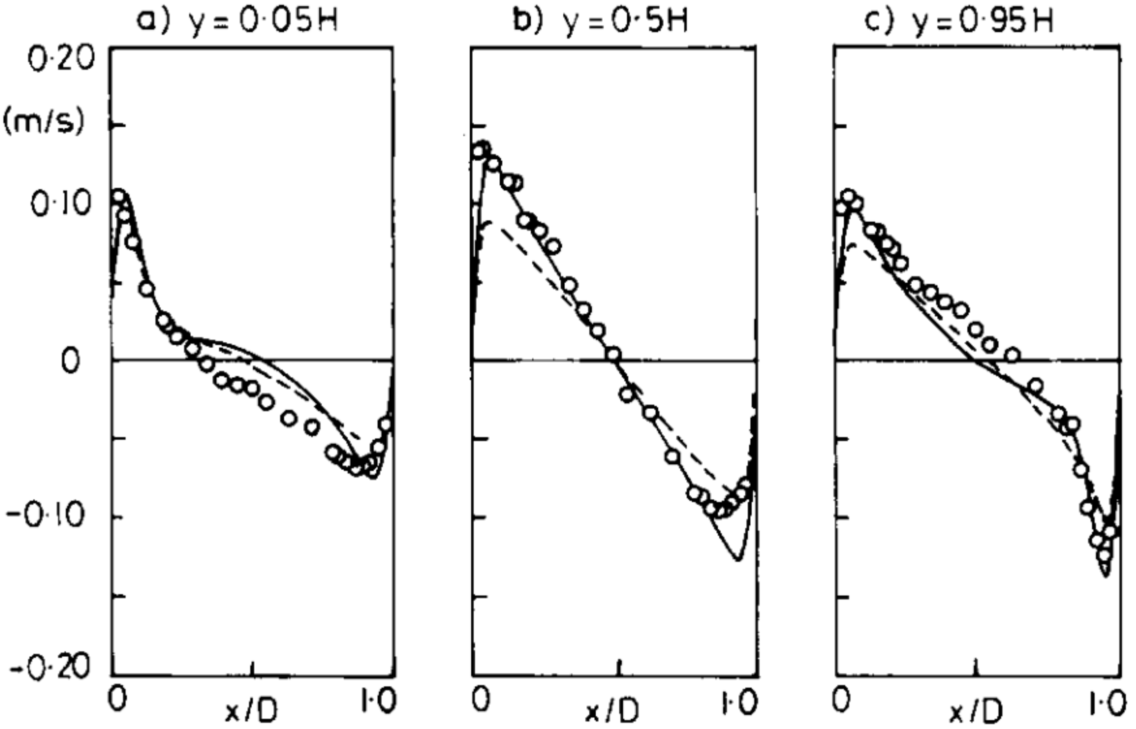

(a) High-aspect-ratio comparison (A = 30)

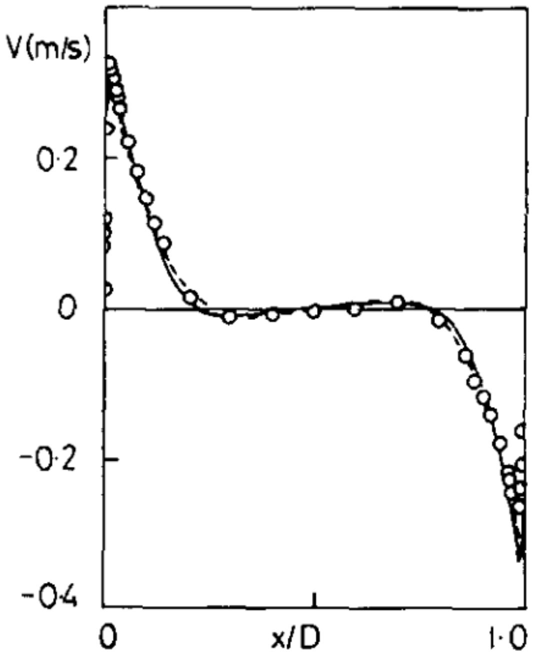

(b) Low-aspect-ratio comparison (A = 5)

Figure 3.6: Velocity profiles taken from Ince and Launder[8]. Subfigure (a) is the velocity comparison for the high-aspect-ratio case against data from [9]. Subfigure (b) is the low-aspect-ratio comparison against data from Cheesewright[10].

general, they noted the RANS models qualitatively predicted the flow and thermal fields. The $v^2 - f$ model by Durbin[95] had better agreement with experimental data for the vertical case. In the inclined cavity case, the $v^2 - f$ model did not converge and instead the modified version by Laurence[96] had better predictions.

Barhaghi and Davidson[79] used coarse DNS and LES to study the natural convection boundary layer in a sealed-tall cavity with an aspect ratio of 5. In their LES computations, the dynamic, Smagorinsky and WALE models were tested. The authors further considered the influence of the grid resolution on the obtained results, by refining the streamwise and spanwise mesh resolutions by a factor of two for the LES computations. In the wall-normal direction, the grid was maintained at 98 divisions with a given y^+ value of ≈ 0.6. Results obtained suggested the convectional grid resolutions used in shear flows were not appropriate for use in natural convective flows. In particular, within the transition region the accuracy of the solution was highly grid dependent. While in the turbulent region the solution was indifferent to the grid resolution. The authors also noted the onset of transition was predicted at different locations by the various subgrid models, with the authors contending transition onset was better predicted using the Dynamic model. Kizldarg et al.[97] investigated the onset of transition in a water-filled cavity with a Prandtl number of 4.31 and an aspect ratio of 5. They compared several subgrid models against DNS data and found the WALE model to perform better than the other models tested with excellent comparisons against the DNS data.

Shati et al.[98] numerically and theoretically studied natural convection in rectangular cavities with and without the effects of surface radiation. Temperature ratios up 2.6 and aspect ratios ranging from 0.06 to 16 were investigated. For their numerical simulations, turbulence was modelled using the RNG $\kappa - \epsilon$ model and radiation using the Discrete Radiation Transfer model. Correlations for a new dimensionless group were produced by the authors. In a later paper, Shati et al.[99] provided an empirical solution for such enclosures and a correlation to calculate the total Nusselt number.

A numerical investigation for laminar natural convection in a sub-channel of a seven-rod bundle array was carried out by Rao and Glakpe [100, 101] for Rayleigh numbers ranging from 10^2 to 10^8. Predictions at low Rayleigh numbers showed that the flow was in the pseudo-conduction regime. At higher Rayleigh numbers thermal stratification was the result of strong boundary layer flow. It was noted that using mixed boundary conditions (heat flux on the rod walls and isothermal containment) in comparison to isothermal boundary conditions, led to differences in the flow and temperature fields. Heat transfer characteristics were also affected.

3.2 Porous media approach

Reactor cores are complex environments typically consisting of hundreds of fuel channels. Each channel would contain a fuel bundle in turn comprising of numerous rods, differing types of sub-channels, bracers, etc. A common problem for nuclear thermal analysts more so during the mid-to-end of the 20th century when computational power was a scare commodity, was how to effectively analyse such systems especially for non-design conditions. Ultimately, this led to the development of 1-D system codes where for example the fuel channel or the entire reactor core is treated as a lumped region thus a representation of the flow in the entire reactor system could be obtained and 1-D sub-channel codes where the lumped regions correspond to the sub-channels. Although such methods have their use, there is still a desire to take into account the 3-D flow phenomena without necessarily incurring the computational cost of traditional CFD methods. This has resulted in other simplifications being developed such as the porous media methodology[102] or the much more recent coarse grid CFD methods[103, 104].

Generically, a porous medium consists of both solid and fluid phases. Within this mixture, pores or voids exist such that the solids are only in direct contact with the fluid at the interfaces, this can be observed in Figure 3.7.

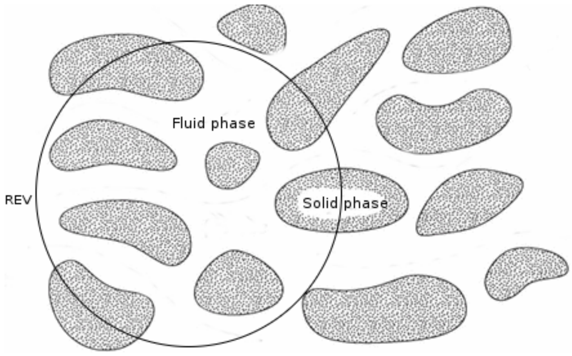

Figure 3.7: Definition of a Relative Elementary Volume for a porous medium[11]

Directly simulating these solid-fluid interactions and attempting to resolve the boundary layer flow would be complicated and numerically expensive. A common approach adopted for analysing such mediums is to divide the domain of interest into multiple regions as defined by Relative Elementary Volume (REV). In defining the size of the REV, the following guidelines are in place:

- The REV should be smaller than the large scale flow phenomena of interest.
- Conversely, the REV must be larger than local microscopic scales.

As stated earlier, the porous medium approach is based on defining volume averaged regions. Within these regions, the solids are assumed to be homogeneously dispersed, their geometric effect on the flow (reduction in flow area) is accounted via porosity and the physical effects (flow resistance and heat transfer) are recovered through the distributed resistance and volumetric heat generation terms. These terms are further described later in this section.

To derive the incompressible macroscopic governing equation for momentum the *Navier-Stokes* equation given in Equation 3.3 is averaged in time and space. Equation 3.3 is written without any averaging operations and neglecting buoyancy.

$$\frac{\partial u_i}{\partial t} + \frac{\partial u_i u_j}{\partial x_j} = -\frac{1}{\rho}\frac{\partial P}{\partial x_i} + \frac{\partial}{\partial x_j}\left[v\left(\frac{\partial u_i}{\partial x_j} + \frac{\partial u_j}{\partial x_i}\right)\right] \tag{3.3}$$

Spatial averaging for a porous medium is performed on volume averaged regions as defined by the REV. The volume average operators used are the volumetric average operator $\langle\phi\rangle = \frac{1}{V}\int_{V_f}\phi dV$ and intrinsic average operator $\langle\phi\rangle^i = \frac{1}{V_f}\int_{V_f}\phi dV$. In the fluid momentum and energy equations the intrinsic variable is solved for and the two aforementioned average operators can be related to each other by $\langle\phi\rangle = \alpha_v\langle\phi\rangle^i$ and noting $\phi = \langle\phi\rangle^i +^i \phi$. The term α_v represents the volumetric porosity, which is defined as $\alpha_v = 1 - \frac{V_s}{V_T}$. Where V_s is the solid volume and V_t is the total volume.

The time average operator is defined as $\overline{\phi} = \frac{1}{\Delta t}\int_t^{t+\Delta t}\phi dt$ and is used to take into account fluctuations of the variable ϕ as a result of turbulence.

Volume and time averaging are carried out on the standard Navier-Stokes equation given in Equation 3.3, yielding the macroscopic governing Equation 3.4. For brevity the procedure is not described in this chapter. An in-depth derivation can be found in the paper by Pedras and De lemos[105] and the equation below is from Drouin[106]. .

$$\alpha_v \frac{\partial \langle \overline{u_i} \rangle^i}{\partial t} + \frac{\partial \alpha_v \langle \overline{u_i} \rangle^i \left\langle \overline{u_j} \right\rangle^i}{\partial x_j} = -\frac{1}{\rho} \frac{\partial \alpha_v \left\langle \overline{P} \right\rangle^i}{\partial x_i} + \frac{\partial}{\partial x_j} \left(v \frac{\partial \alpha_v \langle \overline{u_i} \rangle^i}{\partial x_j} \right) - \frac{\partial \alpha_v \left\langle \overline{u_i' u_j'} \right\rangle^i}{\partial x_j}$$
$$- \frac{\partial \alpha_v \left\langle \delta \overline{u}_i \delta \overline{u}_j \right\rangle^i}{\partial x_j} + \alpha_v \left\langle \left(v \frac{\partial \overline{u}_i}{\partial x_j} - \frac{\delta \overline{P}}{\rho} \delta_{ij} \right) n_j \delta \right\rangle^i \tag{3.4}$$

As can be noted three additional terms arise out of the double averaging procedure.

- The third term on the right-hand side $\left(\frac{\partial \alpha_v \left\langle \overline{u_i' u_j'} \right\rangle^i}{\partial x_j} \right)$ is the macroscopic shear stress and modelled using a turbulence model.
- The fourth term on the right-hand side $\left(\frac{\partial \alpha_v \left\langle \delta \overline{u}_i \delta \overline{u}_j \right\rangle^i}{\partial x_j} \right)$ represents dispersion[106] and can be treated as an additional momentum loss. In general dispersion is ignored or coupled with the distributed resistance term.
- The final term on the right-hand side $\left(\alpha_v \left\langle \left(v \frac{\partial \overline{u}_i}{\partial x_j} - \frac{\delta \overline{P}}{\rho} \delta_{ij} \right) n_j \delta \right\rangle^i \right)$ represents the total drag imposed by solid phase within the porous medium. It consists of contributions due to form and viscous drag. In this thesis this term is called distributed resistance.

The fluid phase energy equation can be derived in a similar manner. Equation 3.5 represents the typical governing equation assuming non-thermal equilibrium[107].

$$\alpha_v \rho_f \mathrm{Cp}_f \left[\frac{\partial \langle \overline{T} \rangle^{f,i}}{\partial t} + \frac{\partial \langle u_i \rangle^{f,i} \cdot \langle \overline{T} \rangle^{f,i}}{\partial x_i} \right] = \frac{\partial}{\partial_{x_i}} \cdot \left[\alpha_v k_f \frac{\partial \langle \overline{T} \rangle^{f,i}}{\partial x_i} + \frac{1}{V_T} \int_{A_{fs}} k_f \overline{T} dA - \right.$$
$$\left. \alpha_v \rho_f \mathrm{Cp}_f \left(\langle {}^i\overline{u}_i^i \overline{T} \rangle^i + \overline{\langle u_i' \rangle^i \langle T' \rangle^i} + \left\langle \overline{{}^i u_i' \cdot {}^i T'} \right\rangle^i \right) \right]$$
$$+ \frac{1}{V_T} \int_{A_{fs}} k_f \frac{\partial \overline{T}}{\partial x_i} dA \tag{3.5}$$

Looking at 3.5 heat transfer between the two phases occurs through, $\frac{1}{V_T} \int_{A_{fs}} k_f \frac{\partial T}{\partial x_i} dA$, which is the interfacial heat transfer term. In literature this term is equated to Newton's law of cooling[107, 108]. Other terms of note contained in:

$$\alpha_v \rho_f \mathrm{Cp}_f \left(\langle {}^i\overline{u}_i^i \overline{T} \rangle^i + \overline{\langle u_i' \rangle^i \langle T' \rangle^i} + \left\langle \overline{{}^i u_i' \cdot {}^i T'} \right\rangle^i \right) \tag{3.6}$$

refer to thermal dispersion, turbulent heat flux and turbulent thermal dispersion, respectively. Turbulent heat flux can be modelled using the eddy viscosity assumption and specifying a turbulent Prandtl number.

The above cited equations are derived for a generic porous medium and contain terms which can be combined, dropped or simplified for the present purpose. The equations are now re-written in a simplified form and with regards to how they are implemented in *Code_Saturne*.

The momentum and energy equation for an incompressible fluid are shown in equations 3.7 and 3.8, respectively.

$$\alpha_v \frac{\partial \rho \langle \overline{u_i} \rangle^i}{\partial t} + \frac{\partial \rho \alpha_{ij} \langle \overline{u_i} \rangle^i \langle \overline{u_j} \rangle^i}{\partial x_j} = -\frac{\partial \alpha_v \langle \overline{P} \rangle^i}{\partial x_i} + \alpha_v \rho g + \frac{\partial}{\partial x_j} \left[(\mu + \mu_t) \left(\frac{\partial \alpha_{ij} \langle \overline{u_i} \rangle^i}{\partial x_j} + \frac{\partial \alpha_{ij} \langle \overline{u_j} \rangle^i}{\partial x_i} \right) \right] + \alpha_v S_v \tag{3.7}$$

$$\rho_f \mathrm{Cp}_f \left[\alpha_v \frac{\partial \langle \overline{T} \rangle^{f,i}}{\partial t} + \langle \overline{u_i} \rangle^{f,i} \cdot \alpha_{ij} \frac{\partial \langle \overline{T} \rangle^{f,i}}{\partial x_i} \right] = \frac{\partial}{\partial_{x_i}} \cdot \left[\alpha_v \left(k_f + \frac{\mu_t \mathrm{Cp}_f}{Pr_t} \right) \frac{\partial \langle \overline{T} \rangle^{f,i}}{\partial x_i} \right] + \alpha_v Q_{s/v} \tag{3.8}$$

As can be noted for the momentum equation the term for distributed resistance is now represented by S_v. This term is derived from resistance correlations specific to AGR bundles. Similarly, for the energy equation a source term $Q_{s/v}$, describing heat transfer between the solid and fluid phases is included. In the model this would typically describe a heat source due to the presence of the fuel pins. Another term to be modelled is turbulent viscosity (v_t), which describes the turbulent diffusion of momentum. Finally, the above equations introduce the term α_{ij}, which is the area porosity tensor. This term differs from volumetric porosity as it describes the flow area available in a particular direction, while the volumetric porosity term is essentially a scalar.

3.2.1 Numerical studies using the porous medium approach

Commix-1 is a rod bundle thermal hydraulics analysis code utilising the porous medium approach developed by Sha et al.[102]. In their method, they split the fuel assembly into homogenised volumetric regions containing both the fluid and solid. To take in to account the geometric effect of the now dispersed solid both volumetric and anisotropic porosity were used. The pressure loss was taken into account through a distributed resistance term and the heating was accounted for by a volumetric heating source. Compared to the sub-channel analysis approach, which has been traditionally used in nuclear applications, this method has the advantage of a greater range of applicability and is fully 3-D.

In the case of Rahimi and Jahanfarnia[109], they used the porous media approach to predict coolant flow and temperatures in a VVER-1000 reactor core. In their study, each channel was discretised axially and the resulting volume was then treated as a homogeneous porous region. In a later paper, the authors then applied the porous media approach to Super Critical Water Reactor (SCWR)[110].

Chen et al.[111] used the porous media approach to simulate the PWR reactor core and upper plenum. They validated their model by comparing against experimental data for the flow rate and pressure drop from a scaled test section of the reactor. The developed model was then used to investigate flow and thermal behaviour of the coolant after the steam generator had ruptured.

A multi-physics code for the reactor core was developed by the FAST group[112]. The solver for thermal-hydraulic analysis could model the core and other selected zones using the porous medium approach, while the non-porous zones could be modelled using the typical CFD approach and a $k - \epsilon$ model. However, in the porous zone, the $k - \epsilon$ model was not used, and instead, user-defined values were given for k and ϵ. The code could couple the thermal-hydraulic solver to the thermal displacement, neutronics, and conduction solvers.

A model for analysing steam generators in horizontal and vertical configurations by utilising the porous media approach was developed by Hovi et al.[113]. Their approach coupled a 1-D steam generator system code to a porous media CFD model, which was used to calculate the thermal flow for the steam generator's secondary side. The coupling method only permitted the computed outer wall tube temperatures from the system code to be passed as boundary conditions (one-way coupling). Turbulence in the porous model was calculated using the standard k-ϵ model. However, as noted by the authors this does not take into consideration the additional turbulence production and dissipation terms arising due to the dispersed solids. Nonetheless, their comparisons against experimental data showed good agreement.

Miku and Roelofs[114] used porosity to model the intricate mixing vanes, which are used to increase flow mixing through the fuel assembly. To reproduce the secondary flow patterns and magnitudes observed from the "detailed" CFD models, the authors specified additional momentum sources.

Coarse Grid CFD (CGCFD) is an alternative approach to improve upon the 1-D sub-channel and porous media methods but yet still keeping the computational expense at a minimum compared to the traditional CFD approach[103, 104, 115].

Viellieber and Class[103] combine the CGCFD method with the porosity approach to model the influence of the spacers on the flow, as these were not resolved in their CGCFD model. In CGCFD, the mesh is coarse and the flow is considered inviscid thus simplifying the Navier-stokes equations into the Euler form. To take into account the frictional and turbulent losses a volumetric source is added. These volumetric sources were calculated from detailed simulations in a "unit respective region" and the identification of this representative region requires a great deal of care. Volumetric sources obtained from the respective region are parametrised before being applied onto the coarse grid. With this approach, the authors obtained momentum loss due to the influence of the rod bundle. In the spacer region, volume and area porosities were combined with the CGCFD approach so as to describe its geometrical effects, i.e reduction in flow area. Favourable results have been obtained although the authors only compared their results to RANS simulations.

Liu et al.[104] developed a new CGCFD approach termed Sub-Channel CFD (SubChCFD). They used a two-layer mesh approach: The top layer filtering mesh, corresponds to the sub-channel (as typically defined in sub-channel codes) and the bottom layer computing mesh upon which the solution was computed and mixing length turbulence model implemented. Contrasting to the approach by Viellieber and Class[103], Liu et al.[104] use sub-channel empirical correlations to compute the pressure loss and heat transfer.

Capone et al.[116] used a similar approach to Viellieber and Class[103], to model the presence of mixing vanes in a coarse grid representation of reactor fuel assemblies. The authors first conducted a detailed simulation of flow over the mixing vanes, from which they obtained momentum and Reynolds stress source terms. They used the SSG RSM in the detailed model. The source terms were applied to the coarse grid and the results obtained were favourable, although there were inaccuracies for the predicted pressure drop.

Turbulence modelling in porous media is particularly difficult. For example, Hovi et al.[113] resort to using the standard $k-\epsilon$ model without corrections, while the code by Fiorina [112] uses user-defined fixed constants for k and ϵ. In the following paragraphs, EVM models proposed in the literature and those using the RSM are discussed.

Turbulence models used in the porous media approach are derived by double averaging (Temporal and spatial averaging) their microscopic defined counterparts. Unlike the momentum and energy equations where the order of averaging is of no consequence, for turbulent kinetic energy different governing equations are obtained depending on the order of averaging used[105]. Pedras and de lamos[117] have shown that to account for fluctuations at the pore scale the Reynolds average has to be applied first.

Nakayama and Kuwahara[118] developed a turbulence model for flow in porous media. To derive their model they spatially averaged kinetic energy production and dissipation terms for turbulent viscosity, $\mu_t = c_\mu \frac{k^2}{\epsilon}$, from the standard k - ϵ definition. As a consequence of the averaging operation, an additional source term associated with the internal production of turbulence in the porous medium arises in k. Similarly for ϵ, there is an additional dissipation rate source term due to immersed solids. The additional source terms were closed by intrinsically averaging steady-state results obtained from a detailed simulation for transverse flow in an infinite array of square rods. Their proposed turbulence model was validated by comparing macroscopic predicted turbulence quantities to those from a detailed simulation after intrinsic averaging. Results obtained from the comparison showed good agreement away from the domain entrance, while near the entrance there were appreciable differences. In obtaining the additional coefficients the authors assumed that the additional coefficients obtained for developed and steady-state flow were equally applicable when flow conditions do not meet this specification.

Chandesris et al.[119] adopting a similar approach to that used by Nakayama and Kuwahara derived a macroscopic turbulence model based on the k -ϵ equation. A porous medium characterised by elongated geometries and longitudinal flow is defined as the unit structure to obtain the additional source terms. This definition is chosen as they are interested in studying flow in the nuclear reactor core. Contrary to the approach of Nakayama and Kuwahara, a kinetic energy balance is first considered before integrating microscopic results to close the unknowns. Model validation was performed by comparing the results for the decay of turbulent quantities. Comparisons were made against experimental work for rod bundles and a CFD simulation for pipe flow. Kuwata and Suga[120] proposed a macroscopic turbulence model based on the second moment closure. In their model the inertial dispersion term was modelled through the eddy viscosity concept. This is in contrast to the models by Nakayama[118] and Chandesris [119] where the term was combined with distributed resistance (see Equation 3.4 for description of inertial dispersion term). To apply the closure method, the Reynolds stress term is further decomposed into two terms which are macro-scale and micro-scale Reynolds stress. These are shown respectively on the right hand side of the following equation $\langle\overline{u_i'u_j'}\rangle^i = \overline{\langle u_i'u_j'\rangle^i} + \overline{\langle u_i'\rangle^i\langle u_j'\rangle^i}$. Similar to the dispersion term the micro-scale Reynolds stress is modelled through the eddy viscosity concept while the macro-scale Reynolds stress is modelled by adapting the two_component_limit second-moment closure by Craft and Launder. The model was tuned against channel flows and flows through square arrays with satisfactory results.

Moner and Radespiel[121] used the porous media approach to simulate high Reynolds number flow in a channel partially filed with a porous medium. They developed a macroscopic Reynolds stress model and imposed a stress jump condition at the interface between the porous medium and clear flow.

3.3 Conclusion

The literature review has covered over the two main research aims of the thesis that is (i) to investigate the flow physics in rod bundle under forced and buoyancy induced flows, and (ii) to develop and validate a 3D CFD model for fuel bundles based on the porous media approach.

In sub-section 3.1.1 and 3.1.2, phenomena and flow physics in rod bundle arrays for forced convection flows have been investigated. Secondary flows and pseudo-periodic flow pulsations have been observed to be important features of such flows and have been studied by various researchers. The strengths of such flows are a function of the rod gap spacing, e.g. [5, 33]. To simulate such flow phenomena, it has been shown that transient methods such as URANS are necessary to capture the time-varying pseudo-periodic pulsation and anisotropic turbulence models are required to capture the secondary flows, which arise due to the anisotropy of the Reynolds stress. However, as shown by researchers such as Baglietto[55], if the P/D is large in this case > 1.1 then the RANS method is sufficient as the pseudo-periodic pulsation is weak. Studies into damaged rod bundles have shown the flow and thermal characteristics are drastically altered in the constricted sub-channels. However, no numerical simulations have been conducted for any of the typified damage configurations which can arise after a fuel drop in the AGR fuel route. In chapter 7 a damaged Wheatsheaf bundle is numerically investigated to understand the flow phenomena and physics in such a uniquely distorted geometry. Understanding the aforementioned is important with regards to maintaining safety in the unlikely event of dropped/damaged fuel during re-fuelling procedures.

Buoyancy induced flows in a variety of vertical geometries have been covered in subsections 3.1.3 to 3.1.5. These studies have revealed the near-wall behaviour in buoyancy induced flows is different from that for forced convection flows. In cavities, the natural circulation flow regime is shown to be a function of three dimensionless numbers, that is the Rayleigh number, aspect ratio, and Prandtl number. Results from Elder[7] and Betts and Bokhari[77] have highlighted the unique natural circulation flow features in highly turbulent cavities. The literature survey has however pointed out a distinct lack of natural circulation studies in the more complex geometries such as rod bundles. The few studies reported in the literature only provided limited information on heat transfer correlations and nothing on flow physics. In chapters 5 and 6, numerical simulations using the LES method are carried out for an AGR rod bundle (based on a 60 ° sector by taking the advantage of symmetry) of small (height of bundle is 0.25 m) and large aspect ratio (height of bundle is 1 m), respectively.

In section 3.2, the use of the porous media methodology as a tool for simplifying nuclear thermal hydraulics analysis while still retaining the 3-D flow features, and hence improving upon the sub-channel method, has been discussed using multiple case studies in literature. It has been shown that this method has a wide range of applicability making it suitable for the complex fuel bundle damage configurations, which can arise from fuel drops within the fuel route. Although, there has been a particular focus on the modelling of the fluid porous zones there has been no similar level of analysis on the conduction and radiation modelling of the solid components required in the current study as explained later. Drops in the fuel route can lead to scenarios where the flow is blocked and natural convection prevails. In such scenarios thermal radiation becomes an important mode of heat removal. In chapters 8 to 10, the development, validation, and case studies of a new 3-D AGR damaged fuel model are given.

Chapter 4

Turbulent flow modelling and numerical methods

Turbulent flows play a prominent role in a lot of industrial fluid flow scenarios with their importance best demonstrated from the early and well known Osborne Reynolds experiments, where it was shown turbulence greatly enhances the transport and mixing processes. Such flows are chaotic, characterised by fluid fluctuations (spatial and temporal) and eddies of varying scales. This is from the largest anisotropic energy-containing scales, which transfer energy to the smallest isotropic scales where it is dissipated via molecular viscosity. Turbulence modelling involves representing a part (e.g. LES where the unresolved scales smaller than the cut-off length are modelled using a subgrid scale model) or the entirety of the energy cascade process (e.g. URANS where the large and small scales are modelled).

This chapter covers the approaches to turbulent flow modelling, the numerical methods used in the CFD solver *Code_Saturne* and Finite Element Analysis (FEA) software Syrthes. In particular, it focuses on the methodology required for the first part of the thesis, which studies the flow physics and phenomena in rod bundles under a variety of flow conditions.

4.1 Governing equations

Any thermal-hydraulics problem can be described using the (a) continuity, (b) *Navier-Stokes*, and (c) energy equations shown in Equation 4.1 in the incompressible form.

$$\frac{\partial \rho u_i}{\partial x_i} = 0 \tag{4.1a}$$

$$\frac{\partial \rho u_i}{\partial t} + \frac{\partial}{\partial x_j}\left(\rho u_i u_j\right) = -\frac{\partial P}{\partial x_i} + \frac{\partial}{\partial x_j}\left[\mu\left(\frac{\partial u_i}{\partial x_j} + \frac{\partial u_j}{\partial x_i}\right)\right] + \rho g_i \tag{4.1b}$$

$$\rho\left(\frac{\partial T}{\partial t} + \frac{\partial T u_i}{\partial x_i}\right) = \frac{\partial}{\partial x_i}\left(\frac{\mu}{\mathrm{Pr}}\frac{\partial T}{\partial x_i}\right) \tag{4.1c}$$

where ρ is density, Cp is the specific heat capacity, T is the temperature , u_i is the directional velocity component. Although these equations (Equation 4.1) can be solved directly through the Direct Numerical Simulation (DNS) approach this tends to be impractical for most engineering applications due to the complexity of the geometries and high Reynolds numbers frequently encountered. The impracticality of DNS arises as all the temporal and spatial scales have to be resolved. This leads to an ever-increasing computational cost as the Reynolds number increases by approximately Re^3[122].

Two approaches are frequently used for engineering applications. In the first approach, RANS, Equation 4.1 is time-averaged using Reynolds decomposition and the mean variables are solved for (see Section 4.2). However, this statistical averaging process results in a non-linear term of the fluctuating velocity components (arising from the convection term), which have to be modelled. The second approach LES spatially filters Equation 4.1, such that the large anisotropic energy-containing scales are resolved while the isotropic small scales are unresolved. A non-linear stress term arises which represents the influence of the unresolved small scales and is modelled using a sub-grid scale model (see Section 4.4). Both of these approaches have been used in the present thesis.

4.2 URANS approach

Equation 4.1 can be time-averaged by using Reynolds decomposition ($u = \overline{u} + u'$) yielding Equation 4.2.

$$\frac{\partial \rho \overline{u}_i}{\partial x_i} = 0 \tag{4.2a}$$

$$\frac{\partial \rho \overline{u}_i}{\partial t} + \frac{\partial}{\partial x_j}\left(\rho \overline{u}_i \overline{u}_j\right) = -\frac{\partial \overline{P}}{\partial x_i} + \frac{\partial}{\partial x_j}\left[\mu\left(\frac{\partial \overline{u}_i}{\partial x_j} + \frac{\partial \overline{u}_j}{\partial x_i}\right)\right] - \frac{\partial \rho \overline{u_i' u_j'}}{\partial x_j} + \rho g_i \tag{4.2b}$$

$$\rho\left(\frac{\partial \overline{T}}{\partial t} + \frac{\partial \overline{T}\overline{u}_i}{\partial x_i}\right) = \frac{\partial}{\partial x_i}\left(\frac{\mu}{\mathrm{Pr}}\frac{\partial \overline{T}}{\partial x_i} - \rho \overline{u_i' T'}\right) \tag{4.2c}$$

As a result of the averaging process, the Reynolds stress terms arises on the right-hand side $\left(\rho \overline{u_i' u_j'}\right)$ of the momentum equation. In the energy equation, the turbulent heat flux consisting of the fluctuating velocity and temperature variables $\rho \overline{u_i' T'}$ also appears. Both of these terms must be modelled to close the RANS equations.

To model the Reynolds stress term the Boussinesq hypothesis can be invoked in which the term is proportional to the strain rate tensor with the constant of proportionality being the turbulent viscosity (μ_t), for an incompressible flow the relation is given as:

$$\rho \overline{u_i' u_j'} = 2\mu_t S_{ij,\mathrm{strain}} - \frac{2}{3}\rho k \delta_{ij} \tag{4.3}$$

where the term $S_{ij,\mathrm{strain}}$ is the strain rate tensor and defined as:

$$S_{ij,\mathrm{strain}} = \frac{1}{2}\left(\frac{\partial \overline{u}_i}{\partial x_j} + \frac{\partial \overline{u}_j}{\partial x_i}\right) \tag{4.4}$$

By using this approach the problem is now reduced to determining the turbulent viscosity term, which is a function of the flow. The normal stress term $\frac{2}{3}\rho k \delta_{ij}$ is typically added to the pressure. A variety of turbulence models commonly referred to as EVM can be used, these range from but are not limited to zero equation (algebraic) turbulence models where no additional transport equation is solved, one equation models where a single transport equation typically k is solved for and two-equation turbulence models where two additional transport equations are solved.

An alternative to using the Boussinesq hypothesis is to directly model the Reynolds stress term. However, this is usually expensive as six additional transport equations need to be solved. Both of these approaches are of relevance to this thesis as in Chapter 7 RANS is used to study flow in a damaged *WheatSheaf* bundle and a turbulence model study is performed. The turbulence models used, which are the two-equation EVM models k-ϵ and k-ω Shear Stress Transport (SST), and the Speziale-Sarkar-Gatski (SSG) Reynolds stress model.

Turbulent heat fluxes $\left(\rho\overline{u_i'T'}\right)$ can be approximated using the Simplified Gradient Diffusion Hypothesis (SGDH) method:

$$\rho\overline{u_i'T'} = \frac{\mu_t}{\mathrm{Pr}_t}\left(\frac{\partial T}{\partial x_i}\right) \tag{4.5}$$

where μ_t is the turbulent viscosity and Pr_t is the turbulent Prandtl number which is fixed to 0.9.

4.2.1 Two-equation models

The k-ϵ model and k-ω SST model are two equation Eddy Viscosity Models (EVM), which have been used in this thesis. These models are based on the Boussinesq hypothesis and μ_t is obtained by solving two transport equations, one for turbulent kinetic energy and another for turbulent dissipation rate.

$k-\epsilon$ model

Turbulent viscosity is defined as follows for the k-ϵ model:

$$\mu_t = C_\mu \frac{k^2}{\epsilon} \tag{4.6}$$

where C_μ is a constant (this is given later), k is the turbulent kinetic energy and ϵ is the turbulence dissipation rate. The transport equations for k and ϵ are detailed below[123]:

$$\frac{\mathrm{D}(\rho k)}{\mathrm{D}t} = \frac{\partial}{\partial x_j}\left[\left(\mu + \frac{\mu_t}{\sigma_k}\right)\frac{\partial k}{\partial x_j}\right] + P_k - \rho\epsilon \tag{4.7}$$

$$\frac{\mathrm{D}(\rho\epsilon)}{\mathrm{D}t} = \frac{\partial}{\partial x_j}\left[\left(\mu + \frac{\mu_t}{\sigma_\epsilon}\right)\frac{\partial \epsilon}{\partial x_j}\right] + \frac{\epsilon}{k}(C_{\epsilon 1}P_k) - \frac{\epsilon}{k}(C_{\epsilon 2}\rho\epsilon) \tag{4.8}$$

where the constants used in *Code_Saturne* are defined as follows[12]. C_μ = 0.009; σ_k = 1.0; σ_ϵ = 1.3; $C_{\epsilon 1}$ = 1.44; $C_{\epsilon 2}$ = 1.93.

$k-\omega$ SST model

The k-ω SST combines the standard k-ω and k-ϵ models[124], thereby taking advantage of the far-stream performance of the k-ϵ model and the near wall performance of the

k-ω model. Blending of the two standard models is achieved through the function F. Turbulent viscosity is defined as follows:

$$\mu_t = \frac{a_1 k}{\max(a_1\omega, \Omega F_2)} \tag{4.9}$$

where the transport equations solved by the k-ω SST are detailed below:

$$\frac{\mathrm{D}(\rho k)}{\mathrm{D}t} = \frac{\partial}{\partial x_j}\left[(\mu + \mu_t\sigma_k)\frac{\partial k}{\partial x_j}\right] + P_k - \beta^*\rho k\omega \tag{4.10}$$

$$\begin{aligned}\frac{\mathrm{D}(\rho\omega)}{\mathrm{D}t} = \frac{\partial}{\partial x_j}\left[(\mu + \mu_t\sigma_\omega)\frac{\partial \omega}{\partial x_j}\right] + \alpha\frac{\omega}{k}P_k - \\ \beta\rho\omega^2 + 2\rho(1-F)\frac{\sigma_{\omega 2}}{\omega}\frac{\partial k}{\partial x_j}\frac{\partial \omega}{\partial x_j}\end{aligned} \tag{4.11}$$

Constants/parameters for the k-ω SST model used in *Code_Saturne*[12] are: $a_1 = 0.31$; $\beta^* = 0.009$; $\Omega = \sqrt{2S_{ij,\text{strain}}S_{ij,\text{strain}}}$; $F_2 = \tanh\ \max\left(\frac{2\sqrt{k}}{0.009\omega y}, 500\frac{v}{\omega y^2}\right)$; $\sigma_{\omega 1} = 2.0$; $\sigma_{\omega 2} = 1.0/0.856$; $\sigma_{k1} = 1.0$; $\sigma_{k2} = 1.0$; $\beta_1 = 0.075$; $\beta_2 = 0.0828$; $\alpha_1 = \frac{\beta_1}{\beta^*} - \frac{k^2}{\sqrt{\beta^*\sigma_{\omega 1}}}$; $\alpha_2 = \frac{\beta_2}{\beta^*} - \frac{k^2}{\sqrt{\beta^*\sigma_{\omega 2}}}$.

4.2.2 SSG Reynolds stress

The SSG Reynolds stress model[125] is a second-order turbulence model, which directly solves the Reynolds stress terms in the RANS equation. As a result, this model can capture the anisotropy of turbulent stresses. Individual Reynolds stresses are solved along with an equation for turbulent dissipation. Below the transport equation for the Reynolds stresses is shown:

$$\begin{aligned}\frac{\mathrm{D}(\overline{u_i' u_j'})}{\mathrm{D}t} = \frac{\partial}{\partial x_k}\left(v\frac{\partial \overline{u_i' u_j'}}{\partial x_k}\right) + P_{ij} - \frac{2}{3}\delta_{ij}\epsilon \\ + PS_{ij}\end{aligned} \tag{4.12}$$

The modelling of the pressure-strain tensor(PS_{ij}) is important, as this term is responsible for transferring energy from the largest normal stress to the smaller normal stresses. This term is modelled using the pressure strain correlation detailed by Speziale and Gatski[125]. Model constants and parameters are as defined by Speziale and Gatski[125].

4.3 Wall-functions

Close to the wall the effect of viscosity increases and sharp gradients exist for the velocity and computed scalars. To adequately capture the near-wall variation a mesh that gets progressively refined as it approaches the wall is necessary. This in conjunction with a LRN turbulence model that requires the first cell node to be located in the viscous sublayer $\left(y^+ < 1\right)$ is typically sufficient to model the turbulent flow of interest. However, this approach is computationally expensive due to the fine grid required. An alternative but a commonly adopted solution to remove the necessity of fine grids close to the wall is to make use of a wall-function. For wall-bounded turbulent flows, without the presence of adverse pressure gradient, strong buoyancy forces, etc it is known the velocity follows the "law of the wall". The mesh can thus be coarsened with the first node lying in the turbulent region $\left(y^+ > 30\right)$ and the log-law (see Equation 4.13) is used to impose/modify the boundary condition on the flow at the first cell node (i.e. used to estimate the wall shear stress). The Equation for the log-law is given below:

$$u^+ = \frac{1}{\kappa} \ln y^+ + C \tag{4.13}$$

In *Code_Saturne*, κ which is the Von Karman constant is 0.42 and the coefficient C is 5.2[12]. If the roughness of the surface needs to be taken into account the wall-function is modified as follows:

$$u^+ = \frac{1}{\kappa} \ln\left(\frac{y + z_0}{z_0}\right) + C \tag{4.14}$$

In the above equation z_0 is the roughness height. *Code_Saturne* has three types of wall-functions, which are one-scale, two-scale, and scalable available to the user.

4.3.1 One-scale wall-function

The one-scale wall function defines the friction velocity (u^*) using the wall shear stress as $u^* = \sqrt{\tau_w/\rho}$, the non-dimensional velocity can then be defined as $u^+ = u_p/u^*$ where u_p is the node velocity. y^+ is defined as $u^* y/v$, where y is the normal distance of the first cell node to the wall. The definitions for y^+ and u^+ can be substituted into Equation 4.13, which is then solved iteratively to determine u^*.

4.3.2 Two-scale wall-function

In the two-scale wall-function, the friction velocity is recomputed based on the turbulent kinetic energy at the near-wall cell. The friction velocity is now redefined as $u^* = \tau_w/\rho u_k$, where u_k is the velocity based on turbulent kinetic energy. In *Code_Saturne* the term u_k is computed from a blending operation in case of low turbulence levels which is defined as[12]:

$$u_k \equiv \sqrt{F\frac{vu_p}{y} + (1-F)\sqrt{C_u k}} \tag{4.15}$$

where $F = \exp\left(\sqrt{-ky/11v}\right)$. u^+ is computed based on the redefined friction velocity (i.e. $u^+ = u_p/u^*$) similarly the y^+ is computed as $y^+ \equiv yu_k/v$.

4.3.3 Scalable wall-function

In certain cases, for example, if the geometry is complex, there can be difficulties maintaining the required y^+ values for a HRN turbulence model. These models require the first mesh node to have a $y^+ > 30$. To allow for their use, a scalable wall-function can be used which limits the minimum y^+ to 11.06[12]. This prevents the modelling of the viscous sublayer or buffer layer if the first mesh node happens to be within these regions. In *Code_Saturne*, the computed y^+ is redefined as[12]:

$$y_s^+ = \max\left(\frac{u_k y}{v}, y_{\text{lim}}^+\right) \tag{4.16}$$

where y_{lim}^+ is 11.06. As can be seen, the implementation of the scalable-wall function is based on the two scales approach. The redefined dimensionless distance y_s^+ is plugged into the log-law to compute the friction velocity. In this thesis, the scalable wall-function has been used in Chapter 7 to study the *WheatSheaf* bundle.

4.4 LES

The energy cascade has been described earlier but to restate energy is transferred from the large scales (integral subrange), which are said to receive kinetic energy from the mean flow through the inertial subrange to the smallest scales (viscous subrange) where it is dissipated as heat. In LES, the governing equations are spatially filtered such that the large scales are resolved, while the smallest scales are unresolved. A low-pass-filter is applied, where the filtered velocity can be defined as:

$$\langle u\rangle(x,t)=\int u(x',t)G(x,x')dx' \tag{4.17}$$

where the term G is the filter (convolution) kernel. A variety of filters can employed and Pope[122] lists a few of these, however the most common are Box, Gaussian and sharp spectral. Each of these filters has a cut-off length (filter width) $\left(\overline{\Delta}\right)$, which is associated with the control volume. *Code_Saturne* defines the filter width as $\overline{\Delta}=2\left(\Delta x\cdot\Delta y\cdot\Delta z\right)^{1/3}$, as seen the scales twice the size of the control volume are resolved. The decomposition is as follows $u(x,t)=\langle u\rangle(x,t)+u'(x,t)$. where $\langle u\rangle(x,t)$ is the resolved/filtered velocity and $u'(x,t)$ is the residual component. It should be noted unlike in Reynolds decomposition $\langle u'\rangle(x,t)\neq 0$. The influence of the residual (unresolved) scales on resolved scales must be modelled but since the residual components are considered isotropic and universal they can be represented by simpler models (termed subgrid scale models). As the large scales are resolved with the cut-off filter typically located in the inertial subrange LES is generally considered more accurate than URANS.

Applying the filtering operation to the governing Equations (4.1) yields the following spatially filtered equations:

$$\frac{\partial\rho\langle u_i\rangle}{\partial x_i}=0 \tag{4.18a}$$

$$\frac{\partial\rho\langle u_i\rangle}{\partial t}+\frac{\partial}{\partial x_j}\left(\rho\langle u_i\rangle\,\langle u_j\rangle\right)=-\frac{\partial\langle P\rangle}{\partial x_i}+\rho g_i+\mu\frac{\partial}{\partial x_j}\left(\frac{\partial\langle u_i\rangle}{\partial x_j}+\frac{\partial\langle u_j\rangle}{\partial x_i}\right)-\frac{\partial\rho\tau^r_{ij}}{\partial x_j} \tag{4.18b}$$

$$\rho\left(\frac{\partial\langle T\rangle}{\partial t}+\frac{\partial\langle u_i\rangle\,\langle T\rangle}{\partial x_i}\right)=\frac{\mu}{\mathrm{Pr}}\frac{\partial^2\langle T\rangle}{\partial x_i x_i}-\frac{\partial\rho\Pi_{\mathrm{sgs},i}}{\partial x_i} \tag{4.18c}$$

where filtering the momentum equation leaves it open and the term τ^r_{ij}, which represents the residual stress that needs to be modelled. This can be done by computing a subgrid viscosity using a subgrid scale model as shown in Equation 4.19. Similarly, in the energy equation, the term Π needs to be modelled and this can be done using the subgrid viscosity and turbulent Prandtl number.

4.4.1 Subgrid scale models

The residual stress term can be modelled as follows using the subgrid viscosity:

$$\tau_{ij}^{r} = -2v_{\text{sgs}}\langle S_{ij,\text{strain}}\rangle + \frac{1}{3}\tau_{kk}\delta_{ij} \tag{4.19}$$

where $\langle S_{ij,\text{strain}}\rangle$ is defined as $\frac{1}{2}\left(\frac{\partial\langle u_i\rangle}{\partial x_j} + \frac{\partial\langle u_j\rangle}{\partial x_i}\right)$. As discussed earlier, the term Π is computed using the subgrid viscosity and turbulent Prandtl number:

$$\Pi_{\text{sgs},i} = \frac{v_{\text{sgs}}}{\text{Pr}_t}\frac{\partial\langle T\rangle}{\partial x_i} \tag{4.20}$$

The open terms are treated as follows; $\frac{1}{3}\tau_{kk}\delta_{ij}$ is treated by defining a modified pressure (i.e. $\langle P^{*}\rangle = \langle P\rangle + \frac{1}{3}\tau_{kk}\delta_{ij}$), while the turbulent Prandtl number (Pr_t) is defined as a fixed constant.

A variety of subgrid scale models are available to compute v_{sgs}. In *Code_Saturne*, the models available are the Dynamic, Dynamic Smagorinsky and Wall Adapting Local Eddy-viscosity (WALE) model. In the present thesis (Chapters 5 and 6), the subgrid viscosity is computed using the Wall Adapting Local Eddy viscosity (WALE) subgrid model by Nicoud and Ducros[126]. The model improves upon the Smargorinsky by taking into account the strain and rotational rates of the small turbulent structures and the computed subgrid viscosity $\left(v_{\text{sgs}}\right)$ naturally tends to zero near the wall, unlike the other models which can return negative values[126]. This eliminates the need for a damping function and also makes the model numerically stable. Comparisons performed by Nicoud and Ducros[126] also showed the model can handle transitional flows. The WALE model is defined as follows:

$$v_{\text{sgs}} = (\text{C}_{\text{m}}\cdot\Delta)^2 \frac{\left(\langle S_{ij,\text{strain}}^{d}\rangle\langle S_{ij,\text{strain}}^{d}\rangle\right)^{3/2}}{\left(\langle S_{ij,\text{strain}}\rangle\langle S_{ij,\text{strain}}\rangle\right)^{5/2} + \left(\langle S_{ij,\text{strain}}^{d}\rangle\langle S_{ij,\text{strain}}^{d}\rangle\right)^{5/4}} \tag{4.21}$$

where $\langle S_{ij,\text{strain}}^{d}\rangle$ is defined as $\frac{1}{2}\left(\left(\frac{\partial\langle u_i\rangle}{\partial x_j}\right)^2 + \left(\frac{\partial\langle u_j\rangle}{\partial x_i}\right)^2\right) - \frac{1}{3}\delta_{ij}\left(\frac{\partial\langle u_i\rangle}{\partial x_j}\right)^2$. Δ is the grid size, which is computed as $(\Delta x\cdot\Delta y\cdot\Delta z)^{1/3}$. Finally, C_{m} is a model constant and in Code_Saturne is taken to be 0.25.

4.5 Numerical methods in Code_Saturne

Code_Saturne is a finite volume and co-located CFD solver. In the finite volume method, the domain is discretised into a number of control volumes, which can either be structured, unstructured, or a combination of the two. The integral form of the governing equation is solved at each of the control volumes, with the computational node located at the centre.

To begin this section, the generic scalar equation is defined:

$$\underbrace{\frac{\partial \rho\phi}{\partial t}}_{\text{transient term}} + \underbrace{\nabla \cdot (\rho\phi\vec{u})}_{\text{convection term}} = \underbrace{\nabla \cdot (\Gamma\nabla\phi)}_{\text{diffusion term}} + \underbrace{S_\phi}_{\text{source term}} \tag{4.22}$$

where ϕ is a generic variable and Γ is a diffusion coefficient. The scalar equation is integrated over the control volume yielding:

$$\frac{\partial}{\partial t}\int_\Omega (\rho\phi)\, d\Omega + \int_\Omega \nabla \cdot (\rho\phi\vec{u})\, d\Omega = \int_\Omega \nabla \cdot (\Gamma\nabla\phi)\, d\Omega + \int_\Omega S_\phi d\Omega \tag{4.23}$$

As the convection and diffusion terms represent exchanges occurring across the boundaries of the control volume they can be converted into surface integrals using Gauss's theorem, which is written as shown below for vector $\vec{\mathrm{G}}$:

$$\int_\Omega \left(\nabla \cdot \vec{\mathrm{G}}\right) d\Omega = \int_S \left(\vec{\mathrm{G}} \cdot \hat{n}\right) dS \tag{4.24}$$

where $(\hat{n})$ is the unit normal vector at the boundary surface. Applying Gauss's theorem to Equation 4.23 returns:

$$\frac{\partial}{\partial t}\int_\Omega (\rho\phi)\, d\Omega + \int_S (\rho\phi\vec{u}) \cdot \hat{n} dS = \int_S (\Gamma\nabla\phi) \cdot \hat{n} dS + \int_\Omega S_\phi d\Omega \tag{4.25}$$

In the equation, the transient term represents the rate of change of the variable within the control volume, the convective term represents the net flux of the variable across the boundary surfaces due to the flow (transport as a result of convection) and the diffusion term represents the spread of the variable ϕ across the boundaries as a result of diffusion. The source term is the volumetric generation/consumption in the control volume. These integral terms now have to discretised prior to solving the equation, the discretisation process is outlined in the next few subsections for each of the terms.

4.5.1 Spatial discretisation

The spatial discretisation approach in *Code_Saturne* is described in this section. To aid with the visualisation and identification of the geometric notation a sketch of two adjacent control volumes Ω_i and Ω_j is shown in Figure 4.1. In the figure, $\vec{S_{ij}}$ is the

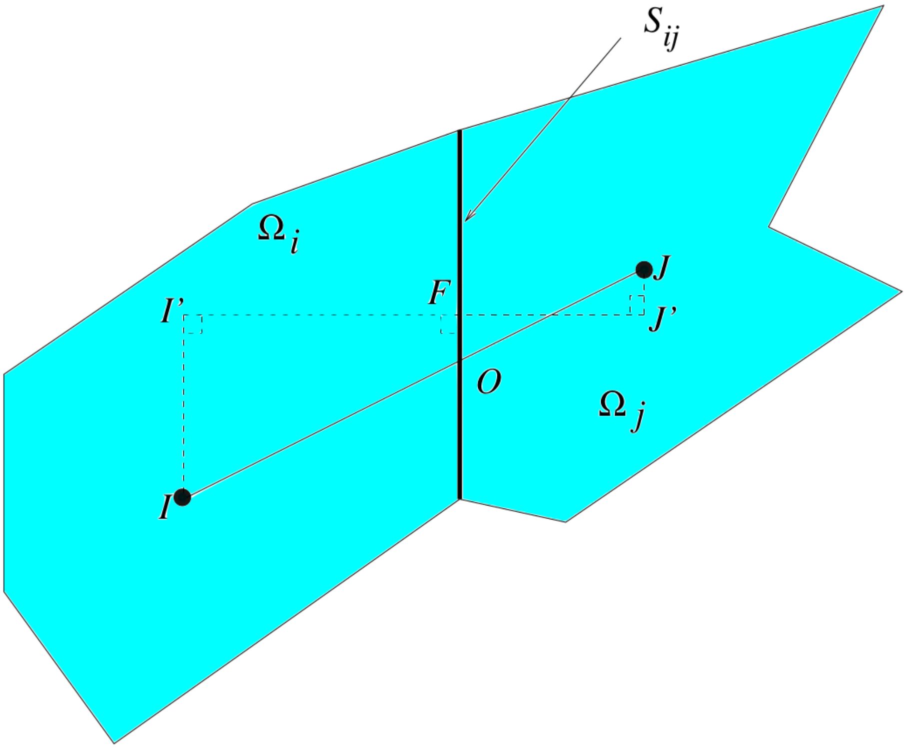

Figure 4.1: Schematic of two arbitrary control volumes (Ω_i and Ω_j) showing the spacial discretisation notation adapted from[12]

normal of the shared face pointing from i to j, the surface area of the shared face would thus be $\|S_{ij}\|$. I and J are the centres of the respective control volumes. O represents the point at which a straight line connecting the respective centres crosses the shared face. I′ and J′ are projections from the node centres I and J, respectively such that when I′ and J′ are connected the line they produce is orthogonal to the shared face, this location is denoted by F.

Transient and source terms

The temporal term can be approximated at the cell centres as:

$$\frac{\partial}{\partial t}\int_{\Omega}\rho\phi_i d\Omega \approx \frac{\partial}{\partial t}\left(\rho\phi_i \mid \Omega_i \mid\right) \tag{4.26}$$

where $\mid \Omega_i \mid$ is the volume of the cell Ω_i. Similarly, the source term is approximated as:

$$\int_{\Omega} S_\phi d\Omega = S_\phi \mid \Omega_i \mid \tag{4.27}$$

S_ϕ can be further split into implicit and explicit components as $S_\phi = S_{\text{imp}}\phi_i + S_{\text{exp}}$.

Convection term

The discretisation of the convection term for the cell Ω_i is shown below for internal faces:

$$\int_S (\rho\phi\vec{u}) \cdot \hat{n} dS = \sum_{j\in F(i)} \rho \|S_{ij}\| \phi_{ij} (\vec{u}_{ij}.\hat{n}_{ij}) = \sum_{j\in F(i)} \phi_{ij} \mathrm{m}_{ij} \tag{4.28}$$

where j is a neighbouring cell to i and set $F(i)$ contains the neighbouring cells. ϕ_{ij} is the surface value of the variable ϕ. The term m_{ij} is the mass flux through the boundary face between the two neighbouring cells.

Since the variables are stored at the centres, the face centre value ϕ_{ij} of the variable ϕ must be calculated by interpolation (the interpolation projects to the location F on the shared face). *Code_Saturne* has three numerical schemes capable of performing this interpolation, which are the first-order upwind scheme, the second-order accurate Second Order Linear Upwind (SOLU) scheme, and the second-order Central Differencing Scheme (CDS). These schemes are briefly described below.

For the first-order upwind scheme, the value of ϕ_{ij} is equated to the value at the centre of the upstream cell. This scheme is numerically stable and always returns bounded solutions. However, compared to the other two schemes is more numerically diffusive. The implementation in *Code_Saturne* is given below:

$$\phi_{ij} = \begin{cases} \phi_i \text{ if } \mathrm{m}_{ij} > 0 \\ \phi_j \text{ if } \mathrm{m}_{ij} < 0 \end{cases} \tag{4.29}$$

The SOLU scheme is second-order accurate and uses the cell gradient of the variable to achieve the higher-order in space:

$$\phi_{ij} = \begin{cases} \phi_i + \nabla\phi_i \cdot \mathrm{IF} \text{ if } \mathrm{m}_{ij} > 0 \\ \phi_j + \nabla\phi_j \cdot \mathrm{JF} \text{ if } \mathrm{m}_{ij} < 0 \end{cases} \tag{4.30}$$

In Chapters 5 and 6, the SOLU scheme is used in the LES study of natural circulation in an enclosed bundle.

For the centred scheme, the cell centre values from the adjacent cells are used to compute the face centre value at the shared face, the implementation is as follows:

$$\phi_{ij} = \gamma_{ij}\phi_i + (1-\gamma_{ij})\phi_j + \frac{1}{2}(\nabla\phi_i + \nabla\phi_j) \cdot \mathrm{OF} \tag{4.31}$$

where $\gamma_{ij} = FJ' \cdot \hat{n} / I'J' \cdot \hat{n}$, is a geometric weighing factor. The last term on the right-hand side is a correction factor for non-orthogonal grids. In the event the centred or SOLU scheme induce instabilities to the computation, the user can activate a "slope test", which can stabilise the computation by locally switching to the first order upwind scheme in regions where oscillations are detected.

Diffusion term

The diffusion term is implemented as:

$$\int_S (\Gamma \nabla \phi) \cdot \hat{n} dS = \sum_{j \in F(i)} \left(\Gamma \nabla \phi_{ij} \right) \cdot \hat{n} \vec{S_{ij}} = \sum_{j \in F(i)} \Gamma_{ij} \frac{\phi_{J'} - \phi_{I'}}{I'J'} \vec{S_{ij}} \tag{4.32}$$

where Γ_{ij} is the value of the diffusion coefficient at the face centre (F), $\phi_{I'}$ and $\phi_{J'}$ are the values of the variable at the projected locations I' and J', respectively. The values at this projected locations can be computed using Taylor's theorem as $\phi_{I'} = \phi_i + (\nabla \phi_i).II'$ and $\phi_{J'} = \phi_j + (\nabla \phi_j).JJ'$. With these definitions Equation 4.32 can be rewritten and the expression used in *Code_Saturne* is[12]:

$$\sum_{j \in F(i)} = \Gamma_{ij} \| S_{ij} \| \left[\frac{\phi_{J'} - \phi_{I'}}{I'J'} + \frac{1}{2} \left(\nabla \phi_i + \nabla \phi_j \right) \cdot \left(\frac{J'J}{I'J'} - \frac{I'I}{I'J'} \right) \right] \tag{4.33}$$

Γ_{ij} the value at the shared face centre and there are two ways it can be computed in *Code_Saturne*. The first is the arithmetic mean, where the value is simply computed as

$$\Gamma_{ij} = \frac{1}{2} \left(\Gamma_i + \Gamma_j \right) \tag{4.34}$$

The second interpolation method is harmonic mean and takes into account the weighing coefficient γ_{ij} and computes Γ_{ij} as:

$$\Gamma_{ij} = \frac{\Gamma_i \Gamma_j}{\gamma_{ij} \Gamma_i + (1 - \gamma_{ij}) \Gamma_j} \tag{4.35}$$

Cell gradient computation

Gradients of the variable within the cell are required for the convection term (see Equation 4.31 for example) and diffusion term (see Equation 4.33). The computations There are two gradient calculation methods available in *Code_Saturne*[12]:

- The iterative method is a robust method, which uses the values in the adjacent cells with a shared face to compute the gradient. The LES computations carried out in this thesis have used the iterative method.

- The least-squares approach has two implementations in *Code_Saturne*. It can be based on the cells, which have a shared face or it can take into consideration the extended neighbourhood, these are all the cells that share a vertex with cell Ω_i. Although this approach is faster than the iterative method, it is however numerically diffusive. Further details about the least-squares approach and its implementation can be found in the *Code_Saturne* manual[12].

The gradient of the variable ϕ at the cell centre can be defined as:

$$\nabla\phi_i = \frac{1}{\mid \Omega_i \mid} \int_{\Omega} \nabla\phi_i d\Omega \tag{4.36}$$

where $\mid \Omega_i \mid$ is the volume of the cell Ω_i. Using Gauss's theorem (Equation 4.24) the equation is rewritten as:

$$\frac{1}{\mid \Omega_i \mid} \int_{S} \phi_{ij} \cdot \hat{n} dS = \frac{1}{\mid \Omega_i \mid} \sum_{j \in F(i)} \phi_{ij} \cdot \hat{n}\vec{S_{ij}} \tag{4.37}$$

To obtain the value ϕ_{ij}, which is the face value at F the Taylor series expansion can be used as:

$$\phi_{ij} = \phi_O + \nabla\phi_O \cdot OF \tag{4.38}$$

Linear interpolation can be used to obtain the value of ϕ_O and the gradient $\nabla\phi_O$ can be computed as the average of the gradients in the adjacent cells (i.e. $\nabla\phi_i$ and $\nabla\phi_j$) thus the gradient ϕ_i becomes as seen below and can be solved for in an iterative manner further details can be found the *Code_Saturne* guide[12].

$$\nabla\phi_i = \frac{1}{\mid \Omega_i \mid} \sum_{j \in F(i)} \left[\gamma_{ij}\phi_i + \left(1 - \gamma_{ij}\right)\phi_j + \frac{1}{2}\left(\nabla\phi_i + \nabla\phi_j\right) \cdot OF \right] \hat{n}\vec{S_{ij}} \tag{4.39}$$

4.5.2 Time Advancement

If an unsteady problem is to be considered then Equation 4.25 has to be integrated in time. Taking the example (for simplicity) of the integration in time of a function $f(\phi(t))$ over a small time-step $\Delta t = t^{n+1} - t^n$ the following is obtained:

$$\frac{d\,\phi(t)}{dt} = f(\phi(t)) \tag{4.40a}$$

$$\phi^{n+1} - \phi^n = f(\phi(t))\,\Delta t \tag{4.40b}$$

The term $f(\phi(t))\,\Delta t$ is the estimate of the integral and the values of the variable ϕ in this term can be defined at a several time-steps. The term can be computed in an explicit manner if ϕ is defined at $(t = n)$ or where the values of ϕ are known. Alternatively, the term can be handled in an implicit manner if ϕ is defined at $(t = n + 1)$. In *Code_Saturne* there are two time schemes avialable for the variable ϕ; the first order implicit Euler scheme where ϕ is evaluated at $t = n + 1$ and the second order implicit Crank-Nicolson scheme at $t = n + 1/2$[12]. Conveniently, both schemes are implemented as:

$$\phi^{n+\theta} = \theta\phi^{n+1} + (1 - \theta)\,\phi^{n} \tag{4.41}$$

where $\theta = 0.5$ for the Crank-Nicolson scheme and $\theta = 1$ for the Euler scheme. It should be noted if the Crank-Nicolson scheme is selected the time-step is constant. For completeness, the transient term for the governing equation is shown in discretised form:

$$\frac{\partial}{\partial t}\left(\rho\phi_i \mid \Omega_i \mid\right) = \rho \mid \Omega_i \mid \; \frac{\phi_i^{n+1} - \phi_i^{n}}{\Delta t} \tag{4.42}$$

Barring the variable ϕ other quantities such as the mass flux m_{ij}, properties and source terms have time schemes applied to them. These are briefly described below:

Physical properties

The physical properties can either be extrapolated using the Adam-Basforth scheme or made explicit[12]. Extrapolation is necessary as the properties typically can only be known once the scalars are computed. The time scheme for the properties in *Code_Saturne* is conveniently written as:

$$\Phi^{n+\theta} = (1 + \theta)\,\Phi^{n} - \theta\Phi^{n-1} \tag{4.43}$$

where, if $\theta = 0$ the properties are computed explicitly, If $\theta = 1$ or $1/2$, the properties are extrapolated using a first order and second order scheme, respectively.

Mass flux

For the definition of the mass fluxes several time schemes are available in *Code_Saturne*[12]:

- The mass flux can be made explicit $(t = n)$ for the computation of momentum. Later on when the scalars are computed the updated mass flux at $t = n + 1$ can be used.

- The second time scheme makes both the computation of momentum and scalars explicit (i.e. $t = n$ for both).

- Taken at $\theta = 1/2$, making the defined mass flux second order. For momentum the mass flux m_{ij} is extrapolated as:

  $$\mathrm{m}_{ij}^{n+1/2} = 2\mathrm{m}_{ij}^{n-1/2} - \mathrm{m}_{ij}^{n-3/2} \tag{4.44}$$

  At the computation of the scalers and turbulence, the mass flux at m_{ij}^{n+1} is now known and here an interpolation is carried out:

  $$\mathrm{m}_{ij}^{n+1/2} = \frac{2}{3}\mathrm{m}_{ij}^{n+1} + \frac{1}{3}\mathrm{m}_{ij}^{n-1/2} \tag{4.45}$$

Source terms

The source terms in *Code_Saturne* can either be implicit or explicit. If the former, the source term is discretised using the same time-scheme as that of the variable being solved, this is done for consistency and ensure the order of convergence. If the latter, then the discretisation approach mirrors that described for the physical properties.

4.5.3 Pressure-Velocity coupling

For incompressible flows, the pressure is independent of density thus there is no independent equation for pressure or a clear way to couple pressure and velocity. To resolve the aforementioned issue, *Code_Saturne* solves continuity and momentum using a fractional step scheme based on the Semi-Implicit Method for Pressure Linked Equations Consistent (SIMPLEC) method by Doormaal and Raithby[127]. There are two steps performed by the algorithm[12]:

- Prediction step: The predicted velocity is computed by solving the momentum equation with pressure gradient used being from the previous time step. The resulting predicted velocities do not satisfy continuity and have to be corrected.

- Correction step: In this step the pressure and velocity are corrected. The pressure increment is computed from the Poisson equation, then the pressure and velocity fields are updated. After this stage the variables for turbulence and scalars are computed. A method based on the Rhie and Chow interpolation[128] is a applied to the pressure-correction equation to prevent a checker boarding or oscillation of the pressure/velocity fields that can occur.

4.5.4 Boundary conditions

Typically boundary conditions can be imposed as:

- Dirichlet: where the value of the variable at the boundary surface is prescribed
- Neumann boundary condition: where the flux of the variable is prescribed on the boundary surface.
- Mixed boundary condition: which can be considered a mixture of the Dirichlet and Neumann boundary conditions

In *Code_Saturne*, the boundary conditions are specified through two pairs of coefficients before being input into the linear system to be solved[12]. These two pairs are for the convective and diffusion terms, respectively with the first pair of coefficients (C_a, C_b) in Equation 4.46(a), used to define the value of the variable at the boundary face ϕ_F. The second pair of coefficients (C_c, C_d) in Equation 4.46(b) are used to define the flux $\left(q''_{\phi_F}\right)$ of the variable at the boundary surface. To help identify the locations of the various geometric parameters Figure 4.2 has been included.

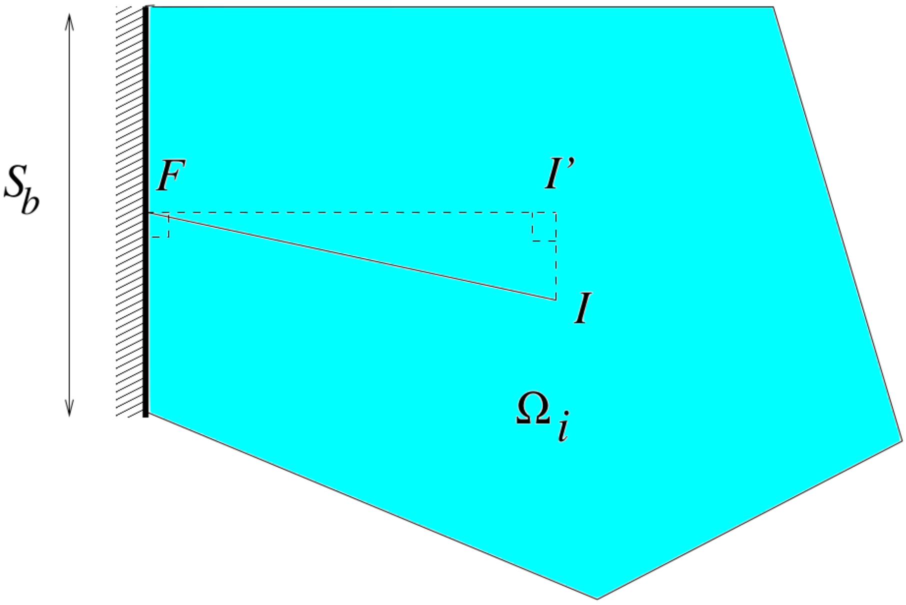

Figure 4.2: Schematic showing boundary a cell Ω_i adjacent a boundary surface[12].

$$\phi_F = C_a + C_b \phi_{I'} \tag{4.46a}$$

$$q''_{\phi_F} = -\left(C_c + C_d \phi_{I'}\right) \tag{4.46b}$$

where $\phi_{I'}$ is the value of the variable in the fluid at point I' (see Figure 4.2). Assuming, the variable of interest is the temperature then for a Dirichlet boundary condition, where T_F is now the prescribed wall temperature can be defined as ; $(C_a, C_b) = (T_F, 0)$ and those for the second pair are $(C_c, C_d) = \left(-h_{\phi_F}, q''_{\phi_F}\right)$. In the expressions, $h_{\phi_F} = \lambda / I'F$ which is obtained from equating $q''_{\phi_F} = -\lambda \left(T_{I'} - T_F\right) / I'F = h_{\phi_F} \left(T_{I'} - T_F\right)$. $I'F$ is the distance between the projected cell centre and wall. If the boundary condition is a Neumann type with the applied heat flux represented by q''_{ϕ_F} then the pairs of coefficients are; $(C_a, C_b) = \left(q''_{\phi_F} / h_{\phi_F}, 1\right)$ and $(C_c, C_d) = \left(q''_{\phi_F}, 0\right)$.

Standard boundary conditions available in the solver are briefly listed below[12]

- inlet: A Dirichlet boundary condition is imposed on the boundary face for the variable ϕ (i.e. all transported variables). For the pressure a homogeneous Neumann boundary condition (zero derivate) is applied by default, however there is an option for extrapolating the pressure at the surface from the cell centre.

- outlet: A homogeneous Neumann boundary condition is applied for ϕ. Pressure is handled using a Dirichlet boundary condition.

- Walls: For velocity a Dirichlet boundary condition is imposed. The velocity component along the wall is typically set to zero at the wall or a fixed value in the event of a sliding wall. The component normal to the boundary surface has zero mass flux. Neumann or Dirichlet conditions for the scalars can be assigned at the wall. For the pressure the boundary condition is homogeneous Neumann.

- Symmetry: Homogeneous Neumann conditions are imposed for the scalars and tangential velocity component.

4.6 Numerical methods in *Syrthes*

Syrthes is a finite element solver used for the conduction and thermal radiation analysis of materials[25]. The solver is transient and uses a first order time scheme to advance the solution. 2-D or 3-D solid conduction can be solved and the material properties can be defined as either anisotropic or isotropic. In the event that an interface exists between two adjunct components, it is possible to specify a contact resistance. Multiple boundary conditions are available to the user; these include to name but a few Dirichlet, Neuman, mixed and symmetry boundary conditions. Additional heat generation within the solid can be specified through introducing a source term either in the Graphical User Interface (GUI) or user subroutines. Source terms in *Syrthes* can be constants, vary temporally or spatially. The code is used to simulate conjugate heat transfer by coupling it with *Code_Saturne*. If coupled the two codes will exchange temperatures and heat transfer coefficients.

Radiation can transport thermal energy in the presence or absence of matter. In scenarios where convective heat transfer is severely limited, radiative heat transfer would play a significant role in cooling the debris. Spectral and directional dependences make it difficult to analyse radiation problems, to simplify the calculation the following simplifications are made by the solver[25].

- Only solid surfaces through a transparent medium are involved in radiation exchange
- Radiation is not transmitted through the body(Opaque body)
- Radiation intensity is independent of direction (diffuse emitter)
- Grey surfaces(by band)

The radiation solver for *Syrthes* requires an independent surface mesh (if 3-D geometry). This mesh is separate from that used for conduction analysis. The radiation mesh should form a closed shell which comprises all the surfaces involved in the radiation exchange. Since the mesh can be equated to an enclosure, the following conservation statement for view factors can be defined $\sum_{j=1}^{N} F_{ij} = 1$. To solve for radiation the concept of radiosity is used. Radiosity can be defined as the total sum of energy leaving a surface face, this would comprise emittance and the reflected portion of incident radiation. A linear set of equations in the form shown in Equation 4.47 is solved.

$$J_i - \gamma_i \sum_{j=1}^{N} F_{ij} J_j = E_i \tag{4.47}$$

In this algebraic equation J_i, is the radiosity leaving the computational face and is being solved for[25]. γ_i is the radiation reflected by the surface of the cell and is equal to $1 - \epsilon_i$, ϵ is the emissivity. Equation 4.47 basically states that the total radiation leaving surface i minus the sum of the reflected portion of radiation leaving surface i being received by multiple surfaces is equal to the emitted radiation. Once the net radiation leaving the cell surface is solved from Equation 4.47, the net flux from the surface is calculated and imposed as an additional boundary condition for conduction analysis[25].

In the conduction equation shown below the term $Q_{s/v}$ would represent the contribution of the various coupling methods available for use in *FREEDOM*, radiative effects or the user defined sources for example fuel decay heat.

$$\rho_s \mathrm{Cp}_s \frac{\partial T_s}{\partial t} = \frac{\partial}{\partial_{x_j}} \big(k_s \frac{\partial T_s}{\partial_{x_j}} \big) + \dot{Q}_{s/v} \tag{4.48}$$

Chapter 5

LES of natural convection in a shortened bundle

Natural circulation is the dominant mode of heat transfer at a variety of stages within the AGR fuel route. Moreover, many of the envisaged non-design scenarios would entail a loss of forced cooling. Investigations into natural circulation have mostly pertained to the simplified geometries, while those into vertical rod bundles are rather limited. In the instances where rod bundles are considered, there is little to no discussion on the detailed turbulence and flow phenomena. This chapter aims to add new understanding by investigating natural circulation in an enclosed rod bundle cavity of small aspect ratio but large Rayleigh number of $\approx 10^{11}$ (based on height) using Large Eddy Simulation (LES) method.

5.1 Modelling description

Figure 5.1 gives an illustration of the modelled domain. The geometric configuration and heating rod arrangement is typical to that for AGR rod bundles. However, the height of the CFD model has been shortened to 0.25 m[i]. The heated rod surfaces are considered smooth, with a constant heat flux applied. These surfaces are coloured red in Figure 5.1. Two heat fluxes given in Table 5.1 are considered.

The rod and containment diameters are 0.0153 m and 0.1923 m, respectively. At the containment surface (coloured in blue), a convective boundary condition is applied,

---

[i] A typical AGR bundle has a height of ≈1 m

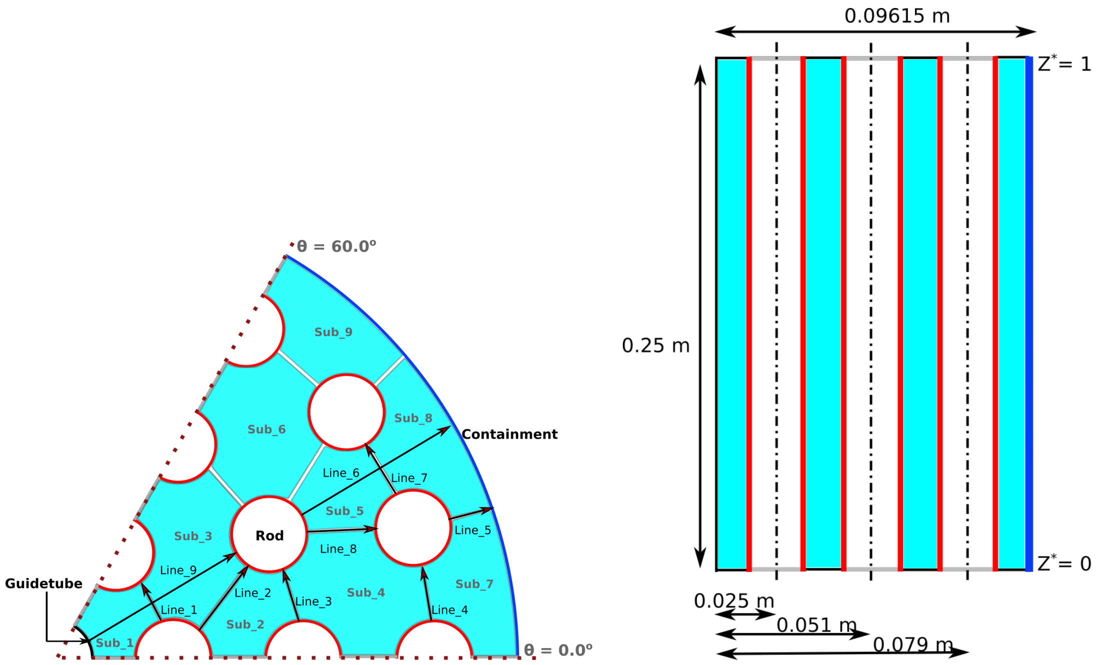

(a) Cross section

(b) Vertical plane at $\theta = 0.0°$

Figure 5.1: Schematic showing the modelled geometry, sub-channel divisions (denoted by Sub_*) and dimensioned vertical plane.

Table 5.1: Case definition

Case name	Heat flux
Case-1	1154 W/m^2
Case-2	289 W/m^2

with a sink temperature of 110 °C and a heat transfer coefficient of 700 $W/m^2\,°C$. The central rod termed the "guide tube" is modelled as an adiabatic surface. Similarly, the top and bottom walls are considered adiabatic with all such surfaces coloured in black. Azimuthal surfaces (edge surfaces for a 60 ° sector) are assigned rotational periodicity boundary conditions. It should be noted that all the surfaces are considered no-slip, and the effects of solid conduction and thermal radiation are neglected.

5.1.1 Fluid properties

The coolant is carbon dioxide at a pressure of 3 MPa. Density variation as a function of temperature is modelled with a lookup table using data obtained from the National Institute of Standards and Technology (NIST) database[129]. All the remaining physical properties are fixed constants and the values used are given in Table 5.2.

Table 5.2: Physical property constants imposed on the fluid

Property	Value	Units
Dynamic viscosity	2.712×10^{-5}	Pa s
Thermal conductivity	0.04	W/m°C
Specific heat	1088	J/kg°C
Prandtl number	0.737	-

5.1.2 Non-dimensional parameters

Non-dimensional parameters are presented for the cases in Table 5.3. The Rayleigh number is computed using both the temperature ($\mathrm{Ra}_{\Delta T}$) and heat flux definitions ($\mathrm{Ra}_{q''}$).

Since the width of the rod bundle cavity can be considered dependent on the rod ranks; two values are given for the first rank (Ra_{L1}) and third rank (Ra_{L3}) rods as they represent the upper and lower limit, respectively. Additionally, it is also possible to define the Rayleigh number based on the height of the domain.

Table 5.3: Rayleigh numbers for the heating cases considered using different length scales.

Parameter	Case-1	Case-2
$\mathrm{Ra}_{H,\Delta T}$	1.9×10^{11}	1.1×10^{11}
$\mathrm{Ra}_{L1,\Delta T}$	4.3×10^{9}	2.4×10^{9}
$\mathrm{Ra}_{L3,\Delta T}$	6.4×10^{7}	3.6×10^{7}
$\mathrm{Ra}_{H,q''}$	6.8×10^{12}	3.3×10^{12}
$\mathrm{Ra}_{L1,q''}$	4.5×10^{10}	2.2×10^{10}
$\mathrm{Ra}_{L3,q''}$	1.6×10^{8}	7.9×10^{7}

At this stage, it is worth defining the aspect ratios of the modelled domain. Typically in cavities, the characteristic length is defined as the distance between the hot and cold surfaces. In this geometry, as there are three concentric ranks of heated rods, thus three aspect ratios can be defined. With aspect ratio defined as H/L where H is the height and L is the radial distance between the centroid of the heated rod and containment wall, the computed values are 3.5, 5.5, 14.3 going from the first to the third-rank. The representative P/D ratio of the bundle is ≈ 1.8.

5.1.3 Mesh quality statistics and temporal convergence

A fully structured mesh consisting of 25 million elements, shown in Figure 5.2, is used. The first near-wall adjacent nodes have a y^+ value range of $0.0053 \leq y^+ \leq 0.33$, with grid spacing values of $\Delta x^+ = 30.0$ and $\Delta z^+ = 36$ in the span-wise and stream-wise directions, respectively. These values (Δx^+ and Δz^+) are calculated for the highest heating case at mid-height.

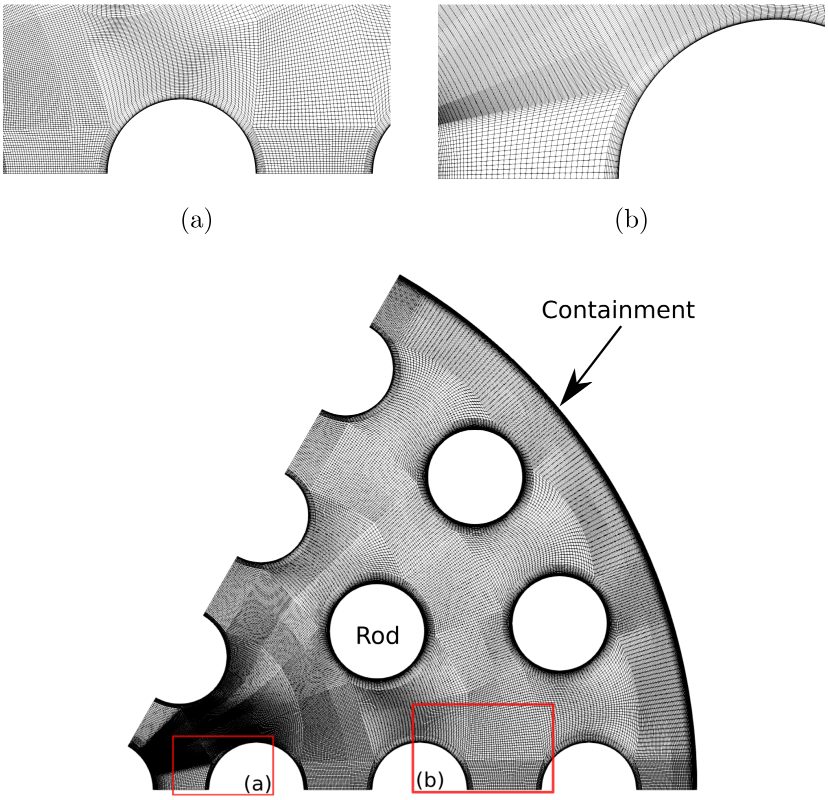

(a)

(b)

(c) Full cross-sectional figure

Figure 5.2: Cross-sectional resolution of the mesh used in the LES computations.

To determine the LES quality of the mesh used, the parameter LES_IQ$_v$ by Celik et al.[130] is used. Meshes used for the LES computations are good if this value is above 80 %. Computing this parameter gives minimum values of 0.92 and 0.94 for the highest and lowest heating case, respectively. These values indicate that the LES simulations are of overall good quality. Contour plots and details on the calculation of LES_IQ_v are provided in the Appendix (see Figure A2, Equation A.1 and A.2).

A fixed time step of 0.0002 s is maintained for the highest heating case, while for the lower heating case the time step is doubled to 0.0004 s. A dimensionless time value can be defined as $t^* = \Delta t V_{n,\Delta T}/\text{Dh}$. Where $V_{n,\Delta T}$ is the buoyant velocity, Δt is the time step and Dh is the hydraulic diameter. For the highest heating case a dimensionless time value of $\approx$0.0001 is computed. The Courant number predominantly ranges from nearly 0 (stagnant sub-channel core) to 0.5. It should be noted that for the highest heating case there is a peak transient fluctuation albeit very brief where the maximum Courant number is approximately 1 before suddenly reducing. However, this does occur in only several cells $<<<$ 1 %.

In Appendix A.1, the profiles at varying intervals in time are shown in order to assess the temporal convergence of the simulation. The profiles indicate a well-converged result.

5.2 Results and Discussion

5.2.1 A qualitative overview of the general flow behaviour

The cases are simulated using the second-order accurate Second Order Linear Upwind (SOLU) scheme for spatial discretisation, while temporal discretisation uses the second-order Crank-Nicholson scheme. Qualitative data presented in this section is predominantly obtained from the highest heating case (Case-1) unless stated otherwise. Vertical contour plots are presented in Figure 5.3 for Case-1 and are taken at $\theta = 30°$. Where applicable, the velocity scales are normalised using the buoyant velocity $V_{n,\Delta T}$, which is defined as $(g\beta\Delta T\nu)^{1/3}$. Where ΔT is the temperature difference, which for the vertical contour plots corresponds to the difference between the peak and minimum domain values. Cross slices taken at varying axial locations are shown in Figures 5.4 to 5.5. Variables in the cross slices are normalised using the local quantities at the extracted location.

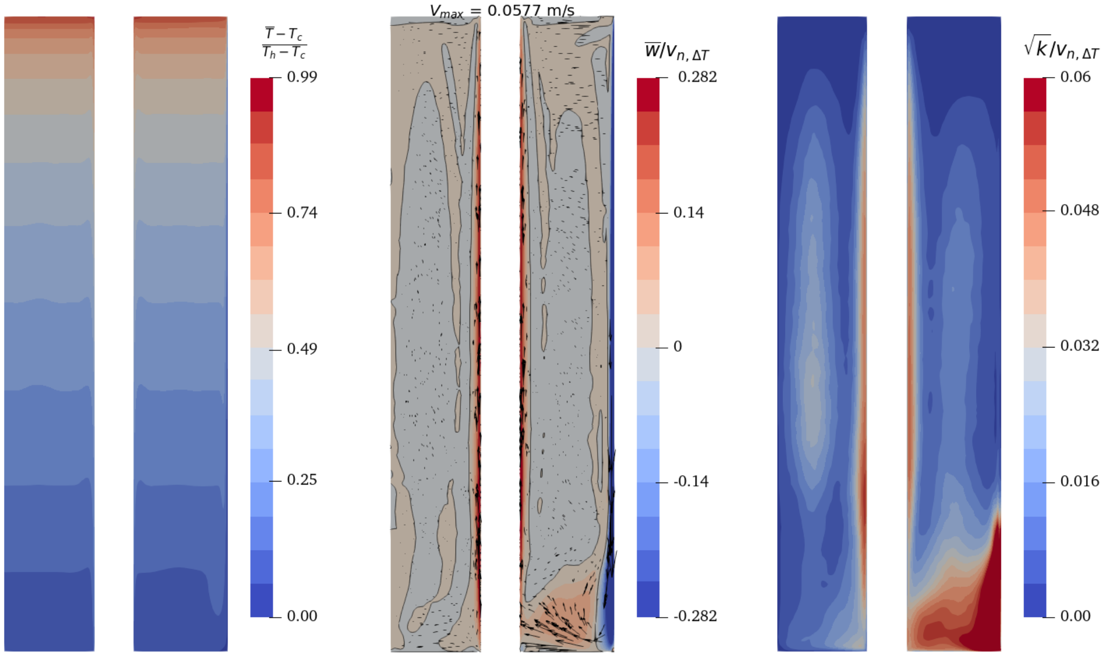

(a) Normalised temperature (b) Normalised velocity (c) Normalised turbulence kinetic energy

Figure 5.3: Contours of temperature, velocity and turbulent kinetic energy taken from Case-1 at $\theta = 30°$.

It can be seen from Figure 5.3 that the flow is largely constrained to the boundary layers. Significant upward and downward flow occurs near the rod and containment surfaces, respectively. However, the core is nearly stagnant with some hints of low magnitude downward flow. Keyhani et al.[81] made similar observations in his experimental work. At the containment wall, boundary layer development can be seen starting from an initially stagnant top-end. The boundary layer thickness grows as the flow descends. Cross-flows are shown to be significant at the ends of the domain (Figure 5.4) with the bottom-end showing greater vector magnitudes. Based on the cross-flow magnitudes and the large observed regions of stagnant flow there appears to be no-interaction between neighbouring rods (except near the domain ends). Thus it can be further stated; away from the domain ends the rods essentially behave as if they are isolated. The flow regime qualitatively evidenced thus far is akin to a boundary layer flow regime.

Peak turbulence levels occur at the containment surface near the bottom-end of the domain see Figures 5.3(c) and 5.5(a). For the fuel rods, it is apparent turbulent

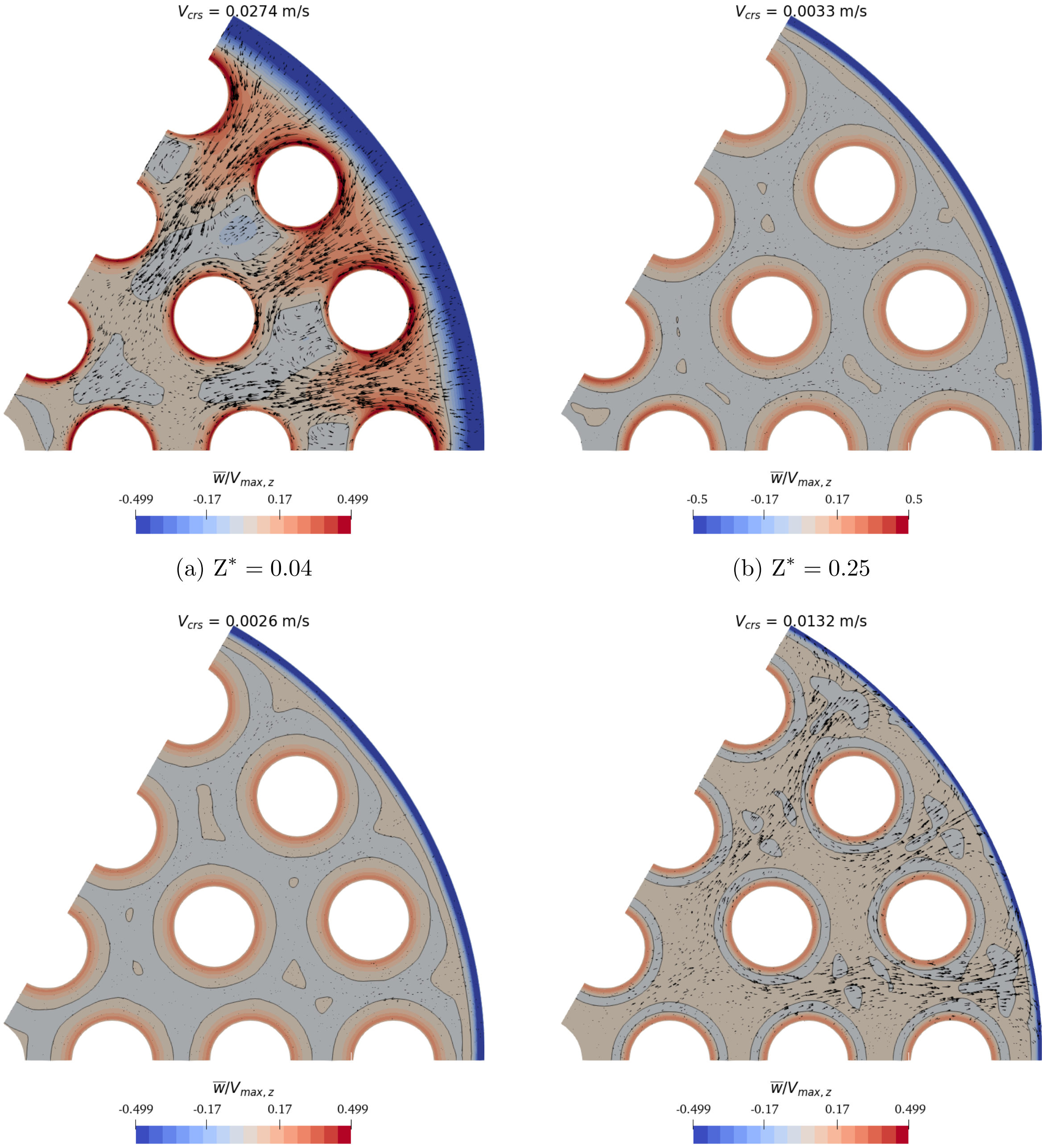

(a) $Z^* = 0.04$

(b) $Z^* = 0.25$

(c) $Z^* = 0.5$

(d) $Z^* = 0.96$

Figure 5.4: Contours of the axial velocity extracted from Case-1 and taken at varying heights. The cross-flow vector peak (V_{crs}) is given in each subfigure and the value is dimensional.

kinetic energy peaks near the wall, which is synonymous with shear flows. For the containment surface, there is no turbulence at the top of the domain but high levels at the bottom end. Coupled with the observed axial velocity contours, it is evident there is a natural convection boundary layer forming on this surface, which is initially laminar but transition to a turbulent state occurs near the bottom-end. This will be discussed further later. Development to a fully turbulent core as observed for example

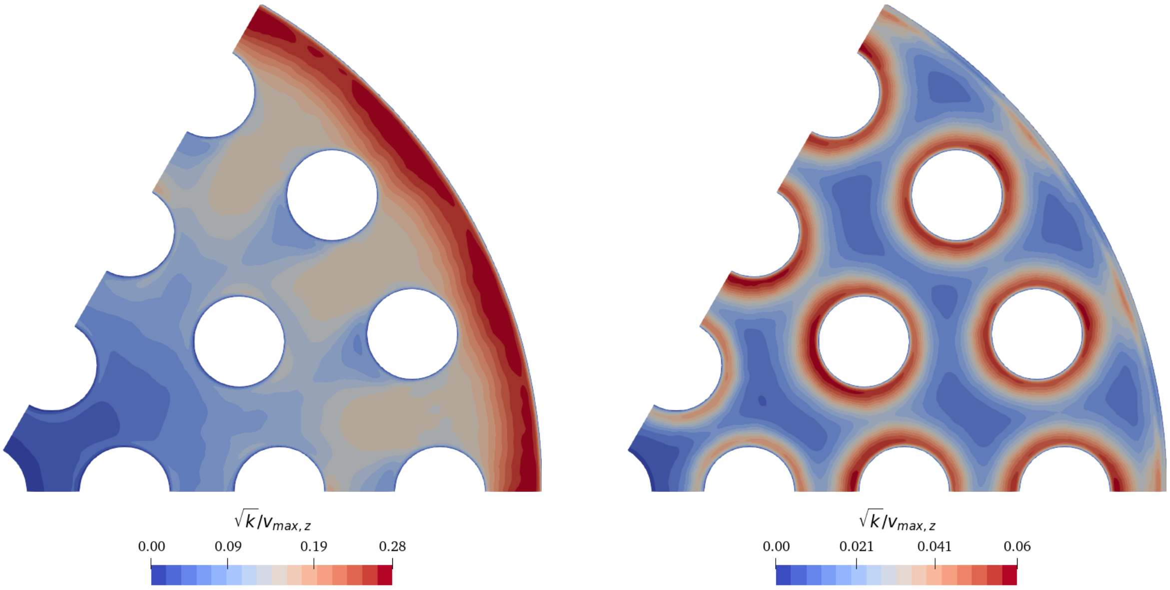

(a) $Z^* = 0.04$ (b) $Z^* = 0.25$

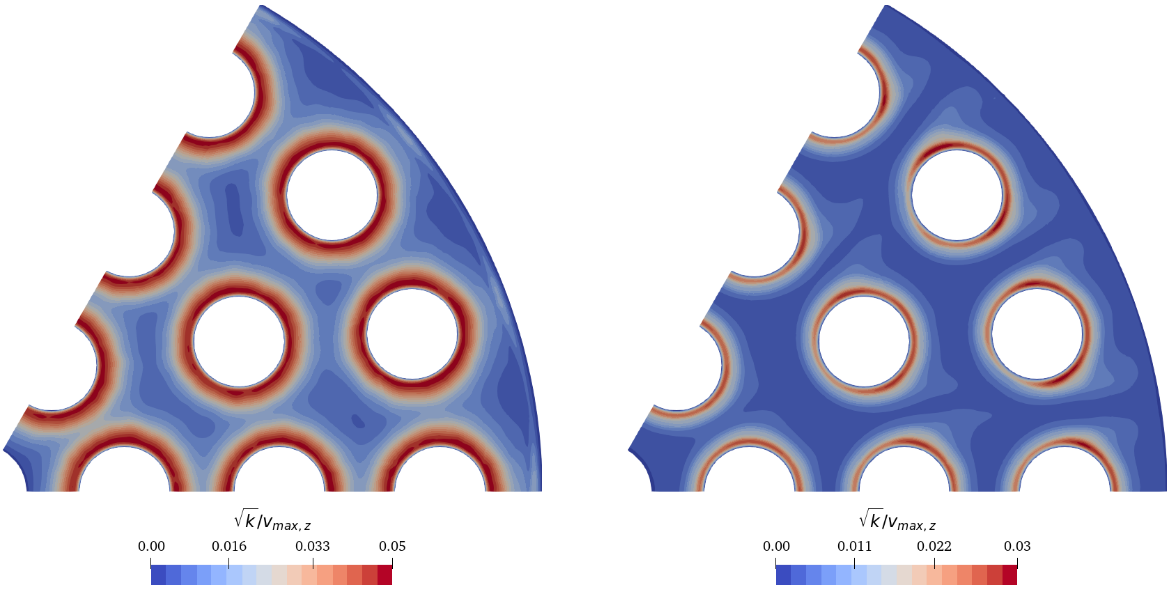

(c) $Z^* = 0.5$ (d) $Z^* = 0.96$

Figure 5.5: Contours of turbulent kinetic energy extracted from Case-1 at varying heights.

in Elder's[7] or Betts and Bokhari's[77] work is impeded by the short nature of the modelled domain. Enhanced turbulence levels can be observed on the rods away from the top and bottom-ends. Unlike the containment wall, there is a rapid development to a turbulent state. It is worth noting, the turbulence peaks are again located near the walls. To better visualise the turbulent flow, coherent structures can be identified using the Q-criterion. Iso-surfaces computed using this parameter are presented in Figure A4 in the Appendix. The iso-surfaces show that there is intense activity along the rod walls and bottom-end of the containment wall. In the core, no such structures are evident.

Vertical temperature plots (Figure 5.3 (a)) clearly show a stratified core. The core is shown to be a region of uniform temperature with horizontal temperature variation occurring close to the walls (across the thin boundary layers).

5.2.2 Quantitative analysis of flow, heat transfer and turbulence quantities

Figure 5.6 shows plots for the axial velocity extracted across different lines and heights for the cases under consideration. In each of the sub-plots, black-thin lines are superimposed and represent the profile computed at mid-height. To aid in showing flow development, velocity profiles are normalised using a constant buoyant velocity. Additional profiles close to the bottom and top wall are presented in Figures 5.7 and 5.8, respectively.

Profiles in Figure 5.6 clearly show a nearly stagnant core at all data extraction points. Flow is constrained to the near-wall regions. Subfigures 5.6 (a, b & c) are taken across the rod gaps and their behaviours are similar. Consider Case 1 along Line_1 for example (Figures 5.7(a) and 5.8(a)). The flow boundary layer is formed on the rod surface at the bottom of the domain, which grows in terms of both the boundary layer thickness and the peak velocity with the height until around $Z^* = 0.2$. The peak then reduces and the boundary layer thickness broadens. Later we will see that the flow is initially laminar and transition occurs around $Z^* \approx 0.1$. Between $Z^* \approx 0.3$ or 0.4 and 0.7, the profiles at the gaps are effectively identical and retain the peak velocity. Past $Z^* = 0.7$, the flow starts to decelerate as the end effects of the confined domain gradually increase in influence. Close inspection reveals Line_1,

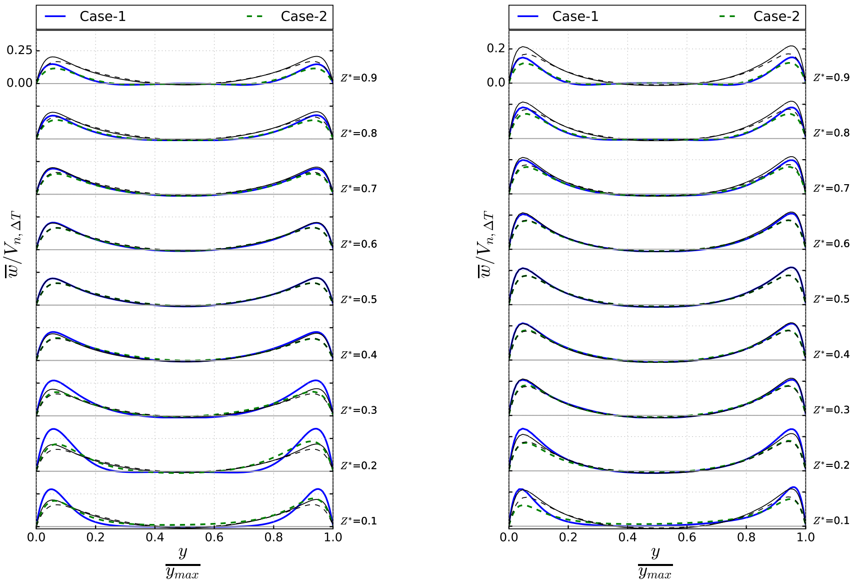

(a) Line_1 (b) Line_3

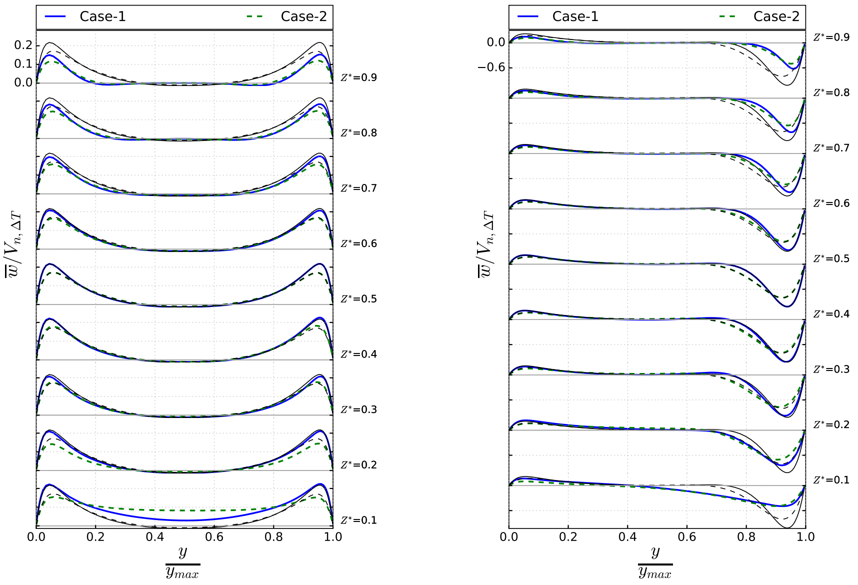

(c) Line_4 (d) Line_5

Figure 5.6: Axial velocity profiles plotted at different axial locations. The superimposed black-thin lines are for the profiles taken at mid-height $Z^* = 0.5$.

Line_3, and Line_4 show different flow development lengths. These lines are extracted across the rod gaps and are at varying proximity to the containment wall. Line_1 extracted for the first rank rods starts to retain the mid-height velocity profile at $Z^* = 0.4$ and shows signs of departure (profiles start changing in comparison to mid-height profile) at $Z^* \approx 0.7$. Similarly, Line_3 and Line_4 depart at $Z^* = 0.7$, but fully develop earlier at $Z^* = 0.3$. Interestingly, at $Z^* = 0.1$ and below, Line_4 has a

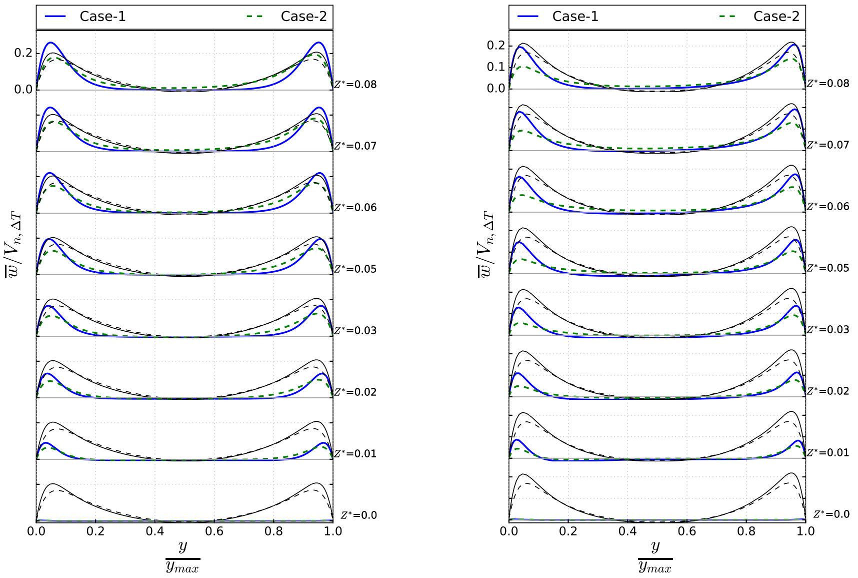

(a) Line_1 (b) Line_3

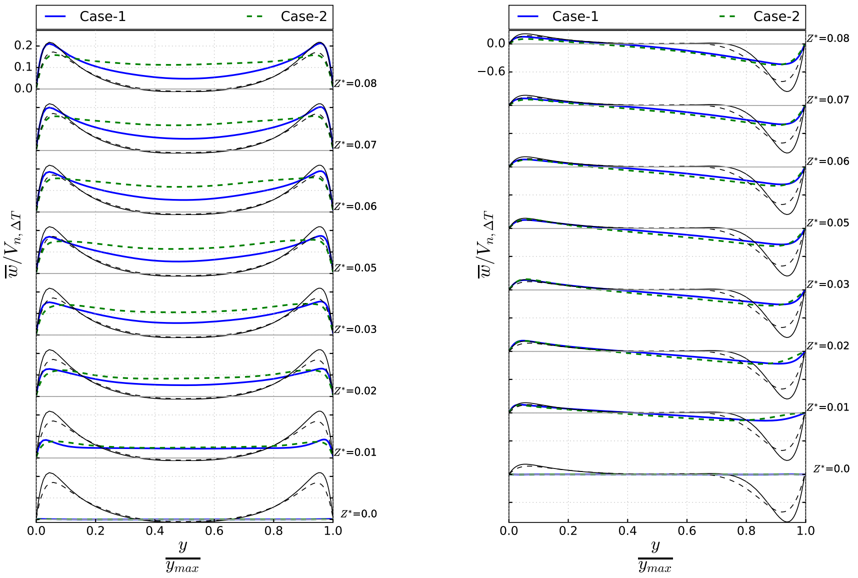

(c) Line_4 (d) Line_5

Figure 5.7: Axial velocity profiles plotted near the bottom wall. At heights between $Z^* = 0.0$ to 0.08. The superimposed black-thin lines are for the profiles taken at mid-height for the cavity.

net upward flow through the rod gap. At this location, the flow behaves almost like a heated vertical pipe. Line_1 and Line_3, largely exhibit a typical buoyancy driven boundary layer development. While the initial development for Line_4 is almost akin to forced/mixed convection flow (see Figure5.7 (c)) before transitioning to the more typical buoyancy driven flow past $Z^* = 0.1$. Differences in the flow development can be attributed to the spread of turbulence after the containment surface transitions. As

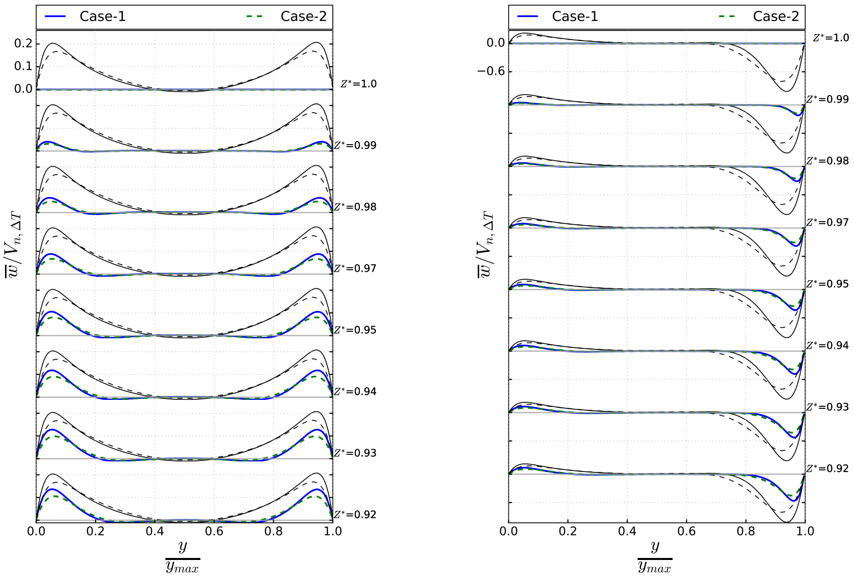

(a) Line_1 (b) Line_5

Figure 5.8: Axial velocity profiles plotted near top wall taken at a height $Z^* = 0.92$ to 1.0. The superimposed black-thin lines are for the profiles taken at mid-height for the cavity.

seen in Figure 5.3(b&c) were strong turbulence generation occurs here along with a strong entrainment and ejection of the flow between the containment wall and interior sub-channels. Turbulence transition on the containment is further discussed later.

The flow at the rod gaps is shown to be fully developed between ($Z^* \approx 0.3$) and until the flow approaches the top-end ($Z^* \approx 0.7$). This behaviour is worth discussing: Assuming an isolated vertical plate with a constant heat flux applied at the heating wall, it is expected the boundary layer would grow with vertical distance. The far field temperature is fixed to that of the quiescent region and this would be invariant with height, while the wall temperature increases with height, consequently so does the buoyancy force. However, in the current geometry the flow is constrained. The far field temperature is associated with that of the sub-channel cores and as demonstrated in Figure 5.3(a) varies with height. The retention of the profiles once the flow is developed strongly indicates the temperature difference between the wall and core is largely maintained. This implies, within this developed region the vertical temperature gradient of the wall and core are largely the same.

The flow development along the containment shows a similar trend as well, but the flow is from top to bottom as fluid is cooled here. Also, significantly different is that there is no overshoot of the velocity profile development. The boundary layer develops between $Z^* = 1$ down to around $Z^* = 0.6$, after which the profile remains largely unchanged until $Z^* = 0.3$. From here the velocity reduces as the flow goes toward the bottom wall. It will be shown later, turbulence transition occurs a lot later on this wall at around $Z^* = 0.3$. Comparing, the different cases it can be noted typically at most locations, Case-1 has the peak velocity.

Temperature profiles are presented in Figure 5.9 between $Z^* = 0.1$ and $Z^* = 0.9$. Profiles close to the top and bottom ends are presented in Figure 5.10. To normalise, the peak wall temperature $T_{h,z}$ and minimum temperature $T_{c,z}$ of the profile are used. The rod gap profiles between $Z^* = 0.1$ upto $Z^* = 0.9$ largely do not show significant variation. For, Line_1 similarity is reached at $Z^* = 0.2$ and maintained until $Z^* = 0.7$. In comparison, for velocity development is reached at $Z^* \approx 0.33$. It is interesting to note, temperature reaches similarity much sooner than velocity does for the rod gaps and the thermal boundary layer thickness is largely maintained. However, near the containment surface, the temperature development closely mirrors the observations made for velocity. Using Line_5 as an example, temperature profiles develop (from top to bottom) reaching similarity at $Z^* = 0.6$ with the profiles remaining unchanged until $Z^* = 0.33$.

Temperature profiles at the top and bottom ends are given in Figure 5.10. At the containment surface, the temperature differential is largest at the top-end as the hot gas begins its descent. Looking at Figure 5.10(b) the temperature gradient at the containment surface decreases as distance increases from the top surface.

At the bottom-end for the rod gaps, the relative temperature differential is typically steeper than at mid-height. Cold gas arriving from the containment wall approaches the heated rods and ascends, which would explain the steeper gradient. Temperature inversion occurs at the top-end of the domain between $Z^* = 0.9$ to $Z^* = 0.99$. As height increases, the inversion progressively worsens. Right at the top wall $Z^* = 1.0$ a parabolic temperature profile is observed. As seen from Figure 5.8, here the axial velocity has stagnated even at the boundary layers and this would help explain the drastic shift from the temperature inversion profile.

Turbulent kinetic energy is shown in Figure 5.11. Normalization is carried out using the peak velocity of the profile. Figure 5.12 shows the profiles close to the bottom-end of the domain and are normalised using the buoyant velocity. It is necessary to use

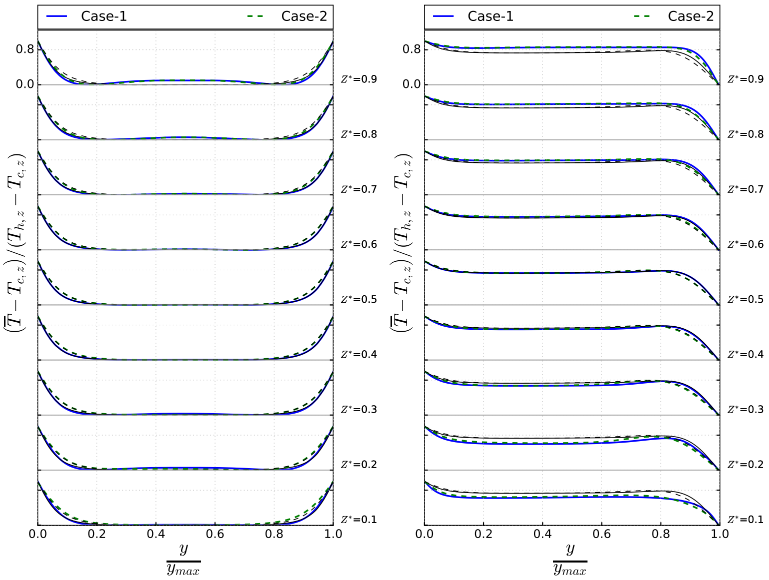

(a) Line_1 (b) Line_5

Figure 5.9: Temperature profiles plotted at differing axial locations. The superimposed black-thin lines are for the profiles taken at mid-height for the cavity.

the buoyant velocity as close to the domain ends, the computed peak velocity is nearly zero.

Turbulence peaks largely occur near the wall as expected. At the top, the flow tends to laminarize with no turbulent kinetic energy levels at $Z^* = 1.0$ (profiles are not shown). This is largely due to the flow stagnating at this region. On the containment wall (Line_5), turbulence remains very low and the flow is laminar until down to around $Z^* = 0.2$, where transition apparently occurs. Below turbulence appears to spread broadly away from the containment wall and into the inner sub-channels.

Figures 5.3(b&c), 5.4(a) and 5.5(a) paint a picture on how the resulting jet flow convects turbulence towards the interior. Due to the cross-flow, the jet would also generate shear turbulence on the rod surface. As the jet flow transverses into the interior it weakens reducing the spread of turbulence. Line_4 (third rank rods) at Z^* = 0.1 has uniform turbulence distribution across the core. This distribution is a result of convected turbulence increasing the free stream turbulence.

Ascending with height, the turbulent kinetic energy profile immediately transitions to a typical shear profile. Lines_1 (rod rank one) and Line_3 (rod rank two), give a further indication of the declining influence of the jet. With increasing distance from the containment wall, turbulence levels in the core reduce along with the peaks becoming

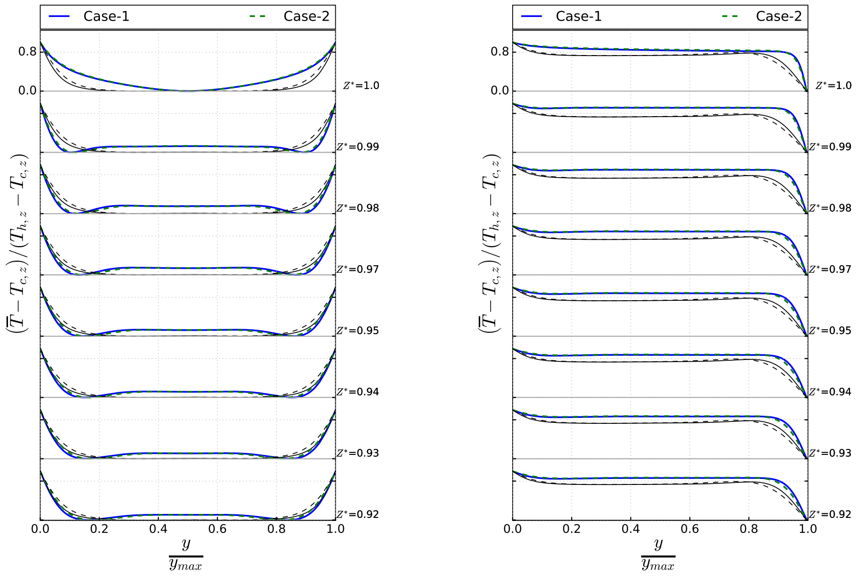

(a) Line_1 - top

(b) Line_5 - top

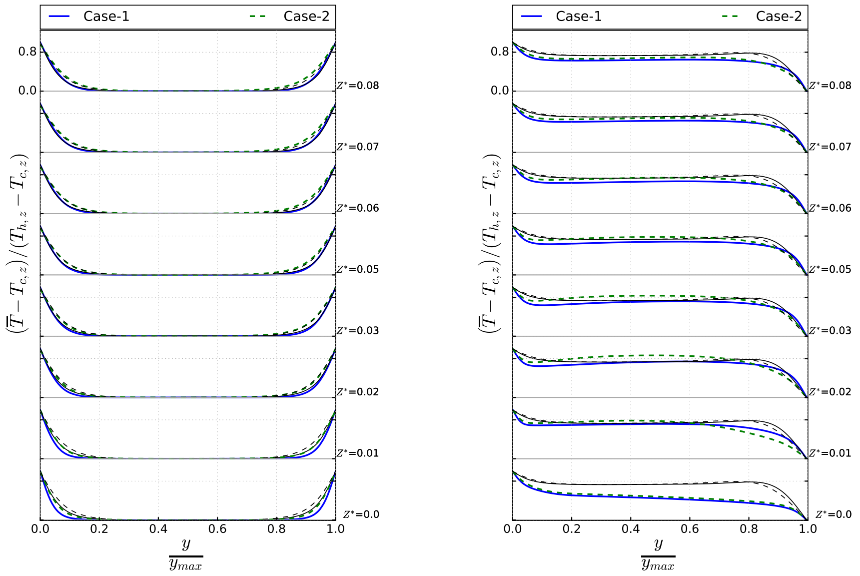

(c) Line_1 - bottom

(d) Line_5 - bottom

Figure 5.10: Temperature profiles plotted near the bottom wall $Z^* = 0.01$ to 0.08 and near the top wall $Z^* = 0.92$ to 1.0. The superimposed black-thin lines are for the profiles taken at mid-height for the cavity.

more biased towards the rod surface. Development profiles below $Z^* = 0.1$ clearly evidence this (Figure 5.12). The transition locations appear different, this has also been evidenced in the velocity profiles. Line_1, which is furthest away from the containment transitions at $Z^* \approx 0.33$, while Line_3 transitions earlier at $Z^* \approx 0.2$. Line_4 initially transitions much earlier and remains relatively unchanged between $Z^* = 0.03$ and

$Z^* = 0.08$. However, at $Z^* \approx 0.2$ there is another transition to the characteristic turbulence distribution observed at the other rod gap locations further away from the containment wall.

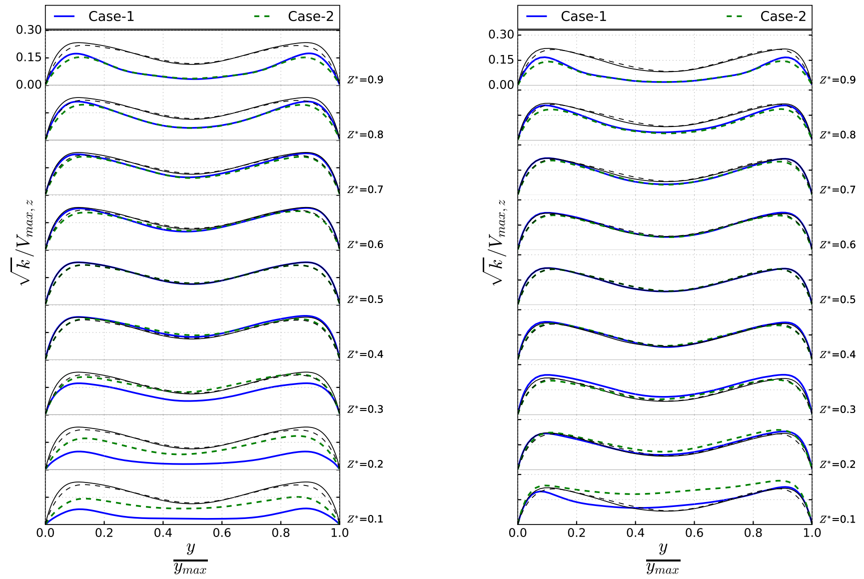

(a) Line_1 (b) Line_3

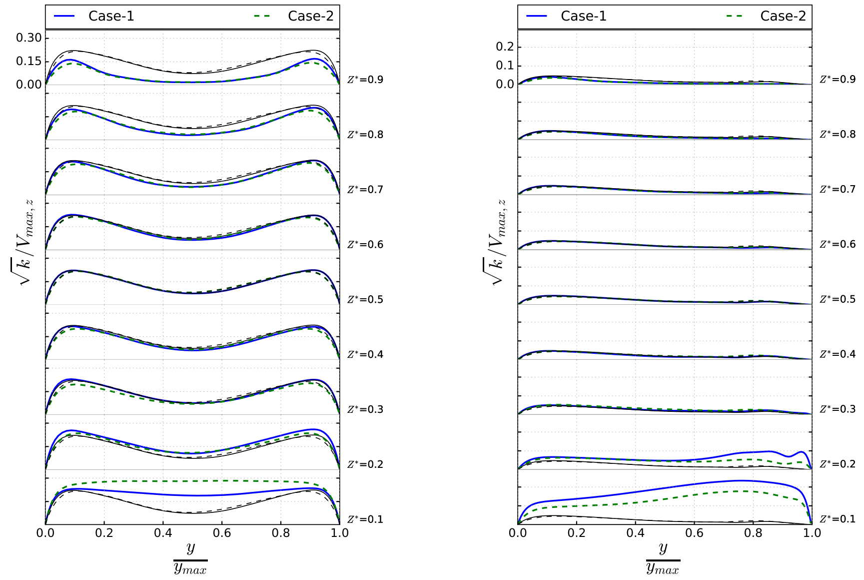

(c) Line_4 (d) Line_5

Figure 5.11: Profiles of turbulent kinetic energy plotted at differing axial locations.

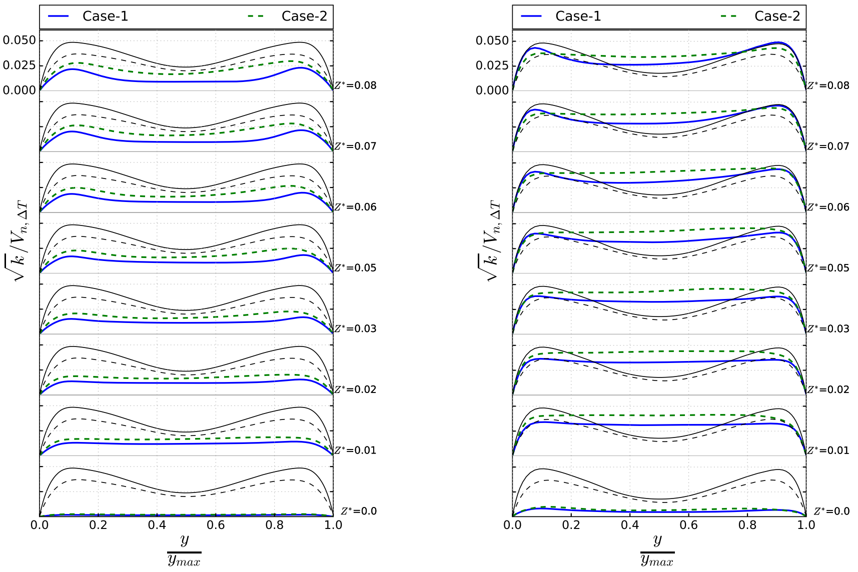

(a) Line_1

(b) Line_3

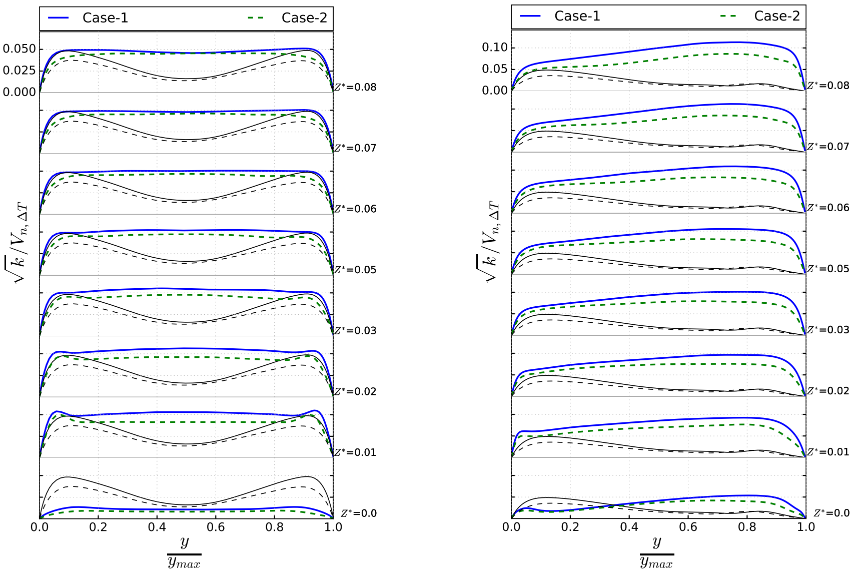

(c) Line_4

(d) Line_5

Figure 5.12: Turbulent kinetic energy profiles plotted near bottom wall upto a height of $Z^* = 0.0$ to 0.08. The superimposed black-thin lines are for the profiles taken at mid-height for the cavity.

5.2.3 Laminar boundary layer

Containment wall

Previously explored qualitative data has suggested the containment surface is laminar at the top and the components (rods and containment) behave as if they were isolated. Based on this, it is therefore worth considering for the large diameter containment, how well the LES data compares against a similarity solution for laminar natural convection flow on a vertical flat surface. The similarity solution by Ostrach[13] is used. A detailed overview of the similarity solution, computation and validation is given in the Appendix (A.4).

As can be seen (Figure 5.13), even though the containment surface is cylindrical and within a confined domain, there are very good comparisons at the upper sections, where the flow is laminar as earlier suggested.

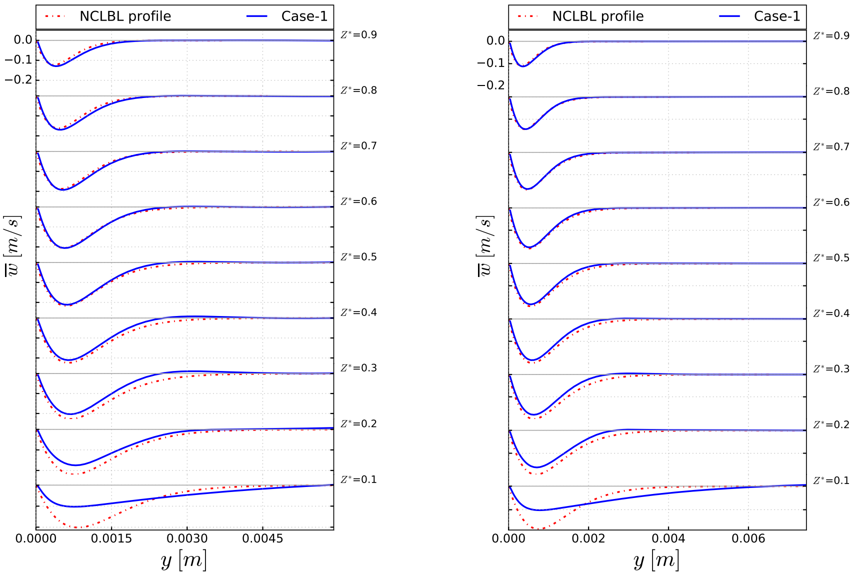

(a) Line_5 (b) Line_6

Figure 5.13: Comparison of LES data for Line_5 and Line_6 from Case-1 against the similarity solution by Ostrach[13]. Data is extracted from the containment surface (now given as $y = 0$) to the stagnant flow region.

Ostrach's similarity solution for laminar flow is compared against the LES temperature data extracted for Line_5 and Line_6. Figure 5.14 shows the results of this comparison. It is clear that the velocity development over the containment wall predicted by the LES follows the similarity solution closely until around $Z^* = 0.3$, where transition has observed earlier to occur. Consequently, the boundary layer on the containment wall is not only laminar but also the same as that over a flat plate in a quiescent environment, that is not affected by the rods.

Rod wall

Profiles extracted across the rod gap at Line_1 are compared against the similarity solution for slender vertical cylinders reported by Popiel[131] but originally published

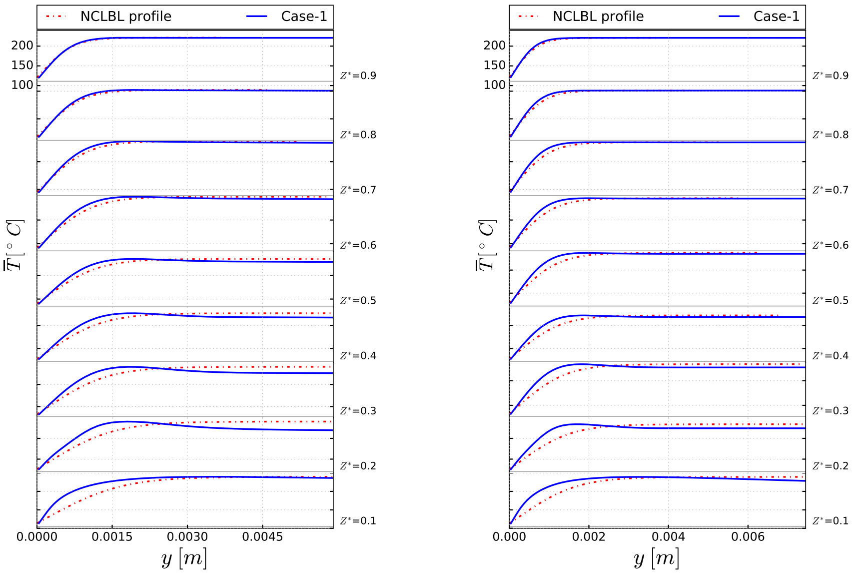

(a) Line_5 (b) Line_6

Figure 5.14: Comparison of LES data for Line_5 and Line_6 from Case-1 against the similarity solution by Ostrach[13] for temperature. Data is extracted from the containment surface now located at $y = 0$.

by Sparrow and Gregg[14]. The computation and validation of the similarity solution is given in Appendix A.5.

Figure 5.15(a) compares the data extracted along Line_1 against the similarity solution by Sparrow and Gregg[14]. Below $Z^* = 0.1$ there is good agreement and above this height the extracted data departs from the similarity solution. Velocity profiles have shown for Line_1 at $Z^* = 0.33$ the flow is fully developed. Up until $Z^* = 0.1$, the flow is clearly laminar. Above $Z^* = 0.1$ and below $Z^* = 0.33$, the flow is within the transition regime with transition to turbulence occurring by $Z^* = 0.33$. On the rods it is evident there is natural convection boundary layer forming but with a much reduced development length in comparison to the containment.

Results in Figure 5.15(b) for the temperature show good comparisons, at or below $Z^* = 0.1$.

5.2.4 Correlations

Heat transfer correlations are presented for the containment surface, rod surfaces and the sub-channels. The Fanning friction factor computed at the containment surface is also reported. Figure 5.16(a) presents the Nusselt number at the containment surface.

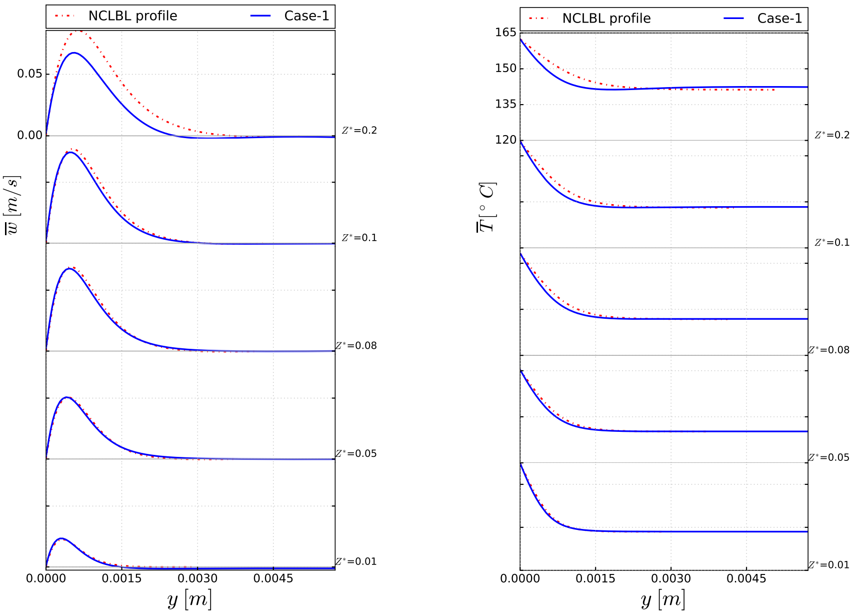

(a) Velocity (b) Temperature

Figure 5.15: Comparison of LES data for Line_1 from Case-1 against the similarity solution for cylinders by Sparrow and Gregg[14]. Data is extracted from the cylindrical rod surface at $y = 0$ to the stagnant flow region.

Rayleigh is computed using the temperature difference and the length scale is the distance from the top of the domain. The profiles show a linear increase of Rayleigh number, up until $\mathrm{Ra}_{z,\Delta T} \approx 10^{10}$ and 5×10^{10} for the lowest heating cases and highest heating case, respectively. Afterwards, there is a sudden jump in Nusselt number indicating turbulence transition. Correlating the LES data for the laminar portion yields $0.17\mathrm{Ra}_{z,\Delta T}^{0.28}$. Assuming a flat vertical plate, the laminar correlation for Nusselt number has an exponent of 0.25. This shows a remarkable similarity between this geometry (for flow at the containment surface) and an unconfirmed vertical surface, further showing the underlying physics can be considered somewhat the same.

Next, the Fanning friction factor for the containment surface is presented in Figure 5.16(b) as a function of Rayleigh number. To compute, the fanning factor the peak axial velocity is used. Similar to the Nusselt plot, an initial laminar region is seen with a transition region occurring at higher Rayleigh numbers.

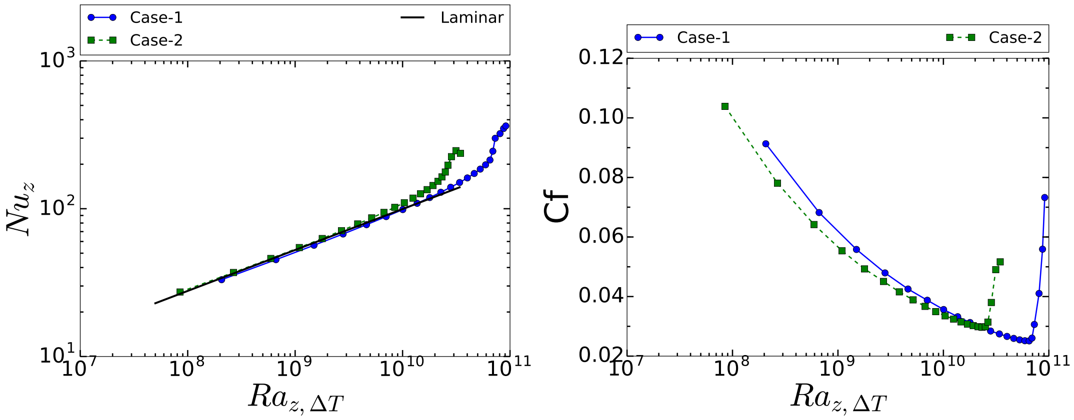

(a) Nusselt number (b) Fanning friction factor

Figure 5.16: Variation of Nusselt and Fanning friction factor as a function of Rayleigh for the containment surface.

Correlations at the fuel rods

The Nusselt number on the fuel rods has also been calculated. To relate the derived correlation to those obtained for rectangular cavities, a mirror profile approach is adopted. This approach was proposed by Trinca[26] in earlier preliminary work. Figure A5 illustrates this approach. In rectangular cavities, the dimensionless variables are computed using the hot and cold wall temperature difference. Using the mirror profile approach the following equivalent definitions are used:

$$\mathrm{Nu} = \frac{q''L}{2\Delta T\lambda} \tag{5.1a}$$

$$\mathrm{Ra} = \frac{g\beta L^3\left(2\Delta T\right)}{\alpha v} \tag{5.1b}$$

where ΔT is the difference between the wall and minimum temperature. The characteristic length scale used L is defined as the rod gap spacing.

Results obtained from this approach are presented in Figure 5.17. The aspect ratio, defined as H/L where H is the height and L is the rod gap length, ranges from 14 to 26. Data from the LES simulation is extracted between $Z^* = 0.3$ and 0.7, as the flow at the top and bottom is known to be laminar.

Heat transfer correlations for rectangular cavities obtained by Macgregor and Emery[6]

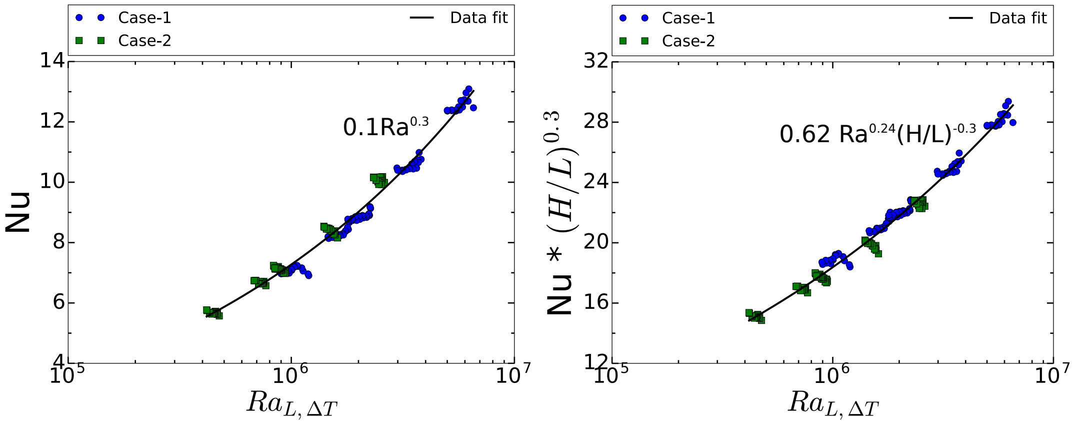

(a) Without aspect ratio scaling.

(b) With aspect ratio scaling.

Figure 5.17: Nusselt values computed across the rod gap using the mirror profile approach. Correlation for subfigure (a) is Data fit $= 0.1\mathrm{Ra}_{L,\Delta T}^{0.3}$ and for subfigure (b) is Data fit $= 0.62\mathrm{Ra}_{L,\Delta T}^{0.24}\left(H/L\right)^{-0.3}$.

are given below with and without Nusselt scaling by the aspect ratio:

$$\mathrm{Nu} = 0.046\mathrm{Ra}_{L,\Delta T}^{0.333} \tag{5.2a}$$

$$\mathrm{Nu} = 0.42\mathrm{Ra}_{L,\Delta T}^{0.25}\mathrm{Pr}^{0.012}\left(H/L\right)^{-0.3} \tag{5.2b}$$

Equation 5.2(a) is valid for aspect ratios up to 40 with a Rayleigh number range of 10^6 to 10^9. Equation 5.2(b) is valid for Rayleigh numbers 10^4 to 10^7 and aspect ratios up to 40.

The LES derived data correlations are $0.1\mathrm{Ra}_{L,\Delta T}^{0.3}$ and $0.62\mathrm{Ra}_{L,\Delta T}^{0.24}\left(H/L\right)^{-0.3}$ comparing to the forms proposed by Macregor and Emery[6], respectively. It can be noted the exponents are very similar, even though there is a significant difference in the geometry. Similarly, the correlations from Keyhani et al. [81] had exponents of 0.323 and 0.332 for the differing rod bundle configurations. In general, Nusselt number values for turbulent flow are known to follow the relation $C\mathrm{Ra}^{0.33}$ for rectangular cavities and flat vertical surfaces. For the more complex geometry and conditions investigated herein, this dependence has been shown to still hold, which is a remarkable result.

In a precursor simulation to those presented herein by Trinca[26] an unstructured (prismatic) grid was used to simulate a short geometry bundle. A single heating case of 325 W/m^2 at a pressure of 4 Mpa was investigated. Using the mirror profile approach, the correlations obtained were $0.095\mathrm{Ra}_{L,\Delta T}^{0.32}$ and $1.081\mathrm{Ra}_{L,\Delta T}^{0.22}\left(H/L\right)^{-0.3}$. The obtained correlations are similar to those from the updated simulations.

5.3 Conclusion

LES simulations have been conducted for a sealed short rod bundle. The flow and temperature distributions observed are akin to the boundary layer flow regime[6, 7]: Flow occurs in the boundary layers and the core is largely stagnant with a uniform stratified temperature field. The formation and development of momentum and thermal boundary layer on the rods and containment wall are important feature of the flow system.

Flow at the containment surface gradually develops from laminar and transitions to turbulence occurs close to the bottom-end. After the point of transition, turbulence generated here is spread to the interior sub-channels by the ensuing jet flow. The spread of turbulence is demonstrated to affect boundary layer development on the rods. The rod ranks closest to the containment wall are shown to transition faster. While rods in the first rank, which is furthest from the containment are largely unaffected and transition to turbulence later. Using the Q-criterion, turbulence structures are evidenced within the vicinity of the fuel rod surfaces and lower half of the containment wall.

Correlations extracted for the rod surfaces using a mirror profile approach have shown the Nusselt number has a Rayleigh dependence of $\mathrm{Nu} = 0.1\mathrm{Ra}^{0.3}$, which is similar to that for a rectangular cavity. Nusselt number and friction factor correlations at the containment wall confirm transition occurs close to the bottom-end. The formation of a fully turbulent core as seen by other investigators such as Elder[74] and Betts and Bokhari[77] has not been observed in this short geometry. Thus it is likely if a larger domain is modelled the flow and heat transfer characteristics would be appreciably altered.

Chapter 6

LES of natural convection in a tall bundle

A low aspect ratio rod bundle of height 0.25 m has been investigated in Chapter 5. The resulting flow in the system was largely consistent with that for a boundary layer flow regime. In this chapter, the geometry is altered by increasing the height of the bundle to 1 m (typical of an AGR stringer). The alteration not only increases the aspect ratio but also induces the formation of a fully turbulent flow regime, contrasting the one in the previous chapter. To the author's knowledge, this is the first time highly turbulent natural circulation in a rod bundle geometry has been investigated using LES. The work in this chapter has been published in a paper by the author[132].

6.1 Modelling description

Barring the change in height, the rod arrangement and radial gap spacings are identical to that given in Chapter 5. A block structured mesh consisting of ≈ 77 million elements is generated. Using data from the highest heating case and the distance between the first cell node and wall the peak y^+ value is ≤ 0.52, indicating the first mesh cell nodes are within the viscous sublayer. The values for the spanwise and streamwise grid spacing calculated at mid-height are $\Delta x^+ = 44.5$ and $\Delta z^+ = 35.7$, respectively. The mesh cross-section is as given in Figure 5.2.

Fluid properties, boundary conditions and the numerical setup are as discussed in Chapter 5.

6.1.1 Non-dimensional parameters

Natural circulation flow in cavities can be characterised by the Rayleigh number, aspect ratio and Prandtl number. As before (see Table 5.2), the Prandtl number is fixed to 0.74. The aspect ratio (A) is defined as H/L where H is the height and L is length scale of the flow passage. Taking the length scale to be the distance between the heating rod surfaces and the cooling containment wall, the aspect ratios are 14, 22 and 57 ordered from the first to last rank. Using the mean internal sub-channel hydraulic diameter as the length scale gives an aspect ratio of 23. The Rayleigh numbers based on the heat flux and temperature definition are now computed using the bundle height (H), minimum and maximum length scales (i.e. L1 and L3 for Rank-1 and Rank-3, respectively). These values are given in Table 6.1.

Table 6.1: Rayleigh numbers for the heating cases considered using different length scales. $\mathrm{Ra}_{\Delta T}$ is computed using the overall domain maximum and minimum temperatures.

Parameter	Case-1	Case-2
$\mathrm{Ra}_{H,\Delta T}$	1.24×10^{13}	7.6×10^{12}
$\mathrm{Ra}_{L1,\Delta T}$	4.5×10^{9}	2.7×10^{9}
$\mathrm{Ra}_{L3,\Delta T}$	6.7×10^{7}	3.4×10^{7}
$\mathrm{Ra}_{H,q''}$	1.5×10^{15}	7.97×10^{14}
$\mathrm{Ra}_{L1,q''}$	3.4×10^{10}	2.1×10^{10}
$\mathrm{Ra}_{L3,q''}$	1.4×10^{8}	7.5×10^{7}

6.2 Results and Discussion

In the simulations, a fixed time step of 0.0004 s is used for all the cases. Taking the highest heating case (Case-1), the dimensionless time value (t^*) is ≈ 0.00022. Using this time step gives an overall peak Courant number of ≈ 1, with a few isolated cells ($<< 0.1\%$) periodically fluctuating above this. In the majority of the cells, the peak Courant values are well below 0.5 and the peak spatial mean is ≈ 0.1 at any given instance. A further reduction in the time step value to control the fluctuating peak Courant value in the isolated cells would mean a large portion of the domain would have cells with essentially zero Courant numbers (bringing the spatial mean to well below 0.1).

To assess the convergence of the simulation at the time of data extraction, profiles are compared at varying intervals along Line_1 and Line_5 in Figure B1 (see Figure 5.1 for the data extraction location). The comparison shows a well converged solution.

LES_IQ$_v$ is used to determine the LES simulation quality[130]. Computing this parameter gives a minimum value (considering both cases) of 0.91. The contour plots of the distribution of this parameter are given in Figure B2.

6.2.1 Global - flow pattern

The general behaviour of the flow, turbulence, and thermal fields is illustrated on a vertical plane at $\theta = 30°$ in Figure 6.1. From left to right, the walls are those for the insulated guidetube, side walls (left and right) of a heated second rank rod, and the cooled containment wall. Consequently, the "channel" on the left is typical of an asymmetrically heated channel, whereas that on the right is typical of a heating and cooling channel. The velocity and turbulent kinetic energy are normalised using the buoyant velocity ($V_{n.\Delta T}$), which is defined as $V_{n,\Delta T} = (g\beta\Delta T\nu)^{1/3}$, while the temperature is normalised using the difference between the domain maximum (T_h) and minimum (T_c) temperature values. Contour plots illustrating the cross-sectional behaviour are extracted at several axial locations and shown in Figures 6.2 and 6.3, for the velocity and turbulent kinetic energy, respectively. Considering figures 6.1, 6.2 and 6.3 in conjunction, the flow can be split into three definitive vertical regions, which are initially briefly introduced in listed form below. Demarcating dashed lines with the Z^* value for these regions are given in Figure 6.1.

- The top region: This region is largely made of a stagnant stratified fluid with a thin downward laminar boundary layer on the cooling containment wall and turbulent upward boundary layers on the heated rods.

- The middle (main section) region: In this region, the flow is highly turbulent with a large scale downward flow near the containment and an upward interior flow in the sub-channels formed between the fuel rods/guidetube.

- The bottom region: This region is characterised by the downward flow impingement and a cross-flow.

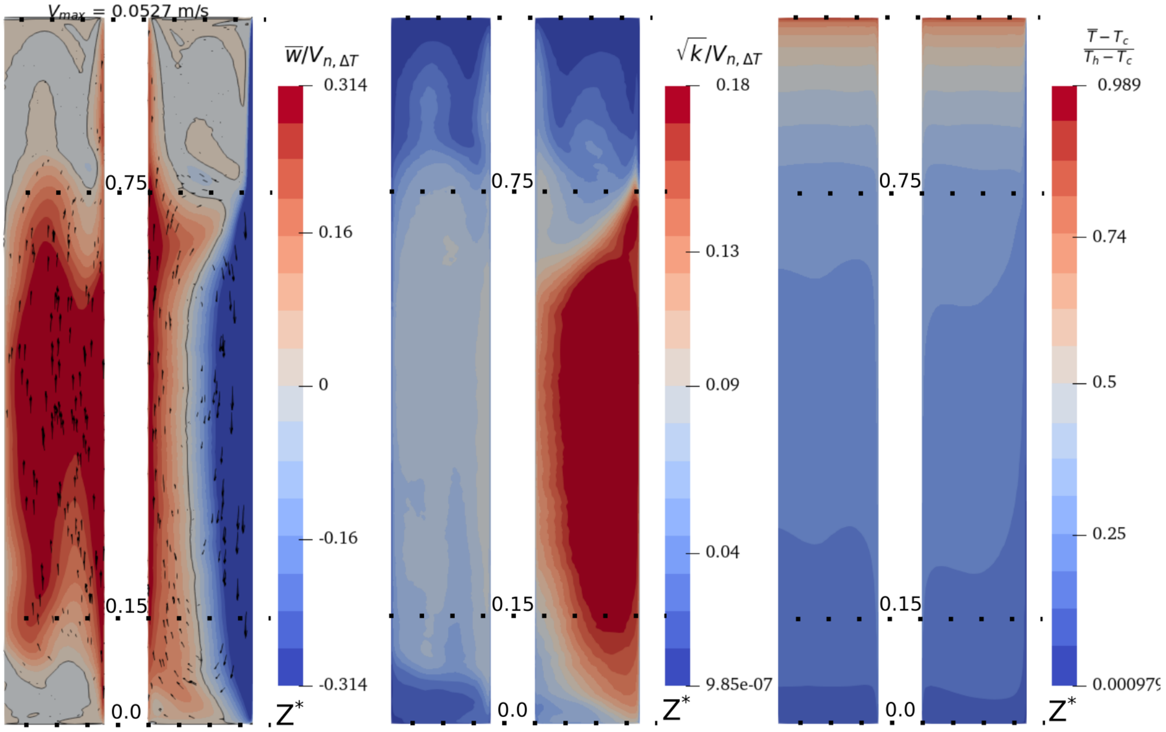

(a) Velocity (b) Turbulent kinetic energy (c) Temperature

Figure 6.1: Contours of turbulent kinetic energy, velocity and temperature extracted from Case-1. Slices are taken at $\theta = 30°$. To better represent the data, the height of the domain is shrank by a factor of 4.

The top region

Figure 6.1(a) particularly highlights the developing boundary layer flow at the containment surface, boundary layer flow at the rods and a largely stagnant region away from the walls. Little or no turbulence levels are observed at the containment surface. However, transition to turbulence occurs towards the lower part of this region and when this occurs, turbulence is initially generated where the gap is narrowest with the third rank rods (Figure 6.3(e)). These peaks form close to the containment surface and are a result of the shear production of turbulence. The onset of transition in enclosures is known to be aspect ratio dependent and this seemingly leads to initial

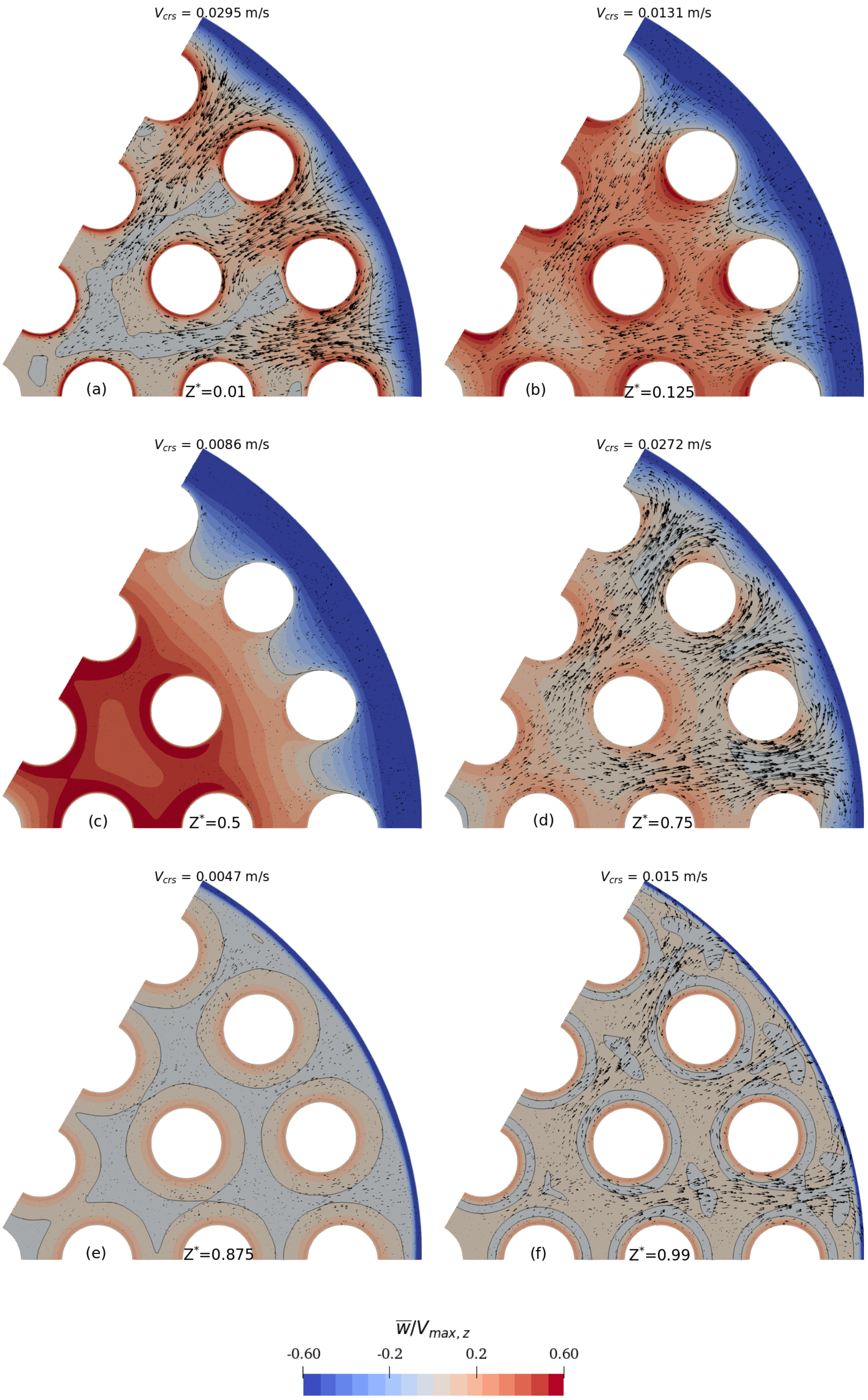

(g) Scalebar

Figure 6.2: Axial velocity contours extracted for Case-1. Contours at $\overline{w}/V_{\max,z} = 0.0$ are marked with a black line.

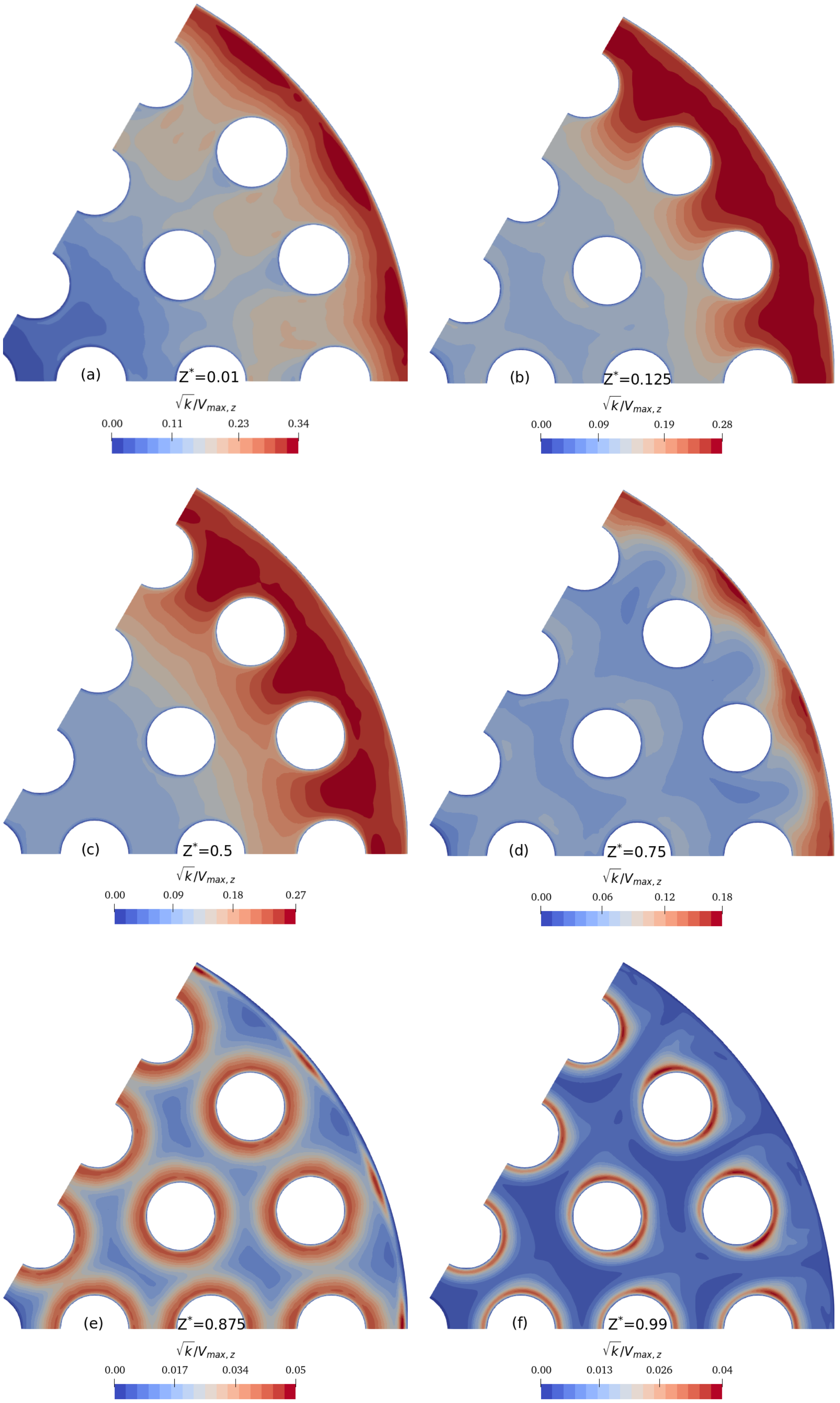

Figure 6.3: Contour plots turbulent kinetic energy extracted for Case-1. The contours are normalised using the peak velocity of the slice and a scalebar is shown for each subfigure to maximise the variation.

turbulence generation occurring where the distance between the hot and cold surfaces is at a minimum and thus aspect ratio is largest.

Figure 6.1(a) also shows the flow on the rods is constrained to the boundary layers, which reduce in thickness as the flow ascends. Eventually, close to the top wall, the boundary layer flow stagnates due to the end effects and stratification. Turbulence is shown to occur in the regions surrounding the rods with little or no turbulence at the cores, which also happen to be regions of stagnant flow. One of the characteristics of boundary layer flow regimes in cavities is vertical temperature stratification. As seen in Figure 6.1(c), the vertical temperature distribution is heavily stratified for the top region. The cross-sectional temperature distribution (not shown) is uniform with significant temperature gradients only occurring across the boundary layers.

Due to the effects of buoyancy, the flow ascends at the heated rod surfaces and descends at the cooled containment wall with a general clockwise rotation thereby forming the primary flow circulation. Figure 6.2(f) shows close to the top wall as part of this circulation, the hot gas traverses from the interior sub-channels to the containment wall with relatively high cross-flow magnitudes.

Middle region

The middle region makes up most of the cavity and is dominated by turbulence effects. Transition to turbulence at the containment surface is qualitatively shown to occur at a dimensionless distance (Z^*) of approximately 0.8, with the turbulent region commencing at $Z^* \approx 0.75$. This is particularly illustrated in Figures 6.1(a & b) by the sudden expansion of the boundary layer thickness and the drastic increase in turbulence levels at this location.

At the point of transition, the flow is entrained from the interior towards the containment wall due to the rapid growth of the boundary layer thickness. Figure 6.2(d) shows the cross-flow vector magnitudes are significantly greater than those observed close to the top wall. Enhanced chaotic mixing occurs from here on and is perhaps best characterised by the ensuing nearly uniform vertical fluid temperature. This is in stark contrast to the top region, which is heavily stratified.

When transition occurs, the turbulence peaks are initially located close to the containment surface. However, with depth a large scale downward flow structure exists on the right-hand side where cooling occurs. This flow structure is strong and extends well beyond the containment wall. Figure 6.2(c) shows the flow is entirely downward up to the third rank rod gap, essentially there is heated downward flow or buoyancy opposed flow at this surface. On the left-hand side, the interior channel flow is entirely upwards. The vertical vector plots in Figure 6.1(a) indicate an acceleration of the interior channel flow from the bottommost to approximately the mid-height $Z^* = 0.5$. This is seemingly followed by a deceleration region, culminating to much-reduced flow vector magnitudes at the top of the middle region.

These two opposing flows interact at the gaps of the third rank rods and the black contour line for $\overline{w}/V_{max,z} = 0$ demarcates them. Below $Z^* = 0.75$, turbulence peaks are located near here indicating this shear layer dominates turbulence production. Turbulence spreads from here to the interior sub-channels and this is best illustrated by Figure 6.3(c). At the interior rod gaps, high free-stream turbulence levels are evident and from a qualitative viewpoint appear to prevail over the local turbulence production at the rod surfaces.

Earlier on, two channels separated by the second rank rod were identified (see Figure 6.1). On the right-hand side (heating and cooling) channel, the flow strongly resembles that of the Betts and Bokhari case study [77], and for the left-hand side channel, the behaviour is that of a heated upward flow. Third rank rods encapsulated within the right-hand side channel appear to act as mere obstructions to the flow and generation of turbulence (see Figures 6.2(c) and 6.3(c)). It is quite interesting to note, at the third rank rod walls facing the containment surface, there is no evidence of upward flow in the turbulent region. On this portion of the rod wall, the local mean flow opposes the buoyancy force (buoyancy opposed flow) and the lack of upward flow near here gives a further indication of the strength of the downward flow.

Keyhani et al.[81] conducted experiments in a 3 x 3 and 5 x 5 rod bundle. The reported flow visualisation results in their paper were based on the 3 x 3 rod bundle at a Rayleigh number (based on the containment diameter) of 2.97×10^7. The Prandtl number was 46 as ethylene glycol with suspended aluminium particles was used to aid flow visualisation. The flow descriptions in their study closely resembled those of the top region in the present simulations. Boundary layer flow was observed and the rods did not interact with each other. In cavities, the flow regime is dependent on the Rayleigh number, Prandtl number and aspect ratio. A higher aspect ratio decreases the critical Rayleigh number required for the onset of transition, while a higher Prandtl number increases the critical Rayleigh number. The aspect ratio for their study based on the 3 x 3 hydraulic diameter is ≈ 13, compared to 23 for the current study. In the visualisation study by Keyhani et al.[81], the Prandtl number was higher 46 compared to 0.737 in the present simulations. Finally, the Rayleigh number (based on the containment diameter) in the current study is $\approx 2.5 \times 10^9$, which is larger than those considered in their flow visualisation experiments. The difference in flow visualisation reflects the differences in the flow regimes that exist in the two studies: largely laminar in Keyhani et al.[81] whereas mostly turbulent herein.

Bottom region

The bottom region starts below $Z^* = 0.2$, where the boundary layer at the containment wall begins to show a decrease in thickness. Within this region, the flow is diverted towards the interior from the containment and it is shown, the cross-flow vector magnitudes increase approaching the bottom wall (see Figure 6.2(a & b)). In Figure 6.3, the overall local peak turbulence values occur at $Z^* = 0.01$ and close to the containment wall. At this location, the downward flow impinges onto the bottom wall increasing turbulence production.

In the interior, the flow begins its ascent from the bottom of the rods. It is readily apparent the boundary layer at the rods has a shorter development length in comparison to that observed at the containment wall. However, as seen in Figure 6.1 there is a difference in the rod flow development based on the two channels identified earlier. On the left-hand side channel, the heated rod wall is on the leeward side of the cross-flow. Away from the rod wall (going further left to the adiabatic wall) there is stagnant to very low magnitude downward flow. Initially, a boundary layer is observed on this surface. In contrast, on the right-hand side, where the rod is directly facing the cross-flow no stagnant region is observed. Instead the upward and descending flows still interact even quite close to the bottom wall. Visually, the development of the boundary layer on the rod here appears somewhat affected by the impinging cross-flow and stronger convected turbulence.

6.2.2 Statistical distributions

Global contour plots have shown the overall flow behaviour in the bundle differs not just vertically but also based on the sub-channel. The channels are split by the second rank rod as seen in Figure 6.1. The discussion of the profiles is therefore further split into two regions based on the defined channels which are; the heating and cooling outer channel, likened to Betts and Bokhari case study[77] including sub-channels 4 to 9 and the heated upflow central channel, including sub-channels 1 to 3.

Outer region

Velocity, temperature, and turbulent kinetic energy profiles are shown in Figures 6.4 to 6.6. The profiles are extracted from Line_5 and Line_6, representing the narrow and large gaps existing in this region respectively, with the locations of these lines illustrated in Figure 5.1. First we note that the profiles for cases 1 and 2 are very close to each other and in the following discussion, we will not distinguish between them unless stated otherwise.

Line_6 is extracted from the second rank rod to the containment surface. This line exhibits the typical behaviour expected of an opposing upward and downward flow in a heating and cooling channel. In the top region, the boundary layer is thin (and of laminar nature as will be further shown later) at $Z^* = 0.8$ and $Z^* = 0.9$. This is supported by the turbulence kinetic energy profiles, which show little to no turbulence levels here. In the next section, a similarity comparison is carried out for the laminar containment flow. At $Z^* = 0.7$, the flow is clearly turbulent but still developing and it becomes fully developed between $Z^* = 0.6$ to $Z^* = 0.3$, as seen from the identical profiles for turbulence and velocity. Below $Z^* = 0.2$, the flow profiles start to alter due to the encroaching end effects.

The temperature profiles are also similar to each other between $Z^* = 0.6$ to $Z^* = 0.3$. Temperature variation is quite significant near the walls, however away from the walls a uniform temperature core is seen and this remains true from the top wall right-down to the bottom wall. In contrast for velocity, the core is initially stagnant at the top region ($Z^* = 0.9$ and $Z^* = 0.8$). In the middle highly turbulent region, the boundary layers between the opposing flows strongly interact with each other resulting in a linear gradient profile across the gap. Turbulence peaks as observed in the contour plots occur in the core as a result of the second shear layer. The aforementioned flow behaviour is similar to the observations made by Betts and Bokhari[77].

Line_5 is extracted from the third rank rod to the containment wall. At the top region, the flow is constrained to the boundary layers, with a stagnant core similar to that along Line_6 even though with a thinner boundary layer. But in contrast to that along Line_6, in the turbulent region the entire flow is going downwards, clearly dominated by the strong cooling effect on the containment wall. This region of buoyancy opposed flow on the rod extends from $Z^* = 0.7$ to $Z^* = 0.2$. This is the only location in the domain where such a scenario arises. At all the other heated or cooled surfaces buoyancy aided flow is prevalent. It should be noted however that the buoyancy does cause the velocity gradient to be lower on the rod than on the opposite wall as expected. Turbulence peaks across this gap are shown to be broad and flat in comparison to those for Line_6, which have a peak in the interior.

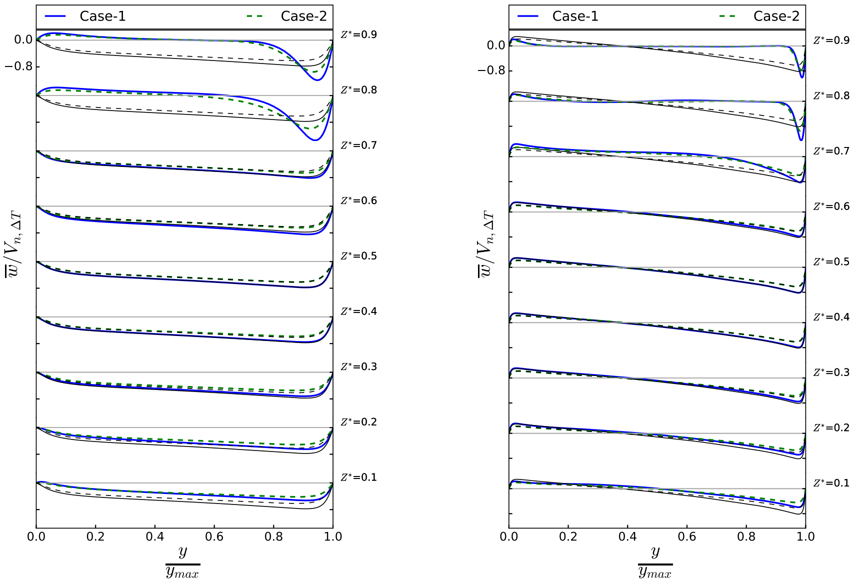

(a) Line_5 (b) Line_6

Figure 6.4: Outer region profiles for the axial velocity at different heights. The profile at mid-height ($Z^* = 0.5$) is added to each subplot using black-thin lines.

Central region

Velocity, temperature, and turbulent kinetic energy profiles for this region are given in Figures 6.7 to 6.9. The flow in the left-hand side region is primarily heated upflow

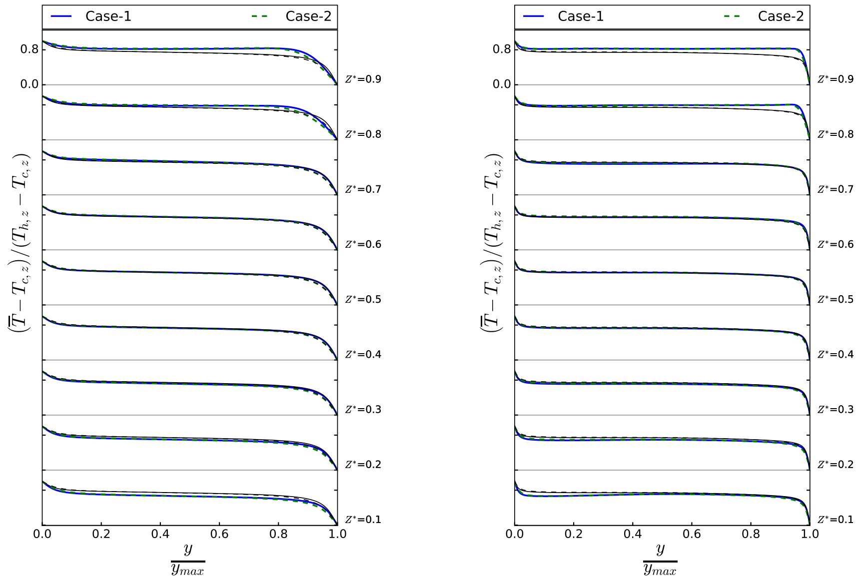

(a) Line_5 (b) Line_6

Figure 6.5: Outer region temperature profiles extracted at differing axial locations. The profile at mid-height ($Z^* = 0.5$) is added to each subplot using black-thin lines.

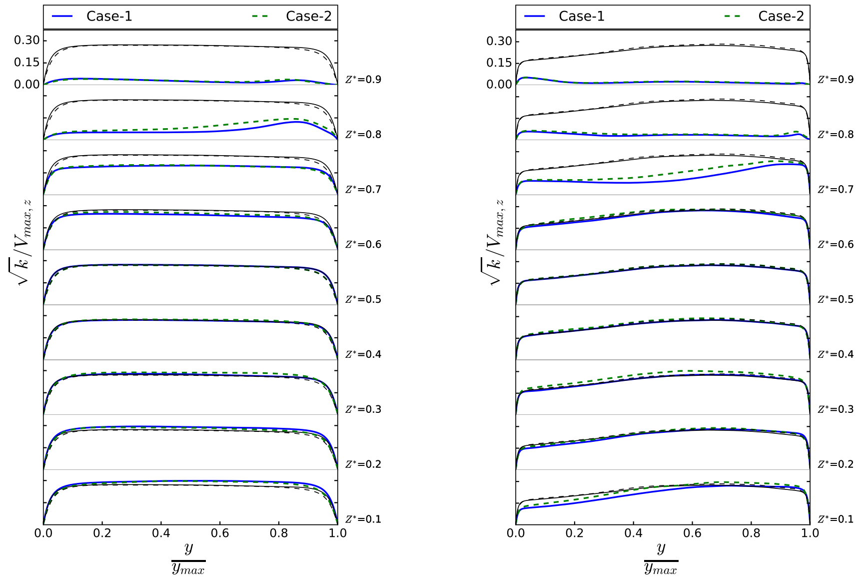

(a) Line_5 (b) Line_6

Figure 6.6: Outer region turbulent kinetic energy profiles extracted at differing axial locations. The profile at mid-height ($Z^* = 0.5$) is added to each subplot using black-thin lines.

but with interference from the right-hand side region. The profiles shown are obtained from Line_1, Line_2, and Line_9. Line_1 and Line_2 are extracted across the rod gaps, while Line_9 can be considered an extension of Line_6 to the left-hand side region and spans from the heated second rank rod to the adiabatic guide tube wall.

At the rod gaps (Line_1 and Line_2) as the flow ascends, the boundary layers on the opposing rod surfaces merge. Between $Z^* = 0.1$ and 0.7, the free-stream turbulence levels at the gap centres are quite significant. This is due to turbulence spreading from the right-hand side, thus we see a departure from the typical natural convective flow profile to one more typical for forced/mixed convection flows between $Z^* = 0.2$ to $Z^* \approx 0.6 - 0.7$. Above these heights in the top region, free-stream turbulence levels began to drop at the rod gaps as there is less turbulence convected from the right-hand side. The flow is now constrained to the boundary layers. The increasing end effects and stratification eventually destroys the vertical boundary layer flow. The profile for Line_2 is asymmetric at $Z^* = 0.1$, 0.7, and 0.8. This occurs as the profile straddles the first and second rank rods, thus is heavily influenced by the cross-flow at these locations.

The temperature profiles for Line_1 and Line_2 show the boundary layer thickness is largely unchanged with height and hence showing the profile typical of a fully developed internal channel/pipe flow. Changes in the thickness can however be seen at the transition from laminar to turbulence. Similar to the profiles shown for the right-hand side region, there is a largely uniform temperature core with significant temperature variation occurring across the boundary layers.

It is interesting to note for both Line_1 and Line_2, the peak amplitude of the velocity profile alters with height between $Z^* = 0.2$ and 0.7. In particular, for Line_1, it can be noted below the mid-height flow acceleration occurs. Above mid-height between $Z^* = 0.6$ and 0.7, the flow decelerates although the shape of the profile largely remains the same. Past $Z^* = 0.7$, the flow continues to decelerate though this is now coupled with a change in the profile shape. The flow does not appear to fully develop between $Z^* = 0.2$ and 0.7. Across this gap, the flow is akin to that in a heated channel but due to its open boundaries, the chimney effect may draw flows from neighbouring such-channels causing the flow to accelerate. For example, results of Ohk and Chung[71] show due to the chimney effect flow acceleration occurred in their case study. A similar effect occurs here until $Z^* = 0.5$. Past the mid-height, cross-flow from the interior (left-hand side region) towards the containment (right-hand side region) gradually increases starting the deceleration process. Later on, inner scaling laws are used to check the selfsimilarity of the profiles in the turbulent region and bulk quantities at a sub-channel level are used to assess the influence of the cross-flow and bulk behaviour of the flow.

Line_9 generally follows similar trends to those discussed for the rod gap profiles, although there are a few dissimilarities. At the top region ($Z^* = 0.9$ and $Z^* = 0.8$) there is heated boundary layer flow on the rod surface. Away from this surface, the flow is stagnant up to the adiabatic guide tube wall as to be expected. In the middle region, there is an upward flow throughout the entirety of the profile. The influence of the strong downward flow structure in the outer region and the spread of turbulence as seen in Figure 6.7 and 6.9 propagates all the way to the guide tube wall. Away from the top/bottom developing regions, the flow is akin to a forced convection on the insulated guide tube side. Close to the heated rod however, the velocity profile shows a characteristics of one in a strongly heated upward pipe flow, which normally show a M-shape profile.

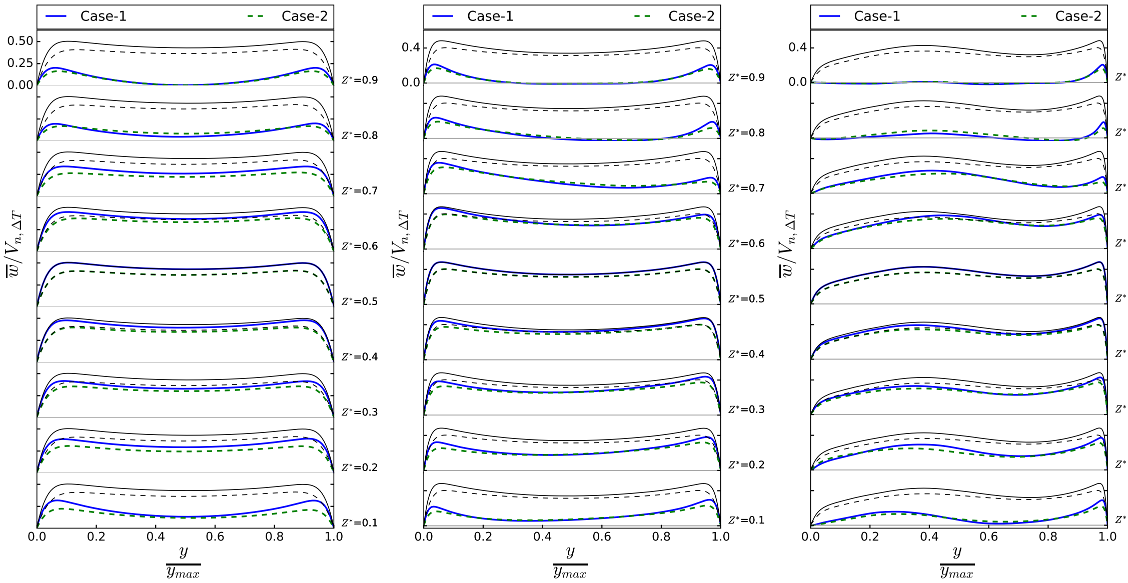

(a) Line_1 (b) Line_2 (c) Line_9

Figure 6.7: Central region profiles for the axial velocity at different heights. The profile at mid-height ($Z^* = 0.5$) is added to each subplot using black-thin lines.

6.2.3 Laminar boundary layer

The initial flow at the top of the containment wall is laminar before transitioning to turbulence. Similarly, at the rods the flow would develop from an initially laminar

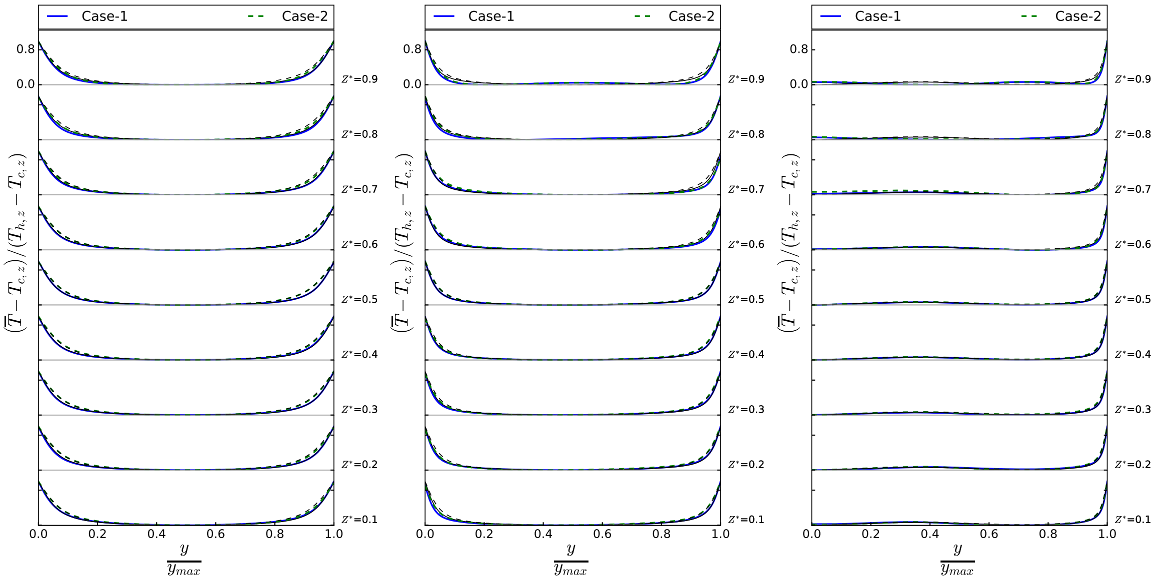

(a) Line_1 (b) Line_2 (c) Line_9

Figure 6.8: Central region temperature profiles extracted at differing axial locations. The profile at mid-height ($Z^* = 0.5$) is added to each subplot using black-thin lines.

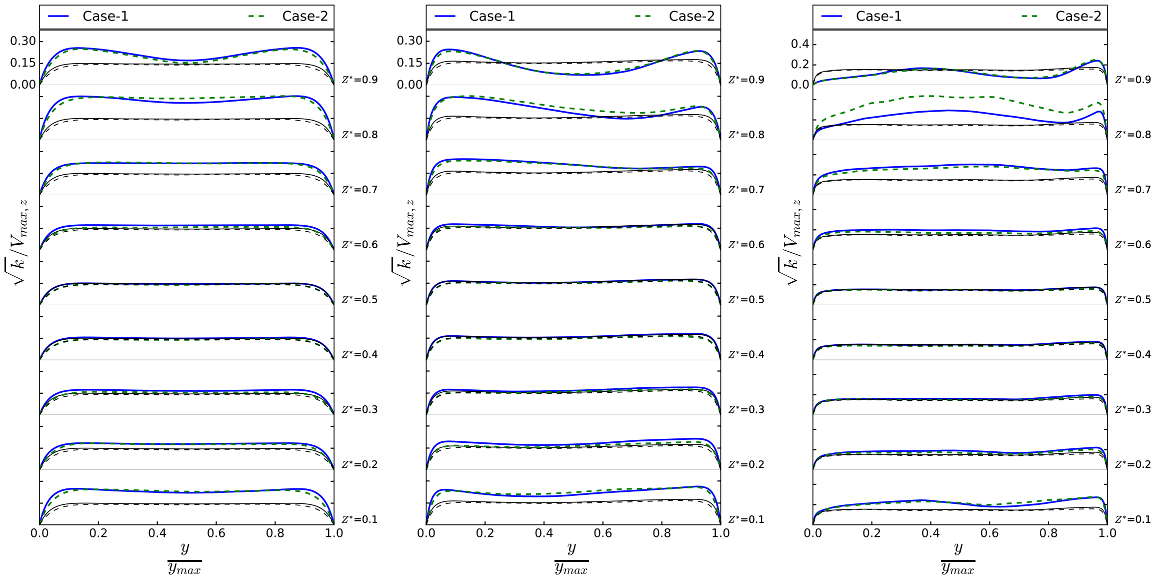

(a) Line_1 (b) Line_2 (c) Line_9

Figure 6.9: Central region turbulent kinetic energy profiles extracted at differing axial locations. The profile at mid-height ($Z^* = 0.5$) is added to each subplot using black-thin lines.

state as it begins its ascent from the floor, although for these surfaces this has not been sufficiently demonstrated thus far. Two similarity solutions are considered; at the containment surface the comparison is made against the similarity solution for buoyant flow on flat vertical surface by Ostrach[13]. At the rod surfaces, the comparison is against the slender cylinder similarity solution republished by Popiel[131] but originally from Sparrow and Gregg[14]. Details of the solutions is given in the Appendix Section A.4 and A.5.

Similarity solution - Containment

Similarity solution for velocity and temperature are shown in Figure B3 and B4 at the containment surface using Line_5 and Line_6 to compare with the LES simulation. The agreement is good for $Z^* > 0.83$ for Line_5 and $Z^* \geq 0.79$ for Line_6 showing that the flow is effectively a laminar boundary layer in a large quiescent space. The difference in the location of the transition for Line_5 and Line_6 is likely due to the lengths of the lines, that is the gap sizes of the "channels". This is known to influence the the location of the transition. Comparisons of the similarity solution against temperature show fairly reasonable agreement. Similar to velocity it is noted that Line_5 starts showing significant deviations at a shorter development length compared to Line_6.

Similarity solution - Rods

The slender cylinder similarity solution from Sparrow and Gregg[14] is compared against a first rank heating rod. Figure B5 shows the similarity comparison for temperature and velocity. The flow at the rods is seen to agree quite well at $Z^* = 0.01$ but develops much faster compared to the containment wall and by $Z^* = 0.04$ it has largely deviated from the similarity solution. Temperature comparisons show quite good agreement at $Z^* = 0.01$, however even at $Z^* = 0.07$ there is just a slight deviation from the similarity solution.

6.2.4 Near wall behaviour in the turbulent region

Non-dimensional near wall profiles normalised using viscous wall units are presented in this section for velocity, temperature, streamwise turbulence and turbulent heat flux. The velocity profiles are normalised using the friction velocity $(\overline{w}_\tau)$ and plotted against the dimensionless distance $\left(y^+\right)$ at Line_1 and Line_6. Friction velocity $\overline{w}_\tau$ is defined as $\sqrt{\tau_w}/\rho$, where the τ_w is the wall shear stress defined as $\mu d\overline{w}/dy \mid_{y=0}$. As to be expected for natural convective flows, the velocity profile deviates from the viscous sublayer profile $\left(\overline{w}^+ = y^+\right)$ at $y^+ \approx 1$ and the log-law region typical to forced convection flows does not exist. Adopting the approach from Tsuji and Nagano[64], the inner layer is defined as the region from the peak of the profile to the wall. The outer layer is the region outside of this. The peaks for both lines are located between $y^+ = 20 - 30$. The profile for Line_1 at $Z^* = 0.8$ can be considered an outlier and peaks much closer to the wall at $y^+ \approx 10$, but this is likely due to the end effects as ascending flow is gradually arrested for example in the rectangular cavity by Barhaghi and Davidson[79], at x/L = 0.9 (close to the domain top end) the peak is closer to $y^+ = 10$. In Tsuji and Nagono's[64] experimental work the peaks were located around $y^+ = 30 - 40$ for the turbulent region and around $y^+ = 10 - 20$ for the laminar and transitional regions. Line_1 shows the peak amplitude and its location varies with the Grashof number. Up until the mid-height, the peak amplitude increases and slightly moves outwards with an increasing Grashof number. However, past the mid-height this reverses with the peak amplitude decreasing and its location moving closer to the wall with an increasing Grashof number.

Profiles for Line_6 are largely self-similar below $Z^* = 0.6$. Compared to the profiles at $Z^* = 0.8$ and 0.9 (transitional and laminar flow), the peak values are much reduced with a broader region of occurrence. Looking at Line_1, the profiles are self-similar from $Z^* = 0.2$ to 0.6. The y^+ location of the peaks and the distribution for Line_6 is largely the same as that for Line_1. It is noted, within the turbulent region up until the mid-height there is a positive correlation between the increase in peak value and increase of Grashof number. However, below the mid-height, the peak starts decreasing with increasing Grashof number. The peak values are much higher at the containment than at the rods and the developed Line_6 profile at $Z^* = 0.5$ imposed onto Figure 6.10(a) clearly demonstrates this, however the inner layer is reasonably similar. Earlier contours and global lineplots have shown remarkable differences between the flow profiles for Line_1 and Line_6, but as seen and discussed here the near wall behaviour is largely as expected for natural convective flows.

Figure 6.11 shows the plot for T^+ against y^+. The Line_1 profiles are almost identical at $Z^* = 0.4$ and 0.5, and have a degree of similarity along other lines as well. For Line_6, the profiles are identical from $Z^* = 0.7$ and below. Near the wall a constant heat flux region is present and can be represented by the profile $T^+ = \mathrm{Pr} y^+$. For both

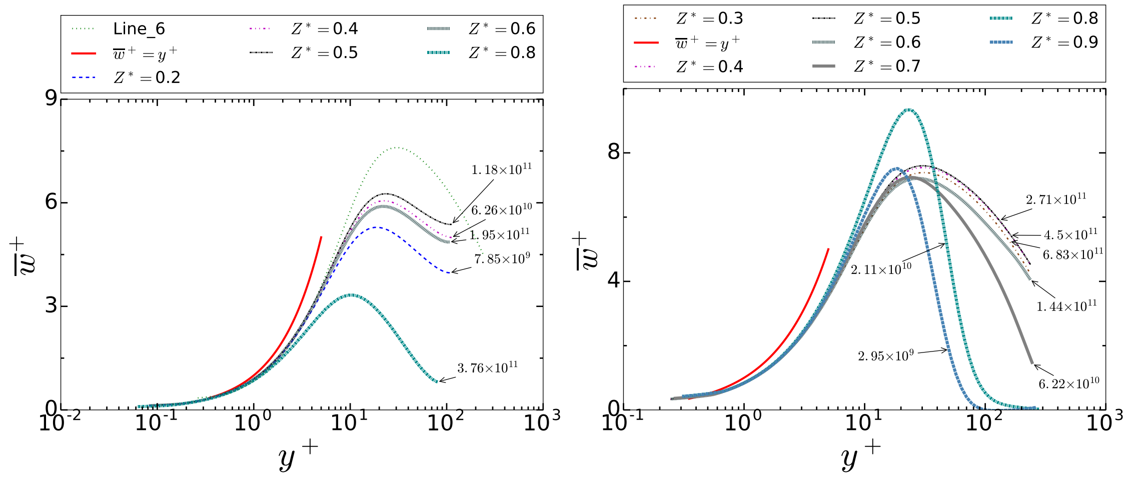

(a) Line_1

(b) Line_6

Figure 6.10: Non-dimensional near wall profiles for $\overline{w}^+$. Data is extracted from Case-1. In subfigure (a), Line_6 refers to the developed profile at $Z^* = 0.5$ taken from Line_6. The local Grashof $\left(\mathrm{Gr}_{z,\Delta T}\right)$ numbers are given for each respective line with the annotated arrows. The limits of the profiles in y/y_{max} units is 0.5 and 0.2 for Line_1 and Line_6, respectively.

lines, departure from the profile ($T^+ = \mathrm{Pr}y^+$) occurs at $y^+ \approx 6$. Looking at Figure 6.11, the developed profile from Line_6 at $Z^* = 0.5$ is nearly the same with the profiles for Line_1 at $Z^* = 0.4$ and 0.5.

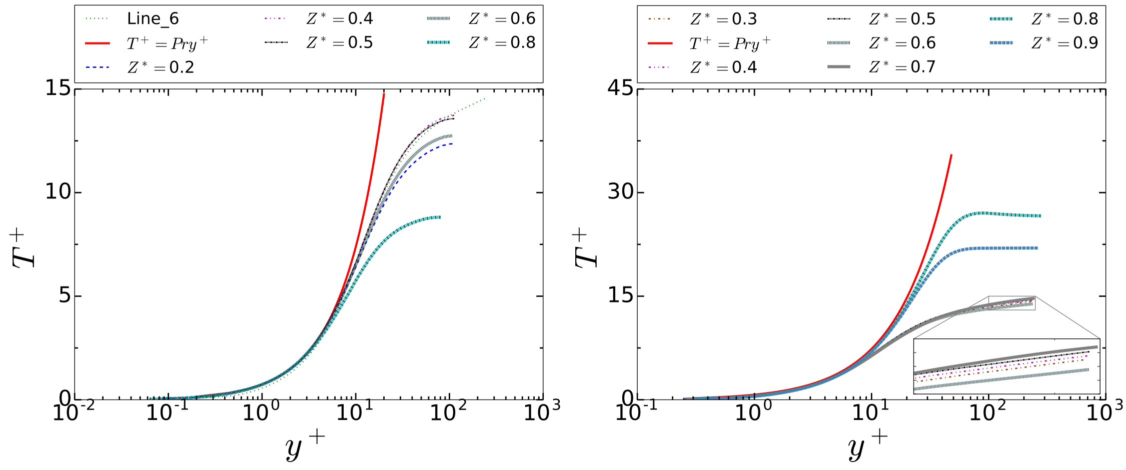

(a) Line_1

(b) Line_6

Figure 6.11: Non-dimensional near wall profiles for T^+. Data is extracted from Case-1. In subfigure (a), Line_6 refers to the developed profile at $Z^* = 0.5$ taken from Line_6. The limits of the profiles in y/y_{max} units is 0.5 and 0.2 for Line_1 and Line_6, respectively.

Streamwise normal stress profiles plotted against y^+ are presented in Figure 6.12.

Profiles for Line_1 show a degree of similarity from $Z^* = 0.2$ to 0.6. Interestingly, the peaks for Line_1 also occur on the bounds of the inner layer $y^+ = 20 - 30$. In the flat vertical plate studies by Nakao et al.[67] and Tsuji and Nagano[64], the peaks occurred past $y^+ = 100$, so well within the outer layer. The streamwise stress profiles for the square cavity by Sebilleau et al.[80] had peaks within the $y^+ = 10 - 100$ range. The variation was largely dependent on development distance and the Rayleigh number. For Line_6, where the flow is descending downwards; the boundary layer development to the fully turbulent condition is evident with reasonably self-similar profiles between $Z^* = 0.6 - 0.3$. The first near wall peak for this line is around $y^+ = 40$ but turbulence is seen to increase again well past $y^+ = 100$ in some profiles. The peak value increases slightly (note Grashof number is not shown here) from $Z^* = 0.9$ to $Z^* = 0.4$. Below this ($Z^* = 0.3$), the peak value reduces with increasing Grashof number. However, at Line_1 the variation of the peaks with the local Grashof number appears erratic, but the difference is small.

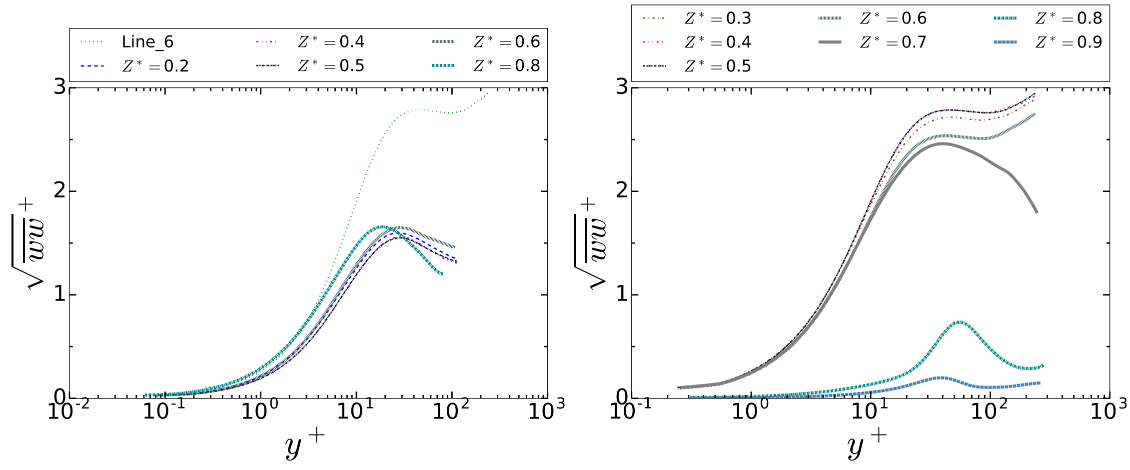

(a) Line_1

(b) Line_6

Figure 6.12: Non-dimensional near wall profiles for the streamwise velocity fluctuation $\overline{ww}^+$. Data is extracted from Case-1. In subfigure (a), Line_6 refers to the developed profile at $Z^* = 0.5$ taken from Line_6. The limits of the profiles in y/y_{max} units is 0.5 and 0.2 for Line_1 and Line_6, respectively.

In Figure 6.13, the turbulent heat flux for the streamwise direction is shown. As can be seen, the peaks for both lines largely coincide with those from the velocity profiles (see Figure 6.10). This is largely consistent with the flat plate observations from Tsuji and Nagano[64] and the 5:1 cavity observations from Barhaghi and Davidson[79].

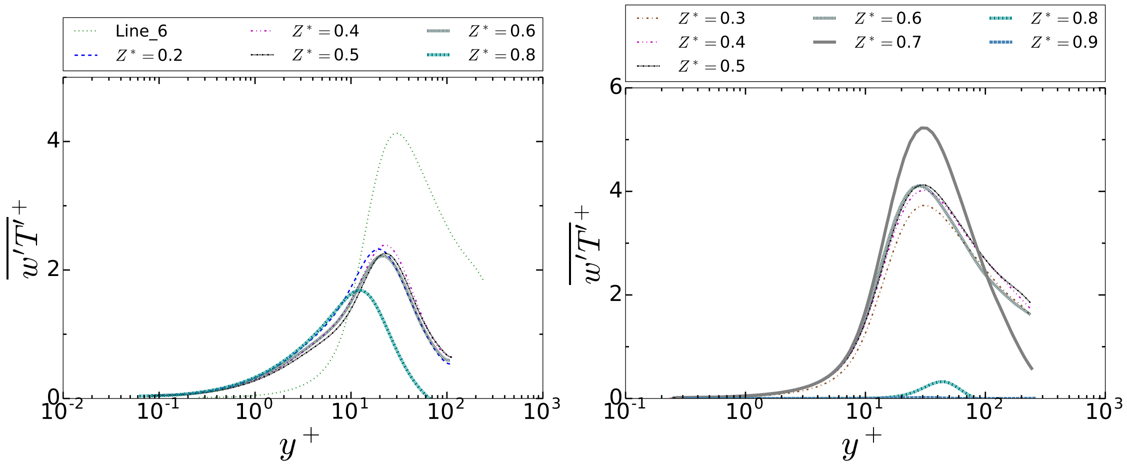

(a) Line_1

(b) Line_6

Figure 6.13: Non-dimensional near wall profiles for the streamwise turbulent heat flux. Data is extracted from Case-1. In subfigure (a), Line_6 refers to the developed profile at $Z^* = 0.5$ taken from Line_6. The limits of the profiles in y/y_{max} units is 0.5 and 0.2 for Line_1 and Line_6, respectively.

6.2.5 Nusselt and friction factor at the containment surface

At the containment surface, the flow transitions from an initially laminar top-end to fully developed turbulence in the middle region. Correlations on this surface are given for the Nusselt number and friction factor coefficient in Figure 6.14.

There is a clear sudden increase in the Nusselt number indicating a transition to turbulence. The point of transition based on the Rayleigh number differs between the two heating cases; Case-1 transitions at 1.5×10^{10} and Case-2 at 6×10^{9}. These transition Rayleigh numbers are significantly higher than that of natural convection over a vertical plate at $\mathrm{Ra}_{\mathrm{cr}} = 8 \times 10^{8}$[64].

Using the current LES data, Nusselt number correlations as a function of the Rayleigh number are computed for the laminar and turbulent regions, yielding Equation 6.1a and Equation 6.1b, respectively.

$$\mathrm{Nu}_z = 0.5\mathrm{Ra}_{z,\Delta T}^{0.25} \tag{6.1a}$$

$$\mathrm{Nu}_z = 0.16\mathrm{Ra}_{z,\Delta T}^{0.33} \tag{6.1b}$$

Assuming a flat vertical surface the exponent for the Nusselt number as a function of $Ra_{z,\Delta T}$ is 0.25 and 0.33 for laminar and turbulent flow, respectively[64]. The similarity of the exponents computed in the present study to those for a flat plate indicates the physical mechanisms are quite the same.

Figure 6.14 presents the friction factor coefficient against the Grashof number. Correlations for the laminar and turbulent region computed using the present LES data are given in Equation 6.2a and Equation 6.2b, respectively.

$$\frac{\tau_w}{\rho V_{n,\Delta T}^2} = 1.17\mathrm{Gr}_{z,\Delta T}^{0.08} \tag{6.2a}$$

$$\frac{\tau_w}{\rho V_{n,\Delta T}^2} = 11.2\mathrm{Gr}_{z,\Delta T}^{-0.025} \tag{6.2b}$$

Comparing against the results from Tsuji and Nagano[64], the laminar correlation is in good agreement to their given exponent of 0.0833. However, in the turbulent region their exponent was 0.084, while that in the present study is -0.025. At the top region, the flow develops from a standing start thus with an increase of the local Grashof number (Gr_z) the friction factor also increases. This initial development is akin to that of a flat vertical plate, which is to be expected based on the good comparisons against the flat plate similarity solution observed earlier. However, once the boundary layer transitions and develops there is a deviation from the flat plate behaviour to that resembling channel flow.

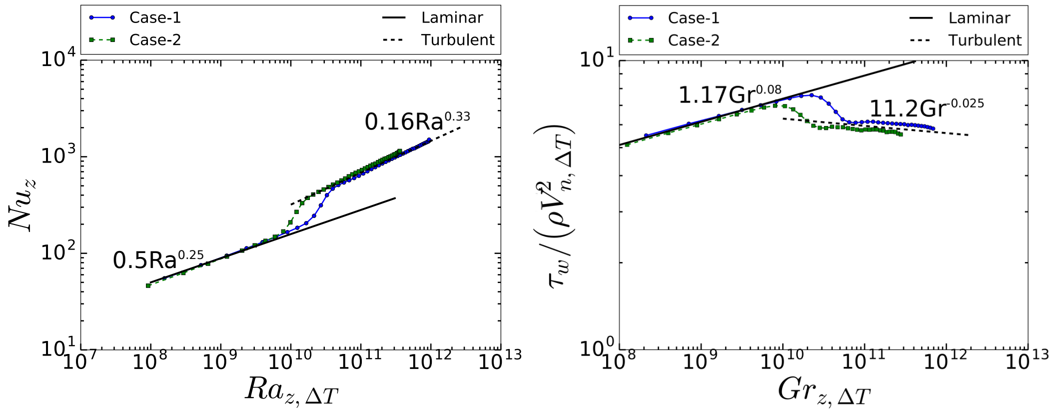

(a) Nusselt number

(b) Friction factor

Figure 6.14: Nusselt number and friction factor plotted against the Rayleigh and Grashof number, respectively at the containment wall.

6.2.6 Sub-channel and bulk behaviour of the flow

Within this subsection, the domain is split into sub-channels as done in typical engineering analysis. Multiple cross-sections in the axial direction are extracted and using the sub-channels divisions given in Figure 5.1, the mass flow, fluid bulk temperature and solid temperature are computed.

Figure 6.15 shows the sub-channel mass flow variation. Below $Z^* = 0.8$, the mass flow is significantly altered; the mass flow in the interior sub-channels decreases significantly and the reverse happens for the exterior sub-channels (7, 8 & 9). At this location, transition at the containment surface occurs. As shown earlier in the contour plots, a strong cross-flow forms as the coolant is entrained towards the containment wall increasing the mass flow for the sub-channels there. The fluid and sub-channel average solid temperature variations are presented in Figure 6.16. At the top-end where the temperature field is stratified, the gradient is significantly steeper. In the turbulent region, the vertical temperature gradient is much shallower and almost flat. The sub-channel fluid temperature shows above $Z^* = 0.8$, there is a clear separation between the exterior and interior sub-channels. However, in the turbulent region, the separation between the exterior and interior sub-channels is non-existent. The sub-channel average solid temperatures largely follow the vertical temperature gradient changes observed for the fluid and they do not show a significant variation between the sub-channels.

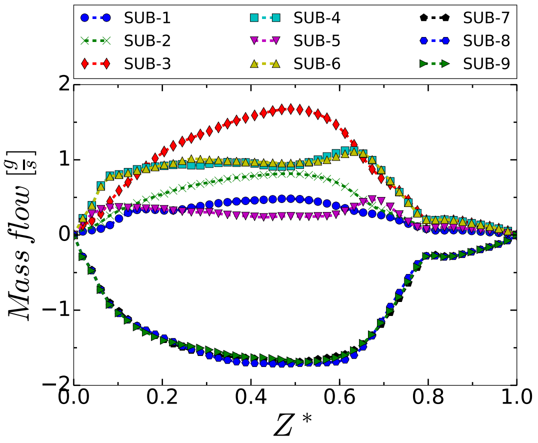

Figure 6.15: Variation of the sub-channel mass flow as a function of height.

Vertical planes connecting rods of the same ranks at the azimuthal rod gap spaces are used to compute the lateral mixing between the sub-channels at the different radii. Line_1 is an example of such a plane. In total six such planes are extracted and then split into fifty axial sections. The variables required are then computed normal to the plane (radial direction) of interest.

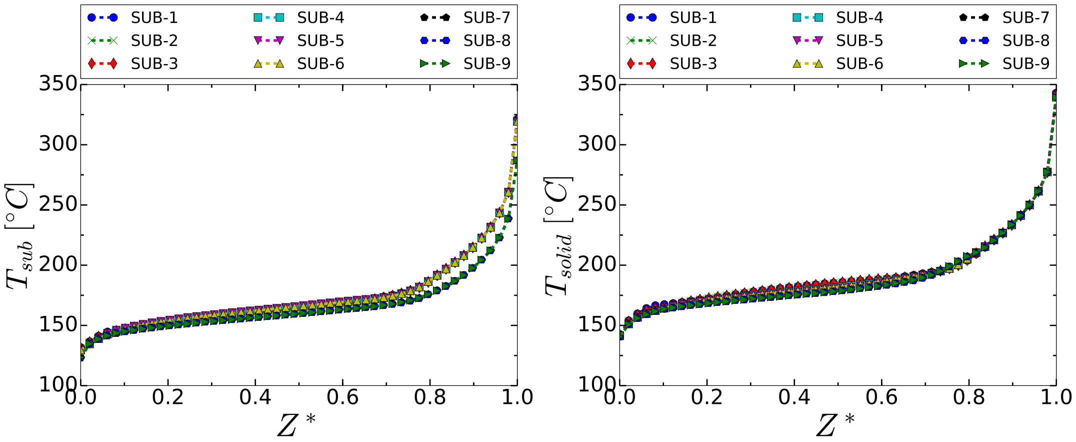

(a) Fluid temperature

(b) Solid temperature

Figure 6.16: Sub-channel solid and fluid temperature variation with height.

The radial mass flow is given in Figure 6.17. Immediately after transition at the containment surface, there is a sudden increase in mass transfer from the interior to exterior sub-channels. This corroborates the axial mass flow plots seen earlier.

Peak levels of radial mass transfer are observed across the third rank rod gaps. This is due to their proximity to the containment surface and also the cumulative effect of the mass transfer from the first and second rank rod gaps. At $Z^* = 0.5$, the radial transfer to the containment has subsided and the net lateral flow direction shifts towards the interior. Mass transfer towards the interior does gradually increase as the flow descends, with peaks being observed at the bottom-end.

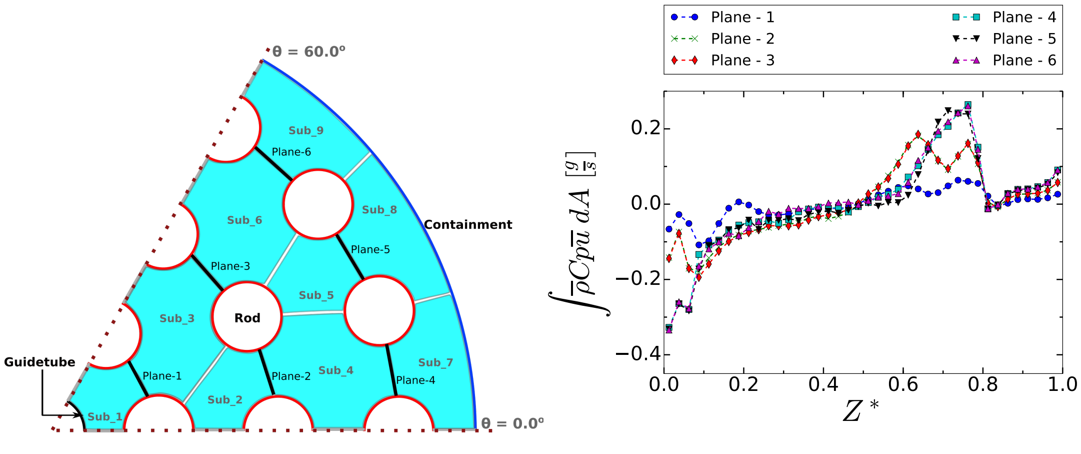

(a) Schematic

(b) Radial mass flow

Figure 6.17: Radial mass flow variation through the rod gaps. A positive value means transfer is directed towards the containment surface. Subfigure (a) shows the location of the extraction planes.

Figure 6.18 shows the heat flow as a result of convection and turbulence mixing. As to be expected, the heat convected largely follows the observations and trends noted for the lateral mass flow. On the other hand turbulent mixing peaks close to the domain mid-height and accounts for a much smaller portion of the heat transfer.

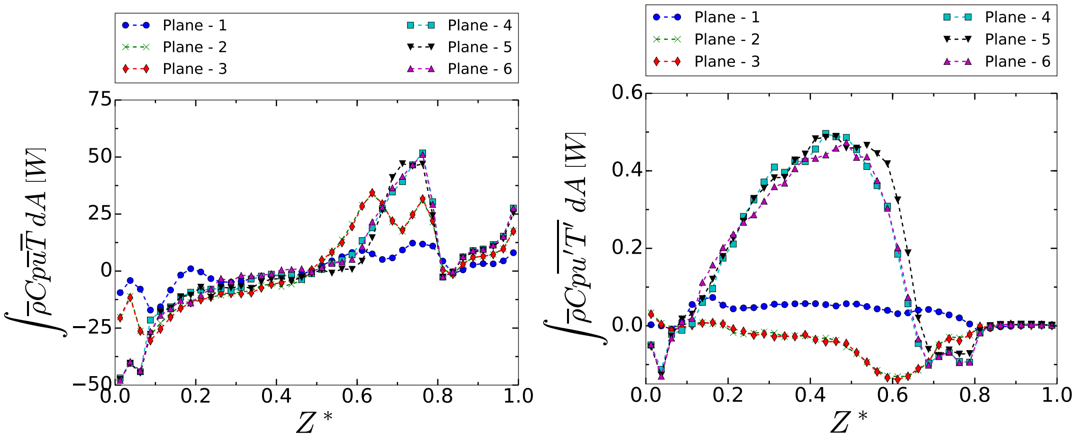

(a) Advection

(b) Turbulent heat flow

Figure 6.18: Radial advection and turbulent heat flow through the rod gaps. Subfigure 6.17(a) shows the location of the extraction planes.

6.3 Conclusions

Natural circulation simulations in a turbulent enclosed rod bundle cavity of large aspect ratio have been carried out. It has been shown the cavity can be split into three distinct vertical regions, simply termed the top ($Z^* > 0.75$), middle ($0.15 < Z^* < 0.75$), and bottom ($Z^* < 0.15$). The axial extent of these regions is mostly dependent on the flow condition at the containment wall. A laminar boundary layer flow regime at the containment wall coupled with turbulent boundary layer flow at the rod walls defines the top region. In the core of this region, the temperature is heavily stratified. Laminar correlations obtained using the LES data for the Nusselt number and friction factor at the containment wall are similar to those for natural convection at a flat vertical surface. The correlations computed are $0.5Ra_{z,\Delta T}^{0.25}$ and $1.17Gr_{z,\Delta T}^{0.08}$. Further comparisons of the LES data against the natural convection flat plate similarity solution by Ostrach[13] were in good agreement.

The middle region encompasses most of the domain, and the flow here is particularly complex and dominated by turbulence effects. Flow at the containment, transitions to turbulence thereby instigating entrainment from the interior sub-channels (at transition location), which is then followed by strong mixing. In this region, the resulting vertical temperature distribution is uniform. The middle region was further split into two parts; the outer region which is between the second rank rods and containment wall and a central region which is between the adiabatic central rod and heating second rank rod. The outer region, is akin to a heating and cooling "channel", with a strong shear layer as the opposing upward interior flow and large scale downward flow at the containment interact. This can be likened to the highly turbulent Betts and Bokhari[77] case study. Heated downward flow is shown to exist at the third rank rod surfaces, which are closest to the containment wall. The central region is typical of a heated upward flow but with strong interference from the outer region leading to mixed/forced convection like profiles across the gaps. Observations have shown the chimney effect occurs to some extent in this "channel". Although flow profiles show a stark difference between the outer and central regions, their near-wall behaviour has the typical characteristics of natural convective flows. Turbulent correlations obtained from the LES data for the Nusselt number at the containment wall have a Rayleigh number dependency of $0.16Ra_{z,\Delta T}^{0.33}$, which is similar to that for a vertical plate. However, for the friction factor, the computed correlation has a Grashof number dependency of $11.2Gr_{z,\Delta T}^{-0.025}$, and hence has an exponent that is very different from that for a flat plate 0.084 from the Tsuji and Nagano case study[64].

The bottom region is characterised by a downward flow impinging onto the floor at the containment wall. Boundary layer development occurs at the rod surfaces as the flow begins its upward ascent. The comparison of the velocity from simulations against the slender cylinder similarity laminar solution shows transition occurs much faster here than on the containment wall.

Chapter 7

Forced flow in a *WheatSheaf* bundle

This chapter investigates the effect of rod distortion on the flow and heat transfer characteristics of an AGR rod bundle using RANS and a variety of turbulence models. The distortion investigated herein is termed *WheatSheaf* and can arise if the irradiated rod bundle is dropped during the refuelling process. A *WheatSheaf* bundle is characterised by a reduction in the pitch-to-diameter (P/D) ratio gradually over the first half of the element, reaching a minimum ($P/D \approx 1.2$) at half height, and then a subsequent increase back to the normal $P/D(\approx 1.8)$ ratio over the second half of the element (see Figure 7.1(a)). Understanding the thermal-hydraulics in such a bundle is important with regards to maintaining safety in the unlikely event a fuel drop occurs. In the literature review, the investigated distorted bundles have either consisted of the rod assembly being translated towards the containment wall[63] or a plate fuel assembly with a buckled channel[61]. The investigated geometry herein is fairly unique as the rods converge and diverge within the bundle. To the author's best knowledge no such bundle has been investigated using traditional CFD methods within the literature. Much of the work reported in this chapter has been published in a paper by the author[133].

7.1 Modelling description

All the calculations performed in this chapter are conducted using the RANS method. For this study, several high Reynolds number turbulence models available in *Code_Saturne* are examined for their impact on the solution. The models investigated are the k-ϵ model, k-ω SST model, and SSG Reynolds stress turbulence model. These turbulence models and the constants used have been described in Chapter 4.

A schematic of the modelled geometry can be seen in Figure 7.1 and consists of two sections. At the bottom is a 0.3 m tall undamaged section, where the flow is mapped back to the inlet at half height. By mapping the downstream values to the inlet it is possible to obtain a fully developed profile. The second section is joined to this development section by conformal joining. This upper section consists of a 1 m tall *WheatSheaf* rod bundle.

At the inlet of the computational domain a uniform inlet velocity boundary condition, with a streamwise value of 4.36 m/s is prescribed, giving a mass flow of 3 kg/s into the bundle. The inlet temperature of the flow is set to 300 °C. For the outlet, an outflow boundary condition is applied. On the azimuthal faces, a symmetry boundary condition is used. It is worth noting as the rods are staggered a rotational periodicity boundary condition is not applicable for a 30 ° sector. Since this simulation is concerned with the thermal hydraulics of an AGR bundle during refuelling, the following conditions are given. The external boundary wall (sleeve) and central rod wall (guide tube) are treated as adiabatic smooth walls. For the rod walls, a constant heat flux of 2.9 kWm^{-2} is applied, in comparison during normal operation, the typical heat flux is $\approx 342\text{kWm}^{-2}$. A reduced heat flux (in comparison normal operating conditions) is used as the distorted bundle scenario arises if the fuel stringer is damaged or dropped during refuelling operations. It should be noted in this case study, the effects of solid conduction and thermal radiation are not considered. The refuelling scenario modelled for this study assumes offload pressurised refuelling. This would entail that although still pressurised the reactor has been shut down. Rod surfaces are treated as either rough or smooth walls depending on the case. Carbon dioxide at a pressure of 3.5 Mpa is the working fluid. The Reynolds number is 201675 and fluid properties are assumed to be constant. The fluid properties are defined as shown in Table 7.1.

When a high Reynolds number (HRN) turbulence model is used, the first node

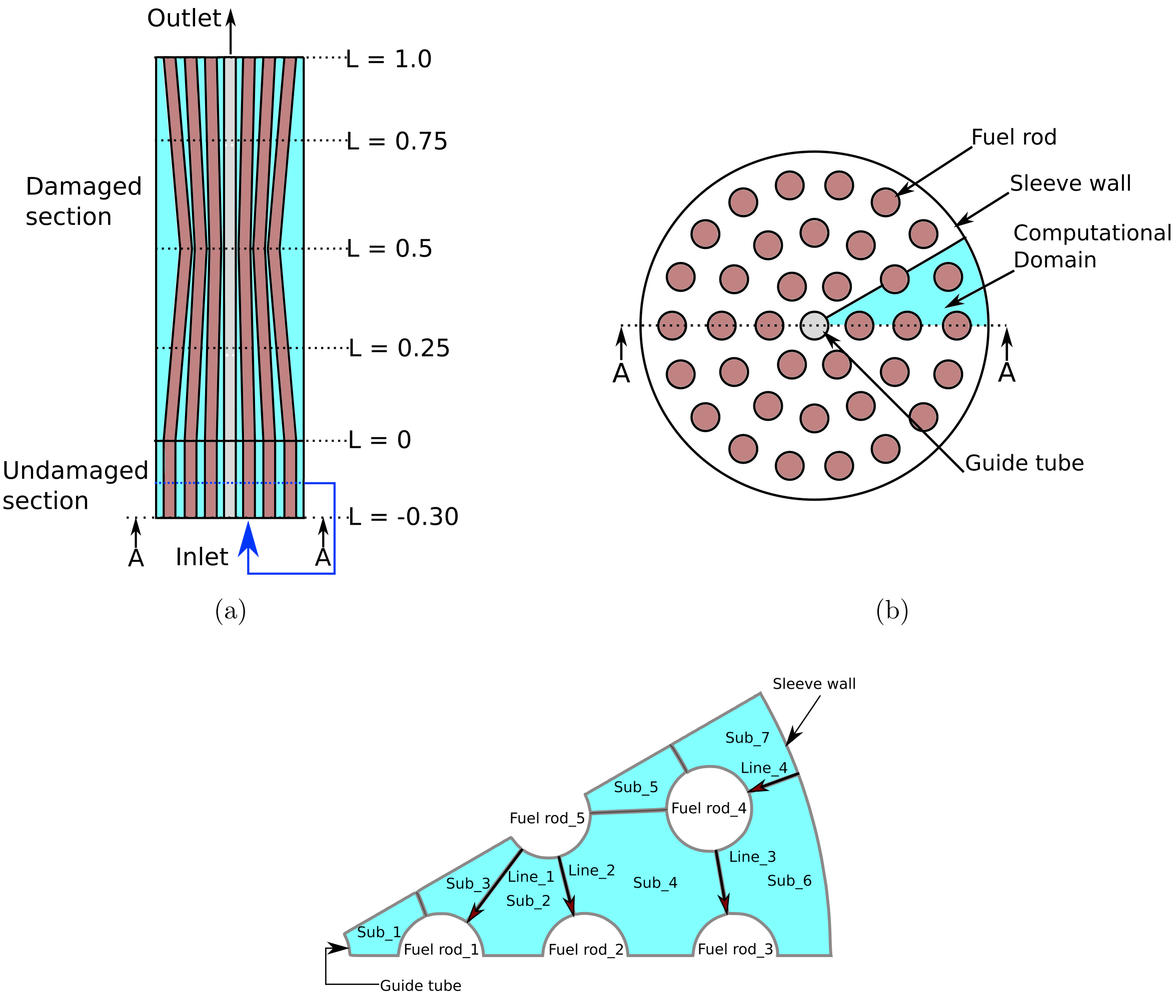

(a)

(b)

(c)

Figure 7.1: Modelled domain and cross-sectional schematic for full and partial sub-channel divisions. (a) Internal view along the plane A-A. L is dimensionless height (b) Top view of an AGR rodbundle (c) Schematic showing cross-sectional divisions of computational domain (30°)

next to the cell must be significantly large, $y^+ = 30$. It is difficult to comply with this requirement for the strongly distorted rod bundle studied here. To rectify this, a scalable wall function has been used which allows the first near-wall node to be at the lower range of the log-law $\approx y^+ = 11$. The approach used is based on limiting the minimum value of y^+ in the fine mesh regions to the minimum of the log-law. In the damaged section, the mesh comprises of tetrahedral elements, of near unity aspect ratio, with several prism element layers close to the wall. The undamaged development section comprises of prismatic elements and hexahedral elements near the wall. At the outlet of the domain, there are layers of extruded prismatic and hexahedral cells. Momentum and turbulent quantities transport equations are discretised using

Table 7.1: Fluid properties defined in the simulations carried out

Property	Value	Unit
ρ	32.72	kg/m^3
μ	2.668x10^{-5}	Pa.s
λ	0.03947	W/m/K
C_p	1093.5	J/Kg/K

the second-order accurate SOLU (Second Order Linear Upwind) scheme.

7.2 Validation

The experimental work of flow in a rod bundle array by Trupp and Azad [4] was used to validate the following (i) mesh resolution requirement/sensitivity, (ii) effect of using different types of meshes (structured/unstructured), and (iii) performance of different turbulence models. From this validation study, it was noted the Reynolds stress model predicted results that best matched experimental data, while eddy viscosity models particularly the $k-\epsilon$ model returned reasonable results. A comparison of different mesh types employed in the validation case showed minute differences provided that the unstructured mesh was at least four-times the density of the structured one. To study flow and heat transfer in the damaged geometry two turbulence models have been selected for further study these were the $k-\epsilon$ and SSG Reynolds stress models. The $k-\epsilon$ model has been selected in addition to the SSG model because for an unstructured mesh the model is more stable, less computationally expensive, and less susceptible to local mesh quality deterioration than the RSM model. Additional details and results from the validation exercise are given in Appendix C.1.

7.2.1 Mesh dependence and turbulence model comparison for *WheatSheaf* bundle

Mesh parameters used in the validation case are applied to the *WheatSheaf* case and in particular, the wall resolution is maintained through limiting the maximum element surface area. The resulting mesh had a density of 21.5 million in the damaged section

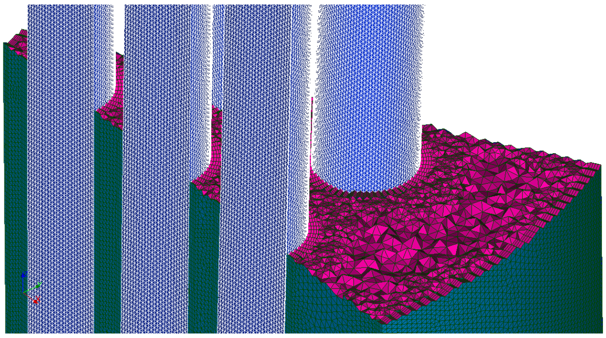

Figure 7.2: Clipping of *WheatSheaf* mesh

(see Figure 7.2). This resolution is used for all the cases described herein. Based on the validation test case the recycling domain has been confirmed to be mesh independent, however this is not applicable to the damaged fuel section. Thus an additional mesh dependence study has been carried out for the damaged section along with a turbulence model comparison. A detailed overview and results from this study are provided in section C.2 in the Appendix. The current mesh density of 21.5 million is shown to provide mesh independent results. Comparisons between the $k - \epsilon$ and SSG Reynolds stress model show that the two models predict similar trends for temperature, axial velocity, and uv. However, within the recirculation zone differences in the overall values are especially noted. Data presented from hereon will be based on the k$-\epsilon$ model.

7.3 Results

7.3.1 Qualitative results smooth rod surfaces

As mentioned earlier results presented from this point onwards are from the standard $k - \epsilon$ model. In Figure 7.3, the normalised velocity field obtained at different axial locations is shown. At L = 0.0, the local maxima occurs in the sub-channel centres. The flow distribution at this height is akin to that obtained from the undamaged bundle. As the rods converge (L = 0.25) the maxima denoted by X shifts towards the outer region. At L = 0.5, the rods are at maximum distortion, with the maxima now fully located in the outer wall sub-channel. Furthermore, within this convergent section (up to L = 0.5), high axial velocity regions form in-between the rod gaps.

As the rods diverge back to the nominal P/D ratio at L = 0.75, the maxima shifts towards the interior. An interesting observation is the delay in flow redistribution to

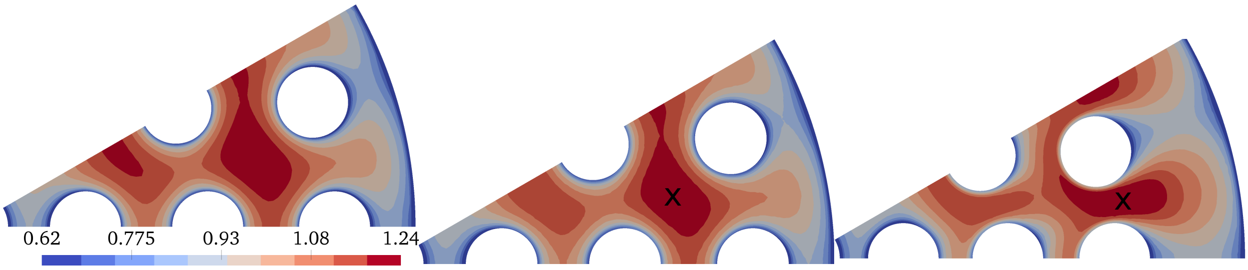

(a) (b) L = 0.0 (c) L = 0.25

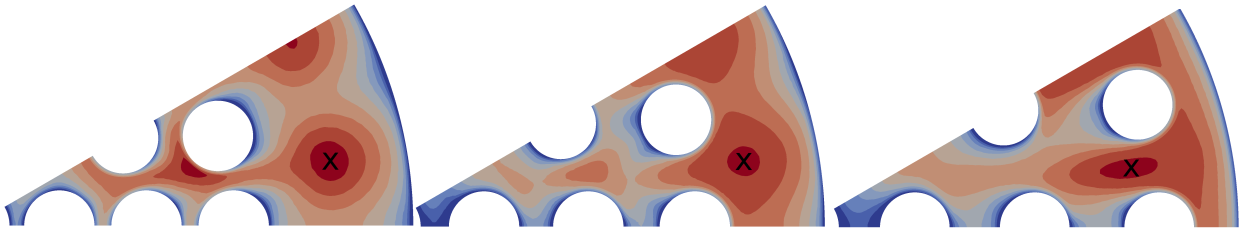

(d) L = 0.5 (e) L = 0.75 (f) L = 1.0

Figure 7.3: Contours of normalised axial velocity; (a) undamaged bundle and (b - f) from *WheatSheaf bundle*.

the changes is rod profile. This can be seen by noting the different contours at L = 0.25 and L = 0.75, where the rod positions are the same. Finally, at L = 1.0 the rods are now back to nominal P/D ratio and as can be seen, the maxima is located in-between the rod gaps and the flow redistribution is clearly significantly different from that at L = 0.0, showing a strong delay. Additional low-velocity subregions form on the leeward rod faces (oriented against the shift of local maxima X). This is true in both converging and diverging sections.

Vector plots of cross-flow velocity are presented in Figure 7.4. The vectors are coloured by the magnitude, which is dimensional and has units of m/s. Due to rod inclination, the sub-channel flow is re-disturbed and driven around the fuel rods. This is evidenced by the vectors starting and oriented away from the rod surface, which appear as a mass “source” in a 2D plot. As the flow is driven around the fuel rod, detachment of the cross velocities occurs and recirculation zones form behind the rods. In the wake region, at the rear of the fuel rod, some of the flow is driven towards the rod surface which appears to be a mass “sink” in a 2D plot. The aforementioned behaviour is evident in each of the contour plots shown and the orientation of “sources” and “sinks” alternates depending on the rod inclination. Flow redirection is clearly seen and the cross-flow velocities can have magnitudes up to 12.1 % of bulk velocity. The magnitudes are especially high in the convergent section and in-between the rod gaps. A strong flow delay is noted at L = 0.5 (location of maximum distortion) where the cross-flow is still directed outwards. The delayed reaction of velocity distribution observed is likely to be caused by the inertia of the outward cross-flow as after rod inclination alters, the outward flow must be arrested and then redirected towards the interior. To show the three-dimensional flow, Figure 7.5 shows the traces of massless particles released at the inlet of the damaged section. It can be seen clearly that fluid particles swirl around the fuel rods. The direction of the swirl reverses as the fuel changes from converging to diverging. The outward cross-flow shown in Figure 7.4 as the rods contract to the center of the bundle is anticipated. The strong swirl flow is however not all that intuitive. This does have strong implications in the mixing of the fluid and the distribution of temperature.

An overview of turbulent kinetic energy (k) inside the domain is given by contours shown in Figure 7.6. Generally, it can be seen on the leeward rod faces, there are regions of low turbulent kinetic energy, especially in the narrow wake where "sinks" are evident(see Figure 7.4). In contrast, the windward facing rod surfaces extending up to the location of cross-flow velocity detachment have high turbulent kinetic energy values. Similarly, recirculation zones show high turbulence levels.

Cross-sectional pressure contour plots are presented in Figure 7.7. In the convergent section, higher pressures occur within the interior sub-channels thus driving the flow from this region. At L = 0.25 and 0.75 a low-pressure zone is clearly evident in the gaps between the third rank rods. As the flow can only escape the sub-channels through the rod gaps, this leads to induced acceleration and thus in-turn to lower pressure within this gap region. A reversal of the pressure field occurs when L = 0.5, as the pressure is now lower within the interior. Furthermore, it is noted at locations of a sudden change in inclination (L = 0.0, 0.5, 1.0) there is a larger range of pressure, the largest of which occurs at L = 0.5. Such increases in the span are probably the result of stagnation points shifting and reforming. For example at L = 0.5, the forward stagnation point alters by 180° leading to a significant increase in pressure.

Results from the thermal field are presented next. Heating is only applied in the damaged section thus results are shown starting at L = 0.25. Figure 7.8 shows the

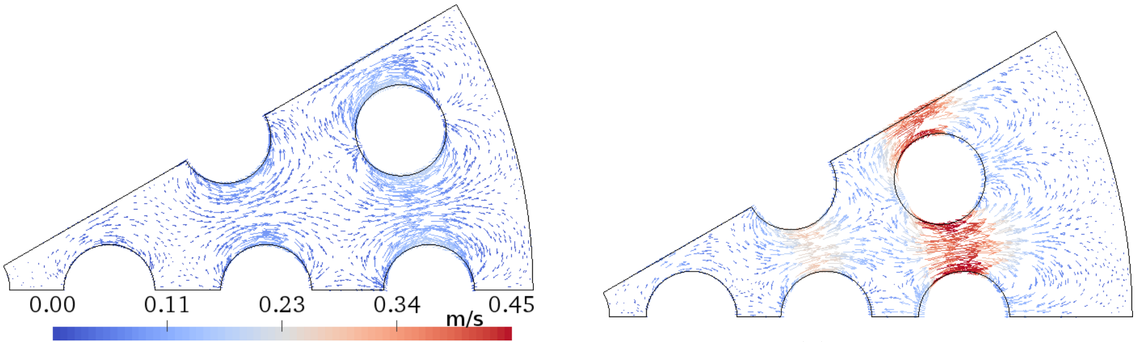

(a) L = 0.0

(b) L = 0.25

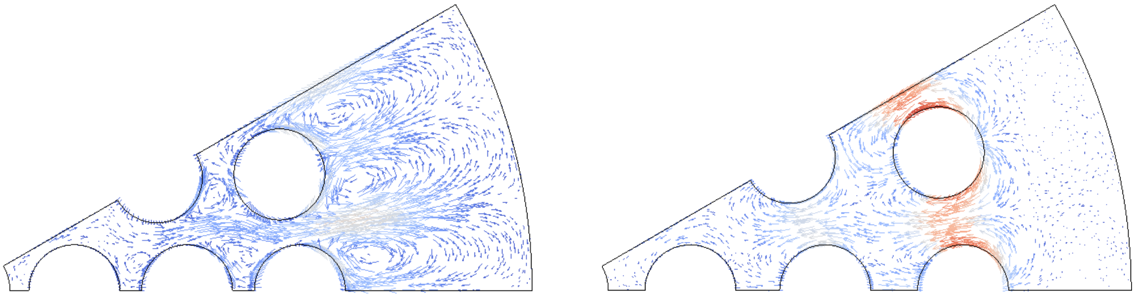

(c) L = 0.5

(d) L = 0.75

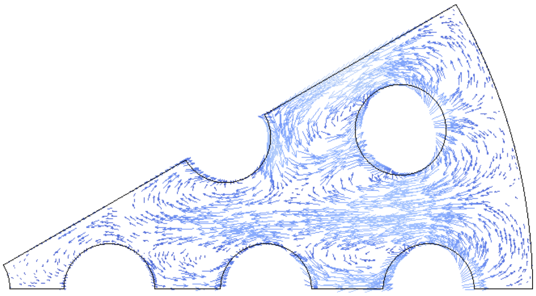

(e) L = 1.0

Figure 7.4: Cross-sectional velocity vectors. Scalebar is in m/s.

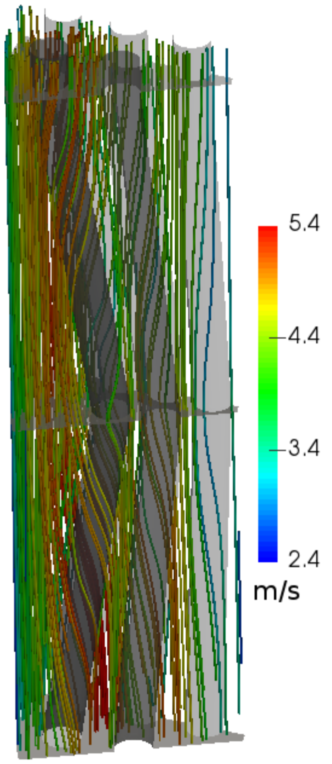

(a)

Figure 7.5: 3D Flow streamlines in simulated domain. Different color preset and angle used to allow for easier visualisation

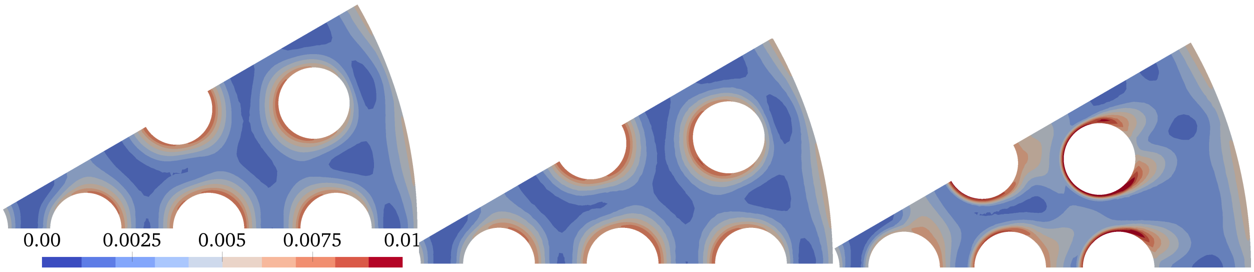

(a) (b) L = 0.0 (c) L = 0.25

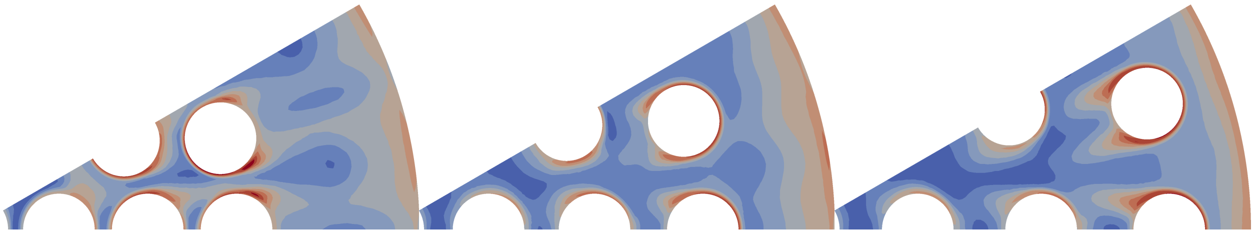

(d) L = 0.5 (e) L = 0.75 (f) L = 1.0

Figure 7.6: Contour of normalised kinetic energy; (a) undamaged bundle and (b - f) *WheatSheaf* bundle.

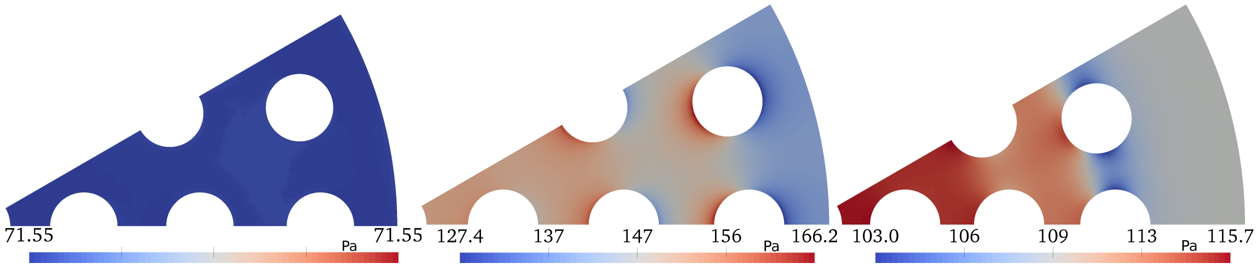

(a) (b) L = 0.0 (c) L = 0.25

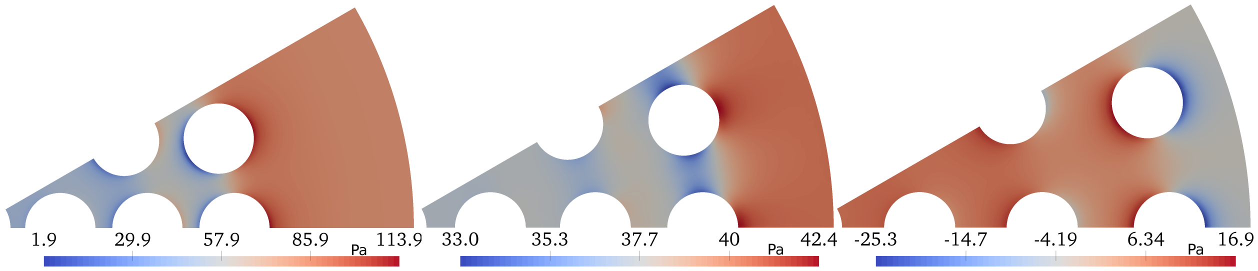

(d) L = 0.5 (e) L = 0.75 (f) L = 1.0

Figure 7.7: Contour of pressure; (a) undamaged bundle and (b - f) *WheatSheaf* bundle. Scalebar is in Pa.

normalised temperature distribution at varying heights. In the plots normalised temperature is defined as $T^* = (T - T_{inlet})/(T_{b,outlet} - T_{inlet})$. Lower fluid temperatures are especially evident in the region between the outer rank and adiabatic sleeve wall. Temperature peaks (hotspots) develop on the leeward rod faces. These hotspots seem to coincide with the cross-flow velocity detachment points. In contrast, on the windward faces, the coolant is pushed against the fuel rod thus enhancing cooling within this subregion of the wall. Furthermore, it is interesting that the temperature of the rod at the smallest gap is rather low for example in rod 4 and rod 3. This is clearly due to the strong cross-flow.

7.3.2 Quantitative results smooth rod surfaces

To substantiate the results presented in the contour plots, profiles along several lines (see Figure 7.1(c), arrowed lines on domain show extraction locations) are given for k, velocity and temperature. Velocity profiles are presented in Figure 7.9. At the inlet of the damaged section, the profiles are largely symmetric. With an increase in height, the velocity profile alters considerably. An apex in the velocity profile develops on the

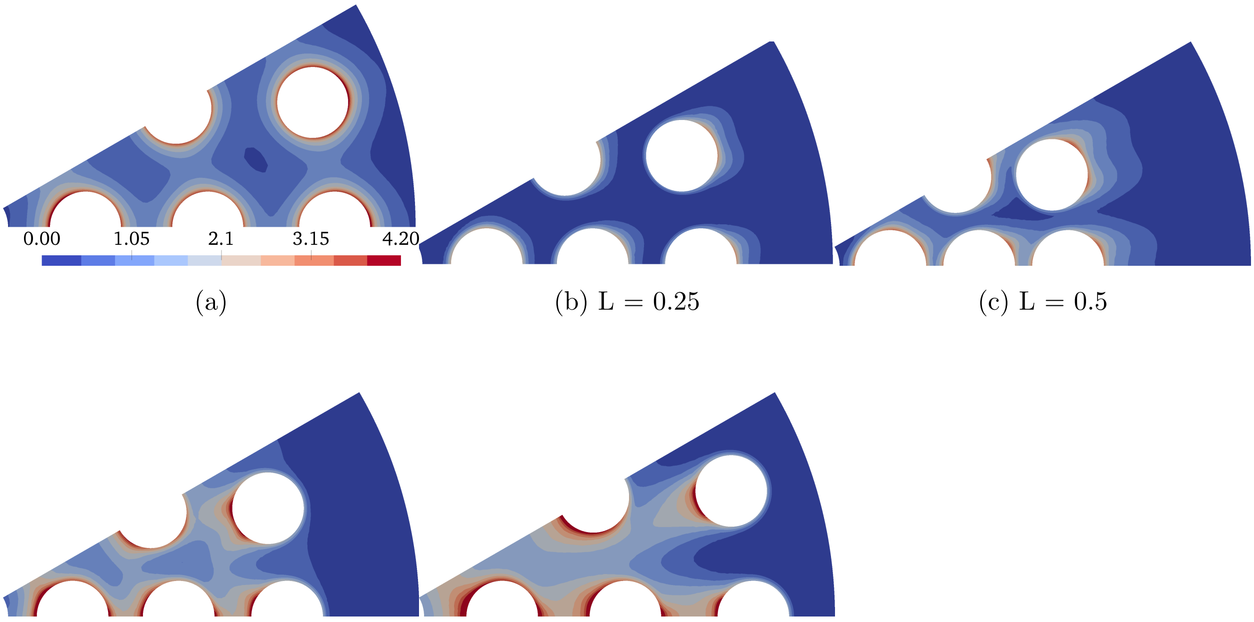

(a) (b) L = 0.25 (c) L = 0.5

(d) L = 0.75 (e) L = 1.0

Figure 7.8: Contour of normalised temperature; (a) undamaged bundle and (b - f) *WheatSheaf* bundle.

windward facing rod. Furthermore, excluding the profile obtained at L = 0.0, peak axial velocity is in the vicinity of the windward rods as the flow accelerates towards these regions. At the rod gap within the second rank, barring the profile at entry, the axial velocity reduces through the domain. In contrast, the profile within the gap for the third rank which shows a decrease from L = 0.25 to L = 0.5, before increasing for the later two upper locations. Profiles at these gaps further highlight the strong delay in flow redistribution, as the maxima identified in the contours is yet to fully traverse back towards the interior, as denoted by the still falling axial velocity in rod rank_2. Line_4 reveals an almost monotonic increase of axial velocity as a function of height.

For k (see Figure 7.10), profiles across Line_1 exhibit significant variation as the flow develops through the domain. At L = 0.0 the profile is symmetric and as height increases, within the convergent section, peak turbulence levels are observed on fuel_rod 5 which is windward facing. On the opposite rod which is leeward facing there is much lower k.After L = 0.5, the profile reverses shape as cross-flow re-direction alters. Profiles across the rod gaps are shown in Figure 7.10(b) and 7.10(c). Similar to the profile obtained for line_1, peak k levels are located in the convergent section. Asymmetry in some of the profiles is evident and these asymmetries appear to arise due to the effect of the far-field rod impending on the cross-flow. In the sub-channel adjacent to the

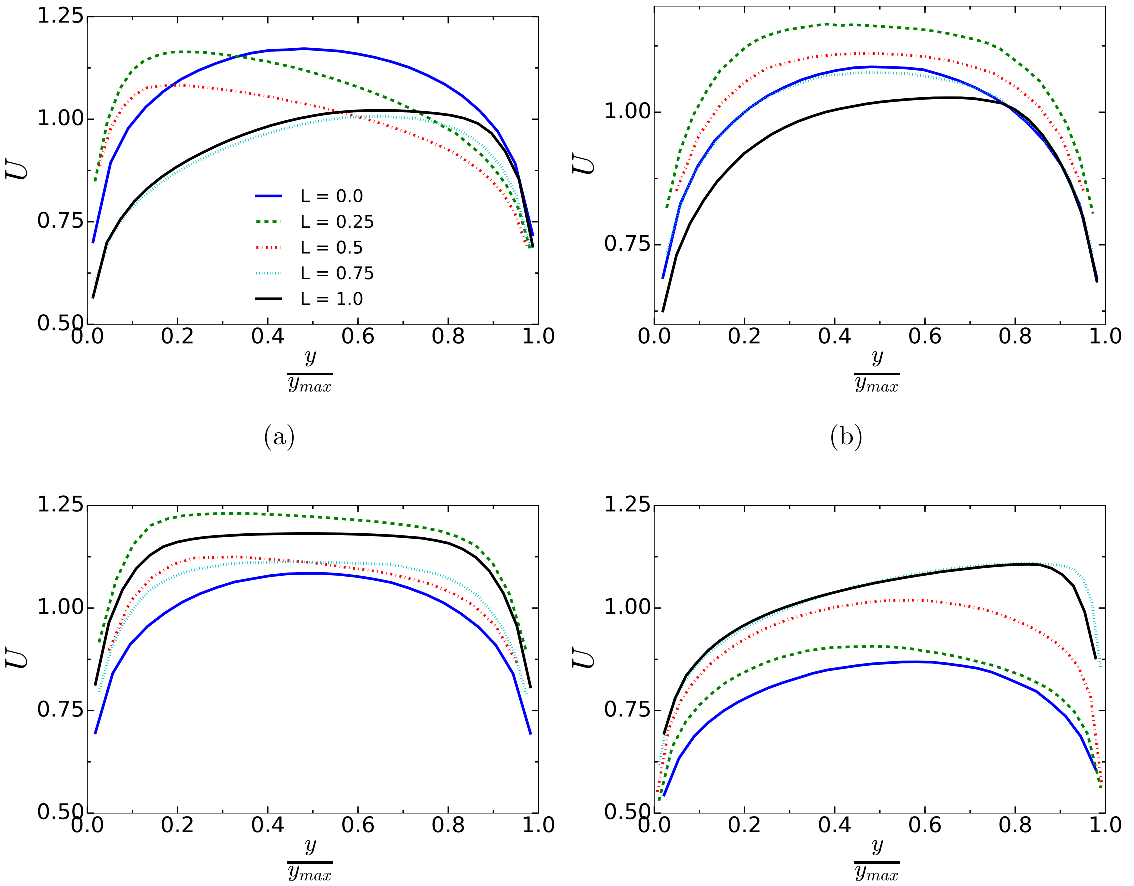

(a)

(b)

(c)

(d)

Figure 7.9: Profiles of normalised axial velocity along (a) Line_1, (b) Line_2, (c) Line_3, (d) Line_4

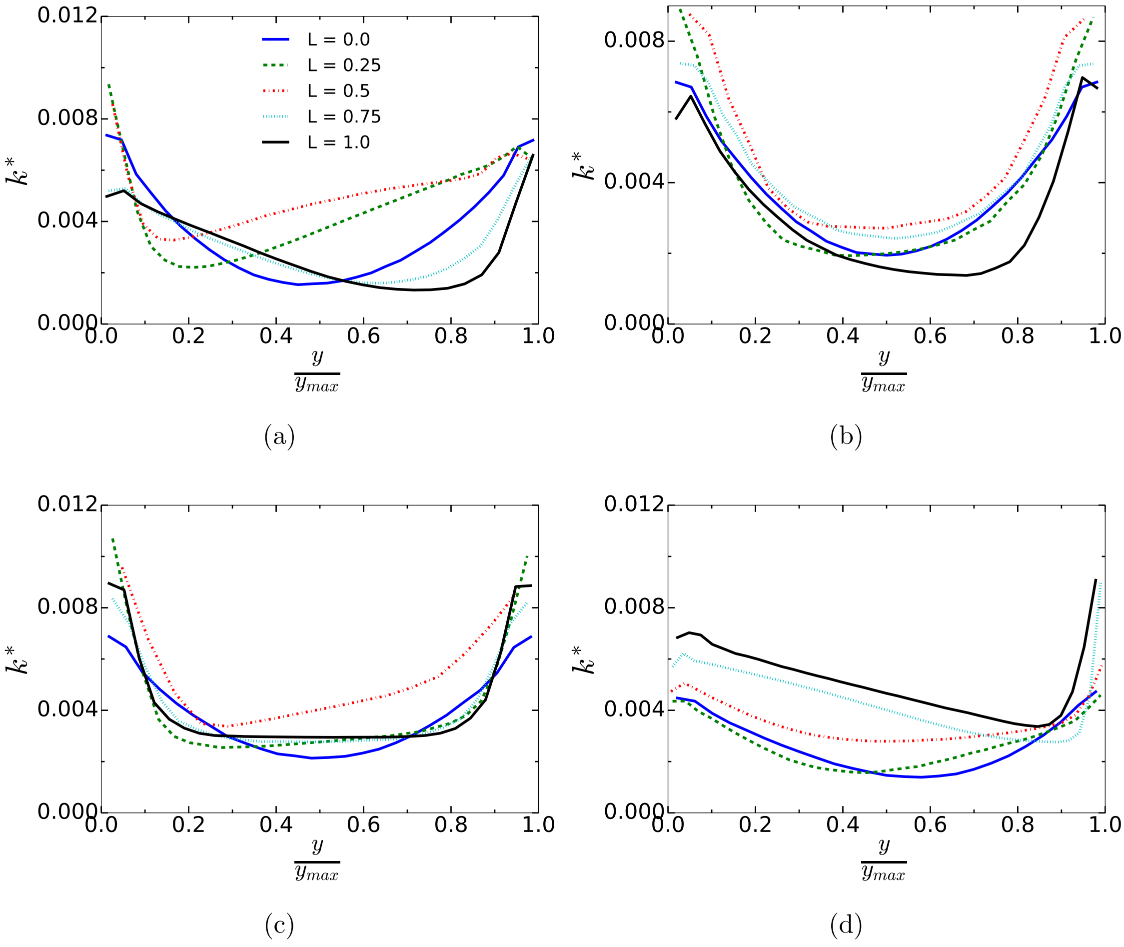

(a) (b)

(c) (d)

Figure 7.10: Profiles of turbulent kinetic energy along (a) Line_1, (b) Line_2, (c) Line_3, (d) Line_4

sleeve wall (Line_4) there is an overall increase of k within the bulk as a function of height. In contrast to profiles obtained previously peak turbulent kinetic energy occurs in the divergent section.

The temperature profiles in Figure 7.11 at Line_1 show high temperatures occurring near the rod in the leeward direction (hence weaker convection), with the peak can temperatures occurring at L = 1.0. Line_1 has the highest temperature values compared to other profile extraction lines. The profiles across the second rank rod gap show a monotonic increase in temperature, with the peak temperatures occurring at L = 1.0. Those across the third rank gap interestingly show peak temperatures at L = 0.75, and at L = 1.0 there is an appreciable drop in temperature. This behaviour can be attributed to the increase in axial velocity observed in Figure 7.9. At L = 0.5, the influence of the far-field rods on the asymmetry of the temperature profile is apparent. In the outer sub-channel however, the peak temperature occurs at L = 0.5, which is

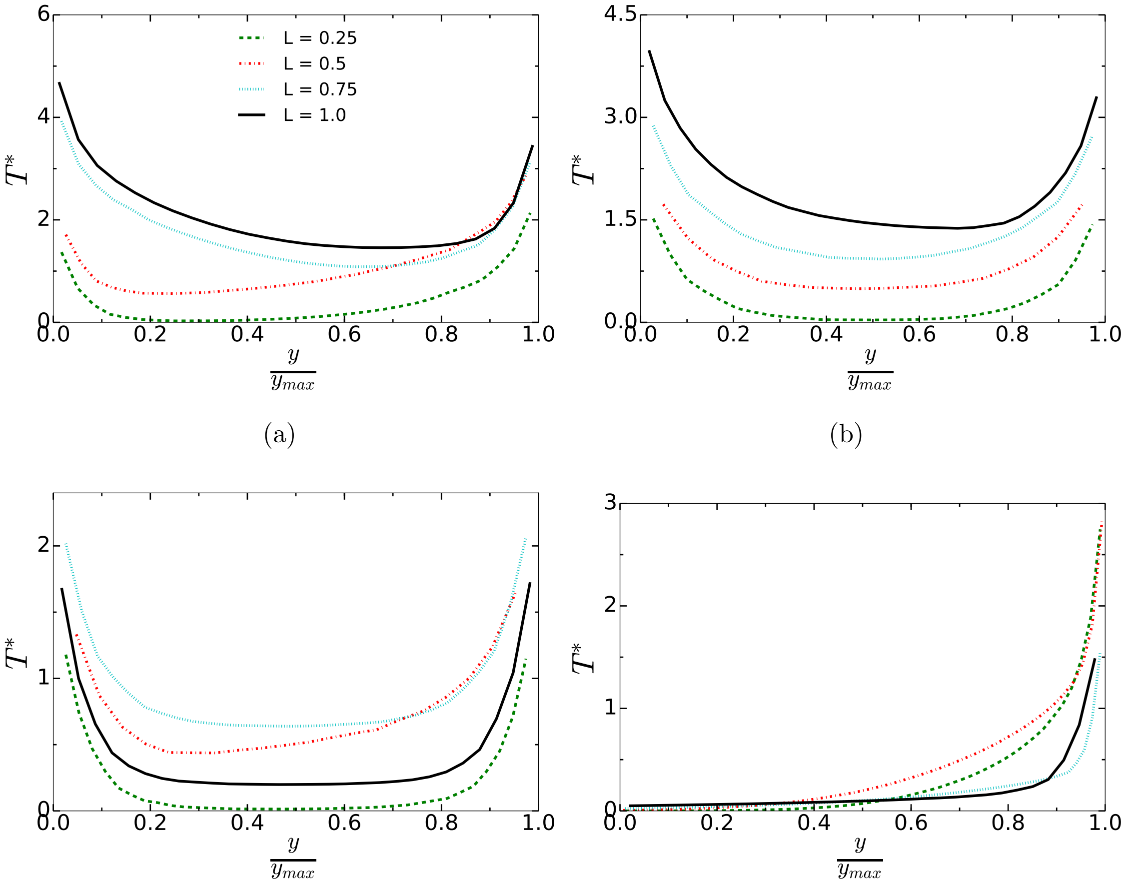

(a) (b)

(c) (d)

Figure 7.11: Profiles of normalised temperature along (a) Line_1, (b) Line_2, (c) Line_3, (d) Line_4

the location of maximum distortion.

To help illustrate the differences between rod wall temperature in an undamaged and damaged scenario temperature variations at several heights for rod 4 and rod 1 are plotted respectively, in Figure 7.12 and 7.13. For the undamaged bundle, the temperature distribution shows some non-uniformity, but this is relatively small. The peak temperature increases steadily with height. For the distorted bundle, the temperature distributions are significantly altered. The worst peak can temperature is not when the fuel rod is at its most distorted (L = 0.5) but is when the distortion has recovered (L = 0.75 for rod 4 and L = 1.0 for rod 1). The peak can temperature increases appreciably in the damaged bundle.

Figure 7.14 shows the distribution of mass flow in the various sub-channels for the damaged and undamaged cases. These profiles are calculated based on the full and partial sub-channels present within the 30 ° sector, the full sub-channels are numbered

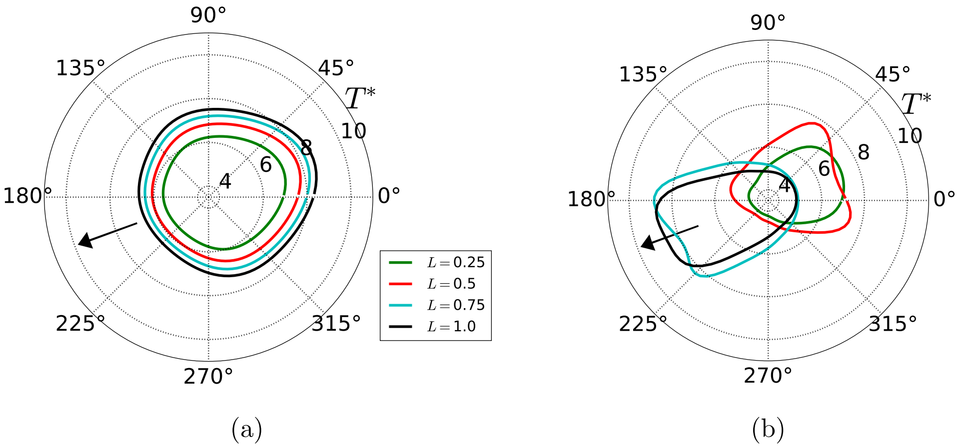

(a)

(b)

Figure 7.12: Circumferential variation of rod temperature for rod 4. The black arrow at 200° is oriented to the rod bundle center. (a) undamaged bundle (b) *WheatSheaf* bundle

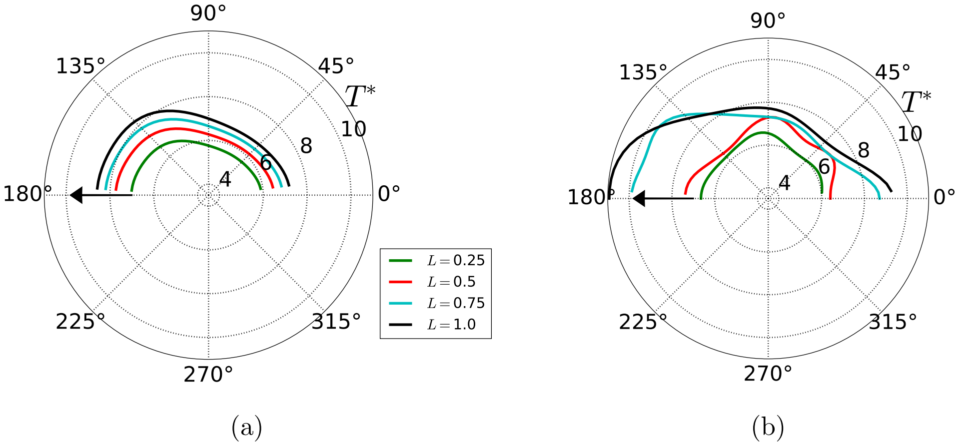

(a)

(b)

Figure 7.13: Circumferential variation of rod temperature for rod 1. The black arrow at 180° is oriented to the rod bundle center. (a) undamaged bundle (b) *WheatSheaf* bundle

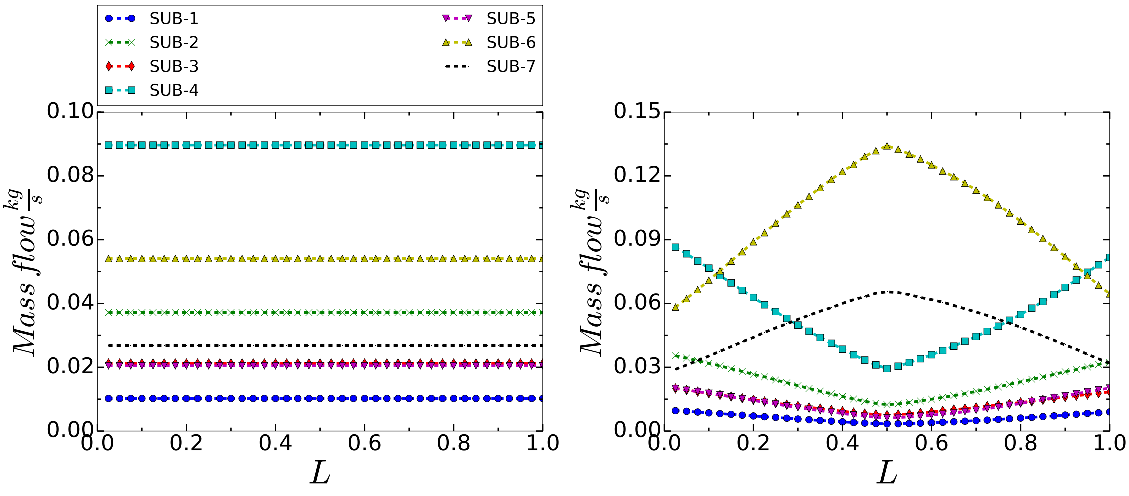

(a) (b)

Figure 7.14: Mass flow variation within the full and partial sub-channels present in the 30 ° sector. (a) undamaged bundle (b) *WheatSheaf* bundle

2, 4, and 6 with the rest being partial (see Figure 7.1(c)). As can be seen for the damaged section, the mass flow for the interior areas reduces in the bottom half and increases in the top section of the geometry. This can be compared to an undamaged bundle, which shows no changes in mass flow. It is most interesting to see that the mass flow rate (or bulk velocity) in the various sub-channels shows a largely symmetric distribution above and between the location of the minimum P/D ratio. For example the flow rates at L = 0.25 and L = 0.75. That is the mass flow rate in a sub-channel is largely proportional to sub-channel areas. This contrasts the observations of the distribution of velocity within each sub-channel shown in Figure 7.3. The distribution at L = 0.25 and L = 0.75 are very different as discussed earlier.

The axial variation of bulk fluid temperature profiles for the undamaged bundle shown in Figure 7.15 is linear as expected for a system with a constant heat flux. In comparison, the variations of temperature within the damaged section, are strongly non-monotonic and complex. This is due to the mixing occurring across the sub-channels as a result of the cross-flow, as well as the variation of mass flow rate in each sub-channel. All the developments for the interior sub-channels in the bottom half of the damaged section have a higher rate of temperature increase compared to the peripheral sub-channels. In the top half section, the temperature variation alters, for example the sub-channels in-between the second and third rank (numbered 4, 5) show temperature decreases, as to be expected as they have cooler flow arriving from

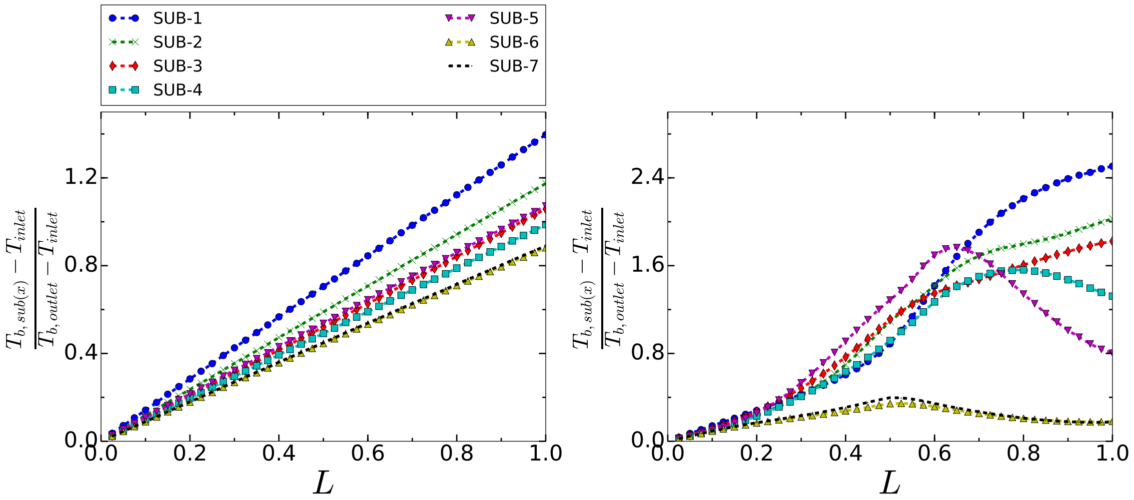

(a) (b)

Figure 7.15: Axial fluid temperature variation within the full and partial sub-channels present in the 30 ° sector. (a) undamaged bundle (b) *WheatSheaf* bundle

the outer/wall sub-channels. The rest of the interior sub-channels (numbered 1, 2, 3) show temperature increase. The most surprising result is the slight decrease in temperature for some sub-channels (numbered 6, 7). In general, the triangular sub-channels have higher coolant temperatures for both undamaged and damaged scenarios. It is noted that the differences between the temperature in the various sub-channels are significantly increased in the distorted channel.

7.4 Effect of rod roughness

The effect of rod roughness is considered through the use of a wall function. A value of 0.000124 is used for effective roughness, and this is based on dividing the average rib height, which for the rods is 0.419 mm, by a constant of 3.36. He[134] showed that a value of 3.36 can be used to calculate the effective roughness for rib roughed surfaces. To assess the suitability of the computed effective roughness, the pressure drop from developed flow in a meter tall sub-channel at various Reynolds numbers is compared to that predicted from EDF correlations[135]. Comparisons obtained showed good agreements (see Table C.3). It should be noted that AGR fuel rods have helicoidal ribs, and adopting the wall function approach means that the induced swirl effect from the ribs is missed. However, this approach does still give an insight into the effect of roughness.

Results show at the convergent section, the velocity profiles have a significant reduction in the peak velocity compared to the smooth rod profiles. The roughness thus appears to divert more of the flow from the interior region. Overall turbulence levels are seen to be greater leading to a reduction to the level of asymmetry evidenced for the earlier temperature profiles. Extracting data from Line_1, the peak temperatures close to the rod wall are shown to be lower. Profiles for the velocity, turbulent kinetic energy and temperature for this study are provided in Appendix C.3.

7.5 Conclusions

Flow and heat transfer in a damaged *WheatSheaf* bundle have been investigated using the RANS method. It is shown that the flow field within the damaged bundle significantly differs from that of an undamaged bundle. The coolant is diverted to regions of less resistance through the rod gaps. The distribution of mass flow rate in the sub-channel at any height is largely proportional to the areas of the sub-channels, but the velocity distribution is strongly influenced by the “history” - that is a strong delay is observed. In addition, the strong cross-flow causes the formation of large flow circulations. Particle tracers demonstrate the flow is not only strongly three dimensional but also swirls around the fuel rods, resulting in unexpected can temperature distributions.

The peak can temperature at the worst damage section (half height) has been surprisingly found to be lower than that of the undamaged bundle at the same height, though stronger circumferential variation is observed. The peak can temperature increases strongly towards the top half of the damaged bundle though here the peak can temperature is higher than that of the intact fuel. In addition to the complex flow distribution which produces strongly non-uniform convection cooling effect, the bulk temperature of the sub-channels shows large variations at any height, and vary non monotonically vertically, all of which contribute to the ”abnormal” can distribution observed.

Chapter 8

Methodology development *FREEDOM*[i]

This chapter outlines the methodology used in the development of *FREEDOM* (formely called *Postr2*) a 3-D thermo-fluid model for the AGR fuel route. This chapter also marks the start of part-2 of the thesis, which covers the development (methodology, validation, and application case) of the 3-D thermo-fluids code *FREEDOM* (also referred to as *Postr2* in some of texts and graphs in later chapters).

FREEDOM can be used for intact or damaged fuel. This thesis primarily focuses on the development of the latter aspect by extending the intact fuel model *POSTR*[26]. The resulting main contributions are listed below to make them clear from the onset:

- Added the capability for automatic mesh generation (fluid, radiation, and conduction) and numerical methods for the computation of geometric parameters (volumetric, anisotropic porosity, etc.) for dropped fuel geometries.
- Added correlations, mainly from existing EDF literature, along with computation methods for damaged fuel bundles, graphite debris regions, and damaged sleeves.
- Added fuel and carbon oxidation methods.
- A volume-to-volume coupling approach is implemented, and a method to account for mass transfer between the fuelled region and annulus.

---

[i] This chapter is largely based on the methodology report[136] with minor changes.

- Implemented a pseudo-transient method for use in safety cases, where the transient duration lasts multiple hours.

FREEDOM is based on the porous media approach. The model is separated into two domains (fluid and solid), which are solved using two separate solvers. *Code_Saturne* to solve for the macroscopic flow and *Syrthes* to compute heat conduction through the solid and radiation exchange between the surfaces. These two solvers are then coupled together through the exchange of temperatures and heat transfer coefficients. The overall structure of *FREEDOM* is given in Figure 8.1 and a detailed overview of the code showing the definitive features of the code is given in Figure 8.2.

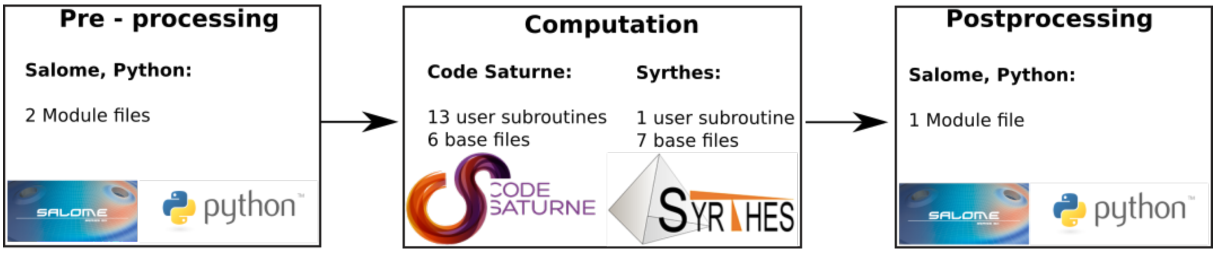

Figure 8.1: Schematic of overall code structure

It is worth noting that while in the fluid domain the porous media approximation is utilised, for the solid domain (solved in *Syrthes*) the solids are explicitly represented.

8.1 Mesh generation and calculation of geometric parameters

Meshes are required for the fluid, conduction and radiation solvers. Additional geometric parameters such as area porosities, bundle inclinations, etc. also need to be calculated for the fluid. This section details the mesh generation capabilities of the model and additionally describes the methodologies used in calculating various geometric parameters, which are used in computing the solution. Figure 8.3 shown below shows the general procedure followed in setting up meshes and geometrical input data.

To generate meshes *FREEDOM* uses the pre and post processing software *Salome*, which is developed in part by EDF. Modules can be easily manipulated through the GUI and functionalities available in the GUI can also be accessed via a python script

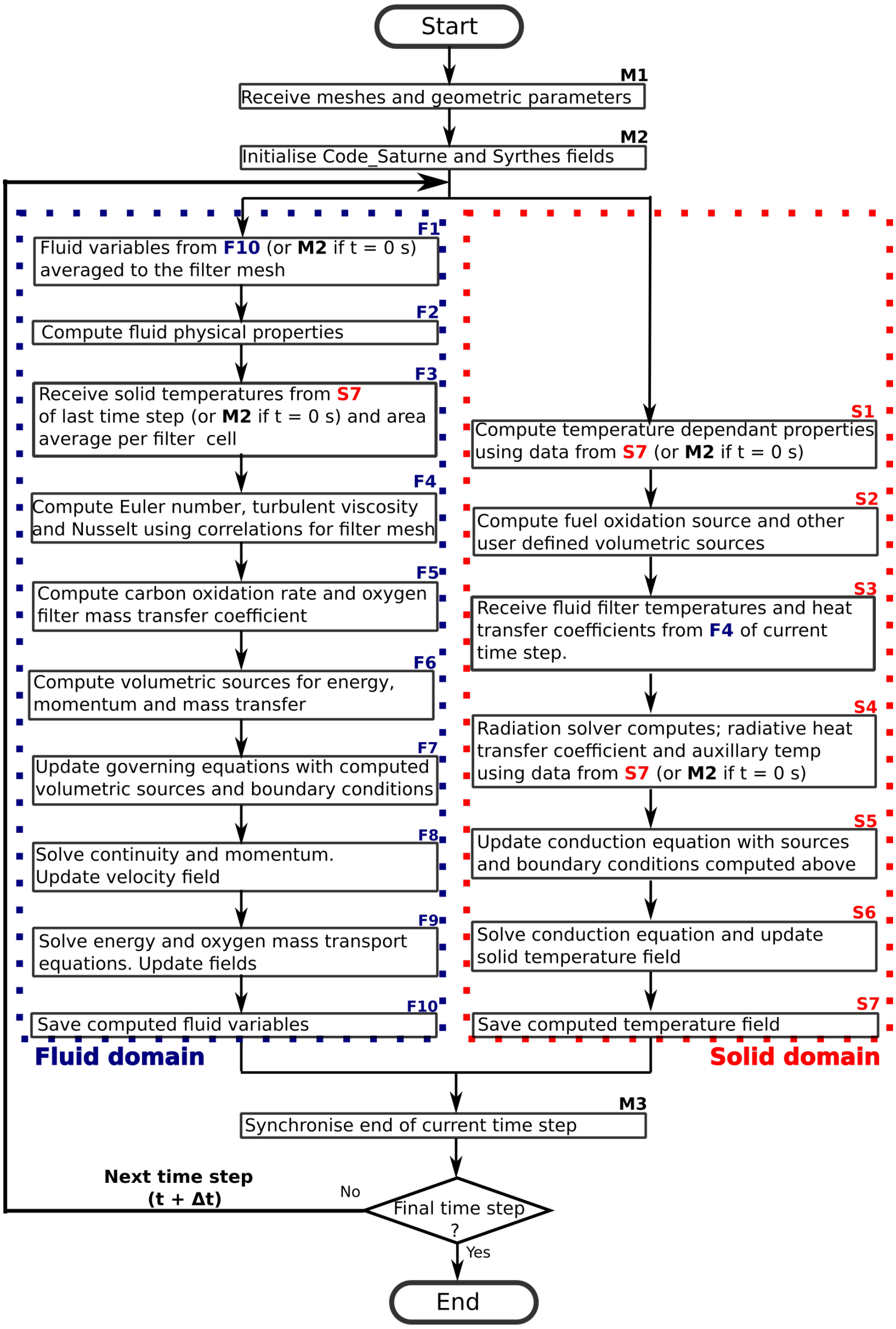

Figure 8.2: Schematic showing the detailed functionality of *FREEDOM*. The functionality chart shown here does not show the internal iterations for the pseudo-transient approach. A schematic of this approach is shown in Figure 8.13.

interfacing with Salome's API's. These python scripts are used to fully specify the geometry and mesh generation stages. In *FREEDOM* a dedicated module simply termed *MESHESMODULE* has been created and this module is responsible for generating all the meshes required based on user input data. The module relies on a standard input file which is called from the *Salome* platform. To ensure conformity the same input file

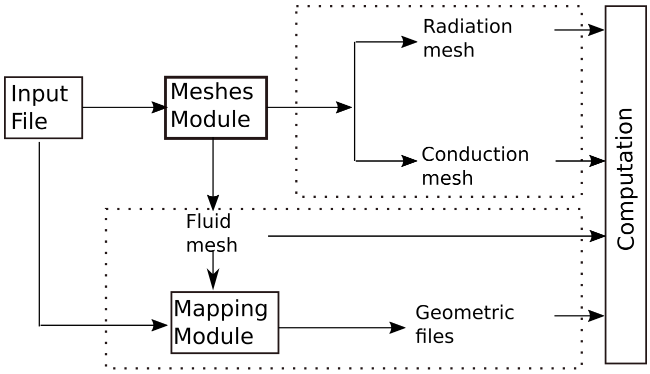

Figure 8.3: Procedure followed in producing mesh and geometric input data

is used for all the various meshes required (radiation mesh, conduction mesh or fluid mesh).

Multiple fuel debris configurations can arise in the event of a dropped fuel incident. From experimental studies several idealised damage configurations have been identified. These damage configurations are listed below:

1. **Intact with minor damage:** Damage caused is not severe enough to cause fuel pin buckling. Graphite sleeve could still be intact, or might be cracked and thus allow radial flow through.

2. **Sinusoidally buckled fuel (Normal buckling) bundle:** The fuel pins are sinusoidally buckled with the bundle centreline being described by an expression. As fuel pins buckle into an S shape, sleeve fragments are pressed up against the containment wall thus preventing further buckling. Please note at time of writing the sinusoidal expression has not been implemented in *FREEDOM*.

3. **Brittle buckling:** The fuel pins are brittle and instead of bending as described in 2 they snap

4. **C buckling** (also called **Overbuckled**): The pin bundle is severely deformed and is now composed of different sections. Typically three sections are assumed, with one of these lying across the fuel bundle. Temperatures obtained from this geometry are considered bounding. C buckling can arise from a full assembly drop.

5. **Wheatsheaf bundle:** The fuel bundle is assumed undamaged at either end

while the center is a location of minimum voidage. Expected to arise in non-contiguous drops where the fuel bundles sequentially strike each other.

6. **Overlapped bundle:** Fuel pins from two bundles overlap and slide against each other. This damage geometry is highly unlikely to occur but is suspected in facilities with a large diameter i.e. Possible for a drop in the decay storage tube.

The model is also capable of taking into account the inter-gaps between the ends of the fuel sleeves. These gaps can either be specified as open to radial flow in the case of severely damaged bundles or they can be blocked off. Alternatively, the gaps can also be specified to allow leakage flow by defining cracks within this region and setting the desired cross-flow resistance. The application of cracks is further discussed in Subsection 8.2.6.

FREEDOM has an in-built mesh generator, developed as part of this thesis, capable of modelling such damage configurations. To achieve this the pins are split into multiple piecewise segments based on already pre-defined geometry data or user defined parameters. To give an example, for an intact bundle only one piecewise segment needs to be defined but for a zigzag bundle multiple piecewise inclined segments may be defined. Figure 8.4 illustrates this approach for an undamaged and WheatSheaf bundle. At the ends of each segment, the fuel pin positions need to be given by the user. As mentioned earlier, the solid domain explicitly represents the fuel debris based on idealised damage deformations. Conversely, for the fluid mesh as the porous methodology is used, no fuel pin boundary surfaces are represented. The domain is instead cylindrical and split into radial and azimuthal segments as defined by the user.

It should be noted that the fluid domain uses a two-level approach, where one mesh is used to define the porosity, flow resistance, energy source terms, etc, and the second is used in the computation of the solution. Using the porous medium approximation requires the computational domain to be split into REVs upon which the Navier-Stokes equations are spatially averaged. A REV has been shown in Figure 3.7 and these REVs have size limits as discussed earlier. Typically, at the lower limit, the REV cannot be smaller than the pores. For pin bundles, this means the REV cannot be smaller than the pin gaps. The filtering mesh, which is the first level of resolution is set up to adhere to these size requirements. Typically in the fuelled region (where fuel pins exist), there would be 6-12 azimuthal divisions and 4-6 radial divisions. If this filtering

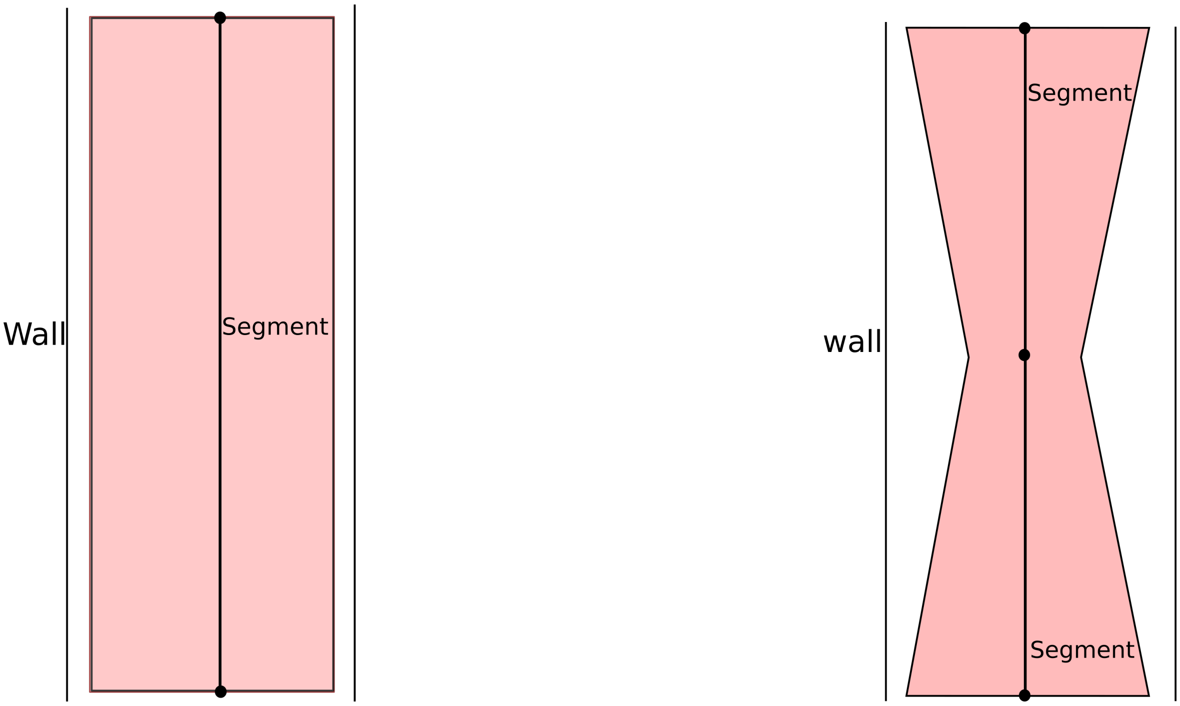

(a) Segment splits for Undamaged bundle.

(b) Segment splits for Wheat-Sheaf bundle.

Figure 8.4: Segment splits for an Undamaged and WheatSheaf bundle.

resolution is used to compute the solution it is apparent discretization errors would be appreciable. Furthermore, this grid cannot be refined as that would go against the defined size limits. To circumnavigate this issue the discretised governing equations are solved on the calculation mesh. Thereby allowing mesh refinement without invalidating the porous medium approach. For reference, Figure 8.5 gives an illustration of the calculation and filtering meshes. Each cell in the calculation mesh is assigned to a filtering mesh cell which bounds it. The filtering mesh cell thus can contain multiple calculation mesh cells but each calculation mesh cell can only belong to one filtering grid.

However, the two-level mesh approach does leave open the interpretation of the small scale variations computed on the calculation mesh. The current approach is to consider the smallest scales possible meaning (flow or thermal) correspond to the filter grid. As at this level, we adhere to the porous medium governing equations. The computed variables, turbulent viscosity and properties are averaged back to the filtering grid as that is considered the scale of interest.

In *FREEDOM*, the cross-sectional divisions for both the filtering mesh and calcula-

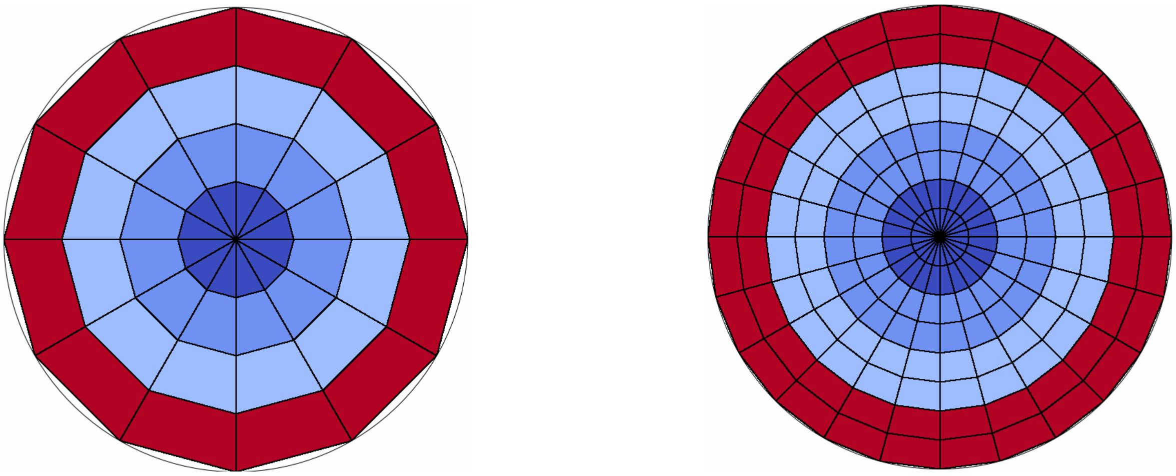
(a) Illustration of filtering mesh

(b) Illustration of calculation mesh

Figure 8.5: Comparison between filtering and calculation meshes

tion mesh are maintained the same axially; that is to say currently there is no provision for localised distortion of the grids to match the predicted damage configuration. Further work would be required to achieve this feature, firstly due to the complications in fluid mesh generation and additionally for severely distorted fuel bundles (C_buckled geometry) localised distortion would result in multiple non-conformal interfaces within the fluid mesh (even for a single bundle case). This would affect the solution computed.

8.1.1 Porosity

Porosity describes the geometric effect of the dispersed solid within the REV. Taking the dispersed solid as isotropic it is possible to define a volumetric porosity. Alternatively, one can also define an area porosity, which represents the fractional area available for the fluid to flow through in a particular direction. Area porosities result in a second order symmetric tensor which describes the anisotropy of the porous medium.

Porosities are calculated in a newly developed *FREEDOM* python module called *MAPMODULE*. The same input file used in mesh generation is required by *MAPMODULE*. Porosity is calculated upon the filtering mesh cells as they adhere to the definition of a REV.

To calculate volumetric porosity, the input geometric data is used to build a profile of each of the piecewise segments that make up a particular pin in a particular bundle. Each pin is then discretised axially, azimuthally and radially. Each discretised volume segment is then assigned to the filtering block which bounds it, Figure 8.6 gives an illustration of the procedure. The volumes of all the discretised pins in a filter mesh cell are then summed up. Porosity per filter cell can then be numerically defined as:

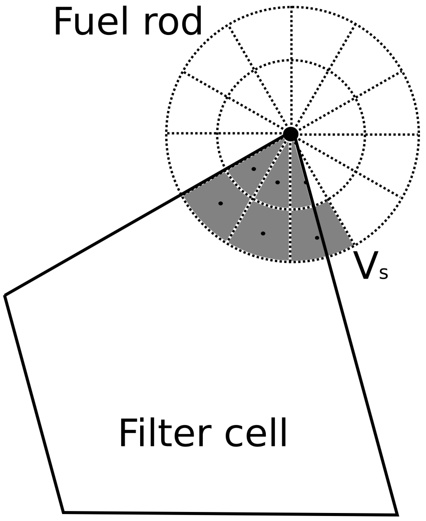

Figure 8.6: Radial and azimuthal pin discretisation prior to location on filter block

$$\alpha_v = 1 - \frac{\sum V_s}{V_T} \tag{8.1}$$

Area porosity defines the fluid flow area available in a particular direction as shown in Equation 8.2. Where A_f is free flow area and A_T is the total area available.

$$\alpha_{ij} = \frac{A_f}{A_T} = 1 - \frac{A_s}{A_T} \tag{8.2}$$

Similar to the volume porosity, the area porosity varies per filter block. The number of fuel pins, which reside in a given filter block and the ranks are identified. Area porosities in the azimuthal and radial direction are then computed as seen in Figure 8.7 using the local pin positions. If a filter block has fuel pins from multiple ranks then a simple weighted average is performed (computed based on the number of pins for a particular rank). In the axial direction, the area porosity equates to the volume porosity.

Area porosity is computed in this manner as cross flow correlations typically define the gap velocity as the characteristic velocity. However as shown in Equation 8.16, Romero[135] redefined the resistance term. It is now derived from blending the axial friction factor and cross flow Euler, with the constituent terms computed using Reynolds based on the velocity magnitude. In Equation 8.4, the axial velocity is used to compute turbulent viscosity. Using area porosity would affect the velocity scales (computed superficial velocities), this would affect the computed turbulent viscosity. All this means that the influence of area porosity must be tested, ideally against validation data. It is also noted the *CoolFuel* codes resort to equating the area porosity to the volume porosity. Fairbairn[15] also cites additional points to consider when adopting the area porosity, especially with regard to the relative pressure distributions.

In *FREEDOM*, the user can scale the area porosity against the volume porosity as done in *FEAT CoolFuel*[15] thus allowing the user multiple tests to assess their influence on the predicted solution.

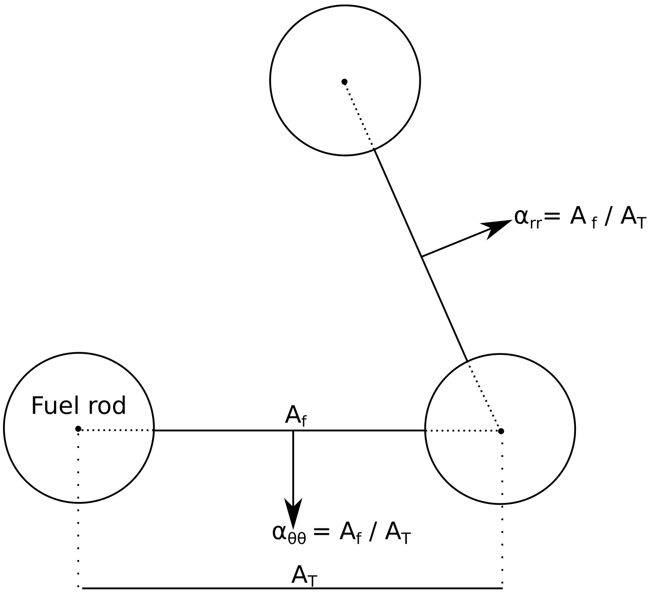

Figure 8.7: Use of pin gaps to calculate radial and azimuthal porosities

Area porosity is initially calculated in cylindrical coordinates, as the geometry is well suited to this reference system but the solver, *Code Saturne*, uses a cartesian reference system thus the area porosity tensor has to be converted. The conversion between the reference systems is performed using the tensor transformation formulae shown in Equation 8.3. Where T_e is the anisotropic porosity tensor, Q_j represents the Jacobian obtained from mapping from a cylindrical reference system to a cartesian system and T_r is the transpose of the matrix.

$$C = [Q_j][T_e][Q_j]^{T_r} \tag{8.3}$$

8.2 Fluid modelling

Porous media governing equations for the fluid are shown in Section 3.2. These equations contain additional terms, which must be modelled. To achieve this,*FREEDOM* predominantly uses the same experimental correlations as the *CoolFuel* codes. Instances where differences arise with relation to the *CoolFuel* correlations will be clearly highlighted.

The *CoolFuel* correlations are appreciably complex as they aim to describe resistance and heat transfer effects at any stage within the fuel route taking into account buoyancy effects where necessary, additionally they consider fuel bundles at varying degrees of inclination and voidages. Compared to POSTR, rod inclinations, voidages, graphite debris regions and damaged sleeves can now be considered.

8.2.1 Turbulence modelling

Turbulence is modelled using a zero equation turbulence model as done in the *CoolFuel* codes, this equation is given below[30, 137].

$$\mu_t = c_1 \left(\frac{f_a}{2} \right)^{0.5} \rho |u| \mathrm{Dh} \tag{8.4}$$

where f_a is the axial component of the friction factor. c_1 is a constant with a value of 0.035. This model is based on pipe flows but is used based on the assumption that it can be related to pin bundle flow through the use of the hydraulic diameter concept. As can be seen, the model does not modify or dampen the turbulent viscosity in the near wall regions. In *FREEDOM* the array for molecular viscosity is overwritten with the effective viscosity, which is the summation of molecular and turbulent viscosity[ii].

Turbulent heat flux and mass diffusivity are calculated by using turbulent viscosity (μ_t). The turbulent Prandtl and Schmidt numbers are both set to a value of unity.

8.2.2 Flow resistance

Empirical correlations are used to compute friction factors and loss coefficients for the fuel bundle, graphite debris, intact/cracked sleeve and containment surfaces on the filter

---

[ii] The approach taken to specify non-standard turbulence models is to setup the case as laminar flow and to overwrite molecular viscosity array with the effective viscosity

mesh, which are then applied to the porous media fluid solver as body forces/source terms. In *Code_Saturne* the explicit source term for the momentum equation is a force $\left(\mathrm{kg} \cdot \mathrm{m}/s^2\right)$. If explicit the source terms are calculated as shown in Equation 8.5.

$$\begin{aligned} \tfrac{\partial p}{\partial x_j} &= -\tfrac{1}{2}\rho \mathrm{Eu}_j |u| u \\ S_{v,e} &= \tfrac{\partial p}{\partial x_j} . V_{\text{cell}} \end{aligned} \tag{8.5}$$

V_{cell} is the cell volume and Eu_j is an Euler number per unit length. Alternatively, the source can be defined as implicit and has units of kg/s. It should be noted, the implicit approach should only be used when, $S_{v,i}$, is negative (i.e. a resistance) and *Code_Saturne* automatically clips it to 0 if not. This is done for stability as a positive term for $S_{v,i}$ could potentially destabilise the diagonal of the matrix. Equation 8.6 shows the calculation if implicit.

$$S_{v,i} = -\frac{1}{2}\rho \mathrm{Eu}_j |u| \cdot V_{\text{cell}} \tag{8.6}$$

In the event the empirical data returns a Fanning friction factor, the conversion to an Euler number per unit length is carried out as shown below:

$$\mathrm{Eu}_j = \frac{4f}{\mathrm{Dh}} \tag{8.7}$$

where Dh is the hydraulic diameter.

The source is applied to the right-hand side of the Navier-Stokes equation as shown in the following equation:

$$\rho \alpha_v \frac{\mathrm{d}u}{\mathrm{d}t} + ... = \alpha_v \left(S_{v,i} \cdot u + S_{v,e}\right) \tag{8.8}$$

where these terms $S_{v,e}$ or $S_{v,i}$ are represented by S_v in Equation 3.7. Dimensionless parameters used in the correlations are defined using properties at film or gas temperature. The film temperature is simply defined as $\left(T_{\text{wall}} + T_\infty\right)/2$[138]. In the code T_∞ is taken to be the filter average gas temperature and T_{wall} would represent the filter average wall temperature.

Fuel bundle

Correlations for the flow resistance due to the presence of a dropped fuel bundle are split into axial and cross flow terms before being blended together to obtain a combined

Euler number per unit length. The axial friction factor, $f_{a,f}$, due to forced contribution is defined as follows[139]:

$$f_{a,f} = c_1 Re^{n_1}.\Big(\frac{T_{\text{gas}}}{T_{\text{wall}}}\Big)^{n_2} \tag{8.9}$$

The exponents and coefficient shown in Equation 8.9 also take into account the bundle voidage. The Reynolds number is defined using properties at gas temperatures and the hydraulic diameter is the reference length scale used. Characteristic velocity is defined as the velocity magnitude as recommended by Romero[135] and Fairbairn[15] In contrast the *CoolFuel* codes use the axial velocity[17, 30]. *FREEDOM* adheres to the recommendations of the original reference and those of the *Feat CoolFuel* method. Reasons for following this approach are explained later when the combined Euler term is described.

A friction factor,$f_{a,n}$ can also be defined for purely natural recirculation conditions as follows[140]:

$$f_{a,n} = c_1 \text{Gr}^{n_1} \tag{8.10}$$

The Grashof number is calculated using properties defined at gas temperatures and is defined as shown in Equation 8.11. Θ represents the angle between the pin bundle axis and horizontal plane. Figure 8.8 illustrates this angle position. De is the equivalent diameter (calculated using only the fuel pin surfaces).

$$\text{Gr} = \frac{\rho^2 * \sin(\Theta) * g * (T_{\text{wall}} - T_{\text{gas}}) * \text{De}^3}{\mu^2 * T_{\text{film}}} \tag{8.11}$$

The buoyancy free and buoyancy influenced frictional factors for pin bundle axial flow are converted into shear stresses using the standard definition for wall shear stress $\tau_{\text{wall}} = f(1/2)\rho u|u|$. In this conversion the buoyancy free contribution, $f_{a,f}$, uses density defined at gas temperature and the axial velocity component along the bundle axis is taken as the characteristic velocity. For the buoyancy influenced contribution,$f_{a,n}$, density is defined at film properties and the characteristic velocity is taken to be the buoyant velocity, which is defined in Equation 8.12.

$$u_n = \Big(\frac{g * \sin(\Theta) * |T_{\text{wall}} - T_{\text{gas}}| * \mu}{T_{\text{film}} * \rho}\Big)^{\frac{1}{3}} \tag{8.12}$$

A composite function shown in equation 8.13 is then used to blend the two contributions together. Final conversion to a composite axial friction factor is achieved by using the mean velocity of the two characteristic velocities[140].

$$\tau_a = \left(\tau_{a,f}^3 + \tau_{a,n}^3\right)^{\frac{1}{3}} \tag{8.13}$$

Flow resistance across the pin bundle is given in terms of an Euler number, which uses an effective Reynolds number as shown below[135].

$$\log \mathrm{Eu}_{crs} = \sum_{i=0}^{3} c_i \Big(\log \mathrm{Re}_{\mathrm{eff}} \Big)^{i+1} \tag{8.14}$$

The effective Reynolds number is defined as follows:

$$\mathrm{Re}_{\mathrm{eff}}^2 = \mathrm{Re}^2 + 2.06\mathrm{Re}\mathrm{Ra}^{0.418} + 1.06\mathrm{Ra}^{0.836} \tag{8.15}$$

Buoyancy contribution to the cross flow Euler number is accounted for through the Rayleigh number as can be seen above. The Rayleigh number is defined as the product of the Grashof and Prandtl number. In defining the Grashof number the term sin(Θ) in Equation 8.11 is replaced with cos(Θ). This is done to take into account the orientation of gravity with respect to the bundle axis. Reynolds number is defined using the fuel pin diameter as characteristic length and uses the velocity magnitude as reference velocity. All gas properties are evaluated at the film temperature. The axial friction factor and the cross flow Euler are then blended together to form a composite Euler number using

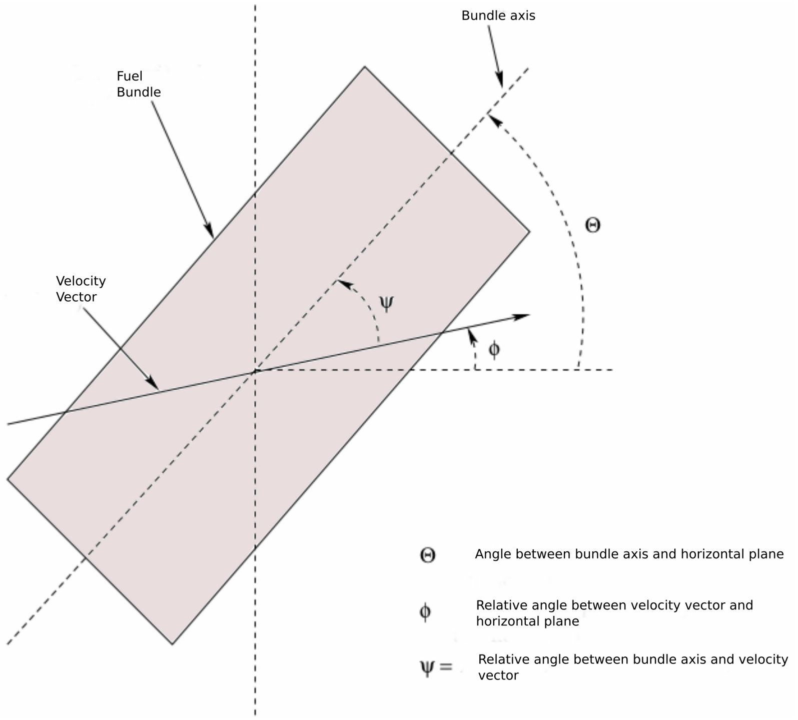

Figure 8.8: Definition of various angles as a result of bundle inclination[15].

the following equation:

$$\left[\frac{d\mathrm{Eu}^{'}}{ds}\right]^2 = \left[\frac{4f_a}{\mathrm{Dh}}\cos^{14}\Psi\right]^2 + \left[1.08\frac{\mathrm{Eu}_{crs}}{\Delta}\sin^{1.32}\Psi\right]^2 \tag{8.16}$$

where Ψ is the relative angle between the bundle axis and and coolant velocity, this angle is illustrated in Figure 8.8. 1.08 is a constant for pitch correction allowing Eu_{crs} to apply to both inline and staggered pin arrays. Δ is the pitch and in *FREEDOM* this is evaluated using the voidage by assuming an equilateral triangle arrangement of the pins $\Delta = D_p\Big(0.907/(1 - \text{Voidage})\Big)$. Voidage can be considered a representation of the effective cooling area of the flow and is defined as follows;

$$\text{Voidage} = 1 - \frac{\pi\Big(N_{\text{pins}}.r^2_{\text{pin}} + r^2_{\text{guide-tube}}\Big)}{\pi r^2_{r-3}} \tag{8.17}$$

Similar to the *CoolFuel* codes $r - 3$ is defined as the third rank pin radius and N_{pins} includes the first rank, second ranks pins but only counts half of the pins in the third rank.

Once the combined Euler number is recovered, it is noted the pressure gradient is aligned with the filter velocity vector thus the pressure gradient in an arbitrary direction can be given as:

$$\Delta P_j = \mathrm{Eu}^{'}.\frac{1}{2}.\rho.|\langle u\rangle^i|.\langle u_j\rangle^i \tag{8.18}$$

where $|\langle u\rangle^i|$ is the magnitude of the filter velocities. The combined Euler number presented in Equation 8.16 calculates the pressure drop along the velocity vector. It is decomposed in Equation 8.18 to give a pressure drop in the three principal directions.

Equation 8.16 is based on yaw dependencies. These yaw dependencies are experimentally derived by Romero[135] and it is recommended that the magnitude of velocity is used in obtaining the axial friction factor and cross flow loss coefficient. If f_a or Eu_{crs} are derived by a Reynolds number using the directional characteristic velocity, then in cases of for example strong unidirectional axial flow the laminar term from the lower Reynolds number radial velocity may in error dominate the combined resistance derived. These arguments are further laid out in the *Feat CoolFuel*[15] report.

Sleeve surfaces, containment wall and annulus region

The sleeve and containment are explicitly represented boundary walls in the fluid domain and are modelled as slip surfaces. Pressure loss due to the presence of the wall in the adjunct filter mesh cell is accounted for through the use of correlations.

Fluid regions are assigned porosity values if either the fuel or graphite debris resides within them. Additional clear flow regions (porosity = 1) can be defined where neither solid component resides. An example would be a filter block region adjacent to the containment wall or sleeve surface, which is typically defined to better capture the flow near here. Since these are slip surfaces, the pressure loss in the filter block as a result of the wall is computed from correlations.

The annulus region is a gap between exterior graphite sleeve surface and the containment surface. Within this region only the gas is assumed to exist thus the porosity is set to 1 (clear flow). Flow within this gas gap is considered to be uniaxial and as a result only the axial frictional losses are specified.

Forced convection correlations for the interior graphite sleeve and containment surfaces assume that they are hydraulically smooth. The following correlation is used[17]:

$$f_{a,f} = \max\left(\frac{24}{\mathrm{Re}}, 1.07\left(0.0014 + 0.125\mathrm{Re}^{-0.32}\right)\right) \tag{8.19}$$

For the graphite sleeve outer surface if the dimensionless rib height e^{+} is less than 5 then Equation 8.19 is used. If e^{+} is greater than 5 then the following expressions are used[139]:

if $\mathrm{e}^{+} < 30$:

$$\begin{gathered} f = 0.0039\left(\mathrm{Re}.\tfrac{\mathrm{e}}{\mathrm{Dh}}\right)^{0.318}\left(\tfrac{\mathrm{De_{ref}}}{\mathrm{Dh}}\right)^{0.425} \\ f_{a,f} = 2f^{1.1891} \end{gathered} \tag{8.20}$$

if $\mathrm{e}^{+} > 30$:

$$f_{a,f} = 0.023\left(\frac{\mathrm{De_{ref}}}{\mathrm{Dh}}\right)^{0.425} \tag{8.21}$$

e^{+} is defined as follows:

$$\mathrm{e}^{+} = \left(\frac{f_{a,f}}{2}\right)^{0.5}\mathrm{Re}\frac{\mathrm{e}}{\mathrm{Dh}} \tag{8.22}$$

where $\mathrm{De_{ref}}$ is specified as 0.023. e is the graphite sleeve rib height with a given value of 0.000635 m. In implementing this algorithm sub-iterations are performed until a converged value for $f_{a,f}$ is obtained. In certain cases it has been noted the correlation oscillates between two values and in such a scenario the mean value is used.

Buoyancy influence on the frictional losses in the annulus can be taken into account as follows. The Grashof number is defined as seen below Equation 8.23[140]:

$$\mathrm{Gr} = \frac{\rho^2 * g * (T_{\mathrm{wall}} - T_{\mathrm{gas}}) * \mathrm{Dh}^3}{\mu^2 * T_{\mathrm{film}}} \tag{8.23}$$

Similarly, the buoyant velocity is re-defined as:

$$u_n = \Big(\frac{g * \big(T_{\mathrm{wall}} - T_{\mathrm{gas}}\big) * \mu}{T_{\mathrm{film}} * \rho}\Big)^{\frac{1}{3}} \tag{8.24}$$

All fluid properties are obtained at the film temperature. The buoyant contribution to the axial friction factor is calculated using the Grashof number as shown in Equation 8.10, this is converted to a wall shear stress using the buoyant velocity.

A combined wall shear stress term is recovered by blending the natural recirculation and forced contribution together using Equation 8.13. These correlations are split into laminar, transitional and turbulent conditions. For a damaged sleeve a different set of coefficients and exponents. A sleeve is considered damaged if it is radially pushed out and the annuli gas gap is reduced.

The blending of the natural recirculation with the forced contribution terms would predict increases in wall shear stress. However, the *Feat CoolFuel* report states this behaviour is incorrect and it is recommended that the buoyancy contribution term be neglected[15]. A user defined conditional has been implemented to allow the user to either switch on or off the annulus buoyant contribution term for the frictional losses.

Graphite particulate region

In some severe dropped fuel scenarios, the graphite sleeve is fractured under the high impact load leading to the formation of a graphite debris region. From drop tests[30] it is assumed the graphite fragments are pushed outwards and are in contact with the containment wall. In *FREEDOM* these regions are treated as porous to allow radial and axial flow. Graphite debris resistance in the axial direction is given in the form of an Euler number per unit length as follows[141]:

$$\mathrm{Eu}_a = \Big[\frac{c_1}{\mathrm{void}_{\mathrm{GD}}^2}\Big(\frac{0.5}{\mathrm{Dh}_{\mathrm{GD},a}}\Big)\mathrm{Re}_{\mathrm{GD}}^{n_1} + c_2\Big]\frac{L_{\mathrm{GD}}}{0.5} \tag{8.25}$$

A loss coefficient in the radial direction is given as [141].

$$\mathrm{Eu}_{crs} = \frac{c_1}{\mathrm{void}_{\mathrm{GD}}^2}\Big[1 + \frac{c_2}{\mathrm{Re}_{\mathrm{GD}}^{n_1}} - \frac{c_3}{\mathrm{Re}_{\mathrm{GD}}^{n_2}}\Big]\frac{L_{\mathrm{GD}}}{\mathrm{Dh}_{\mathrm{GD},crs}} \tag{8.26}$$

The debris correlations are based on the superficial (or volume averaged) velocity thus the Reynolds number is defined as:

$$\mathrm{Re}_{\mathrm{GD}} = \frac{\rho |u| \mathrm{Dh}_{\mathrm{GD}} \mathrm{void}_{\mathrm{GD}}}{\mu} \tag{8.27}$$

$\mathrm{Dh}_{\mathrm{GD},crs}$ and $\mathrm{Dh}_{\mathrm{GD},a}$ are the equivalent hydraulic diameters for the radial and axial direction, respectively. They are defined using equivalent graphite particle sizes $\mathrm{SPH}_{\mathrm{GD}}$. Equation 8.28 and 8.29 are the hydraulic diameter definitions for the axial and radial terms.

$$\mathrm{Dh}_{\mathrm{GD},a} = \frac{0.423.\mathrm{void}_{\mathrm{GD}}^{1.25}.\mathrm{SPH}_{\mathrm{GD}}}{1 - \mathrm{void}_{\mathrm{GD}}} \tag{8.28}$$

$$\mathrm{Dh}_{\mathrm{GD},crs} = \frac{1.77.\mathrm{void}_{\mathrm{GD}}^{2.815}.\mathrm{SPH}_{\mathrm{GD}}}{1 - \mathrm{void}_{\mathrm{GD}}} \tag{8.29}$$

All the gas properties are evaluated using the gas temperature. Coefficients and exponents are based on the equivalent spherical diameter used, of which the user can select one of three pre-defined values. In Equation 8.27 the velocity used is either the axial or radial component depending on the loss term being calculated. Validation exercises for *CoolFuel* 3-D recommend the Reynolds numbers be limited for either loss terms dependent on the equivalent particle size selected[142]. This recommendation has been implemented in *FREEDOM*.

8.2.3 Heat transfer

This section describes the methods and correlations used to model heat transfer between the fluid and solid domain. Equation 3.8 shows the fluid domain energy equation, with the source given as $Q_{s/v}$. All the sources to the energy equation are explicit.

Fuel bundle

For the fuel bundle region the source $Q_{s/v}$ uses the surface-to-volume coupling approach, where the cell volumes of the fluid are coupled to the pin surfaces. When this coupling approach is initiated, the two solvers (*Code_Saturne* and *Syrthes*) exchange locations for the coupled surfaces and cells. In this exchange, the pin surface is coupled to the closest calculation mesh cell in the fluid domain. Since the fluid domain uses the porous media approach, the source Q_{filter} is calculated on filter averaged quantities and is defined as:

$$Q_{\text{filter}} = h_{\text{filter}} A_{\text{filter}} \Big(\langle T_{\text{wall}} \rangle^{a} - \langle T_{\text{gas}} \rangle^{i} \Big) \tag{8.30}$$

where A_{filter} is the sum of the pin surface areas located in the filter block. $\langle T_{\text{wall}} \rangle^{a}$ is the area averaged pin surface temperature for the filter block. $\langle T_{\text{gas}} \rangle^{i}$ is the intrinsic averaged gas temperatures for the filter (averaged using the fluid volume) and h_{filter} is the heat transfer coefficient, the calculation of which is discussed later. When $Q_{s/v}$ is passed it has units of Watts and assigned to the calculation mesh cells thus Q_{filter} must be first converted to a volumetric heat generation for the filter and multiplied by the local cell volume as follows.

$$Q_{s/v} = \frac{Q_{\text{filter}}}{V_{\text{filter}} . \alpha_{v}} . V_{\text{cell}} \tag{8.31}$$

where V_{filter} is the total filter volume, which in the preceding equation is multiplied by the volume porosity giving the filter fluid volume. V_{cell} is total volume of the local calculation mesh cell. It should be stated V_{cell} is not multiplied by porosity at this stage as later internally *Code Saturne* multiplies the source $Q_{s/v}$ by porosity before it is put to the right-hand side of the linear algebraic matrix. The implementation of the source in the energy equation can be seen in Equation 3.8.

The temperatures computed on the filter grid blocks are always physical, as this is the scale of interest and consistent with the porous medium approximation. Filter block values are computed by averaging the computation mesh results to this level of resolution. Values on the computational mesh are local variations, which are at scales smaller than the filter block. Calculation mesh values are typically not evaluated in isolation as they are inconsistent with the porous medium approximation. However, since there is this calculation mesh data available, it would be nice to try and exploit it and gain meaningful information at this level of resolution. To achieve this would require a bit more work and further thought. In part this would involve adjusting how values are passed between the two mesh resolutions. It should be noted, the solid temperatures are computed on a separate solid mesh, which is coupled to the filter mesh. See Section 8.3 for the implementation of solid-to-fluid domain coupling. The results on the solid mesh are extracted locally.

h_{filter}, which is the heat transfer coefficient is defined using dimensionless numbers and properties computed at the filter mesh level. The remainder of this subsection describes the correlations and their implementation for the fuelled region.

Heat transfer in the axial direction h_a is computed by blending the forced and buoyant contributions using a composite expression. The composite expression is implemented in terms of Nusselt number as seen below[140]

$$\mathrm{Nu} = \left(\mathrm{Nu}_{a,f}^3 + \mathrm{Nu}_{a,n}^3\right)^{\frac{1}{3}} \tag{8.32}$$

Forced axial heat transfer is calculated from a set correlations taking into account the Reynolds number and voidage. These correlations return Stanton numbers as in Equation 8.33, where they are later converted to the forced axial Nusselt number counterpart by using the standard definition (St = Nu/(Re.Pr)).

$$\mathrm{St}_{a,f} = c_1 \mathrm{Re}^{n_1} . \frac{T_{\text{filter}}}{T_{\text{wall}}}^{n_2 * n_3} \tag{8.33}$$

Exponents $n_2 * n_3$ vary on the basis of voidage. Reynolds number is calculated using properties at gas temperature and the effective diameter (comprising only heating surfaces) is used. Since the final heat transfer coefficient is recovered using the blending approach based on yaw factors, the magnitude of velocity is used in calculating Reynolds numbers. Buoyancy influenced axial heat transfer is directly recovered as a Nusselt number using the correlation below for both laminar and turbulent ranges:

$$\mathrm{Nu}_{a,n} = 0.068\left(\mathrm{GrPr}\right)^{0.367} \tag{8.34}$$

Properties are calculated using gas temperatures.

For the crossflow component, the contribution to the pin bundle heat transfer is calculated by blending the buoyant and forced contribution terms together using a similar expression used for axial flow as in Equation 8.32.

The cross flow forced contribution uses the following correlation [135]:

$$\log\left[\frac{\mathrm{Nu}_{f,crs}}{\mathrm{Pr}_{\text{film}}^{0.36}\left(\frac{\mathrm{Pr}_{\text{wall}}}{\mathrm{Pr}_{\text{film}}}\right)^{0.25}}\right] = \sum_{i=0}^{4} c_i \left(\log \mathrm{Re}\right)^i \tag{8.35}$$

This correlation is applied over the whole Reynolds number range. In calculating the Reynolds number gas properties and dimensionless numbers are evaluated at film temperatures. Furthermore the characteristic length scale used is the pin diameter and velocity scale is based on the magnitude of velocity. When converting the Nusselt number to a heat transfer coefficient the thermal conductivity is calculated at film temperature (i.e. $h_{f,crs} = \mathrm{Nu}_{f,crs} . k_{\text{film}} / \mathrm{D}_p$).

Under the influence of natural convection the following expressions are to be used for cross flow, the expression chosen is dependent on the Rayleigh number[135].

if Ra < 2.5 x 10^6

$$\mathrm{Nu}_{n,crs} = 0.4\mathrm{Pr}^{0.0432}\mathrm{Ra}^{0.25} + 0.503\mathrm{Pr}^{0.0334}\mathrm{Ra}^{0.0816} \tag{8.36}$$

if Ra $\geq$ 2.5 x 10^6

$$\mathrm{Nu}_{n,crs} = 0.13\mathrm{Ra}^{\frac{1}{3}} \tag{8.37}$$

All properties are evaluated using the film temperature. For the buoyant contribution the Grashof number uses the pin diameter as the length scale and the gravity vector is re-oriented against the bundle axis using cos(Θ) see Equation 8.38.

$$\mathrm{Gr} = \frac{\rho^2 * \cos(\Theta) * g * (T_{\mathrm{wall}} - T_{\mathrm{gas}}) * \mathrm{D}_p^3}{\mu^2 * T_{\mathrm{film}}} \tag{8.38}$$

Calculation of the heat transfer coefficient from $Nu_{n,crs}$ uses the pin diameter and thermal conductivity calculated at film temperature.

The pin bundle heat transfer coefficient is then obtained by blending the axial and cross flow terms together using yaw factors as done for the resistance correlations, this is shown below:

$$h_{\mathrm{filter}}^2 = \left(h_a \cos^{0.5}\Psi\right)^2 + \left(h_{crs} \sin^{0.5}\Psi\right)^2 \tag{8.39}$$

The exponent values are based on the recommendations of the *CoolFuel* validation report[137]. Volumetric heat sources for the fluid domain are computed using the heat transfer coefficient (h_{filter}) as shown in Equation 8.30. At coupling, the solid domain updates its convective boundary conditions using the heat transfer coefficient (h_{filter}) and filter averaged temperatures received from the fluid domain.

Sleeve surfaces, containment wall and annulus region

Correlations and the heat transfer modelling approach for the explicitly represented surfaces are discussed here. These boundary surfaces are coupled with *Syrthes* and modifications are made to the near-wall cells to correctly capture the heat loss.

The corrections detailed in the following equations are made to the surface-to-surface coupling approach, where an explicitly represented surface in the fluid is coupled to its counterpart in the solid domain (This is for the sleeve and containment surfaces). The other coupling methods, which involve computing volumetric sources are not subject to this correction. Also, the porosity term is included in Equation 8.40 because the default implementation in *Code_Saturne* scales the wall area by the near-wall cell porosity. Typically, in *FREEDOM*, when a surface-to-surface coupling is initiated the cell porosity is set to 1.

The method used was first implemented by Trinca[26]. Heat flow through the walls, if unmodified, would be defined as:

$$Q_{\text{unmod}} = (\lambda + \lambda_t) A_{\text{cell}} \alpha_v \frac{\langle T_{\text{wall}} \rangle^a - T_{\text{gas}}}{d} \tag{8.40}$$

where d would the wall normal distance. In actuality, the heat flow through the boundary should be using a heat transfer coefficient obtained from correlations and filter averaged values as follows:

$$Q = h_{\text{filter}} A_{\text{cell}} \alpha_v \left(\langle T_{\text{wall}} \rangle^a - \langle T_{\text{gas}} \rangle^i \right) \tag{8.41}$$

A heat transfer coefficient can be specified for Equation 8.40 by using the following re-arrangement:

$$h_{\text{unmod}} = \frac{\lambda + \lambda_t}{d} \tag{8.42}$$

Equating the two heat flows together (Equations 8.40 and 8.41) such that h_{unmod} is modified to represent the desired heat flow(based on filter values and correlations) the following expression is obtained:

$$h_{\text{unmod}} = h_{\text{filter}} \frac{\langle T_{\text{wall}} \rangle^a - \langle T_{\text{gas}} \rangle^i}{\langle T_{\text{wall}} \rangle^a - T_{\text{gas}}} \tag{8.43}$$

Within the code the array for turbulent conductivity is then re-written to give the following wall turbulent conductivity.

$$\lambda_t = h_{\text{filter}} \frac{\langle T_{\text{wall}} \rangle^a - \langle T_{\text{gas}} \rangle^i}{\langle T_{\text{wall}} \rangle^a - T_{\text{gas}}} d - \lambda \tag{8.44}$$

This correction of the wall turbulent conductivity is only ever done if h_{filter} has a value. If the value is null nothing is done.

Axial heat transfer correlations are specified for the annulus gap and interior sleeve surface. As with the resistance correlations it is assumed the flow is mostly axial within the annuli region or near the sleeve inner surface thus only the axial component of velocity is used. For the graphite interior sleeve the forced contribution uses four expressions split by the Reynolds number as follows[15].

if $\mathrm{Re} < 400$:

$$\mathrm{Nu}_{a,f} = 3.78 \tag{8.45}$$

if $400 < \mathrm{Re} < 5000$:

$$\mathrm{Nu}_{a,f} = 0.12108\mathrm{Re}^{0.589}\mathrm{Pr}^{\frac{1}{3}}\left(\frac{\mu_{\text{film}}}{\mu_{\text{wall}}}\right)^{0.14} \tag{8.46}$$

if $5000 < \mathrm{Re} < 10^4$:

$$\mathrm{Nu}_{a,f} = 0.0033\mathrm{Re}^{1.013}\mathrm{Pr}^{\frac{1}{3}}\left(\frac{\mu_{\text{film}}}{\mu_{\text{wall}}}\right)^{0.14} \tag{8.47}$$

if $\mathrm{Re} > 10^4$:

$$\mathrm{Nu}_{a,f} = 0.023\mathrm{Re}^{0.8}\mathrm{Pr}^{\frac{1}{3}}\left(\frac{\mu_{\text{film}}}{\mu_{\text{wall}}}\right)^{0.14} \tag{8.48}$$

At the containment inner surface the following correlations are used[139]:

if $\mathrm{Re} < 2000$:

$$\mathrm{Nu}_{a,f} = 4.0 \tag{8.49}$$

if $2000 < \mathrm{Re} < 10^4$:

$$\mathrm{Nu}_{a,f} = 3.8 \times 10^{-4}\mathrm{Re}^{1.233}\mathrm{Pr}^{\frac{1}{3}} \tag{8.50}$$

if $10^4 < \mathrm{Re} < 3 \times 10^4$:

$$\mathrm{Nu}_{a,f} = 0.057\mathrm{Re}^{0.69}\mathrm{Pr}^{\frac{1}{3}} \tag{8.51}$$

if $\mathrm{Re} > 3 \times 10^4$:

$$\mathrm{Nu}_{a,f} = 0.0164\mathrm{Re}^{0.81}\mathrm{Pr}^{\frac{1}{3}} \tag{8.52}$$

The outside surface of the graphite sleeve uses the following heat transfer correlations for the laminar flow range, $\mathrm{Re} < 2000$, as shown below. Above this range the correlations used are similar in form to Equation 8.50.

$$\mathrm{Nu}_{a,f} = 5.12 \tag{8.53}$$

Buoyancy effects use the same correlation shown in Equation 8.34 and the implementation is as described earlier. All the properties in the preceding correlations shown for this subsection are evaluated at gas temperature.

Graphite debris region

If a graphite particulate region is formed it is postulated graphite fragments will be pushed hard against the containment surface. Thus effectively heat transfer to the containment at this surface occurs in a complicated manner comprising solid conduction where the graphite pieces are in contact with the containment, gas conduction due to stagnant gas, convective heat transfer and finally radiation. Within the core of the graphite debris region heat transfer occurs between the gas and the solid where fluid-surface interactions exist. At the interior surface of the debris there is convective heat transfer between the exposed slabs of graphite and the hot flowing gas. There is also radiation exchange occurring between the interior surface and fuel pins. As can be noted modelling heat transfer within this region is rather complicated.

FREEDOM has two main methods of treating this region loosely based on the thermo-fluid codes *CoolFuel* and *FOXDROP/HOTDROP*.

FOXDROP is a one dimensional axisymmetric code used for dropped fuel safety cases[143]. The damaged fuel bundle is split into multiple solid annular regions. The first annular region would be that of the fuel debris, separated by a void from the next annular region which would be for the graphite debris or sleeve. After the debris region the user can either allow direct thermal contact between its exterior surface and containment wall or another void can be specified. Effective conductivities are specified for each of the solid regions and for the voids only radiative heat transfer can occur. With regards to the graphite debris, thermal contact is assumed to be perfect. The effective conductivity model used for the debris is numerically based. It was derived by representing the graphite debris region as a series of concentric annuli consisting of graphite and air regions. In the air regions the conductivity multipliers were used to take into account improved heat transfer from radiation and graphite particulate conduction[144]. Conduction through the graphite particles was calculated from idealised damage scenarios and assumes various forms of contact of the debris with containment surface.

CoolFuel treats the graphite debris as a porous region only in the fluid domain with an altered thermal conductivity. An experimentally derived correlation for small graphite particles is used to compute the thermal conductivity. Thermal equilibrium is assumed between the fluid and solid particles[17], thus conduction for the debris (in the solid domain) is not modelled. However, radiative heat transfer between the fuel pins and the debris interior surface is taken into account. *CoolFuel* 1-D models the interior surface by defining it as an infinitely thin porous sleeve. At the exterior surface, the debris region is assumed to be in contact with the containment wall.

The thermal equilibrium approach can be, typically, considered as optimistic concerning graphite temperatures. For example; under natural convection, heat is primarily received via radiative heat transfer from the fuel pins. Peak temperatures would be at the debris inner surface for the graphite debris, and this would make the solid phase higher than the fluid phase. Thermal equilibrium is optimistic in such a scenario. However, this is conditions dependent. An example is the upper fuel bundles in a stringer for a forced convection case. In this scenario, it is likely the heat transfer is from the gas to the graphite particulates. Thermal equilibrium is likely pessimistic in the given scenario. .

FREEDOM adopts the following modelling approach for the graphite debris. The region is assumed porous and the porosity defined is equated to the graphite debris voidage. It is further assumed that the gas and debris particles are not in thermal equilibrium. Non-thermal equilibrium entails both the solid and fluid domain representations of the debris are modelled. For effective conductivity *FREEDOM* can use correlations from either *CoolFuel* or *FOXDROP*, these are described later in this section. These correlations are applied in the solid domain, while in the fluid domain the gas conductivity is used.

Heat transfer mechanisms occur as follows; at the interior graphite debris surface, convective heat transfer from the hot gas and radiative heat transfer with the pins is modelled. Inside the graphite debris, in-pore heat transfer between the solid and fluid domain is taken into account. Finally, for the exterior surface in contact with the containment two options are available. The user can either set up the heat loss to the containment via either the solid or fluid domain with the other domain being treated as adiabatic. The default model assumes heat loss is through the solid domain and a schematic of this setup is shown in Figure 8.9.

CoolFuel uses a correlation based on experimental data [17] to give a thermal conductivity for the graphite debris. The experiment used small graphite particles approximately 8 mm or less. The correlation is valid at temperatures below 500 °C. Above

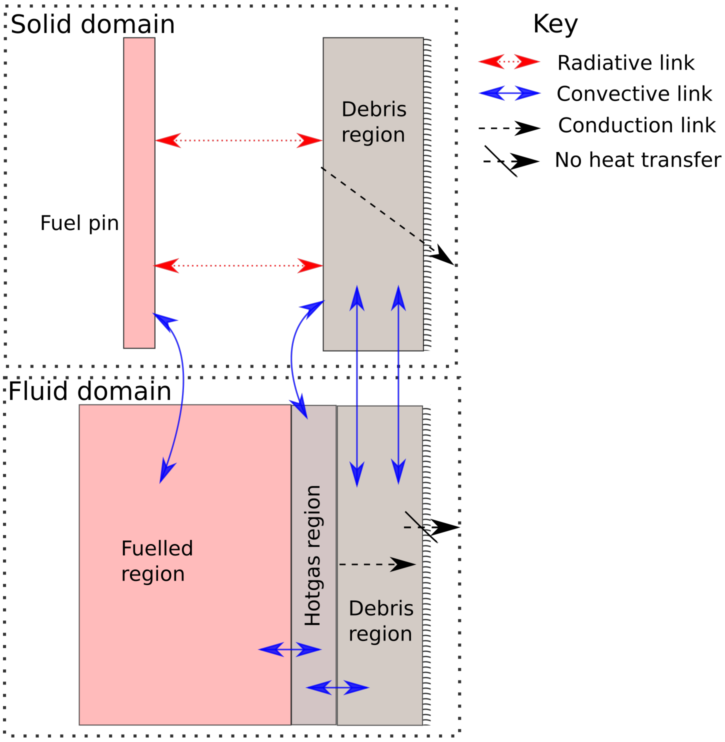

Figure 8.9: Schematic of heat transfer links for the modelling of the graphite debris region. This schematic is for the default setup which allows heat loss through the containment wall in the solid domain. All the various links can be adjusted depending on user preference

this range the use of the correlation is allowed on the basis it is conservative. The correlation is given below[17]

$$\kappa_{\mathrm{eff}} = 13\kappa + 90D_{\mathrm{reff}}\left(\frac{T}{1000}\right)^3 + \frac{wC_pD_{\mathrm{ref}}}{B} \tag{8.54}$$

Starting from the left the terms represent conduction, radiation and convection, respectively. Where κ is the gas conductivity,D_{reff} is the particle diameter which is fixed to 0.01 and B is a constant. It should be noted B is given a value of 10^{10} in *FREEDOM* thereby neglecting the convection term. This is done based on the recommendations of the *CoolFuel* validation report[142].

Apart from using the small particulate model, the graphite conductivity can also be given using the model used in *FOXDROP*. The model for *FOXDROP* gives effective conductivity values for graphite debris at voidages of 20 % and 54 %. The values are given by a set of linear expressions for each voidage split by temperature[143].

The in-pore heat transfer coefficient is calculated using the following correlation[145]:

$$h = \kappa\left[2 + 1.1\mathrm{Pr}^{\frac{1}{3}}\left(\frac{\rho|u|\mathrm{SPH}_{\mathrm{GD}}}{\mu}\right)^{0.6}\right]/\mathrm{SPH}_{\mathrm{GD}} \tag{8.55}$$

This correlation assumes the graphite debris can be represented as a bed of spherical particulates. The equivalent spherical diameter $\mathrm{SPH}_{\mathrm{GD}}$ from the graphite axial resistance correlations is used. $|u|$ in the equation is referring to the velocity magnitude.

For the heat transfer coefficient between the debris interior surface and hot gas, the correlations for the ribbed outer graphite sleeve are used.

8.2.4 Mass transfer

Over time as the fuel resides within the reactor carbon deposits may build on the surfaces of fuel pins as a result of the reaction between methane and the coolant forming hydrocarbons[146]. In addition to the likely impairment of heat transfer due to the deposition layer there is also the added risk of carbon oxidation. In an environment where oxygen is present, for example in the Irradiated Fuel Dismantling Facility (IFDF), and if the fuel pin cladding temperatures are sufficiently high, the carbon deposits would start oxidising. This would consequently increase the cladding temperatures, which then would increase the oxidation rate until diffusion acts to limit it. Oxidation would continue until all the deposits are oxidised. Additional details about the carbon oxidation modelling are given in Section 8.5, this section will primarily discuss the species transport equation and how oxygen consumption is calculated.

When carbon oxidation is activated, by default, *FREEDOM* solves an additional transport equation (Equation 8.56) for the mass fraction of oxygen. Turbulent mass diffusion is modelled using the eddy viscosity assumption with the further assumption that the turbulent Schmidt number Sc_t is unity. The modelling of turbulence is described in Section 8.2.1. In the active filter mesh cells where oxygen is consumed a sink term is applied to the transport equation and at the containment surfaces the user can specify boundary conditions for the mass fraction. The solved transport equation is presented in Equation 8.56:

$$\frac{\partial \alpha_v \rho \langle \overline{C_I} \rangle^i}{\partial t} + \frac{\partial \rho \alpha_{ij} \langle \overline{u_i} \rangle^i \langle \overline{C_I} \rangle^i}{\partial x_i} = \frac{\partial}{\partial x_i} \left[\alpha_v \left(\rho D_{O-A} + \frac{\mu_t}{Sc_t} \right) \frac{\partial \langle \overline{C_I} \rangle^i}{\partial x_i} \right] + S_I \tag{8.56}$$

where C_I is the oxygen concentration, S_I is a sink term and D_{O-A} is the binary mass diffusion of oxygen in air. This term is temperature dependent and is solved using

Equation 8.60.

Carbon oxidation of the deposits can be considered to have two limiting modes, which are:

- Chemical dynamics - Computes oxidation rate based on the assumption oxygen is always sufficiently available and the oxidation rate purely limited by the number of available reaction sites. A chemical rate equation is used (see Equation 8.65) and Equation 8.56 is not required for this computation.
- Diffusion of oxygen - Computes the oxidation rate by considering the availability of oxygen. It is assumed the chemical rate is quite effective. Oxidation is instead limited how much oxygen is transferred to the carbon deposit surface. Equation 8.56 is used to compute the advection, diffusion and consumption of oxygen in the domain. The computed oxygen concentration is used to calculate the oxidation rate (see Section 8.5).

There are two ways of calculating the oxygen consumption based on the limiting modes discussed above. If oxygen concentration levels cannot sustain the chemical rate (the limiting mode is the availability of oxygen), then the oxidation sink is calculated from the mass transfer rate of oxygen from the far-field to the carbon deposit surface. Two assumptions are made in this computation. Firstly the surface oxygen concentration (at the carbon deposit) is taken to be 0. Figure 8.10 illustrates this. This assumption is pessimistic, as it is unlikely the concentration would ever be 0 at the surface.

Secondly, it is assumed that the heat mass transfer rate, h_m can be calculated by using the heat/mass transfer analogy. For heat and mass transfer, the forms in the governing equation for advection and diffusion are essentially the same. As shown in Incropera[147] an analogy exists between the roles of Prandtl and Schmidt numbers in the governing equation, this can be further extended to Sherwood and Nusselt numbers which are defined as $\mathrm{Sh} = f\left(\mathrm{Re}, \mathrm{Sc}\right)$ and $\mathrm{Nu} = f\left(\mathrm{Re}, \mathrm{Pr}\right)$. Based on the heat/mass transfer analogy an analogy factor can be given as $\mathrm{Nu} = \mathrm{F} * \mathrm{Sh}$ where the analogy factor F can be obtained as follows:

$$\mathrm{F} = \frac{\mathrm{Nu}}{\mathrm{Sh}} = \left(\frac{\mathrm{Pr}}{\mathrm{Sc}}\right)^{n_1} \tag{8.57}$$

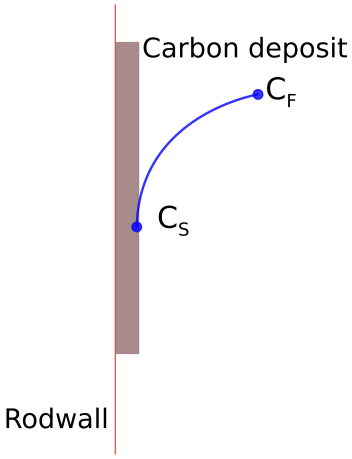

Figure 8.10: Illustration of mass transfer computation. C_s is assumed to be zero and C_F is taken to be the filter average species concentration in kg/m^3.

In *FREEDOM*, n_1 is taken to be 1/3 and Sherwood is calculated using the heat/mass analogy through the process described above[147]. From the Sherwood number the mass transfer coefficient can be obtained.

The sink in the species transport equation is then computed using the following equation:

$$\mathrm{No} = h_m A_{\text{filter}} \left(\langle C_F \rangle^i - C_S \right) \tag{8.58}$$

where C_S is pessimistically taken to be zero and No is the rate of oxygen transferred to the carbon deposit surface. The sink No has units of kg/s. All the terms in the preceding equation are calculated in terms of filter cell values. At the calculation mesh level the source is defined as:

$$\mathrm{No}_{\text{cell}} = \frac{\mathrm{No}}{V_{\text{filter}} \alpha_v} * V_{\text{cell}} \tag{8.59}$$

This definition of the source at the calculation mesh is similar as that for the energy equation and again it should be noted *Code Saturne* later internally multiplies this source by volume porosity.

Alternatively, if the chemical rate is the limiting mode the rate of oxygen consumption is calculated from Equation 8.65. The referenced equation returns the rate of carbon oxidation in g/hr, assuming purely carbon dioxide is produced from the oxidation process. The rate of oxygen consumption is computed using the ratio 32/12. Where 12 and 16 are the carbon and oxygen molar mass, respectively. A further unit conversion to kg/s is carried out before equating the resultant value to No.

8.2.5 Fluid properties

All physical properties in *FREEDOM* are treated as temperature dependent. Density by default in *FREEDOM* is calculated using the ideal gas law as done in the *CoolFuel* codes[17, 30]. For the remaining properties, barring the mass diffusivity of oxygen in air, their dependence on temperature is modelled through linear expressions obtained from the National Institute of Standards and Technology (NIST) database.

If carbon deposition oxidation is to be computed, the temperature and pressure dependence of the mass diffusivity of oxygen must be computed. Currently, *FREEDOM* is only setup to compute the mass diffusivity of oxygen in air and uses the method from Incropera[147]. Assuming ideal gas behaviour, the binary mass diffusion can be approximated as follows:

$$D_{O-A} = p^{-1}T^{\frac{3}{2}} \tag{8.60}$$

Binary mass diffusion for oxygen in air at 298k and atmospheric pressure is obtained from the data tables in Incropera[147], this is then scaled according to the relation cited above to approximate the temperature dependency.

8.2.6 Flow through graphite cracks

The damage sustained by the graphite sleeve may be relatively mild such that a graphite particulate region is not formed. Instead the sleeve is cracked or split into large graphite chunks. These cracks or split locations lead to radial flow paths through the sleeve connecting the annuli and fuelled regions. Previously, the regions would have been separated by an intact graphite sleeve. In order to model radial flow from the separate regions, an intact sleeve is modelled but with mass source terms defined at the crack locations. Mass flow is then computed by checking the pressure difference and specifying a resistance, the following equation is used:

$$p_2 - p_1 = \frac{R_b}{\rho_{b^*}} W_b |W_b| \tag{8.61}$$

By rearranging the above equation it can be seen the resistance, R_b has units of m^{-4} and is defined as $R_b = \rho \Delta p / W_b^2$. Initial reference values for the resistance term can obtained by for example referring to the *CoolFuel* or other relevant EDF documents. The user can then adjust the specified resistance to match validation data if it is available. ρ_{b^*} is taken to be the upwind branch density. p_2 is the total pressure in the ring adjacent the sleeve for each respective region. To further clarify, p_2, is the circumferential average of all the filter blocks adjacent the sleeve. Once the mass flow is calculated sources or sinks are appropriately assigned within the respective regions. Another important feature to capture is the temperature differences either side of the cracked sleeve. Thus when a positive source is calculated the temperature of the source is specified as equal to that of the upwind region.

Multiple axial crack locations can be specified. It should be noted all the above is computed using filter cell values.

8.3 Solid modelling

The solid domain comprises the solid components within the stringer of interest. This would include, the fuel pins (with claddings), guidetube, tie bar, containment and sleeve. If so required conditionals exist to exclude some of the aforementioned components from the computation[iii]. A representation of the solid domain is shown in Figure 8.11

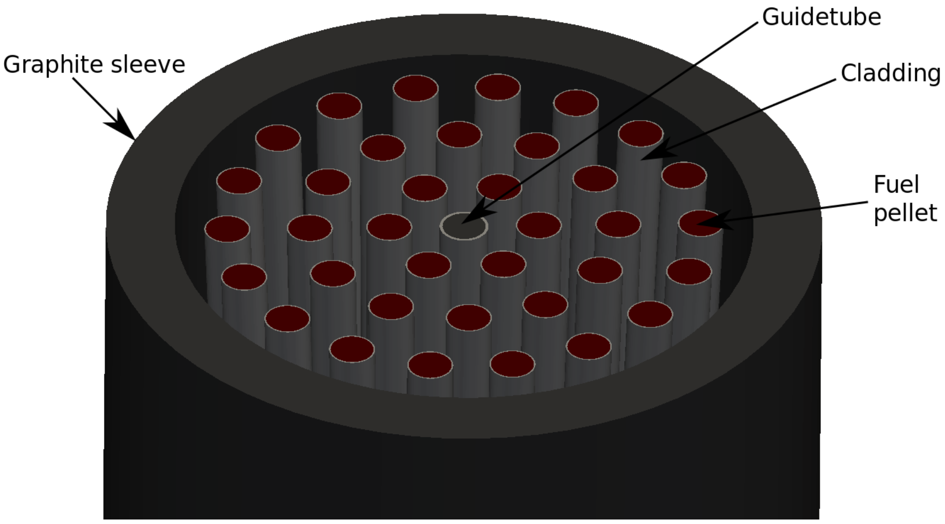

Figure 8.11: Solid domain modelling approach

Within this domain solid heat conduction and thermal radiation is modelled. Fluid convection and the resulting effect on the solid temperatures is taken into account by conjugate heat transfer. The methods used to couple the two domains together are described in Section 8.4.

[iii] This is true for all components except for the fuel pins

8.3.1 Fuel pins, tiebar and claddings

The fuel bundle is modelled using the idealised damage configurations described in Section 8.1. The pins are explicitly represented in the solid domain, with conduction and radiation being treated in a 3-D manner. This approach is in keeping with *CoolFuel* 3-D. However, *CoolFuel* 1-D and *FEAT CoolFuel* only consider conduction in the radial direction. As *FREEDOM* is a 3-D solver there would be a loss of conservatism in comparison to the 1-D models. In certain scenarios where the damage configuration specifies the number of breaks, it is possible to split the conduction mesh into multiple independent sections to limit the extent of axial conduction. Additional information about the modelling of conduction and radiation is given in Section 4.6.

The exterior fuel surface and interior cladding surface are modelled as if they were in perfect thermal contact. In reality there would be instances where the pellet is in contact with the cladding but predominantly it would be radiation and conduction through the fission gases responsible for heat transfer. A gap resistance needs to be given to take this into account, and in *FREEDOM* a fixed contact resistance of 1623.188 W/m K [148] is applied. For the tiebar and guide tube the contact resistance is specified to the same value. Physical properties are specified using constant values, which are given below:

Table 8.1: Physical properties for Fuel pins, claddings and tie bar

Component	ρ $\left(\text{kg}/m^3\right)$	C_p $\left(J/\text{kg}°C\right)$	κ $\left(W/m°C\right)$
Tie bar	7980	620	17
Guide tube			
Fuel cladding			
Fuel pellet	10650.0	303.0	3.0

Properties given in the preceding table are taken from CoolFuel [148] and Nuclear systems 1[149]. Heat generation as result of decay heat or nuclear heating can be specified (only to the fuel) by giving volumetric heat generation rates. The axial rating shape of the stringer can be specified if required. A source as a result of fuel oxidation can be given, Section 8.5 describes the calculation and implementation of the fuel oxidation source. Carbon oxidation heats the fuel pin from the cladding surface and is computed as shown in Section 8.5.

If the radiation solver is activated, radiative exchange between the external cladding surfaces and surroundings is taken into account. Typically, the pins can only see the internal graphite surface but if the damage is severe enough radiative exchange can occur between the fuel pins and containment.

8.3.2 Sleeve

Most of the physical properties for the sleeve are defined using fixed values[15, 148]. C_p is the exception, which is implemented using a temperature dependent correlation. Thermal conductivity (κ) has a value of 16 W/m k. Density (ρ) is fixed to 1851.0 kg $/m^3$. Finally, (C_p) is given using the equation below:

$$C_p = 802 \cdot (1 + 0.000973 T_c) \tag{8.62}$$

It is possible to specify a volumetric heat source as a result of graphite heating. Radiation exchange can be modelled either side of the graphite sleeve. At the interior graphite sleeve radiative exchange occurs with the fuel pins and at the exterior surface the exchange occurs with the containment wall.

8.3.3 Graphite debris

The newly implemented graphite particulate region is modelled as an annular region with an external surface in thermal contact with the containment wall. This follows from drop tests that show that the graphite sleeve fragments are pushed hard against the containment surface. Thermal conductivity is calculated as described in Section 8.2.3 using either Equation 8.54 or conductivity data tables from the *FOX-DROP* model[143], both these definitions take into account the enhancement of material conductivity by thermal radiation. In the absence of case specific information, the remaining physical properties are calculated using porosity as shown below.

$$\phi_{\text{property}} = \phi_{\text{solid}} \left(1 - \alpha_v\right) + \phi_{\text{fluid}} \alpha_v \tag{8.63}$$

A volumetric heat generation source due to in-pore heat transfer with the gas can be applied, this is described in Section 8.2.3. Radiative heat transfer is taken into account between the fuel pins and the debris interior surface. The default/base model treatment of the exterior debris surface is to assume there is perfect thermal contact.

8.3.4 Containment wall

Within the solid domain the containment wall is typically modelled as a thin solid. The external boundary condition on the containment wall is usually given as a sink temperature and heat transfer coefficient. A thin solid is modelled, instead of simply a surface, to take into account radiation. To limit the resistance through the containment the conductivity is set arbitrarily high. A low density and specific heat capacity are given to limit the influence of this modelling approach during transient analysis.

For certain cases a containment conductance is given and this has to be converted to a heat transfer coefficient. Conductance, $\kappa_{\text{conductance}}$, is given as $\kappa.A/d$. Writing the heat flow using conductance equating to the form using a heat transfer coefficient, it is shown that the transformed heat transfer coefficient is defined as $h_{\text{transformed}} = \kappa_{\text{conductance}}/A_{\text{bundle}}$. A_{bundle} is the area per bundle and is used as conductance is typically specified as conductance per bundle. In general the heat transfer coefficient is usually given as a fixed value but specifically for the IFDF there are temperature dependent correlations included for the various locations within the facility[19]. These correlations are given in terms of conductance per bundle and are converted to a heat transfer coefficient using the method above.

Radiation exchange between the containment and graphite sleeve (or fuel pins if the damage is severe enough) is taken into account.

8.4 Coupling approaches

The coupling approaches used to take into account conjugate heat transfer between the solid and fluid domains are presented below.

8.4.1 Surface-to-Surface coupling

This coupling approach is used for the containment and/or sleeve boundary surfaces. This coupling approach is for surfaces that coincide explicitly in the fluid and solid domains. In Subsection 8.2.3 it was shown how the heat transfer correlation for the boundary surface is converted into an effective conductivity giving Equation 8.44.

This value is sent to *Syrthes* as $\kappa_{\text{effective}}/d$ (essentially a local heat transfer coefficient) along with the fluid temperature to calculate the surface flux. In *Code_Saturne* the received temperature is imposed as a Dirichlet boundary condition.

8.4.2 Surface-to-Volume coupling

The surface-to-volume coupling approach is used when there is no explicit representation in the fluid domain for the solid surface to be coupled. The surface of the solid is then coupled with the filter volume in which it resides, which is shown schematically in Figure8.12. This approach was not originally present in *Code_Saturne* and *Syrthes*, it was implemented as part of the PhD project by Trinca[26]. A heat transfer correlation is specified as described in Section 8.2.3. A overall source to filter volume is calculated as shown in Equation 8.30 and its application to the calculation mesh is as shown in Equation8.31. This coupling approach is used for the fuel pins, guidetube and debris interior surfaces. The debris interior surface has to be coupled with the hot gas region and in order to achieve this, there is a slight asymmetry between the radial lengths of the graphite debris region in the fluid and solid domain. The graphite debris representation in the solid domain is marginally thicker. It is necessary to ensure the surface cells are located in the hot gas region, as the goal is to couple the debris interior surface elements with this region. If the debris interior surface is not slightly biased, the fluid and solid domain representation would be coincident in theory, but there is a risk some of the surface elements (interior debris surface) would be coupled with the fluid debris

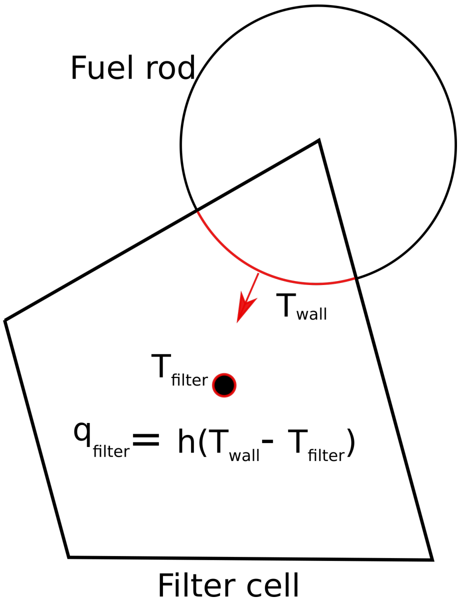

Figure 8.12: Schematic of the surface-to-volume coupling approach

region.

8.4.3 Volume-to-Volume coupling

A volume-to-volume coupling approach has been specifically implemented in this work to take into account the in-pore heat transfer. In this approach the volume of the solid is coupled to that of filter volume. The heat transfer coefficient is calculated using Equation 8.55. An in-pore area is calculated using the hydraulic diameter defined for the axial correlations, this is given in Equation 8.28. From the hydraulic diameter the following definition is used to calculate the in-pore area:

$$\frac{\left(\mathrm{Dh}_{\mathrm{GD},a} + \mathrm{Dh}_{\mathrm{GD},c}\right)}{2} = \frac{4.V_{\mathrm{filter}}.\alpha_v}{A_{\text{in-pore}}} \tag{8.64}$$

8.5 Oxidation sources

Drops in facilities where oxygen is present or leaked into the system could potentially lead to additional heat generation due to carbon and/or fuel oxidation occurring. Furthermore recent inspections have shown thicker than expected carbon deposition levels on the fuel pins, thereby making carbon oxidation an important heat generation source to take into account. Methods accounting for these oxidation sources are now implemented in *FREEDOM* as part of this project.

8.5.1 Carbon oxidation

Multiple oxidation methods have been identified and implemented for use in *FREEDOM*. The modelling of the oxidation process also takes into account that there is a finite amount of carbon available for oxidation; which once consumed the process stops. The methods used to calculate the oxidation rate, track heat release and finally pass the source to *Syrthes* are described below.

The carbon deposit layer can be considered to act as an insulating layer, largely resulting in convective heat transfer impairment. Heat transfer impairment can be quite significant for reactor conditions, where the heat fluxes are high. However, the heavily deposited cases which *FREEDOM* considers are for the IFDF where the stringer power is much lower < 20 kW. In these cases, heat transfer impairment is not considered that significant as it would raise the cladding temperature by only a few degrees.

FREEDOM does not take into account heat transfer impairment because of the aforementioned reasons. If the model is to be used in cases where the stringer power is significantly higher than those of the IFDF then heat transfer impairment has to be considered.

1 - Chemical dynamics equation

This method is used for oxygen rich environments under which there is sufficient oxygen flow available, for example in forced convection scenarios. Under such scenarios, the heating is limited by chemistry and the EDF correlation (chemical rate equation) can be used to compute the oxidation rate. The chemical rate equation is given as [150]:

$$\mathrm{R}_{\text{bundle}} = 4.62 \times 10^{8} * A^{0.6} * D \exp^{\overline{\frac{-18600}{(T_{\text{wall}}+273)}}} \tag{8.65}$$

where $\mathrm{R}_{\text{bundle}}$ is the rate of carbon oxidised given in g/hr, which is applied to the whole fuel bundle. A represents in percentage terms the amount of air present in the facility. T_{wall} and D are the maximum pin wall temperature within the filter and the deposit mass, respectively. The wall temperature in Equation 8.65 is specified in degrees Celsius.

Equation 8.65 is a function of a fixed deposit mass, which makes it pessimistic. In reality, carbon oxidation is typically considered a surface reaction and the deposit mass would reduce as oxidation occurs. To try and mitigate the pessimisms with the model, carbon mass tracking can be considered. If carbon mass tracking is activated, the amount of carbon consumed is tracked and this is used to reduce the deposit mass value D. At each instance, in time, the carbon mass consumed is computed per filter block and summed to an array tracking accumulation. D is then redefined as $D = D_{\text{initial}} - D_{\text{tracked}}$. Where D_{initial} is the initial deposit mass and D_{tracked} is the mass-consumed since start of carbon oxidation. Section 8.2.4 shows how the rate of oxygen consumption is computed; D_{tracked} is computed using similar considerations but solving for carbon consumption.

Oxidation of carbon at a rate of 1 g/hr releases 9.11 W [150]. Thus the oxidation source applied to the fuel cladding is given as:

$$Q_{\text{bundle}} = 9.11 * \mathrm{R}_{\text{bundle}} \tag{8.66}$$

Since the source given in equation 8.66 is in terms of the overall fuel bundle, it has to be scaled down with regards to the filter block oxidising as shown below:

$$Q_{\text{filter}} = Q_{\text{bundle}} * \frac{A_{\text{filter}}}{A_{\text{bundle}}} \tag{8.67}$$

2 - Diffusion Method

Diffusion can be taken into account in scenarios where the sufficient flow conditions assumption does not hold. In adopting this method it is assumed the chemical rate is quite effective and heating is instead limited by the diffusion process (i.e how much oxygen is transferred to the carbon deposit surface).

Physically, the carbon oxidation rate is controlled by the limiting mode between diffusion and the chemical rate, In *FREEDOM* the diffusion method can be coupled with the chemical rate equation, by comparing oxidation rates between the two processes and using the minimum rate to give a better representation.

There are two implementations of the diffusion method available in *FREEDOM* and these are given in the bulleted list below:

- **Diffusion method - Fixed concentrations:** In this method, the scalar transport equation (Equation 8.56) is not solved. Instead, the bulk fluid oxygen mass concentration is fixed to 0.23. The heat/transfer analogy is then used to compute the carbon oxidation source as described in Section 8.2.4.

- **Diffusion method - Transport equation:** This method solves the mass transport equation for oxygen (Equation 8.56). The far-field fluid concentration corresponds to that in the filter block. The heat/mass transfer analogy (see Section 8.2.4) is used to compute the carbon oxidation rate and is in turn used to determine the rate at which to remove oxygen from the system (sink term is applied to mass transport equation).

Equation 8.58 gives the calculated oxygen transportation rate for the diffusion approach. C_{F} represents either the filter average concentration or the fixed species concentration depending on which method is selected. This oxygen transportation rate is then re-written in terms of a carbon oxidation rate (N_{c}) by using the ratio 12/32 to convert, where 12 and 16 are the carbon and oxygen molar mass, respectively. In using the ratio it is assumed purely carbon dioxide is formed from the exothermic reaction of carbon and oxygen.

It can be noted in Equation 8.58 the rate is derived using A_{Filter} and the source per filter for the diffusion model is given as:

$$Q_{\text{filter}} = 9.11 * \mathrm{N_c} \tag{8.68}$$

Overall implementation

The two main methods for taking into account carbon oxidation have been described above. By default the model calculates the oxidation rate as the minimum of both models. This modelling approach is better representative, as stated earlier the oxidation rate is controlled by the limiting process.

In reality the heat generated by the oxidation process would in part be passed to the gas as well as the fuel pin cladding. In the model it is pessimistically assumed all the heat from oxidation is received by the cladding. The carbon oxidation heat source is applied to the fuel pin cladding surface by altering the filter temperature $\left(\langle T_{\text{gas}}\rangle^i\right)$ sent to *Syrthes*. The following method is used to achieve this:

- For unmodified blocks with no carbon oxidation the *Code_ Saturne* sends filter averaged temperatures and heat transfer coefficients giving;

  $q_{\text{convected}} = h_{\text{filter}}\left(\langle T_{\text{gas}}\rangle^i - T_{\text{wall}}\right)$

- If the filter block has a carbon oxidation source this is added to $q_{\text{convected}}$ thus yielding

  $q_{\text{mod}} = q_{\text{convected}} + q_{\text{oxidation}}$

  This can be expanded and rewritten as:

  $q_{\text{mod}} = h_{\text{filter}}\left(\langle T_{\text{gas}}\rangle^i - T_{\text{wall}}\right) + h_{\text{filter}}\Delta T$

  $= h_{\text{filter}}\left(\langle T_{\text{gas}}\rangle^i - T_{\text{wall}}\right) + h_{\text{filter}}\Delta T$

  $= h_{\text{filter}}\left(\langle T_{\text{gas}}\rangle^i + \Delta T - T_{\text{wall}}\right)$

  where ΔT is defined as $q_{\text{oxidation}}/h_{\text{filter}}$

From the method shown above the carbon oxidation source is passed to the surface by altering the filter temperature sent to *Syrthes* with ΔT, thus the modified temperature sent is $\left(\langle T_{\text{gas}}\rangle^i + \Delta T\right)$.

There is a finite carbon deposit mass available for reaction. To take this into account the total energy release possible has to be defined. The deposit releases 32.83 kJ per gram of carbon oxidised. The total available energy release per bundle is then given as $D * 32.83$kJ, where D, is the carbon deposit mass available and is specified for the whole bundle. In *FREEDOM* the energy release per bundle is further scaled down to that per filter block using the ratio of the filter fuel pin area and total fuel bundle area. D is specified as a fixed constant for every bundle modelled, in reality as argued in the Heysham 2 safety cases[19] carbon deposition levels vary based on bundle position with fuel bundles four and above having thicker carbon deposits. When running multiple fuel bundle cases, the peak deposit value possible (taken from the upper bundles) is specified for all the bundles. The simplification is pessimistic as the increased bulk temperature from the lower bundles (over-estimated bundles) would lead to pessimistic temperatures at the top (where the deposit mass corresponds to the correct value). It should be noted, there is a version of *FREEDOM*, where bundle-wise deposit mass can be specified. So this limitation in the code is no longer strictly there (although this version of the code needs to undergo independent verification).

8.5.2 Fuel oxidation

After a dropped fuel event the fuel pin claddings could either sustain multiple punctures or in severe cases the pins could snap allowing the coolant to freely access the fuel. If oxygen has access to the fuel pellets an exothermic reaction would occur forming U_3O_8 from uranium dioxide.

As the level of damage affects how much access oxygen has to the fuel, there are two fuel oxidation rates which can be defined as a result. The two rates are the bare and defect fuel rate, with the former used when assuming oxygen has free access. The latter is when there is only open access at segment ends but limited access at puncture holes/pin bores[150]. The algorithm used to calculate the fuel oxidation sources is taken from the thermo-fluid code *FOXDROP*[143].

The bare fuel rate equations for the energy release per bundle are shown below[150]: If the fuel temperature $T \leq 550$°C:

$$Q_{\text{bare,bundle}} = 5.337 \times 10^7 \exp^{\frac{-79444}{T+273}} \tag{8.69}$$

if the fuel temperature 550°C $< T <$ 800°C and the negative temperature feedback is to be accounted for:

$$Q_{\text{bare,bundle}} = 1.357 \exp^{\frac{6447}{T+273}} \tag{8.70}$$

If the temperature is greater than 550 °C and the negative temperature feedback is not to be accounted for, the fuel oxidation source is calculated using Equation 8.69 and the temperature of the fuel is fixed at 550 °C.

If the negative temperature feedback is taken into account (Equation 8.70), at fuel pin temperatures above 800 °C, where the equation is no longer valid, the fuel oxidation source is fixed to that calculated at the maximum temperature (800 °C).

The equations presented in 8.69 and 8.70 are the bare fuel rate equations. To take into account fuel oxidising at defect fuel rates the equations have to be scaled down and the following method is used[150].

The effective bore area is calculated as:

$$A_{\text{bore}} = 2 * 2\pi a \left(\frac{a \cdot D_{\text{bore}}}{2\beta} \right)^{\frac{1}{2}} \tag{8.71}$$

a is a fixed constant with a value of 0.0032m. D_{bore} is the bore mass diffusion which is calculated as function of temperature using $D_{\text{bore}} = 2 \times 10^{-5} \left[(T + 273) / 2.73 \right]^{1.79}$ m^2s^{-1}. β is given using the following two equations as a function of temperature:

if temperature is $T <$ 270°C:

$$\beta = 4.07 \times 10^{13} \exp^{\left[\frac{-2.195 \times 10^4}{T+273} \right]} \tag{8.72}$$

if temperature is $T \geq$ 270°C:

$$\beta = 2.08 \times 10^{2} \exp^{\left[\frac{-7.794 \times 10^3}{T+273} \right]} \tag{8.73}$$

A_{bore} is the defect fuel area and is then converted into a fractional bore area, which represents the ratio of the defect fuel area and the area available at bare fuel rates (maximum pin surface area available) using the following equation[150].

$$\text{FA}_{\text{bore}} = \frac{A_{\text{bore}} + \left(2 * 1.33 \times 10^{-4}\right)}{0.02} \tag{8.74}$$

where 1.33×10^{-4} m^2 is the assumed cross sectional area for the fuel and in the derivation of these equations it is assumed there is free access at two open ends. This cross sectional area is added to A_{bore} as shown above.

The aim is to calculate the defect fuel rate using Equations 8.69 and 8.70, which are for the bare fuel rate. Thus the following scaling terms are applied to take this into account:

If temperature $T < 270°\text{C}$:

$$\text{SCALE} = 10^{11.906 - \frac{6083}{T+273}} \tag{8.75}$$

If temperature $270°\text{C} \leq T < 450°\text{C}$:

$$\text{SCALE} = 10^{0.616 + \frac{65}{T+273}} \tag{8.76}$$

If temperature $450°\text{C} < T \leq 550°\text{C}$:

$$\text{SCALE} = 10^{-4.066 + \frac{3450}{T+273}} \tag{8.77}$$

if temperature $T > 550°\text{C}$ and the negative feed back of temperature is taken into account then :

$$\text{SCALE} = 10^{-3.529 + \frac{2800}{T+273}} \tag{8.78}$$

if temperature $T > 550°\text{C}$ and fuel oxidation rate is fixed to 550°C then:

$$\text{SCALE} = 1.34 \tag{8.79}$$

The scaling term calculated above is then multiplied against the fractional bore area to give EFA_{bore}. In the code the user then specifies the ratio of fuel oxidising at bare fuel rates BFR. This term BFR is then summed with EFA_{bore} to give TFR. Since it is possible for TFR to be greater than 1 in the code the following implementation is used:

$$\text{TFR} = \min\left(\text{EFA}_{\text{bore}} + \text{BFR}, 1\right) \tag{8.80}$$

The oxidation source at either defect or fuel rates is then calculated using the terms TFR and EFA_{bore} based on the cumulative heat release. The total possible heat release is given as 1.909×10^7 J per bundle if all the fuel is oxidised. In the code an accumulated heat release $\text{CM}_{\text{bundle}}$ is calculated per bundle and the source is defined as follows:

The oxidation source is a function of the bare fuel rate if the cumulative heat release is $\text{CM}_{\text{bundle}} < \left(1.909 \times 10^7\right) * \text{TFR}$. The source is then calculated as

$$Q_{\text{bundle}} = \text{TFR} * Q_{\text{bare,bundle}} \tag{8.81}$$

Once the cumulative heat release is $\mathrm{CM}_{\mathrm{bundle}} \geq \left(1.909 \times 10^{7}\right) * \mathrm{TFR}$ the fuel is then considered to be oxidising at defect fuel rates and the source is defined as:

$$Q_{\mathrm{bundle}} = \mathrm{EFA}_{\mathrm{bore}} * Q_{\mathrm{bare,bundle}} \tag{8.82}$$

Oxidation at the defect fuel rate continues until the cumulative heat release is equal to the theoretical value for the whole bundle. After this point fuel oxidation is no longer taken into account.

Since the oxidation rate is defined per bundle, the peak temperature in the bundle is used. The calculated source is fixed for the whole bundle. The fuel oxidation algorithm is directly implemented in *Syrthes* as no flow parameters are required. To further clarify, in current modelling the consumption of oxygen by fuel oxidation is not taken into account. This modelling approach is severely pessimistic as carbon and fuel oxidation would be competing for oxygen, thus further depleting the amount of oxygen available at the fuelled region. Adjusting the code and making fuel oxidation transport limited requires further work and will be implemented in the near future. However, although fuel oxidation is not transport limited there is a provision to limit the peak fuel oxidation rate (for cases where sufficient flow assumption does not hold) based on an approach used in *FOXDROP*[143].

Although the availability of oxygen is not taken into account with regards to the fuel oxidation rate, its effect on the bare fuel rates is considered through the introduction of a multiplier. If natural recirculation flow is predominately responsible for the transport of oxygen then the assumption used in defining the bare fuel rates i.e. oxygen is always sufficiently available is no longer valid. To take this into account, the multiplier Bare Fuel Rate Multiplier (BFRM) is given a value less than one and scales Equation 8.81 giving:

$$Q_{\mathrm{bundle}} = \mathrm{TFR} * Q_{\mathrm{bare,bundle}} * \mathrm{BFRM} \tag{8.83}$$

BFRM is used to modify the fuel oxidation rate based on the recommendations of a study on fuel pin bore flows[16]. Under forced convection (sufficient flow conditions), the multiplier BFRM is set to 1 as the estimated flows could sustain the bare fuel rate. In natural convection scenarios, the value of BFRM is reduced to 0.3.

8.6 Pseudo-transient approach

FREEDOM can be set up for transient simulations but an issue arises if the transient period to be investigated lasts several hours. Even for a porous model with fairly large computing mesh cells, the fluid time scales are still appreciably lower and would thus limit the transient period that could be investigated. To speed up the conjugate heat transfer problem the fluid can be assumed to be pseudo-steady. The solid is thus still treated as unsteady but with a steady-state fluid solution provided at each thermal time step. Such an approach herein termed “pseudo-transient” is implemented in *FREEDOM* and discussed below.

The pseudo-transient approach alters the coupling frequency between *Code_Saturne* and *Syrthes*. By default the two codes exchange information at every iteration. Instead in *FREEDOM* the fluid domain couples one instance per solid time step. After exchanging information, the fluid domain performs multiple internal iterations until a converged fluid solution is obtained. During the internal iterations, solid temperatures at the last coupling instance are saved and used as boundary conditions. At each coupling instance, the fluid domain will present a steady-state result. The solid domain would remain unsteady and is therefore presented with a series of steady-state results from the fluid.

Before the next time step is initiated a check must be made on the convergence of the fluid domain solution. This is carried out by calculating the energy balance. By default the code checks the energy balance is under 1 % before re-initiating coupling with the solid. A schematic of the overall approach is given in Figure 8.13

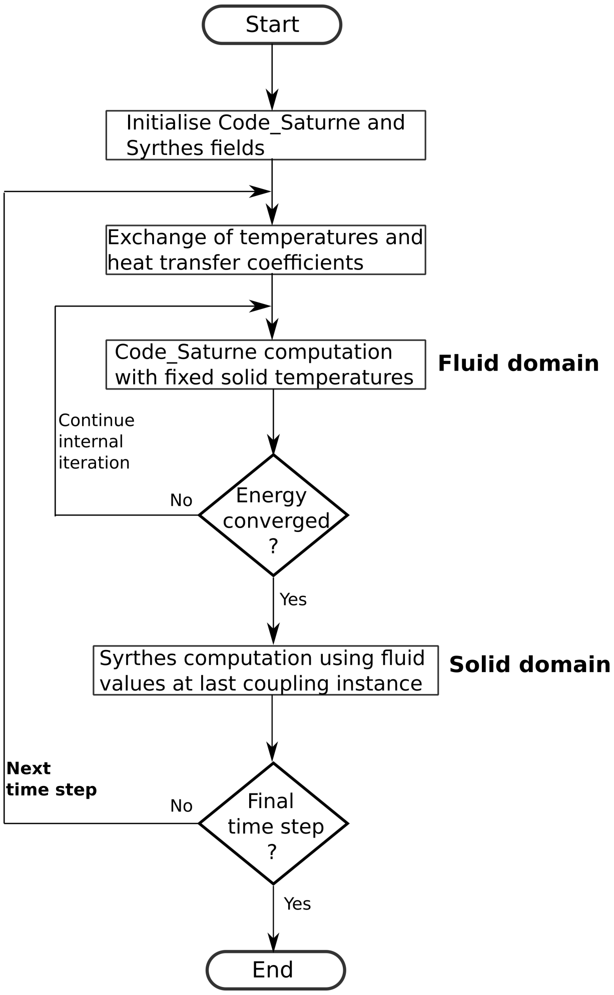

Figure 8.13: A simplified schematic showing the general layout of the pseudo-transient approach.

8.7 Conclusion

This chapter outlines the modelling methodologies and overall structure of the thermo-fluid model *FREEDOM*. The model comprises two domains, which are the fluid domain used to compute fluid flow, and the solid domain used to compute thermal conduction and radiation.

In the fluid domain, *FREEDOM* uses the porous media approach which has been described from the fundamental governing equations to actual implementation within the code. To close the governing equations for a porous medium terms for heat transfer, distributed resistance and turbulence are modelled through the use of correlations. A detailed description of the correlations used and the influence of the debris geometry and flow condition in their computation has been provided. A description of modelled parameters and computation of properties for the solid domain has also been given.

Details are given on how *FREEDOM* models the complex fuel damage geometries and graphite debris. The range of debris geometries that can be modelled and approaches used to achieve this are provided within the chapter.

The code can also take into account carbon deposit and fuel oxidation. Details on the computation of these additional sources has been provided. Finally, the implementation of the pseudo-transient method used for cases where the transient duration to be modelled is appreciably long has been given.

Chapter 9

Validation of the *FREEDOM* model[i]

This chapter outlines the validation for *FREEDOM*. It is envisaged that *FREEDOM* would be a useful tool in the thermal-hydraulics analysis of the fuel route by supporting the 1-D models in use at EDF Energy. To demonstrate the suitability of *FREEDOM*, validation exercises have been performed in this chapter for natural and forced convection cases using a variety of idealised damage configurations. Thus the primary focus is on the damaged fuel parts, as these were developed as part of this thesis.

9.1 Description of experiments and model setup

9.1.1 Description of *Overlapped* setup

A test rig was built in the early 1990s at Nuclear Electric now EDF energy to investigate the influence of natural convective flow on the cooling of damaged fuel debris.

Description of the experimental rig

The test rig was housed in a cylindrical pressure vessel made from carbon steel. The internal diameter of the test rig was approximately 0.3 m. Inside the test rig four fuel bundles could be inserted. Of these, two were distorted to conform to the idealised *Overlapped* geometry while the remaining bundles were undamaged.

---

[i] This chapter is largely based on the validation report[151] with minor changes.

An *Overlapped* bundle comprises of two fuel bundles, which are undamaged at either-end, but within the interior of the bundle, the bundles displace radially outwards. At the overlap site, the two bundles co-exist forming hexagonal fuel arrays which are identical and mirrored about a central plane. A sketch of this geometry is shown in Figure 9.1.

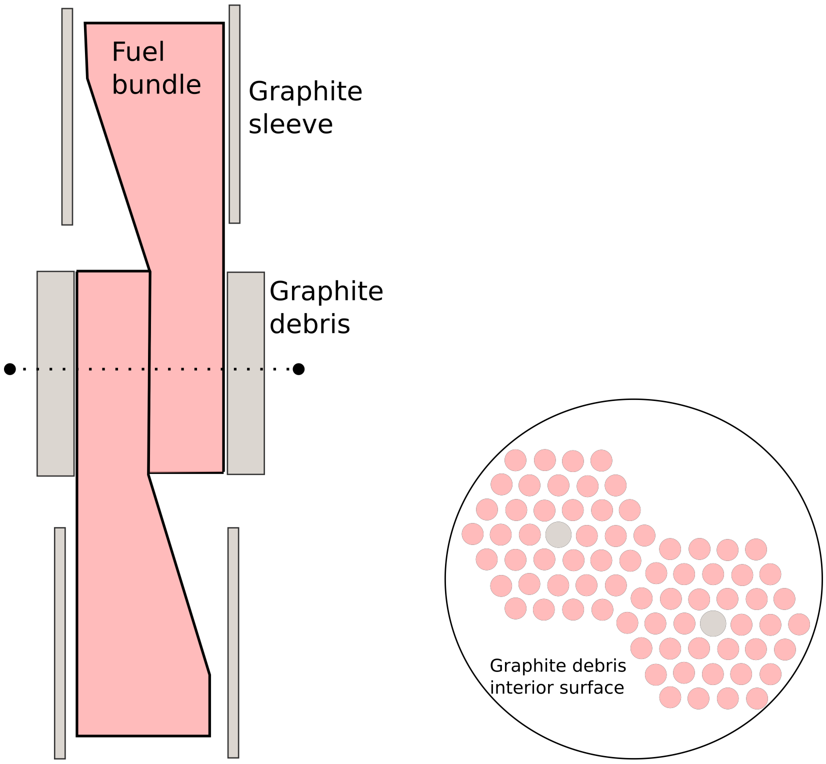

(a) Sketch of *Overlapped* bundle

(b) Fuel pin positions at overlapped site

Figure 9.1: Illustration of the *Overlapped* bundle and pin positions at this location

The undamaged ends of the *Overlapped* pins were housed in short intact sleeves, while at the overlap region (where the two bundles coexist) the fuel pins are surrounded by a graphite debris region. In constructing the graphite debris region, graphite fragments were packed from the edges of the fuel pins to the containment wall. The graphite debris region was 0.498 m tall and had a radial length of 0.048 m.

In the experiment, the location of the *Overlapped* bundle was interchangeable giving rise to three-possible geometric builds. Additionally, the sleeve ends were machined such that a cylindrical collar could be inserted thus blocking radial flow from the fuelled region to the annuli region. This gave rise to multiple sub-configurations for each build and these are shown in Figure 9.2.

Model setup in *FREEDOM*

The *Overlapped* bundle is modelled using the dimensioned assembly diagram shown in Figure D2. As can be seen, at the overlapped site the fuel pins have approximately the same height as that of the graphite debris region. In adopting this dimensioned diagram, it is implicitly assumed the graphite fragments were packed up to the top of this containment basket. Later sketches of the overlapped site shown in the experimental report are not always consistent with Figure D2 and furthermore, *CoolFuel* 3-D models the graphite debris region to be appreciably shorter, in comparison to the fuel pins at the overlapped site. This modelling assumption of the graphite debris length used in FREEDOM has an influence in the graphite debris temperature profile, which is discussed later. A sketch of the *CoolFuel* geometry is shown in Figure D1.

In the description of F-type flow blockages[18], it can be noted that at the overlapped site, the major axis of the fuel pins cuts into the debris region by ≈ 0.012 m at eitherside. In *FREEDOM*, the co-existence of fuel pins and a graphite debris region in the same physical space cannot be modelled thus the debris is slightly pushed outwards to ensure this does not occur. In the geometric sketches given for the *CoolFuel* codes a similar approach has been adopted[142]. It should be noted that this entails the containment is slightly wider by ≈ 0.016 m than that used in the experiment.

The bundle voidage at the overlap site is 35 %, with the surrounding graphite particulate region having a given voidage of either 38 % or 52 %, depending on the build and configuration used. Voidage can be directly related to porosity thus the porosity for the debris region is equated to the given voidage.

Inter-bundle gaps are modelled with a given thickness of 0.026 m. Depending on the build configuration under investigation these gaps could either be blocked off or left open. If blocked, resistance has to be specified at these axial locations. In the *CoolFuel* models a resistance of 1×10^5 m^{-4} was given. In *FREEDOM*, the resistance was increased to 1×10^6 m^{-4} in order to stabilise the computed velocity fields.

In the experiment, the containment wall was cooled using a water jacket and in order to model this surface a convective boundary condition with a fixed heat transfer coefficient of 565 $\mathrm{Wm}^{-2}K^{-1}$[142] is used. The environment temperature is then set to the mean of the entry and exit water jacket temperatures.

Within the test section, the stated powers in the experiment, as read from the transducer did not represent the true power output from the cartridge heaters[18]. Calibrated heat sources are used in present simulations and the relation between the sources is shown in Figure D3. A table of the builds and configurations used in the present *Overlapped* validation study are shown below (Table 9.1).

Table 9.1: Table of cases considered for the *Overlapped* comparison

Build	Case name	Pressure (bar)	Power per bundle (kW)	Blockage location
Build 1	OLB1C1	40	10	C G
	OLB1C2	5	4.3	B G
Build 2	OLB2C3	40	10	C G H
	OLB2C3-5	5	4.3	
Build 3	OLB3C4	40	10	D E
	OLB3C4-5	5	4.3	

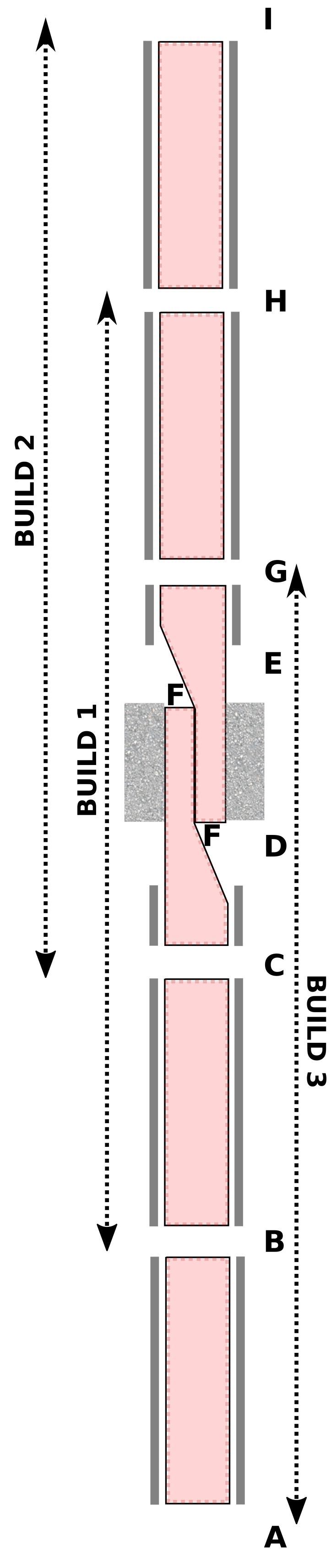

Figure 9.2: Builds and configurations in the *Overlapped* bundle experiment

9.1.2 Description of *ZigZag* and *WheatSheaf* setup

Description of the experimental rig

A *WheatSheaf* bundle has been described earlier (see Chapter 7). In the experiment, the voidage at the location of narrowest constriction (minimum voidage) was 53 %, while at the undamaged ends the voidage was ≈ 73 %. The length of the fuel bundle was 0.937 m, with a standard pin diameter, specified as 0.0153 m in the model. A peak inclination angle to the vertical of ≈ 2.6 ° is calculated.

The pin bundle was housed in an insulated cylindrical rig, which had an interior diameter equivalent to that of an undamaged graphite sleeve (0.1923 m). Air was the working fluid with a given inlet mass flow rate of 1.1 kg/s. Temperature at the inlet was 61.1 °C and the given power of the bundle was 29.4 kW [137].

The *ZigZag* bundle was housed in the same cylindrical test rig. At either-end of the bundle, the pin bundle was undamaged, but within the interior there was a location of minimum voidage at the midway point. Unlike the *WheatSheaf* bundle at this location, the pins were radially displaced outwards by 0.034 m and the minimum voidage was 36 %[137]. The radial displacement gives a bundle angle of ≈ 4.16 ° to the vertical axis. Airflow into the test section was 1.1 kg/s, with an inlet temperature of 60.4 °C. Power into the test section was fixed at 30.0 kW.

Sketches of both the *WheatSheaf* and *ZigZag* geometries are given in Figure 9.3 and Table 9.2 shows the case setups.

Table 9.2: Table of the cases considered in forced convection comparison

Damage	Power (kW) per bundle	Inlet temp °C	Mass flow (kg/s)
WheatSheaf	29.4	61.1	1.1
ZigZag	30.0	60.4	

Model setup in ***FREEDOM***

Following the arguments from the *CoolFuel* validation[137] and also noting forced convection significantly dominates heat transfer, radiation was not taken into account. The interior sleeve wall is considered adiabatic in both cases. At the inlet, a mass flow boundary condition is prescribed.

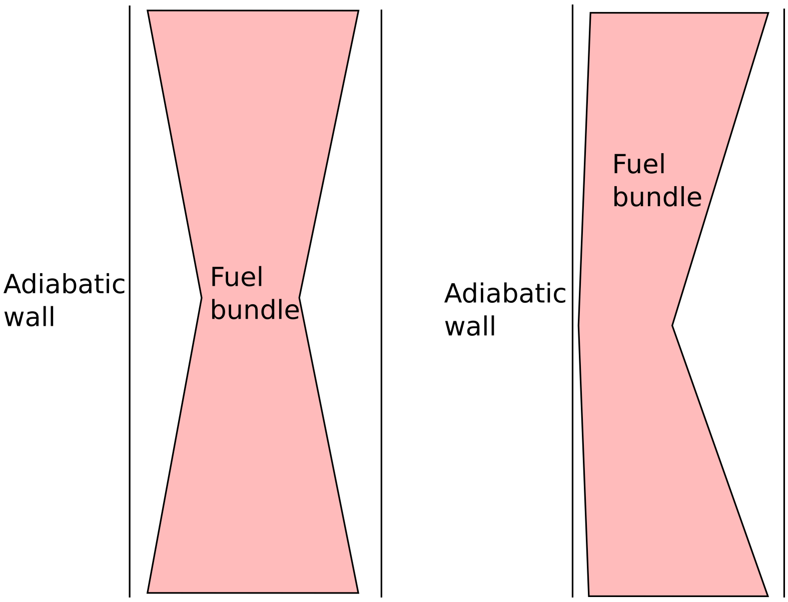

(a) Sketch of WheatSheaf bundle (b) Sketch of ZigZag bundle

Figure 9.3: Illustration of the *WheatSheaf* and *ZigZag* bundles

9.1.3 Description of *C_buckled* model setup

A further natural convection comparison case has been made for a severely distorted *C_buckled* bundle. The comparison case is taken from the pin-bore-flow study by Thomas and Hughes[16] and considers a fuel drop in the carousel region of the IFDF. It should be noted this case is a code-to-code comparison as no experimental data is available for this geometry thus temperature predictions from *CoolFuel* 3-D are therefore compared against.

The modelled domain consists of four *C_buckled* bundles. Figure 9.4 shows a schematic of a *C_buckled* bundle[16]. Typically, for severely distorted bundles the graphite sleeve is assumed to be present and fractured but as can be seen in this safety case, the graphite debris region is not modelled. This modelling choice is based on the likelihood that for large diameter facilities, the graphite fragments tend to fall away. Due to the manner in which the geometry is generated in *CoolFuel* 3-D, the sleeve could not be suppressed for the horizontal section. To try and negate the influence of this issue, the sleeve was modelled as "a small and very thin section". In *FREEDOM*, this short thin sleeve around the horizontal section is not modelled as it is judged to have negligible influence on the temperature predictions.

Within the IFDF, the fuel pellets could be exposed to oxygen if the bundles are severely damaged. As a result, the pellets would oxidise and the ensuing reaction is exothermic in nature. The additional heat generation from this process needs to be taken into account. In this analysis, fuel oxidation is taken into account by a fixed input thermal source, which is added to the assumed decay heat. Table 9.3 below outlines the setup parameters used in the study.

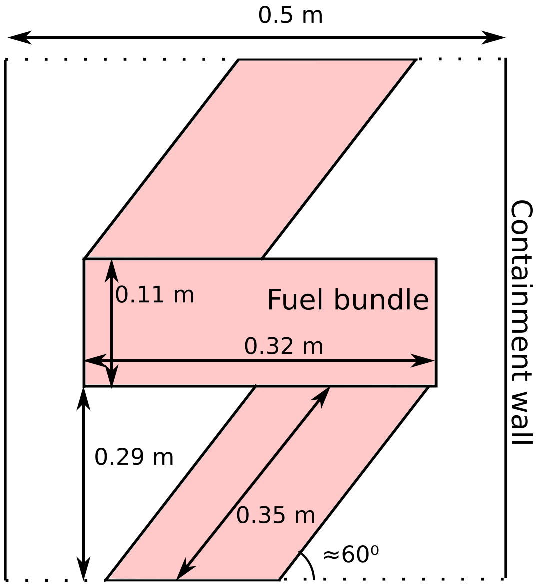

Figure 9.4: Sketch of a *C_buckled* bundle. In this illustration the graphite debris region is assumed to have dropped off. The small and thin sleeve section modelled at the horizontal bundle in the reference report[16] has not been reproduced in the *FREEDOM* model.

Table 9.3: Model parameters for *C_buckled* case

Specification	Value	units
Q_{total}(for four bundles)	5.2	kW
T_{sink}	100.0	°C
Pressure	1	bar

9.2 *WheatSheaf* geometry forced convection study

In this section, the results for the validation and sensitivity runs are presented for the forced convection study based on the *WheatSheaf* geometry. Multiple sensitivity runs have also been conducted to investigate the influence of various parameters and are presented along with the main results. Figure D4 in the Appendix gives an example of the type of fluid and solid conduction mesh used for the *WheatSheaf* geometry.

FREEDOM defines the base filtering mesh for the *WheatSheaf* geometry using a similar number of radial and azimuthal mesh divisions as done in the *CoolFuel* validation study. The filtering grid used for the *CoolFuel* code had six azimuthal divisions and ten radial divisions[137]. A difference arises between the two set-ups with regards to the number of axial divisions used. *FREEDOM* uses twenty axial divisions, while *CoolFuel* uses fourteen divisions[137]. For the solid domain, the number of azimuthal divisions used is sixteen per pin, while *CoolFuel* used eight divisions per pin[137]. It is worth noting, the *CoolFuel* filter grid resolutions are stated to give a form of reference to those used in *FREEDOM.* Due to the differences in the solvers, implementation and computation of geometric quantities(i.e. porosity), it should not be expected that the filtering grid used in *CoolFuel* 3-D is directly applicable to that used in *FREEDOM.*

The comparison for the base reference case is shown in Figure 9.5. The results for this bundle are split into three for the respective pin ranks. Looking at the comparison plots, it can be noted that there is relatively good agreement between the codes and experimental data. Figure 9.5(a), shows the comparison for the first pin rank. There is quite good agreement, although *FREEDOM* overpredicts by about 20 °C, at the top of the bundle. In comparison, *CoolFuel* overpredicts by roughly 10 °C. The minimum temperatures are in general overpredicted by both codes, at the worst this was by about 13 °C. Figure 9.5(b), shows the comparisons for the second rank pin temperatures. At the top of the bundle both codes are shown to underpredict the peak bundle temperature, this is by about 20 °C and 10 °C for *CoolFuel* and *FREEDOM* respectively.

Finally, the third rank pins show that both codes underpredict the peak cladding temperature, this is by 8 °C and 15 °C for *CoolFuel* and *FREEDOM* respectively. The temperature profile is relatively well captured in both models.

Both models as stated earlier are in fairly good agreement with the experiment. Overpredictions, especially at the entrance of the bundle could be a result of the braces and entrance effects, which are neglected in both computational models. At the top and bottom of the bundle there are braces used to hold the pin bundle in place. These braces would improve the localised heat transfer leading to the lower pin temperatures.

At the entrance the heat transfer effects would be much greater as the thermal boundary layer is still developing.

Another issue noted is although the simulations (both *FREEDOM* and *CoolFuel* 3-D) bound the experimental results, the local pin rank comparisons are not always adequately captured. This is the result of using such a coarse filtering grid, where the localised details of the flow are not captured, thus in turn localised peaks or minimums may not always be adequately represented by the model.

9.2.1 Mesh sensitivity studies

The filter grid resolution used in the reference computation is similar to that for the *CoolFuel* 3-D run. Since the model (*FREEDOM*) is likely to be dependent on the filtering grid and solid mesh resolution used, sensitivity runs have been carried out to investigate this aspect of the model. Radial, azimuthal and axial filter grid refinements have been carried out. While for the solid domain the fuel pin circumferential divisions have been altered. The conduction mesh for the pins is unstructured thus the resolution can simply be varied by altering the number of circumferential and axial divisions. Axial refinement of the solid and fluid domains can not be done independently, as the axial filter block divisions have to match between the two domains. Therefore the effect of the solid domain axial refinement is taken into account during the alteration of the axial divisions for the filtering grid.

Radial filter grid refinement

In the radial direction, the radial refinement of the filtering grid is reduced from ten to five. Figure D8 shows a comparison of the results obtained from this sensitivity run. Temperature predictions for the first and second rank are fairly consistent with those from the base validation run. It is noted that for the last rank the temperature profiles are not well captured and in turn there is a greater underprediction. This behaviour could be attributed to the coarsening of the grid. As stated earlier, averaging over a larger filter volume entails that the local details of the flow are not well captured. However, looking at the overall bundle, the maximum cladding temperatures predicted are still in good agreement with the experiment.

Azimuthal filter grid refinement

The filtering grid is further refined in the azimuthal direction from the base value of six to twelve divisions. As can be seen from Figure D11 temperature predictions from this sensitivity run are similar to those for the base calculation. This indicates for the *WheatSheaf* geometry the number of azimuthal divisions have limited impact on the computed solution. Perhaps the limited impact is due to the relatively high voidage, ranging from 53 % to 73 % and the axisymmetric nature of the geometry.

Axial filter grid refinement

Two additional runs have been carried out with fourteen and twenty-eight filter divisions in the axial direction. Results from these runs are shown in figures D9 and D10. As can be seen, the influence on the overall peak and minimum is quite small. There is however a marginal translation of the temperature profile near the location of minimum voidage.

Influence of solidmesh refinement

The effect of the solid computation mesh resolution on the overall predicted peak temperature is shown in Table 9.4. It is also worth stating the variation exhibited in this study is influenced by the coupling between the solid and fluid domains, which would help explain in part the lower temperature predictions for the coarser meshes. During coupling, the boundary face of the cladding wall is assigned to the appropriate filter block by using the computed face center. Thus increasing the mesh density would alter the computed cladding wall area in some of the filter blocks. This in turn would affect the computed volumetric source in the filter block (see Equation8.30).

Table 9.4: Influence of the solid mesh density on the predicted peak temperature

Mesh name	Cells (x10^3)	Azim-divisions	Temperature °C
Mesh 1	114	8	233.53
Mesh 2	246	12	241.46
Mesh 3	355	16	243.11
Mesh 4	516	20	243.94

Based on this study, it can be noted Mesh 3, which is built using sixteen circumferential divisions is an appropriate resolution to use. The mesh parameters used for generating the meshes; this being the number of circumferential divisions and growth rate from the wall to interior are fixed throughout the validation study.

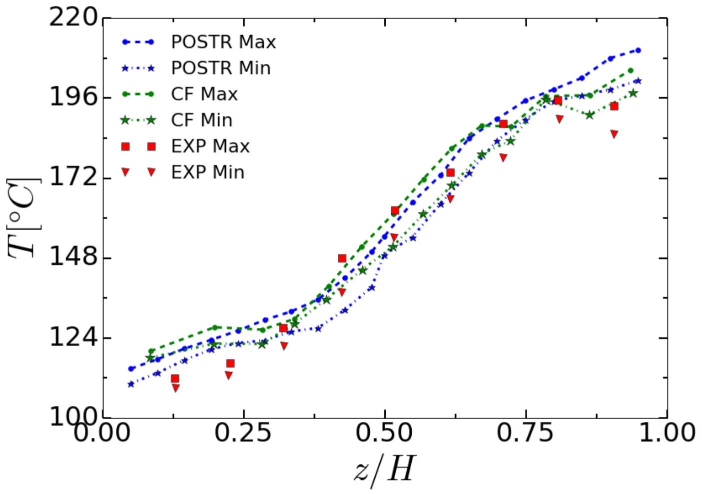

(a) Pin-rank 1

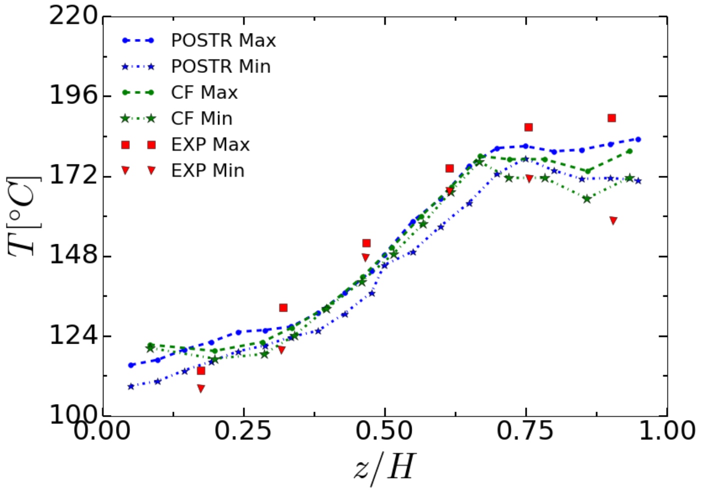

(b) Pin-rank 2

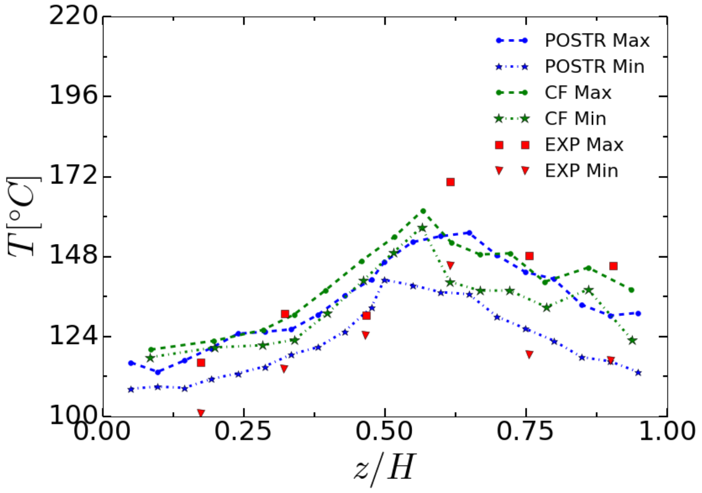

(c) Pin-rank 3

Figure 9.5: Cladding temperature comparisons for a single *WheatSheaf* bundle for forced flow

Influence of fluid calculation mesh refinement

FREEDOM in the fluid domain uses a two level mesh approach. At the filtering level the mesh is used to define the model parameters, while the calculation mesh resolution is used in the computation of the solution (i.e. discretised Navier-stokes equations are solved at this resolution). In this subsection the influence of the computation mesh is assessed. The quantities of ultimate interest, in re-fuelling and cooling analysis are the predicted solid temperatures thus mesh influence is assessed by again looking at the variation of the predicted peak solid temperature. Table 9.5 below outlines results obtained from this study.

Table 9.5: Influence of the fluid calculation mesh on the predicted peak temperatures

Mesh name	Cells	Temperature °C
Mesh 1	10030	245.42
Mesh 2	23040	243.11
Mesh 3	34560	243.27

The mesh dependence study based on the predicted peak temperatures shows that the resolution used for Mesh 2 is appropriate. Parameters used to build Mesh 2 in relation to the filtering grid used are kept consistent throughout this validation study. Although a fluid mesh dependence is carried out, it is worth noting for such porous models the modelling error (associated with the filter grid) greatly outweighs that of discretization (associated with the calculation mesh). Thus the focus from henceforth is predominantly on the filter mesh.

9.3 *ZigZag* geometry forced convection study

A forced convection validation comparison is performed against the experimental and *CoolFuel* results for *ZigZag* bundle. The sensitivity of the predicted solutions to the filtergrid results are also investigated. In the Appendix, Figure D5 gives an example of the type of fluid and solid conduction mesh used for this type of geometry.

The filtering mesh used by *CoolFuel* 3-D for the *ZigZag* geometry has twelve azimuthal, ten radial and sixteen axial divisions. *FREEDOM* uses the same number of azimuthal divisions but in contrast, the radial and axial divisions are altered to five and twenty, respectively. In the solid domain, the number of circumferential pin divisions is maintained at sixteen.

Figure 9.6 shows a plot of the overall maximum and minimum cladding temperatures for the bundle. The comparisons between the two codes and the experiment are in good agreement, with the results from *FREEDOM* and *CoolFuel* 3-D bounding the experimental data. At the top and bottom of the bundle, the two codes show an overprediction of the temperature, by about 10 °C.

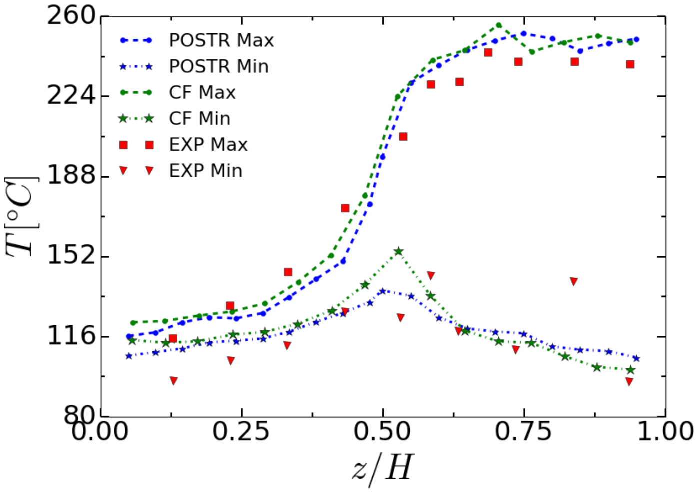

Figure 9.6: Maximum and minimum temperature comparisons for a ZigZag bundle

Sensitivity studies to the filter grid arrangement were also carried out. An increase of the radial divisions to ten was shown to increase the predicted temperatures (See Figure D12). While a coarsening of the azimuthal filter divisions lead to temperature underpredictions (Figure D13). Here, compared to the *WheatSheaf* geometry, the alteration of the azimuthal divisions affected the predictions.

9.4 *Overlapped* geometry natural circulation study

FREEDOM is validated for natural recirculation conditions by comparing against the experimental and *CoolFuel* 3-D data available for an *Overlapped* bundle. Figure D6 illustrates the types of meshes used in this study. Taking into account natural circulation requires an additional set of correlations to be solved. These introduce sensitivity parameters some of which have large factors of uncertainty[140]. Furthermore, the graphite particulate region introduces an additional level of uncertainty.

9.4.1 Validation results & discussion

The filtering grid used in the *CoolFuel* validation study had, six azimuthal, six radial and twenty-six axial divisions. In *FREEDOM*, there are twelve azimuthal and ten radial divisions. In the axial direction, there are ten divisions for the undamaged bundles and fifteen per pin segment for the overlapped bundle giving a total of sixty per bundle. *FREEDOM* utilises more radial divisions as a result of differences in the modelling approach between the two models. In *FREEDOM*, the graphite sleeve boundaries are explicitly represented and to improve the modelled near-wall flow, an additional radial division has been added. Although largely dependent on the conditions modelled, there might be for example downward flow along the sleeve boundaries and upward flow through the pins. Having an additional filter to capture the effects of such boundaries and separate them from those of the pins is beneficial. The graphite debris region also requires a further radial division to couple the interior debris surface to the hot gas region. Finally, at the overlapped section the short intact graphite sleeves are pushed out in comparison to those for the undamaged bundle to ensure a conformal mesh, a radial division governed by the radial displacement between the undamaged sleeve and damaged sleeve is added. The azimuthal divisions, were increased as the geometry (overlap site) is non-axisymmetric and there is relatively low voidage. Results and sensitivities presented for the *ZigZag* bundle, which has similar characteristics supports using this level of filter grid resolution.

Detailed in the Appendix section D.2 are multiple runs conducted to investigate the influence of the sensitivity parameters. Based on this study, the following settings have been adopted for the buoyancy validation runs:

- The pin axial heat transfer is multiplied by a factor of 0.7. This multiplier attempts to take into account heat transfer impairment due to the influence of buoyancy on the fuel bundle. Romero [140], argues that the heat transfer impairment to the fuel bundle is likely to be localised and recommends applying the impairment within the following flow range $10^{-7} < \mathrm{Gr}/\mathrm{Re}^3 < 10^{-5}$. It is further stated that the minimum deterioration is 40% of the Nusselt value predicted by the forced convection correlation. *FREEDOM*, adheres to the aforementioned recommendations. The implementation of the heat transfer impairment in the code is then; $\max(0.4 \cdot \mathrm{Nu}_F, \mathrm{Nu} \cdot 0.7)$.

- At the interior debris surface, the heat transfer coefficient is multiplied by a factor 0.6, while the debris pore heat transfer coefficient is multiplied by a factor of 0.1. These multipliers reflect the level of uncertainty, with regards to the correlations used. There is an additional level of uncertainty, for the debris pore heat transfer, associated with the computed area.

To improve temperature predictions, the *CoolFuel* models used the following bulleted sensitivity parameters;

- A factor of two was applied to the pin convective heat transfer.
- A factor of two was applied to all surface friction factors.

Build - 1

The first build configuration (OLB1), places the *Overlapped* bundle in the middle of the modelled domain. Figures 9.7 and 9.8 show results for this build configuration at 40 bar and 5 bar, respectively. At 40 bar, there is in general quite good agreement with both the experimental data and *CoolFuel* 3-D prediction. At the overlap site it is noted, both *FREEDOM* and *CoolFuel* overpredict the peak fuel temperature by about 50°C. Looking at the graphite debris temperature, *CoolFuel* 3-D overpredicts the experiment results at all probe locations. *FREEDOM* in contrast, slightly underpredicts at the top of the debris region by about 7 °C. Please note, the graphite temperatures of interest are denoted by *POSTR PLANE* and are taken at the location the thermocouples were located.

The axial temperature increase in the overlapped test section is appreciable as can be seen. This is due to the flow being diverted away from the overlapped fuel pins. At this site, the codes predict higher peak temperatures than the experiment. It is worth mentioning due to the limited number instrumented fuel pins there might have been difficulties capturing true experimental maximum. Temperature profiles taken at the graphite debris region, show *FREEDOM* predicts a temperature decrease at the top. This is in contrast to the *CoolFuel* 3-D prediction and that from the experiment. A possible explanation could be the geometric modelling of this site. In *CoolFuel* 3-D, the graphite debris has a shorter length in comparison to the fuel pin length at the overlap site. While *FREEDOM*, models the graphite debris and fuel debris as equal

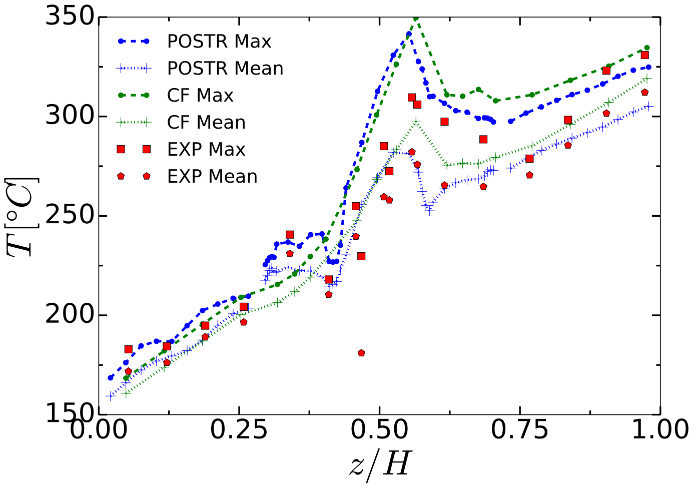

(a) Fuel temperatures

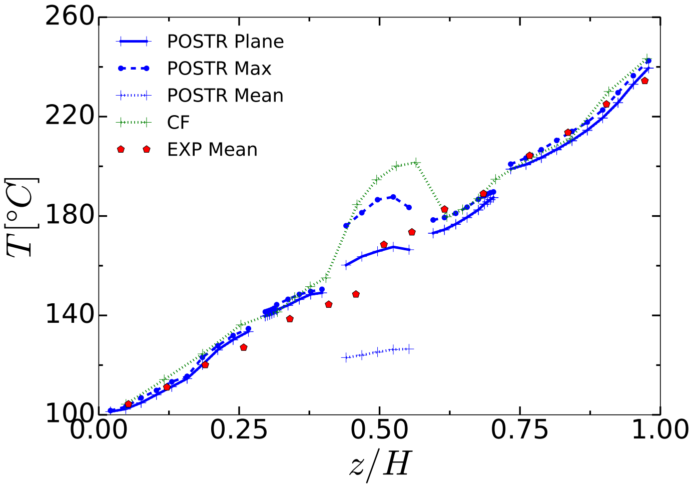

(b) Graphite temperatures

Figure 9.7: Fuel and graphite temperatures for build configuration OLB1C1 at 40 bar

in length, this modelling decision was based on a dimensioned experiment diagram for the overlapped test section, see Figure D2. At the top of the overlapped site pins, *FREEDOM* predicts cold gas from the containment wall is drawn inwards (towards the fuel pins) as the geometry transitions from an overlapped state to its undamaged form. This cold gas being drawn in cools the top of the graphite. Modelling the graphite debris with a shorter length relative to that of the pins would likely mean the effect of this inward flow on the graphite debris is reduced, thereby potentially avoiding the temperature drop at the top of the graphite debris as predicted by *FREEDOM*. Furthermore, in the experimental report it is shown at the major axis the fuel pins cuts into the graphite debris. This feature has not been modelled in *FREEDOM* nor

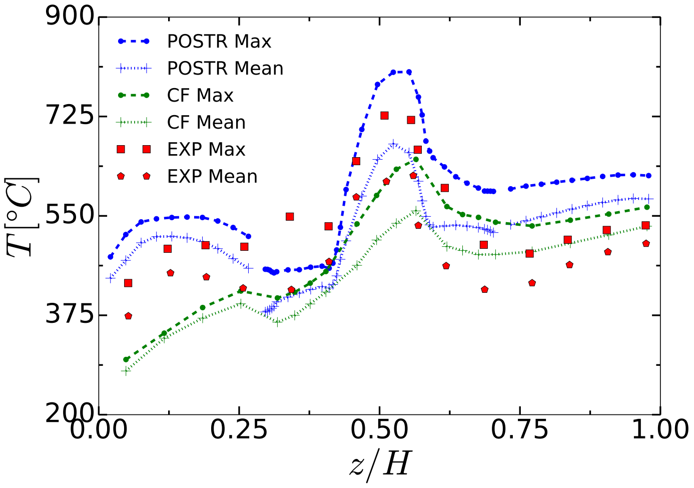

(a) Fuel temperatures

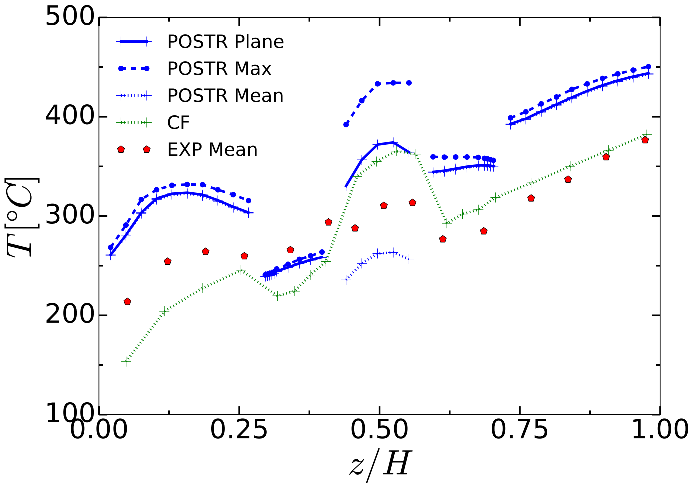

(b) Graphite temperatures

Figure 9.8: Fuel and graphite temperatures for build configuration OLB1C2 at 5 bar

CoolFuel 3-D and would likely mean enhanced heat transfer as a result of conduction. The graphite sleeve thermocouples were inserted to a depth of approximately 10 mm. The exact sitting of the thermocouples would be useful, as based on the variation of the maximum and mean graphite debris temperatures, the plane upon which the results are taken is of importance. The plane measurement is denoted by *POSTR PLANE* and is taken at a depth of 10 mm (as approximated from the experiments).

At 5 bar, the temperature profiles are again in relatively good agreement with the experiment. With regards to the values, *FREEDOM* predicts higher fuel and sleeve temperatures. Looking at the distributions more closely for bundle 1, *CoolFuel* 3-D underpredicts the fuel temperatures by a peak value slightly over 100°C. while for the sleeve this can be by as much as 50 °C. Contrastingly, as mentioned earlier *FREEDOM* in general overpredicts, this is by approximately 80°C at the worst for the fuel and by about 60 °C for the sleeve. At the *Overlapped* bundle, *FREEDOM* agrees quite well with the experiment but it can be noted that the fuel temperatures are underpredicted at the start of the bundle. *CoolFuel* 3-D again underpredicts the fuel temperatures for this bundle, with a maximum underprediction of roughly 80 °C. The graphite sleeve temperatures at bundle 2 are underpredicted at the entrance but at the exit, the sleeve temperature prediction is more in line with the experiment, the same can be said for *CoolFuel* 3-D. At the top bundle, *CoolFuel* 3-D temperatures much closer to the experimental data for both fuel and graphite temperatures, while *FREEDOM* overpredicts for both components.

One potential reason for the observed differences at 5 bar between the two codes is the fuel pin and containment emissivity. As stated earlier, *FREEDOM* uses an emissivity value of 0.4 as this more appropriate for bare fuel pins. Sensitivity studies have shown at high pressures the effect of this choice on the fuel pin temperature is not significant but at low pressures where the effect of radiation is stronger, this leads to an appreciable temperature increase. The containment and fuel surface emissivity values used in the *CoolFuel* 3-D calculations were not directly stated in the validation report[142]. In *FREEDOM*, the containment emissivity was fixed at 0.3, from EDF data this value is usually deemed appropriate (although bounding) for ex-reactor carbon steel facilities[152]. *FOXDROP* for such facilities uses a fixed value of 0.4[153]. Another potential reason could differences in the application of sensitivity parameters between the two codes.

Energy removal paths calculated using *Syrthes* for the two cases are presented in Table 9.6 and 9.7 for the 40 bar and 5 bar runs respectively. As evident, at high pressure natural convection is a significant mode of heat transfer. This shows the circulating flow is quite effective, especially in the relatively tall modelled domain where the stack effect through the fuel bundle would be appreciable. At low pressure, as to be expected, convection becomes less dominant this is evidenced by the higher percentage of power being radiated away. Interestingly, the low pressure result shows convection is weak at the lowest bundle. This is likely due to the fact for configuration OLB1C2, the flow path from the annuli to the fuel is blocked below bundle 1 (see Figure 9.2) thus the cold gas does not enter the fuelled domain at the bottom of bundle 1 meaning the large scale circulating flow bypasses this bundle.

Table 9.6: Fuel surface energy removal path in run OLB1C1. Please note the pin surfaces are numbered from bottom to top

	%	
Surface-name	Convection	Radiation
Bundle 1	97.0	3.0
Bundle 2 (OL)	96.3	3.7
Bundle 3	93.9	6.1

Table 9.7: Fuel surface energy removal path in run OLB1C2. Please note the pin surfaces are numbered from bottom to top

	%	
Surface-name	Convection	Radiation
Bundle 1	53.5	46.5
Bundle 2 (OL)	63.8	36.2
Bundle 3	51.5	48.5

Build - 2

Temperature predictions for Build - 2 are shown in Figures 9.9 and 9.10 at 40 bar and 5 bar, respectively. In this configuration, the *Overlapped* bundle is now located at the bottom of the modelled domain. Results at 40 bar, show there is reasonably good agreement with the experiment and *CoolFuel* prediction. Similar to the predictions for build - 1, temperatures at the overlap site are overpredicted in both models. At the graphite debris region *FREEDOM* underpredicts in comparison to both the experimental and *CoolFuel* prediction. It is noted the graphite debris temperature underprediction is by about 18 °C. Reasons noted earlier for graphite debris temperatures for build 1 can be extended again to this build configuration. It is also worth highlighting the effect of emissivity on the graphite debris temperatures as shown in the sensitivity study.

As the graphite debris region predominantly receives heat by radiation, using a pin emissivity of 0.4 means the graphite temperatures are lower. This would be true at either low or high pressure.

Fuel temperatures at 5 bar show *CoolFuel* 3-D underpredicted the fuel peak temperature at the overlap site by about 142 °C, in contrast the prediction by *FREEDOM* is more in line with the experiment. At bundles 2 and 3, both codes overpredict the fuel temperatures. Graphite debris temperatures are underpredicted at the top of the graphite debris by *FREEDOM*, while for the *CoolFuel* model they are overpredicted.

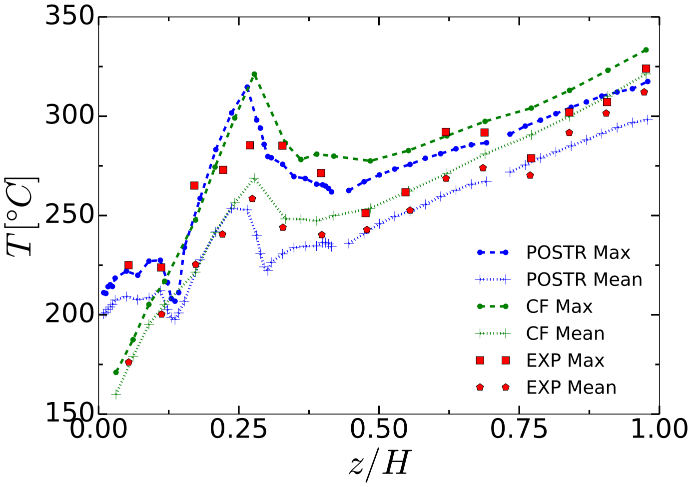

(a) Fuel temperatures

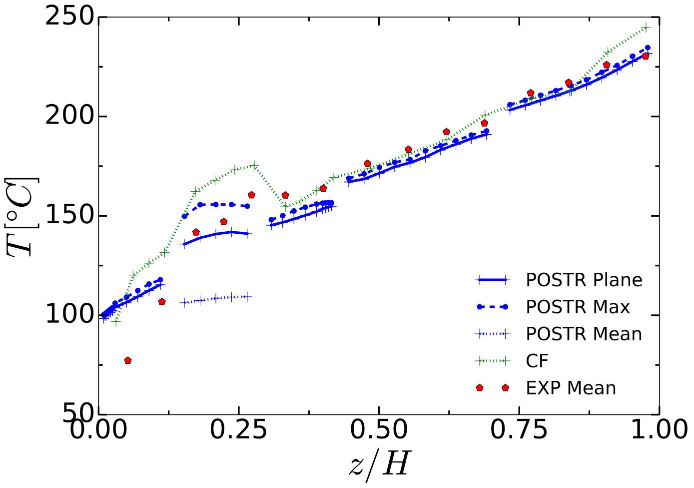

(b) Graphite temperatures

Figure 9.9: Fuel and graphite temperatures for build configuration OLB2C3 at 40 bar

The influence of convection or radiation as a means of heat removal for this configuration is shown in Tables 9.8 and 9.9 at 40 bar and 5 bar respectively. Similar to the

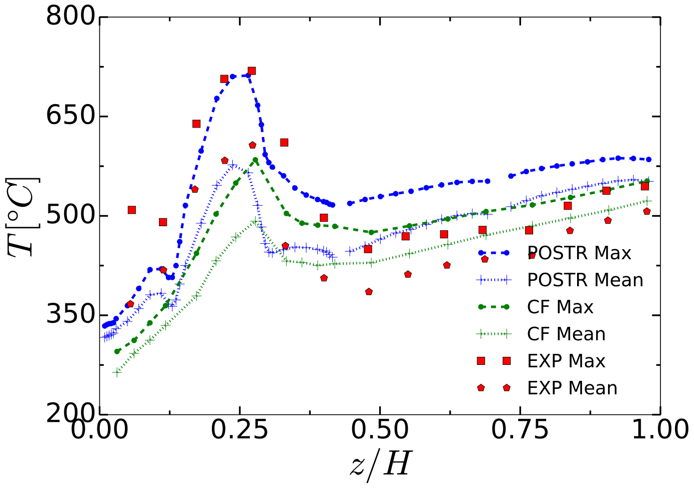

(a) Fuel temperatures

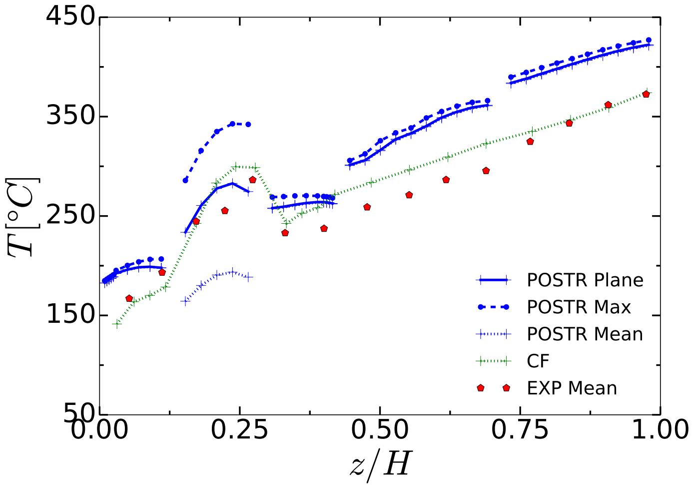

(b) Graphite temperatures

Figure 9.10: Fuel and graphite temperatures for build configuration OLB2C3 at 5 bar

results for build 1, natural convection is almost entirely responsible for heat removal at 40 bar. At this pressure radiation peaks at 5.6% at bundle 3, which is at the top of the domain. At low pressure the role of radiation is again demonstrated to be significant and peaks at 44%.

Table 9.8: Fuel surface energy removal path in run OLB2C3-40bar. Please note the pin surfaces are numbered from bottom to top

	%	
Surface-name	Convection	Radiation
Bundle 1 (OL)	96.8	3.2
Bundle 2	95.3	4.7
Bundle 3	94.4	5.6

Table 9.9: Fuel surface energy removal path in run OLB2C3-5bar. Please note the pin surfaces are numbered from bottom to top

	%	
Surface-name	Convection	Radiation
Bundle 1 (OL)	75.0	25.0
Bundle 2	64.0	36.0
Bundle 3	56.0	44.0

Build - 3

In Build - 3, the overlapped bundle is now located at the top of the modelled domain. Temperature predictions at 40 bar are shown in Figure 9.11 and those at 5 bar are shown in Figure 9.12. The voidage for the graphite debris region is now altered to 38 %, in comparison for the previous builds the voidage was maintained at 52 %. At 40 bar, the fuel and graphite temperatures are appreciably overpredicted by both codes, with *FREEDOM* overpredicting to a larger extent. Looking at the last data point *FREEDOM* overpredicts by about 68 °C. At bundles 1 and 2, the temperature predictions for both codes are representative.

Fuel temperatures at 5 bar are markedly overpredicted by *FREEDOM* at the overlap site by about 140 °C in contrast, *CoolFuel* 3-D agrees quite well with the experimental data. Similarly, there is an appreciable overprediction of the graphite temperatures by both codes. Fuel and graphite sleeve temperatures are again more representative at the lower bundles(1 & 2).

The high pressure result for build 3 shows a marked overprediction for both codes for

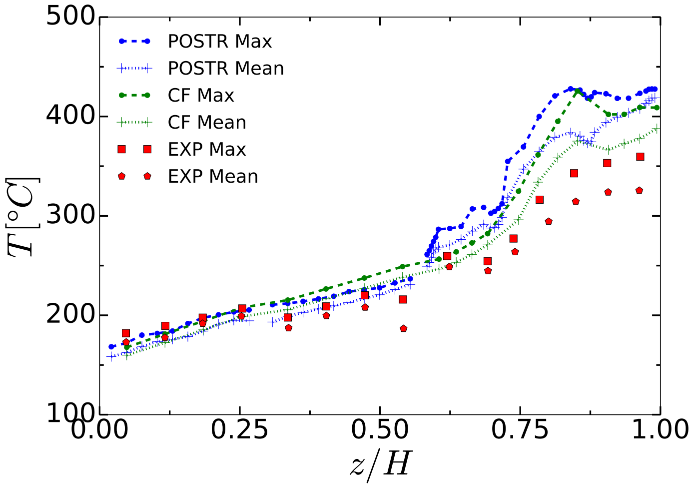

(a) Fuel temperatures

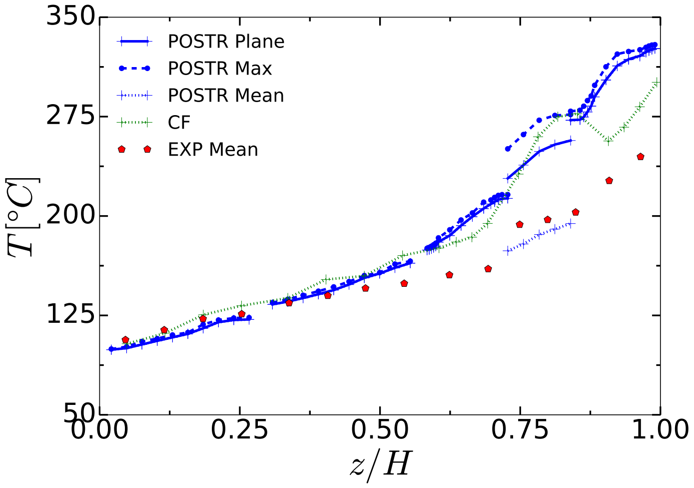

(b) Graphite temperatures

Figure 9.11: Fuel and graphite temperatures for build configuration OLB3C4 at 40 bar

the *Overlapped* bundle. This is likely due to the correlations overpredicting resistance or underpredicting the heat transfer coefficient. At the lower pressure case, this is then exacerbated by the tendency of *FREEDOM* to overpredict graphite and fuel temperatures. As pointed out earlier, this increased overprediction at low pressures could be a result of the emissivity values, which are firstly not a function of temperature and secondly, can be considered the bounding values.

Tables 9.10 and 9.11, show the heat removal paths for the pin surfaces at 40 bar and 5 bar respectively. It is noted, the influence of convection in all the cases investigated is weakest in this build for both high and low pressure runs. This is likely due to the top bundle being the *Overlapped* bundle combined with the reduced graphite porosity

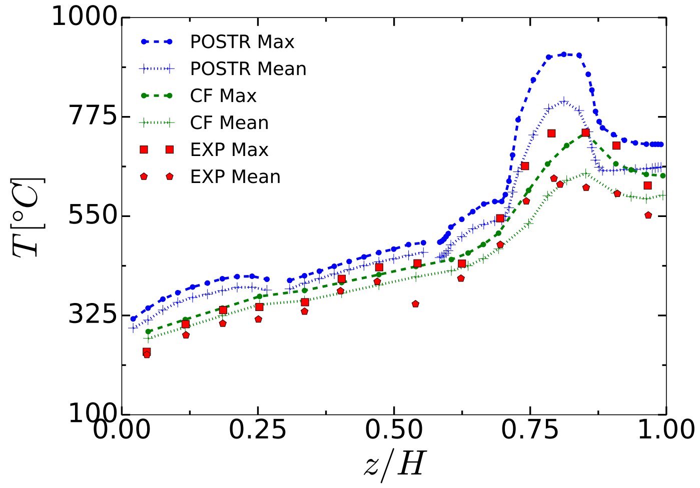

(a) Fuel temperatures

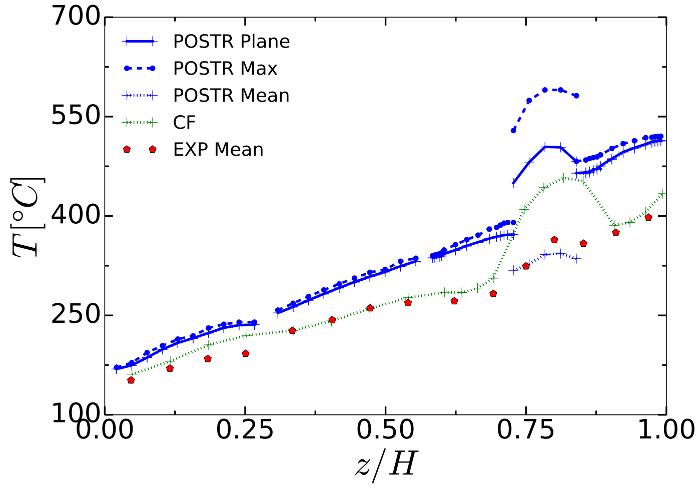

(b) Graphite temperatures

Figure 9.12: Fuel and graphite temperatures for build configuration OLB3C4 at 5 bar

for this case.

Table 9.10: Fuel surface energy removal path in run OLB3C4-40bar. Please note the pin surfaces are numbered from bottom to top

	%	
Surface-name	Convection	Radiation
Bundle 1	97.1	2.9
Bundle 2	96.5	3.5
Bundle 3 (OL)	93.1	6.9

Table 9.11: Fuel surface energy removal path in run OLB3C4-5bar. Please note the pin surfaces are numbered from bottom to top

	%	
Surface-name	Convection	Radiation
Bundle 1	77.7	23.3
Bundle 2	70.8	29.2
Bundle 3 (OL)	46.5	53.5

9.4.2 Mesh sensitivity study

A mesh sensitivity study is again carried out to ascertain the influence of refining the filtering grid on the temperature predictions. This study is limited to axial and azimuthal refinements. In the radial direction, the divisions as stated earlier are constrained by the various features to be modelled. Azimuthal divisions of six and eight were considered. Results in Figure D14 showed that azimuthal refinement had a significant impact on the temperatures at the overlapped site and marginal at the other sites. Axial refinement, was shown to also significantly impact the temperature predictions at the overlapped site. Figure D15 shows that with five axial divisions per pin segment the temperature peaks were much reduced.

9.5 *C_buckled* geometry natural circulation study

A supplementary validation study has been carried out for a severely distorted *C_buckled* bundle. Illustrations of the *C_buckled* solid conduction and the fluid domain mesh used for this geometry type is given in Figure D7 in the Appendix. The modelled domain comprised of four such distorted bundles with the graphite debris suppressed. There is no experimental data available for such distorted geometries thus comparisons can only be made against result from *CoolFuel* 3-D. *FREEDOM* predicted a peak cladding temperature of 537 °C. In contrast, *CoolFuel* 3-D predicted a peak temperature of 436.6 °C, but in the report[16] it is further noted due to a power imbalance an additional increment of 68 °C was calculated, giving a total peak value of 504 °C. In the *CoolFuel* 3-D model, radiation imbalances were a result of errors in the view factor computation at large angles to the vertical (i.e. almost horizontal bundles). As seen *FREEDOM* predicts a higher peak fuel temperature. This is not surprising as from the previous overlapped validation study it can be seen *FREEDOM* is in general quite pessimistic at such low pressures.

9.6 Conclusion

The validation of the thermo-fluids model *FREEDOM* against experimental data and code-to-code comparison with *CoolFuel* 3-D are detailed in this chapter. Validation and sensitivity analysis performed in this chapter aim to demonstrate the suitability of the model for use in nuclear safety applications, where reasonably pessimistic predictions are more readily accepted. The aim is for the model to function as a support tool in scenarios where the current methods (1-D models) in use at EDF Energy prove to be too pessimistic. It should be noted that the results produced in this chapter are based on an independently verified version of *FREEDOM*.

The first validation exercise performed is for forced convection conditions by utilising two idealised damage configurations, which are the *WheatSheaf* and *ZigZag* geometries. The results showed relatively good agreement between *FREEDOM*'s predictions and those from the experiments and *CoolFuel* 3-D.

Validation exercises for natural recirculation conditions are based on the *Overlapped* and *C_buckled* geometry. Temperature predictions for the *Overlapped* geometry showed fairly good comparisons for builds 1 and 2 at 40 bar, but for build 3 it was noted *Overlapped* bundle temperatures were overpredicted to a larger extent. At the low pressure runs (5 bar), *Overlapped* bundle temperatures are fairly well predicted for builds 1 and 2, but for the remaining bundles, they are overpredicted. Similar to the high pressure case, *Overlapped* temperatures are overpredicted to a larger extent for build 3. One potential reason for *FREEDOM*'s tendency to overpredict at low pressures is the use of constant and likely bounding emissivity values. In addition, taking into account buoyancy effects introduces uncertainties up to a factor of 3 due to the correlations.

A code-to-code comparison was performed for the *C_buckled* geometry. Peak fuel temperature comparison between *FREEDOM* and *CoolFuel* 3-D was relatively good, with a discrepancy of 33 °C.

Sensitivity parameters have been defined for the buoyancy influenced correlations. The values used are given in Table D.4. Under forced flow conditions, no sensitivity parameters have been defined.

The overall validation results are deemed acceptable on the basis that in areas where issues arise, predominantly the low pressure runs the model would tend to be pessimistic. Validation studies presented in this chapter are for steady state cases. Transient validation runs have also been performed and can be found in Chapter 10.

Chapter 10

Safety case application using the *FREEDOM* model[i]

The detailed results, specifications, and discussion for the safety case herein have been redacted in this version of the thesis due to export/publication controls. The interested reader is directed to contact the university library for an unredacted version. Below, a short overview is provided.

Recently, thicker than expected carbon deposition levels have been observed on the fuel cladding at the AGR station *Heysham*. In an accident scenario, the carbon deposits could oxidise leading to significant heat generation. Due to this concern, safety cases in the IFDF an air-filled facility, have to be reviewed as historically only low carbon deposition levels have been considered[19].

Initially, the *FOXDROP* model was used to rerun the safety case with higher deposit masses. However, due to the 1-D nature and inherent simplifications in *FOXDROP*, pessimistic fuel and graphite temperatures were predicted. Six cases were considered, and of these at the realistic worst-case deposition level (400 g per bundle), only one had acceptable graphite temperature predictions. At the highest localised deposition level (630 g per bundle), all the cases had unacceptable graphite temperature predictions. Further runs at 300 g per bundle had to be conducted to limit the peak cladding temperatures thereby reducing the graphite temperatures. This alteration led to three of the investigated cases being acceptable.

In this chapter, the safety case is re-addressed using *FREEDOM* and is an ideal

---

[i] This chapter is largely based on the safety case report[154] with minor changes.

scenario to demonstrate its potential benefits. The first study is a radiation-only comparison against the 1-D model *FOXDROP*. Overall, a developed *FOXDROP* equivalent geometry using straight fuel rods, with gap spacing specified using the *FOXDROP* damage parameters and altered properties, returned reasonable temperature comparisons. The remaining models, where the *C_buckled* geometry is explicitly modelled suggested modelling the various components as separate for the fuel and physically applying the oxidation sources (as done in *FREEDOM*) is more pessimistic with regards to peak cladding temperatures.

The next study reproduced the natural circulation high carbon deposition cases conducted by *Wood*[155]. At a deposit mass of 400 g it was found all the *C_buckled* cases predicted acceptable temperatures. However, at a deposit mass of 630 g only two of the cases returned acceptable temperatures. Here, the graphite debris temperature was the main limiting factor. Moving to the *WheatSheaf* geometry, the maximum fuel temperatures were below 450 °C for all the considered drop locations with those in the dismantling tube being the lowest. A full stringer drop resulting in C_buckled elements was considered, with acceptable temperatures being predicted at a deposit mass of 630 g for the tie bar hoist unloading tube.

The final study assumed forced flow could be taken into account. Two drop locations were considered for the *C_buckled* bundle. At a mass flow of 0.0035 kg/s and deposit mass of 630 g per element, the drop in the tilt unit bucket returned unacceptable graphite temperatures, while the shielded guide tube had acceptable graphite temperatures. The difference was due to the improved conductance through the containment wall in the latter. For a *WheatSheaf* drop in the tilt unit bucket a mass flow of 0.0035 kg/s was sufficient to keep fuel temperatures acceptable. A supplementary run for an eight-bundle bundle with a mass flow of 0.007 kg/s predicted unacceptable graphite temperatures.

Overall, the high carbonaceous deposit safety case has demonstrated the benefits of having a 3-D model supporting the 1-D models, especially for the scenarios where the safety case limits are not met. The results from *FREEDOM* have returned much lower temperature predictions, meaning most of the runs are within the safety case limits compared to the much more pessimistic results from *FOXDROP*.

Chapter 11

Conclusions and future work

Nuclear safety is of paramount importance. Not only does a safety-first approach ensure the continuous operation of a valuable asset but most importantly it prevents and mitigates the severe radiological consequences of accidents to the workers, general public, and environment. This thesis aims to contribute to safety by studying the cooling of AGR rod bundles at non-design conditions. Following a general introduction and literature review, the thesis is naturally split into two parts. In part-1 (Chapters 4 to 7), flow physics and phenomena for natural circulation in enclosed rod bundles, and forced convection in a damaged *WheatSheaf* rod bundle are investigated in detail using LES and RANS, respectively. This part of the thesis is motivated by a lack of literature on the detailed flow, heat transfer, and turbulence characteristics for rod bundle geometries at these conditions. Part-2 of the thesis (Chapters 8 to 10) discusses the development, validation, and application of the 3-D thermal analysis tool *FREEDOM* aimed at supporting the current 1-D methods in use at EDF Energy for the thermal analysis of the fuel route.

11.1 Part-1: General physics and phenomena in rod bundles

11.1.1 LES of natural convection in a shortened rod bundle

Natural circulation in a shortened rod bundle of height 0.25 m, a Rayleigh number (Ra_H) of 1.9×10^{11} (for the highest heating case) and aspect ratio of 3.5 (based on height and largest distance between rod and containment wall) was investigated. The flow and temperature distributions were akin to the boundary layer flow regime. This regime is characterised by vertical flow only occurring at the thin boundary layers on the rods and containment surface. The fluid away from the solid surfaces is largely stagnant and thermally stratified. The buoyancy - driven boundary layer on the containment wall is laminar until close to the bottom-end. Turbulence structures are observed spreading towards the interior, causing the upward boundary layers on the rods to transition to turbulence at an early stage (close to the bottom). Correlations for the Nusselt number at the rod surfaces show a Rayleigh number dependence similar to that of a turbulent heat transfer rectangular cavity. On the containment wall, the laminar Nusselt number correlation is similar to that for an unconfined vertical plate.

11.1.2 LES of natural convection in a tall bundle

In the case of the 1 m bundle, typical for an AGR rod bundle the flow is characterised by fully turbulent natural circulation. The flow, turbulence, and thermal characteristics of the system are influenced by the vertically developing buoyancy-driven boundary layer on the containment surface and showed distinct flow features in the top, middle and bottom regions.

- The top-region is largely stagnant with flow constrained to the boundary layers and a strongly stratified temperature field. On the containment wall, the flow develops from laminar to turbulence and it is this transition to turbulence that dominates the system. Flow and heat transfer are well represented by a similarity solution for buoyant laminar flow and a Nusselt number correlation for an isolated flat vertical surface, respectively.

- In the middle region, the flow is highly turbulent and can be naturally split into an outer and interior zone, where the former resembles an asymmetrically heated/cooled cavity and the latter is akin to heated upward pipe/channel flow. Turbulent heat transfer on the containment wall is well represented by an unconfined plate correlation.

- The bottom region is dominated by flow impingement and the resulting cross-flow from the outer to the interior zone.

11.1.3 Forced flow in a ***WheatSheaf*** bundle

An idealised *WheatSheaf* bundle, which is constricted in the middle (damaged portion) and undamaged at either-end was numerically investigated using RANS. It was shown the changes in rod spacing diverts flow to the regions of less resistance, resulting in strong crossflow recirculation zones. As a result, the three-dimensional flow shows large swirling flow structures surrounding the fuel rods. The hotspot on the rods at any height corresponds to the leeward side of the crossflow and it was rather surprising to note the peak rod temperature at mid-height was slightly lower than that for intact fuel. The overall peak fuel temperature is still much higher in the *WheatSheaf* bundle compared to the intact geometry and this occurs at the top of the domain.

11.2 Part-2: Development of 3-D thermal analysis tool ***FREEDOM***

A thermo-fluids model termed *FREEDOM* has been developed for the thermal analysis of the fuel route for both intact fuel and damaged fuel after a dropped fuel event. *FREEDOM* uses *POSTR*[26], the intact fuel model, as the starting point for code development and heavily modifies it to take into account dropped fuel scenarios. Changes made in this thesis encompass, the preprocessing, computing, and postprocessing stages. The main modifications in the computing stages include (i) additional correlations for damaged rods and graphite particulate regions, (ii) fuel oxidation computation methods in the event of snapped rods, (iii) carbonaceous deposits oxidation, (iv) an additional volume-to-volume coupling approach and (v) a pseudo-transient method. *FREEDOM* predicts the critical solid component temperatures (graphite debris, fuel cladding, etc) at any arbitrary facility/location within the AGR fuel route. To achieve this, the model is split into a fluid and solid domain, which are then coupled through an exchange of heat transfer coefficients and temperatures. The fluid domain is implemented in the CFD solver *Code_Saturne* and computes the fluid flow using the porous medium approach. Adopting the porous approach entails the solids to be assumed dispersed in lumped volumetric regions and only the macroscopic details of the flow are recovered. Pressure loss as a result of the dispersed solids and the geometric effect are accounted through the distributed resistance computed from correlations and porosity, respectively. Solid conduction and thermal radiation are computed in the solid domain using the FEA software *Syrthes*. Compared to the fluid domain, the solid domain explicitly represents the idealised damage configuration and uses refined meshes. *FREEDOM* also includes modelling of fuel and carbon deposit oxidation by solving a mass transport equation for oxygen concentration or using a simplified but pessimistic approach.

Validation of the ***FREEDOM*** model

Validation exercises have been carried out for a variety of damaged geometries and flow conditions which have demonstrated the suitability of *FREEDOM* for use in nuclear safety tasks. Forced convection experimental and code-to-code comparisons were initially carried out for single bundle *WheatSheaf* and *ZigZag* bundles. The comparisons for both bundles showed good agreement between the experiment, *FREEDOM* and *CoolFuel* 3-D.

Natural convection was validated by comparing against a four-bundle test rig comprising an *Overlapped* bundle and undamaged bundles. Multiple build configurations at differing pressures and heating rates were considered. At high pressure (40 bar), there was good agreement with the experimental data and *CoolFuel* 3-D results for two out of the three geometric configurations. For the other configuration, the temperatures are over-predicted, which is deemed to be acceptable for safety case purpose. Low pressure runs at 5 bar showed *FREEDOM* predicted acceptable temperatures but had a tendency of overpredicting the debris temperatures. Finally, a comparison was made for the bounding idealised geometry termed *C_Buckled*. This comparison was against temperature predictions from *CoolFuel* 3-D. The peak temperatures between the two codes were in good agreement.

Safety case application using ***FREEDOM***

FREEDOM has been used to support the 1-D thermal code *FOXDROP* in the reassessment of safety cases for fuel drops in the Irradiated Fuel Dismantling Facility (IFDF). The need to revisit these safety cases arose as recent inspections have revealed thicker than expected carbon deposits on the fuel claddings. In an air-filled facility like the IFDF this raises the possibility of runaway carbon oxidation.

Radiation only comparisons showed that when the solid components are modelled separately (i.e. where the fuel pellet and cladding are individually modelled) *FREEDOM* has higher cladding temperatures compared to *FOXDROP*. This scenario highlighted a potential optimism in the *FOXDROP* model as carbon oxidation heat is applied to both the pellet and cladding (homogeneous solid) instead of directly to cladding as would be expected in reality.

The second scenario addressed assumes a loss of the extract system thus natural circulation and radiative heat transfer are responsible for cooling the debris. The 2σ decay heat of 7.5 kW is assumed in all the cases considered by *FREEDOM*. To be pessimistic most of the cases considered assumed the fuel drop would result in a *C_buckled* bundle, although supplementary runs for a *WheatSheaf* bundle have also been carried out. For the *C_buckled* bundle, graphite temperature predictions at a deposit mass of 400 g per bundle were within the safety case limits, and for the cladding at the highest deposition mass investigated (630 g per bundle) seemingly acceptable temperatures were predicted. However as *FREEDOM* does not take into account the oxidation heat generation from the graphite debris, in instances where the predicted graphite temperature exceeds 450 °C, these cladding temperatures may be optimistic. In contrast, the deposition mass had to be lowered to 300 g per bundle for *FOXDROP* to predict acceptable temperatures[155].

The third scenario investigated assumes the extract system is still operational and forced flow can be taken into account. Selected cases were run at multiple mass flow rates. Similar to the extract off cases the 2σ decay heat of 7.5 kW is assumed. Single bundle drops resulting in either *WheatSheaf* or *C_buckled* fuel were investigated at various drop locations. Predicted temperatures were acceptable at a mass flow of 0.007 kg/s with unacceptable temperatures predicted at a mass flow of 0.0035 kg/s for the bounding case. At such low forced flow, the predicted clad temperatures may be worse than those predicted under natural convection. A supplementary analysis for a full stringer drop resulting in all eight bundles being severely buckled was investigated for forced flow. Temperature predictions obtained showed unacceptable graphite debris temperature at a lower bound mass flow of 0.007 kg/s.

11.3 Future work

In this section potential avenues for further research into the areas investigated by this thesis are given. In part-1, the detailed features of the flow have been studied using RANS or LES and highly resolved meshes. The simulations conducted have assumed the rod walls are smooth but this is a simplification as in reality the AGR fuel rods are rib roughened. Taking into account the roughness would appreciably alter the behaviour of the system and also make the simulation results more pertinent to AGR nuclear safety cases. However, directly modelling the ribs would complicate the mesh generation process and significantly increase the mesh density thus some form of a simplified representation of the ribs is required.

It would be interesting to investigate natural circulation and forced convection conditions for other idealised damage configurations, in particular, the *C_buckled* bundle. Although, most of the safety cases at EDF Energy assume this damage configuration, there is no experimental data or highly resolved flow simulations available to provide insights into the detailed flow features. Furthermore, it would be useful to compare the detailed model results against those produced by *FREEDOM*. This comparison can be initially carried out for a *WheatSheaf* bundle and forced flow. Later, this can be extended to natural convection scenarios with the more complex idealised damage configurations.

In the natural circulation cases, the top and bottom walls have been assumed to be adiabatic. Other investigators such as Sebilleau[80] have shown that for a rectangular/square cavity if these surfaces are defined as non-adiabatic, instabilities at the top and bottom surface would lead to the ejection of buoyant plumes to the vertical walls disturbing the flow there. This has the overall effect of increasing turbulence levels in the system and turbulence structures were observed on the entirety of the vertical wall. The influence of the top and bottom walls on the flow in the enclosed rod bundle cavity would be worth investigating.

Pertaining to the development and use of *FREEDOM*, the following recommendations are made:

- Currently *FREEDOM* does not use the computed oxygen concentration levels to limit the fuel oxidation source. Instead the source is limited through the BFRM parameter. It would be worthwhile implementing the option switch between using the BFRM parameter and computed oxygen concentration as the current approach is pessimistic.

- If the volume-to-volume coupling is initiated the exchange of temperatures and heat transfer coefficients between the two codes relies on the use of text files. To make the code easier to use (especially on clusters), a cleaner approach would require this coupling to be handled using PLE (*Code_Saturne's* coupling library).
- Implement a method to allow the user to easily specify localised flow blockages. In addition additional features of the fuel bundle like spacers, bracers should also be considered.

Regarding the safety case application study in Chapter 10 the following recommendations are given:

- In all the forced convection cases investigated in Chapter 10, it has been assumed a BFRM value of 1 is applicable. This value has been used even at quite low flow rates of 0.007 kg/s. It is therefore worth considering the effect reducing the BFRM value has on the peak temperatures.
- The faults investigated have mostly focused on dropped fuel scenarios. However, another fault condition, which can arise in the IFDF may result in crushed fuel. An example would be a fault in the rotary shield plug valve causing shearing damage as it rotates and crushes the fuel. These types of damage configurations have not been considered thus far.

List of publications

Journal publications

1. K. Chinembiri, S. He, J. Li, C. Trinca, "Numerical study of heat transfer in a distorted rod bundle", Nuclear Engineering and Design, vol. 349, pages 63 - 77, 2019.
    - Author contribution - K.Chinembiri: model development, simulations, data analysis, original drafting of the paper. S. He: supervision, contribution to methodology and data analysis, reviewing/editing of the paper. J. Li: industrial sponsor and supervisor, contribution to data analysis, reviewing/editing of the paper. C. Trinca: review/editing of the paper.
2. K. Chinembiri, S. He, J. Li, C. Trinca, "Natural circulation in a short enclosed rod bundle", International Journal of Heat and Mass Transfer (submitted)
    - Author contribution - Same as journal - 1 for K.Chinembiri, S. He and J. Li. C. Trinca: preliminary investigation.
3. K. Chinembiri, S. He, J. Li, "Natural circulation in an enclosed rod bundle of large aspect ratio", Applied Thermal Engineering,188, 2021
    - Author contribution - Same as journal - 1 for K.Chinembiri, S. He and J. Li.

Industrial reports

1. K. Chinembiri and S. He, "Modelling and Methodology report; FREEDOM (previously named as *Postr2*)", tech. rep., FREEDOM/SHF/002, University of Sheffield, Sheffield, 2020.

- Author contribution - K.Chinembiri: model development, simulations, data analysis, original drafting of the report. S. He: supervision, contribution to methodology and data analysis, reviewing/editing of the report. Although not listed as an author, J Li made the following contributions: industrial sponsor and supervisor, initiated problem and contribute to methodology, reviewing/editing of the report.
- Verifier: M. Mohd Amin
- Reviewers: C. Sigournay and J Li.

2. K. Chinembiri and S. He, "Validation report for forced and natural convection flow regimes using FREEDOM (previously named as *Postr2*)" tech. rep., FREEDOM/SHF/003, University of Sheffield, Sheffield, 2020.
   - Author contribution - Same as report 1
   - Verifier: J. He
   - Reviewer: J. Li
3. K. Chinembiri and S. He, "FREEDOM Safety case; High carbon deposition thermal analysis for dropped fuel in the IFDF", tech. rep., FREEDOM/SHF/004, University of Sheffield, Sheffield, 2020
   - Author contribution - Same as report 1
   - Verifier: J. He
   - Reviewer: J. Li

Bibliography

[1] W. Dalrymple, “For the longest time,” *Nuclear Engineering International*, p. 1, jun 2013.

[2] E. Nonbel, “Description of the Advanced Gas Cooled Type of Gas Cooled Reactor (AGR),” tech. rep., Riso National Laboratory, Roskilde, 1996.

[3] J. Dawson and M. Phillips, “Gas cooled Nuclear Reactor Designs, Operation and Fuel Cycle,” in *Nuclear Fuel Cycle Science and Engineering* (I. Crossland, ed.), ch. 12, pp. 300–332, Woodhead Publishing, 2012.

[4] A. C. Trupp and R. S. Azad, “The structure of turbulent flow in triangular array rod bundles,” *Journal of Nuclear Engineering and Design*, vol. 32, no. 1, pp. 47–84, 1975.

[5] T. Krauss and L. Meyer, “Experimental investigation of turbulent transport of momentum and energy in a heated rod bundle,” *Journal of Nuclear Engineering and Design*, vol. 180, no. 3, pp. 185–206, 1998.

[6] R. K. MacGregor and A. F. Emery, “Free Convection Through Vertical Plane LayersModerate and High Prandtl Number Fluids,” *Journal of Heat Transfer*, vol. 91, no. 3, pp. 391–401, 1969.

[7] J. W. Elder, “Turbulent free convection in a vertical slot,” *Journal of Fluid Mechanics*, vol. 23, no. 1, pp. 99–111, 1965.

[8] N. Ince and B. Launder, “On the computation of buoyancy-driven turbulent flows in rectangular enclosures,” *International Journal of Heat and Fluid Flow*, vol. 10, pp. 110–117, jun 1989.

[9] A. Dafa'Alla, *Turbulent natural convection in a tall closed cavity.* PhD thesis, University of Manchester, 1988.

[10] K. Cheesewright, K. King, and S. Ziai, "Experimental data for the validation of computer codes for the prediction of two-dimensional buoyant cavity flows," in *ASME Winter Annual Meeting*, (Anaheim), pp. 75–81, ASME, 1986.

[11] S. Whitaker, "Flow in porous media I: A theoretical derivation of Darcy's law," *Transport in Porous Media*, vol. 1, no. 1, pp. 3–25, 1986.

[12] EDF R&D, "Code Saturne 4.0.0 Theory Guide," tech. rep., 2015.

[13] S. Ostrach, "An analysis of laminar free-convection flow and heat transfer about a flat plate parallel to the direction of the generating body force," tech. rep., National Advisory Committee for Aeronautics, Cleveland, 1952.

[14] E. Sparrow and J. Gregg, "Laminar free convection from a vertical plate with uniform surface heat flux," in *ASME 78*, pp. 435 – 440, 1956.

[15] S. Fairbairn and S. Hickmott, "Thermal Analysis of Dropped Fuel Debris in a Reactor Channel using FEAT," tech. rep., E/REP/BDGBA/0046/AGR/05, British Energy, 2005.

[16] D. Thomas and J. Hughes, "Heysham 2 IFD cell 6kW consolidated safety case: Estimates of pin bore flows and fuel oxidation rates under forced and natural convection using CoolFuel 3-D," tech. rep., TEA/REP/0104/94, Nuclear Electric, 1995.

[17] M. T. R. Fung, "COOLFUEL 3-D V2 Modelling Report," tech. rep., GEN/D-FWG/P(92)4738/B/2, National Nuclear Corporation (NNC), 1995.

[18] E. Romero and D. Thomas, "An experiment to study natural convection cooling of dropped stringer debris in an AGR buffer storage tube," tech. rep., GEN/D-FWG/P(91)4720/B/3, Nuclear Electric, 1992.

[19] R. Keatinge, "Heysham 2 Power Station: IFD 6kW consolidated safety case thermal assesments for damaged fuel," tech. rep., TEA/REP/0029/94, Nuclear Electric, 1995.

[20] U.S. Energy Information Administration, "International Energy Outlook 2016," Tech. Rep. May 2016, U.S. Department of Energy, 2016.

[21] International Energy Agency, "Technology Roadmap Nuclear Enetgy," tech. rep., International Energy Agency, 2015.

[22] J. Huenteler, T. S. Schmidt, and N. Kanie, "Japan's post-Fukushima challenge - implications from the German experience on renewable energy policy," *Energy Policy*, vol. 45, pp. 6–11, 2012.

[23] C. Jorant, "The implications of Fukushima," *Bulletin of the Atomic Scientists*, vol. 67, no. 4, pp. 14–17, 2011.

[24] Amyas Morse, "Nuclear power in the UK," Tech. Rep. July, The Department of Energy and Climate Change Nuclear, 2016.

[25] I. Rupp and C. Peniguel, "SYRTHES 4.2 User Manual," 2014.

[26] C. Trinca, *Nuclear Fuel Route Thermal Hydraulics Analysis for Advanced Gas-cooled Reactors (AGRs).* Thesis, University of Sheffield, Sheffield, 2019.

[27] M. Yule, "Hinkely Point B: Refuelling Cooling Safety Case Head Document," tech. rep., EDF Energy, 2014.

[28] J. Leybourn, "AGR Dropped Damage Data Report," tech. rep., EDF Energy, 2016.

[29] K. Mottershead, D. Beardsmore, and G. Money, "Dropped fuel damage prediction techniques and the DROPFU code," in *Proc of the Int. Fuel Management and Handling. Conf.*, (Edinburgh), pp. 227–232, 1995.

[30] R. P. Hornby, "COOLFUEL 1-D VERSION 2 MODELLING REPORT," tech. rep., GEN/DFWG/P(92)4737/B/2, Nuclear Electric, 1995.

[31] S. J. Graham, "Validation Report For Coolfuel 1-D Version 2 Dropped Fuel Thermal Assesment Code," tech. rep., EDF Energy, 1995.

[32] V. R. Skinner, A. R. Freeman, and H. G. Lyall, "Gas mixing in rod clusters," *International Journal of Heat and Mass Transfer*, vol. 12, pp. 265–278, 1968.

[33] B. Kjellstroem, "Studies of turbulent flow parallel to a rod bundle of triangular array," tech. rep., Aktiebolaget Atomenergi, Sweden, 1974.

[34] W. Seale, "Turbulent diffusion of heat between connected flow passages Part 1: Outline of problem and experimental investigation," *Journal of Nuclear Engineering and Design*, vol. 54, pp. 183–195, oct 1979.

[35] V. Vonka, "Measurement of secondary flow vortices in a rod bundle," *Journal of Nuclear Engineering and Design*, vol. 106, pp. 191–207, feb 1988.

[36] P. Carajilescov and N. E. Todreas, "Experimental and analytical study of axial turbulent flows in an interior subchannels of a bare rod bundle," *Journal of Heat Transfer*, vol. 98, no. 2, pp. 262–268, 1976.

[37] K. Rehme, "The structure of turbulence in rod bundles and the implications on natural mixing between the subchannels," *International Journal of Heat and Mass Transfer*, vol. 35, pp. 567–581, feb 1992.

[38] D. Rowe, B. Johnson, and J. Knudsen, "Implications concerning rod bundle crossflow mixing based on measurements of turbulent flow structure," *International Journal of Heat and Mass Transfer*, vol. 17, no. 3, pp. 407–419, 1974.

[39] J. D. Hooper and K. Rehme, "Large-scale structural effects in developed turbulent flow through closely-spaced rod arrays," *Journal of Fluid Mechanics*, vol. 145, no. -1, p. 305, 1984.

[40] D. Chang and S. Tavoularis, "Numerical simulation of turbulent flow in a 37-rod bundle," *Journal of Nuclear Engineering and Design*, vol. 237, pp. 575–590, mar 2007.

[41] Y. Duan and S. He, "Heat transfer of a buoyancy-aided turbulent flow in a trapezoidal annulus," *International Journal of Heat and Mass Transfer*, vol. 114, pp. 211–224, 2017.

[42] Y. Duan and S. He, "Large eddy simulation of a buoyancy-aided flow in a nonuniform channel Buoyancy effects on large flow structures," *Nuclear Engineering and Design*, vol. 312, pp. 191–204, 2017.

[43] M. M. Amin, Y. Duan, and S. He, "Large Eddy Simulation Study on Forced Convection Heat Transfer to Water at Supercritical Pressure in a Trapezoid Annulus," *Journal of Nuclear Engineering and Radiation Science*, vol. 4, no. 1, p. 14, 2017.

[44] B. Ouma and S. Tavoularis, "Flow measurements in rod bundle subchannels with varying rod-wall proximity," *Journal of Nuclear Engineering and Design*, vol. 131, pp. 193–208, nov 1991.

[45] F. Heina, J; Chervenka, J; Mantlik, "Results of local measurements of hydraulic characteristics in deformed pin bundle," Tech. Rep. UJV-4156-T, Rzez, Czech Republic, 1977.

[46] IAEA, "LMFR core and heat exchanger thermohydraulic design: Former USSR and present Russian approaches," no. January, 1999.

[47] R. C. K. Rock and M. F. Lightstone, "A Numerical Investigation of Turbulent Interchange Mixing of Axial Coolant Flow in Rod Bundle Geometries," *Journal of Numerical Heat Transfer, Part A: Applications*, vol. 40, no. 3, pp. 221–237, 2001.

[48] W. Seale, "The Effect of Subchannel Shape on Heat Transfer In Rod Bundels with Axial Flow," *International Journal of Heat and Mass Transfer*, vol. 24, no. 4, pp. 768–770, 1980.

[49] C. W. Rapley and A. D. Gosman, "The prediction of fully developed axial turbulent flow in rod bundles," *Journal of Nuclear Engineering and Design*, vol. 97, no. 3, pp. 313–325, 1986.

[50] B. E. Launder and W. M. Ying, "Prediction of flow and heat transfer in ducts of square cross-section," *ARCHIVE: Proceedings of the Institution of Mechanical Engineers 1847-1982 (vols 1-196)*, vol. 187, no. 1973, pp. 455–461, 1973.

[51] T. Sofu, T. H. Chun, and W. K. In, "Evaluation of Turbulence Models for Flow and Heat Transfer in Fuel Rod Bundle Geometries," 2004.

[52] E. Baglietto and H. Ninokata, “A turbulence model study for simulating flow inside tight lattice rod bundles,” *Journal of Nuclear Engineering and Design*, vol. 235, no. 7, pp. 773–784, 2005.

[53] J. Z. Shih, Tsan-hsing and J. Lumely., “A New Reynolds Equation Model Stress Algebraic,” Tech. Rep. August, NASA, 1994.

[54] D. Chang and S. Tavoularis, “Unsteady Numerical Simulations of Turbulence and Coherent Structures in Axial Flow Near a Narrow Gap,” *Journal of Fluids Engineering*, vol. 127, no. 3, p. 458, 2005.

[55] E. Baglietto, “RANS and URANS simulations for accurate flow predictions inside fuel rod bundles,” in *International Congress on Advances in Nuclear Power Plants*, (Nice), 2007.

[56] B. H. Yan, Y. Q. Yu, H. Y. Gu, Y. H. Yang, and L. Yu, “Simulation of turbulent flow and heat transfer in channels between rod bundles,” *International Journal of Heat and Mass Transfer*, vol. 47, no. 3, pp. 343–349, 2011.

[57] A. Keshmiri, “Numerical sensitivity analysis of 3-and 2-dimensional rib-roughened channels,” *International Journal of Heat and Mass Transfer*, vol. 48, no. 7, pp. 1257–1271, 2012.

[58] A. Keshmiri, M. A. Cotton, Y. Addad, and D. Laurence, “Thermal-Hydraulic Analysis of Flow in Rib- Roughened Passages with application to Gas-cooled Nuclear Reactors,” in *Proceedings of the 6th International Symposium On Turbulence, Heat and Mass Transfer, THMT’09’.*, no. September, p. 12, 2009.

[59] F. Hofmann, “Velocity and temperature distribution in turbulent flow in sodium cooled fuel elements with eccentric geometry,” *Journal of Nuclear Engineering and Design*, vol. 14, no. 1, pp. 43–50, 1970.

[60] A. Ooi, G. Iaccarino, P. A. Durbin, and M. Behnia, “Reynolds averaged simulation of flow and heat transfer in ribbed ducts,” *International Journal of Heat and Fluid Flow*, vol. 23, no. 6, pp. 750–757, 2002.

[61] A. Davari, S. M. Mirvakili, and E. Abedi, "Three-dimensional analysis of flow blockage accident in Tehran MTR research reactor core using CFD," *Progress in Nuclear Energy*, vol. 85, pp. 605–612, 2015.

[62] A. Salama and S. E.-D. El-Morshedy, "CFD simulation of flow blockage through a coolant channel of a typical material testing reactor core," *Annals of Nuclear Energy*, vol. 41, pp. 26–39, 2012.

[63] A. K. Chauhan, B. Prasad, and B. Patnaik, "Thermal hydraulics of rod bundles: The effect of eccentricity," *Journal of Nuclear Engineering and Design*, vol. 263, pp. 218–240, 2013.

[64] T. Tsuji and Y. Nagano, "Characteristics of a turbulent natural convection boundary layer along a vertical flat plate," *International Journal of Heat and Mass Transfer*, vol. 31, pp. 1723–1734, aug 1988.

[65] T. Versteegh and F. Nieuwstadt, "Turbulent budgets of natural convection in an infinite, differentially heated, vertical channel," *International Journal of Heat and Fluid Flow*, vol. 19, no. 2, pp. 135–149, 1998.

[66] S. Paolucci, "Direct numerical simulation of two-dimensional turbulent natural convection in an enclosed cavity," *Journal of Fluid Mechanics*, vol. 215, pp. 229–262, 1990.

[67] K. Nakao, Y. Hattori, and H. Suto, "Numerical investigation of a spatially developing turbulent natural convection boundary layer along a vertical heated plate," *International Journal of Heat and Fluid Flow*, vol. 63, pp. 128–138, feb 2017.

[68] S. S. Goodrich and W. R. Marcum, "Natural convection heat transfer and boundary layer transition for vertical heated cylinders," *Experimental Thermal and Fluid Science*, vol. 105, pp. 367–380, jul 2019.

[69] E. R. G. Eckert and A. Diaguila, "Experimental investigation of free-convection heat transfer in vertical tube at large Grashof numbers," tech. rep., National Advisory Committee for Aeronautics, Washington, 1952.

[70] W. M. Yan and T. F. Lin, "Theoretical and experimental study of natural convection pipe flows at high Rayleigh number," *International Journal of Heat and Mass Transfer*, vol. 34, no. 1, pp. 291–303, 1991.

[71] S. M. Ohk and B. J. Chung, "Natural convection heat transfer inside an open vertical pipe: Influences of length, diameter and Prandtl number," *International Journal of Thermal Sciences*, vol. 115, pp. 54–64, 2017.

[72] T. Inagaki and S. Maruyama, "Turbulent heat transfer of natural convection between two vertical parallel plates," *Heat Transfer - Asian Research*, vol. 31, no. 1, pp. 56–67, 2002.

[73] W. M. Lewandowski, M. Ryms, and H. Denda, "Natural convection in symmetrically heated vertical channels," *International Journal of Thermal Sciences*, vol. 134, pp. 530–540, dec 2018.

[74] J. W. Elder, "Laminar free convection in a vertical slot," *Journal of Fluid Mechanics*, vol. 23, no. 1, pp. 77–98, 1965.

[75] S. Yin, T. Wung, and K. Chen, "Natural convection in an air layer enclosed within rectangular cavities," *International Journal of Heat and Mass Transfer*, vol. 21, pp. 307–315, mar 1978.

[76] P. D. Weidman and G. Mehrdadtehranfar, "Instability of natural convection in a tall vertical annulus," *Physics of Fluids*, vol. 28, no. 3, pp. 776–787, 1985.

[77] P. Betts and I. Bokhari, "Experiments on turbulent natural convection in an enclosed tall cavity," *International Journal of Heat and Fluid Flow*, vol. 21, pp. 675–683, dec 2000.

[78] A. A. Dafa'Alla and P. L. Betts, "Experimental study of turbulent natural convection in a tall air cavity," *Experimental Heat Transfer*, vol. 9, no. 2, 1996.

[79] D. G. Barhaghi and L. Davidson, "Natural convention boundary layer in a 5:1 cavity," *Physics of Fluids*, vol. 19, no. 12, pp. 1–16, 2007.

[80] F. Sebilleau, R. Issa, S. Lardeau, and S. P. Walker, "Direct Numerical Simulation of an air-filled differentially heated square cavity with Rayleigh numbers up to

10ˆ11,” *International Journal of Heat and Mass Transfer*, vol. 123, pp. 297–319, aug 2018.

[81] M. Keyhani, F. A. Kulacki, and R. N. Christensen, “Experimental investigation of free convection in a vertical rod bundlea general correlation for nusselt numbers,” *Journal of Heat Transfer*, vol. 107, no. 3, pp. 611–623, 1985.

[82] D. M. McEligot, J. E. O’Brien, C. M. Stoots, T. K. Larson, W. A. Christenson, D. C. Mecham, and W. G. Lussie, “Natural convection between a vertical cylinder and a surrounding array,” vol. 146, pp. 267–276, 1994.

[83] G. Batchelor, “Heat transfer by free convection across a closed cavity between vertical boundaries at different temperature,” *Quarterly of Applied Mathematics*, vol. 12, no. 3, pp. 209–233, 1954.

[84] S. Kimura and A. Bejan, “The boundary layer natural convection regime in a rectangular cavity with uniform heat flux from the side,” *Journal of Heat Transfer*, vol. 106, no. 1, pp. 98–103, 1984.

[85] W. Jones and B. Launder, “The prediction of laminarization with a two-equation model of turbulence,” *International Journal of Heat and Mass Transfer*, vol. 15, pp. 301–314, feb 1972.

[86] B. J. Daly and F. H. Harlow, “Transport equations in turbulence,” *Physics of Fluids*, vol. 13, no. 11, pp. 2634–2649, 1970.

[87] R. Kumar and M. A. Kalam, “Laminar thermal convection between vertical coaxial isothermal cylinders,” *International Journal of Heat and Mass Transfer*, vol. 34, no. 2, pp. 513–524, 1991.

[88] S. Paolucci and D. R. Chenoweth, “Transition to chaos in a differentially heated vertical cavity,” *Journal of Fluid Mechanics*, vol. 201, pp. 379–410, 1989.

[89] K. Hsieh and F. Lien, “Numerical modeling of buoyancy-driven turbulent flows in enclosures,” *International Journal of Heat and Fluid Flow*, vol. 25, pp. 659–670, aug 2004.

[90] F. Lien and M. Leschziner, "A general non-orthogonal collocated finite volume algorithm for turbulent flow at all speeds incorporating second-moment turbulence-transport closure, Part 1: Computational implementation," *Computer Methods in Applied Mechanics and Engineering*, vol. 114, pp. 123–148, apr 1994.

[91] Y. Tian and T. Karayiannis, "Low turbulence natural convection in an air filled square cavity: Part II: the turbulence quantities," *International Journal of Heat and Mass Transfer*, vol. 43, pp. 867–884, mar 2000.

[92] T.-H. Shih, J. Zhu, and J. L. Lumley, "A new Reynolds stress algebraic equation model," *Computer Methods in Applied Mechanics and Engineering*, vol. 125, pp. 287–302, sep 1995.

[93] C. Speziale, "On nonlinear K-l and K-ϵ models of turbulence," *Journal of Fluid Mechanics*, vol. 178, pp. 459–475, 1987.

[94] D. Ammour, H. Iacovides, and T. J. Craft, "Model Validation for Bouyancy-Driven Flows Inside Differentially Heated Cavities," in *12th UK National Heat Transfer Conference*, (Leeds), pp. 1–13, 2011.

[95] P. A. Durbin, "Near-wall turbulence closure modeling without "damping functions"," *Theoretical and Computational Fluid Dynamics*, vol. 3, no. 1, pp. 1–13, 1991.

[96] D. Laurence, F. Billard, and J. Uribe Torres, "A New Formulation of the V2F Model using Elliptic Blending and its Application to Heat Transfer Prediction," in *Proceedings of 7th International ERCOFTAC Symposium on Engineering Turbulence Modelling and Measurements*, (Limassol), pp. 89–94, 2008.

[97] D. Kizildag, F. Trias, I. Rodríguez, and A. Oliva, "Large eddy and direct numerical simulations of a turbulent water-filled differentially heated cavity of aspect ratio 5," *International Journal of Heat and Mass Transfer*, vol. 77, pp. 1084–1094, oct 2014.

[98] A. K. Shati, S. G. Blakey, and S. B. Beck, "A dimensionless solution to radiation and turbulent natural convection in square and rectangular enclosures," *Journal of Engineering Science and Technology*, vol. 7, no. 2, pp. 257–279, 2012.

[99] A. K. Shati, S. G. Blakey, and S. B. Beck, “An empirical solution to turbulent natural convection and radiation heat transfer in square and rectangular enclosures,” *Applied Thermal Engineering*, vol. 51, no. 1-2, pp. 364–370, 2013.

[100] Y. Rao and E. Glakpe, “Three-dimensional natural convection in a rod bundleA numerical study in boundary-fitted coordinates,” *Numerical Methods in Thermal Problems*, vol. 7, pp. 446–456, 1991.

[101] Y. F. Rao and E. K. Glakpe, “Three-dimensional natural convection in an enclosed vertical rod bundle with mixed boundary conditions,” *International Journal of Heat and Mass Transfer*, vol. 36, no. 6, pp. 1517–1528, 1993.

[102] W. Sha, H. Domanus, R. Schmitt, J. Oras, E. Lin, and V. Shah, “A new approach for rod-bundle thermal-hydraulic analysis,” in *International Meeting on Nuclear Power Reactor Safety, Brussels, Belgium, October 16 - 19, 1978*, p. 32, Journal of Nuclear Technology, 1978.

[103] M. Viellieber and A. Class, “Anisotropic Porosity Formulation of the Coarse-Grid-CFD,” in *Proceedings of the 2012 20th International Conference on Nuclear Engineering collocated with the ASME 2012 Power Conference ICONE20 -POWER2012 July 30 - August 3, 2012, Anaheim*, (California), pp. 1–11, International Conference on Nuclear Engineering, 2012.

[104] B. Liu, S. He, C. Moulinec, and J. Uribe, “Sub-channel CFD for nuclear fuel bundles,” *Nuclear Engineering and Design*, vol. 355, no. May, 2019.

[105] M. H. Pedras and M. J. de Lemos, “Macroscopic turbulence modeling for incompressible flow through undeformable porous media,” *International Journal of Heat and Mass Transfer*, vol. 44, no. 6, pp. 1081–1093, 2001.

[106] M. Drouin, O. Grégoire, and O. Simonin, “A consistent methodology for the derivation and calibration of a macroscopic turbulence model for flows in porous media,” *International Journal of Heat and Mass Transfer*, vol. 63, pp. 401–413, 2013.

[107] M. B. Saito and M. J. de Lemos, “A macroscopic two-energy equation model for

turbulent flow and heat transfer in highly porous media," *International Journal of Heat and Mass Transfer*, vol. 53, no. 11-12, pp. 2424–2433, 2010.

[108] F. Kuwahara, C. Yang, K. Ando, and A. Nakayama, "Exact Solutions for a Thermal Nonequilibrium Model of Fluid Saturated Porous Media Based on an Effective Porosity," *Journal of Heat Transfer*, vol. 133, no. 11, pp. 1 – 9, 2011.

[109] M. H. Rahimi and G. Jahanfarnia, "Thermal-hydraulic core analysis of the VVER-1000 reactor using a porous media approach," *Journal of Fluids and Structures*, vol. 51, pp. 85–96, 2014.

[110] M. Rahimi and G. Jahanfarnia, "Thermo-hydraulic analysis of the supercritical water-cooled reactor core by porous media approach," *The Journal of Supercritical Fluids*, vol. 110, pp. 275–282, apr 2016.

[111] R. Chen, M. Tian, S. Chen, W. Tian, G. H. Su, and S. Qiu, "Three dimensional thermal hydraulic characteristic analysis of reactor core based on porous media method," *Annals of Nuclear Energy*, vol. 104, pp. 178–190, 2017.

[112] C. Fiorina, I. Clifford, M. Aufiero, and K. Mikityuk, "GeN-Foam: A novel OpenFOAM® based multi-physics solver for 2D/3D transient analysis of nuclear reactors," *Nuclear Engineering and Design*, vol. 294, pp. 24–37, 2015.

[113] V. Hovi, T. Pättikangas, and V. Riikonen, "Coupled one-dimensional and CFD models for the simulation of steam generators," *Journal of Nuclear Engineering and Design*, vol. 310, 2016.

[114] B. Mikuž and F. Roelofs, "Low resolution modelling of mixing phenomena in PWR fuel assemblies," *Nuclear Engineering and Design*, vol. 360, no. May 2019, p. 110504, 2020.

[115] A. Class, M. Viellieber, and A. Batta, "Coarse-Grid-CFD for pressure loss evaluation in rod bundles," in *Proceedings of ICAPP 2011*, (Nice France), pp. 1773 – 1780, 2011.

[116] L. Capone, S. Benhamadouche, and Y. a. Hassan, "Source terms modeling for spacer grids with mixing vanes for CFD simulations in nuclear reactors," *Journal of Computers and Fluids*, vol. 126, pp. 141–152, 2016.

[117] M. H. J. Pedras and M. J. de Lemos, “On the definition of turbulent kinetic energy for flow in porous media,” *International Journal of Heat and Mass Transfer*, vol. 27, no. 2, pp. 211–220, 2000.

[118] A. Nakayama and F. Kuwahara, “Model for Flow in a Porous Medium,” *Journal of Fluids Engineering*, vol. 121, pp. 427–433, 1999.

[119] M. Chandesris, G. Serre, and P. Sagaut, “A macroscopic turbulence model for flow in porous media suited for channel, pipe and rod bundle flows,” *International Journal of Heat and Mass Transfer*, vol. 49, no. 15-16, pp. 2739–2750, 2006.

[120] Y. Kuwata and K. Suga, “Modelling turbulence around and inside porous media based on the second moment closure,” *International Journal of Heat and Fluid Flow*, vol. 43, pp. 35–51, 2013.

[121] M. Mößner and R. Radespiel, “Modelling of turbulent flow over porous media using a volume averaging approach and a Reynolds stress model,” *Computers {&} Fluids*, vol. 108, pp. 25–42, 2015.

[122] S. Pope, *Turbulent flows.* Cambridge: Cambridge University Press., 2000.

[123] B. Launder and D. Spalding, “The numerical computation of turbulent flows,” *Computer Methods in Applied Mechanics and Engineering*, vol. 3, no. 2, pp. 269–289, 1974.

[124] F. Menter, “Zonal Two Equation k-w Turbulence Models For Aerodynamic Flows,” *American Institute of Aeronautics and Astronautics*, 1993.

[125] T. B. Gatski and C. G. Speziale, “On explicit algebraic stress models for complex turbulent flows,” *Journal of Fluid Mechanics*, vol. 254, pp. 59–78.

[126] F. Nicoud and F. Ducros, “Subgrid-scale stress modelling based on the square of the velocity,” *Agricultural Economics Research Review*, vol. 19, pp. 37–48, 2006.

[127] J. P. V. Doormaal and G. D. Raithby, “Enhancements of the simple method for predicting incompressible fluid flows,” *Numerical Heat Transfer*, vol. 7, no. 2, pp. 147–163, 1984.

[128] C. M. Rhie and W. L. Chow, "Numerical study of the turbulent flow past an airfoil with trailing edge separation," *AIAA Journal*, vol. 21, no. 11, pp. 1525–1532, 1983.

[129] E. Lemmon, M. Huber, and M. McLinden, "NIST Standard Reference Database 23: Reference Fluid Thermodynamic and Transport Properties (REFPROP), Version 9.0.," 2010.

[130] I. B. Celik, Z. N. Cehreli, and I. Yavuz, "Index of resolution quality for large eddy simulations," *Journal of Fluids Engineering, Transactions of the ASME*, vol. 127, no. 5, pp. 949–958, 2005.

[131] C. O. Popiel, "Free convection heat transfer from vertical slender cylinders: A review," *Heat Transfer Engineering*, vol. 29, no. 6, pp. 521–536, 2008.

[132] K. Chinembiri, S. He, and J. Li, "Natural circulation in a sealed rod bundle of large aspect ratio," *Applied Thermal Engineering,*, no. 188, 2021.

[133] K. Chinembiri, S. He, J. Li, and C. Trinca, "Numerical study of heat transfer in a distorted rod bundle," *Nuclear Engineering and Design*, vol. 349, no. April, pp. 63–77, 2019.

[134] S. He, "The Effect of Stringer and Channel Bow on Brick Temperature," tech. rep., EDF Energy, 2000.

[135] E. Romero, "Cooling of AGR Fuel Elements by Angled and Cross Flows Correlations for Heat Transfer and Flow Losses," tech. rep., GEN/D-FWG/P(92)4742/B/2, Nuclear Electric, 1994.

[136] K. Chinembiri and S. He, "Modelling and Methodology report; FREEDOM (previously named as Postr2)," tech. rep., FREEDOM/SHF/002, University of Sheffield, Sheffield, 2020.

[137] M. Fung and G. Hulme, "COOLFUEL 3-D (v2) validation report," tech. rep., GEN/DFWG/P(93)4758/B/2, Nuclear Electric, 1995.

[138] F. P. Incropera and D. P. DeWitt, *Introduction to heat transfer.* Wiley, 1990.

[139] E. Romero, “Cooling of dropped AGR fuel elements - Specification of correlations for buoyancy free heat transfer and flow losses - Axial flows,” tech. rep., GEN/DFWG/P(92)4743/B/3, Nuclear Electric, 1994.

[140] E. Romero, “Cooling of Dropped AGR Fuel Elements - Specification of correlations for buoyancy Influenced heat transfer and flow losses - axial flows,” tech. rep., GEN/DFWG/P(92)4744/B/2, Nuclear Electric, 1994.

[141] W. Long, “Flow resistance characteristics of dropped stringer debris in a buffer storage tube,” tech. rep., GEN/DFWG/P(90)4312/B/1, Nuclear Electric, 1992.

[142] W. Kebede, “Validation of CoolFuel 1-D and CoolFuel 3-D thermal assessment codes against data from BNL 4 element experiment,” tech. rep., GEN/DFWG/P(92)4734/B/2, Nuclear Electric, 1992.

[143] J. Robertshaw, “FOXDROP (Version 6) User Guide,” tech. rep., TPAZ/MEM/0109/93, Nuclear Electric, 1993.

[144] J. Derbyshire, “Calculation of Effective Graphite Conductivity for Dropped Fuel Thermal Analysis in Large Diameter Channels,” tech. rep., GEN/DFWG/P(93)4750/B/2, Nuclear Electric, 1994.

[145] G. Amhalhel and P. Furmański, “Problems of Modeling Flow and Heat Transfer in Porous Media,” *Journal of Power Technologies*, vol. 85, pp. 55–88, 1997.

[146] C. Mowforth, “Monitoring of Fuel-Pin deposition and assessment of heat transfer impairment,” tech. rep., E/REP/AGR/0054/00, British Energy, 2000.

[147] F. Incropera, D. Dewitt, T. Bergman, and A. Lavine, *Fundamentals of Heat and Mass Transfer*. John Wiley & Sons, 6th ed., 2007.

[148] R. Hornby, “Data report for the CoolFuel 1-D and CoolFuel 3-D dropped fuel thermal assesement codes,” tech. rep., GEN/DFWG/P(91)4364/B/2, Nuclear Electric, 1992.

[149] N. Todreas and M. Kazimi, *Nuclear Systems*. CRC Press, 2nd editio ed., 2012.

[150] A. Bahia and R. Keatinge, “Specification for a Computer Code (based on existing code HOTDROP-PC) to Model Dropped Fuel Debris Temperatures

with the inclusion of the Heat Release from Debris Oxidation," tech. rep., TPAZ/MEM/0047/93/B/1, Nuclear Electric, 1993.

[151] K. Chinembiri and S. He, "Validation report for forced and natural convection flow regimes using FREEDOM (Previously named as (POSTR2))," tech. rep., FREEDOM/SHF/003, University of Sheffield, Sheffield, 2020.

[152] A. Guest, "Thermo-hydraulic Analysis in Support of Decay Store Tube Judgements Made in the Heysham 2 and Torness IJCOs for Radiolytic Deposit Initial Sensitivity Investigation," tech. rep., 16033/TR/0002, AMEC Nuclear UK Limited (AMEC)., 2010.

[153] A.J.Kirwan, "HOTDROP PC (Version 1.2) DATA REPORT," tech. rep., GEN/DFWG/P(92)4729/B/2, Nuclear Electric, 1992.

[154] K. Chinembiri and S. He, "FREEDOM Safety case; High carbon deposition thermal analysis for dropped fuel in the IFDF," tech. rep., FREEDOM/SHF/004, University of Sheffield, Sheffield, 2020.

[155] A. Knox, "Investigation of sensitivities and possible improvements to FOXDROP Dropped Fuel at IFDF," tech. rep., 208802-0000-DQ00-RPT-0001, Wood, 2019.

[156] J. Warder, "Damage and thermal assesment of a stringer of decay heat 6kW on arrival at Torness IFD2 cell," tech. rep., C9378/DSR/001, Nuclear Electric, 1994.

[157] J. Robertshaw, "HOTDROP PC (Version 1.2) Modelling Report," tech. rep., GEN/DFWG/P(92)4728/B/2, National Nuclear Corporation(NNC), 1993.

[158] S. S. Goodrich, *Natural convection heat transfer and boundary layer transition for vertical heated cylinders.* PhD thesis, Oregon State University, 2017.

Appendix A

A.1 Temporal convergence of turbulent kinetic energy profiles - Short bundle

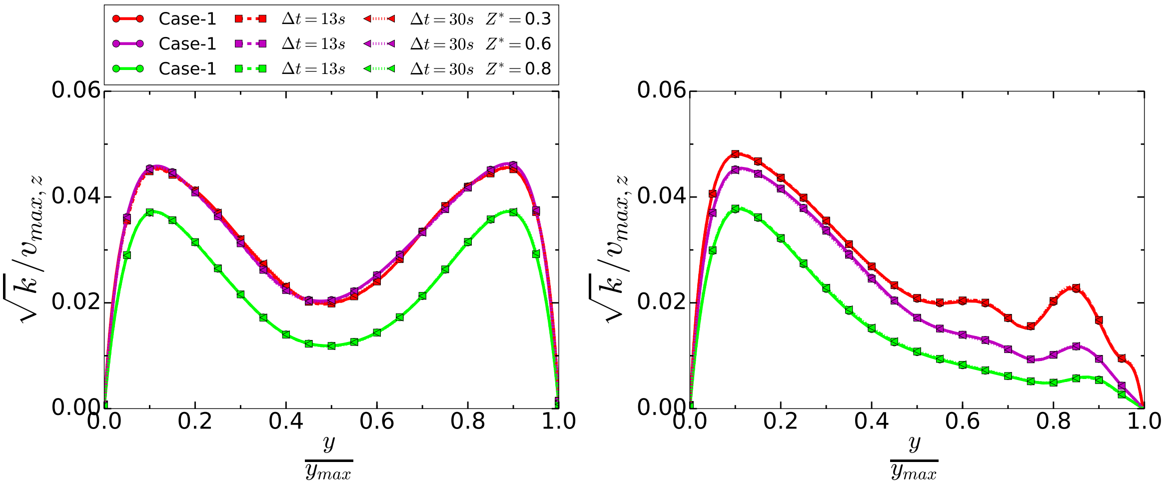

(a) Line_1 (b) Line_5

Figure A1: Profiles of a time convergence study for turbulent kinetic energy variation taken along Line_1 and Line_5 (see Figure 5.1 for extraction locations). The reference velocity $v_{max,z}$ is the peak axial velocity extracted at profile height.

The quality parameter (LES_IQ$_v$) is defined as shown in Equation A.1.

$$\text{LES\_IQ}_v = \frac{1}{1 + 0.05\left(\frac{S^*}{1-S^*}\right)^{0.53}} \tag{A.1}$$

S^* is computed as shown in Equation A.2. Where it has been taken that the subgrid scale diffusion is equal to the numerical diffusion $\left(\mu_{\text{sgs}} \approx \mu_{\text{num-diff}}\right)$.

$$S^* = \frac{\mu_{\text{sgs}} + \mu_{\text{num-diff}}}{\mu_{\text{sgs}} + \mu_{\text{num-diff}} + \mu} \tag{A.2}$$

A.2 LES mesh quality indicator - Short bundle

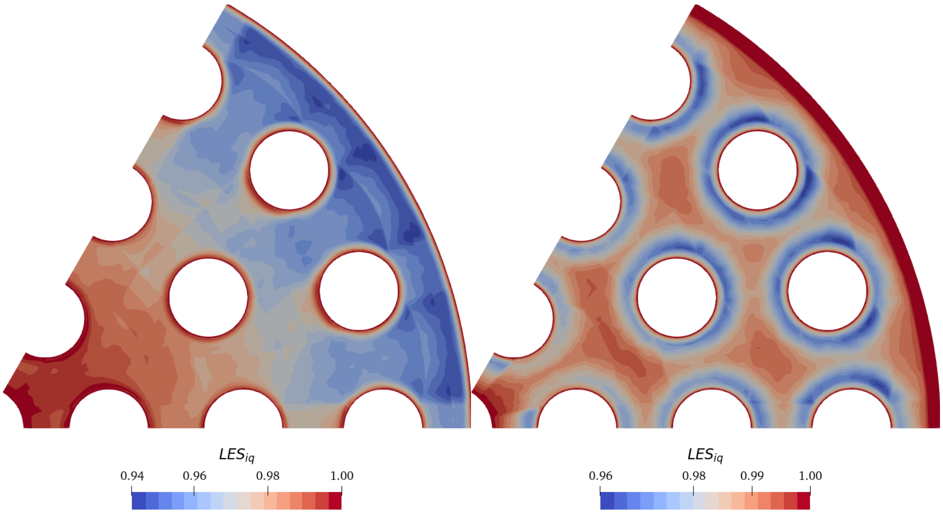

(a) $Z^* = 0.04$ (b) $Z^* = 0.5$

Figure A2: Contours of the LES_IQ parameter at varying heights and taken from Case-1. The scalebar is reset at each axial location to maximise the variation. LES is considered to be good if the values obtained are LES_IQ > 0.8.

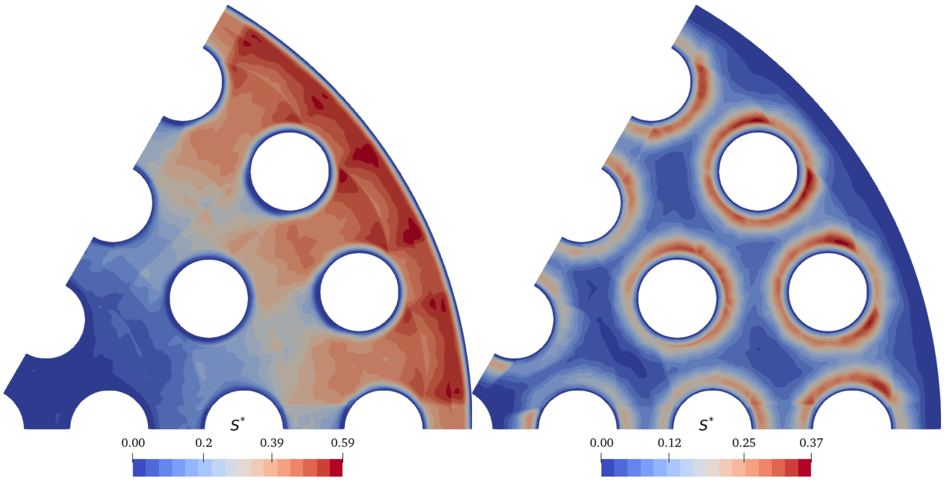

(a) $Z^* = 0.04$ (b) $Z^* = 0.5$

Figure A3: Contours of the S parameter at varying heights and taken from Case-1. The scalebar is reset at each axial location to maximise the variation.

A.3 Q-criterion

The Q-criterion is defined as:

$$\mathrm{Q} = \frac{1}{2}\left(\Omega_{ij,\mathrm{rot}}\Omega_{ij,\mathrm{rot}} - S_{ij,\mathrm{strain}}S_{ij,\mathrm{strain}}\right) \tag{A.3}$$

where $\Omega_{ij,\mathrm{rot}}$ is rotation tensor is defined as:

$$\Omega_{ij,\mathrm{rot}} = \frac{1}{2}\left(\frac{\partial\langle u_i\rangle}{\partial x_j} - \frac{\partial\langle u_j\rangle}{\partial x_i}\right) \tag{A.4}$$

Iso-surfaces computed using Q-criterion and then coloured with the instantaneous streamwise vorticity at values of ± 30.

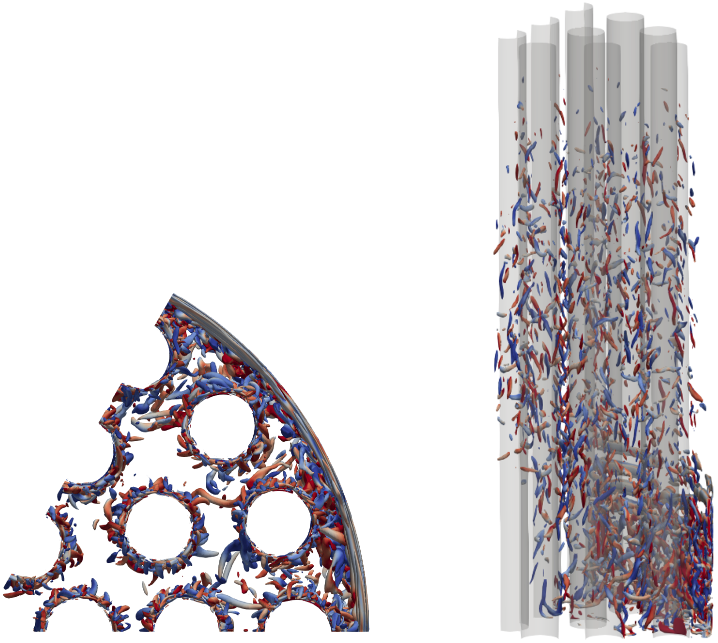

(a) Top down view (b) Oblique view

Figure A4: Iso-surfaces coloured by the streamwise vorticity. Data is taken from the Case-1.

A.4 Ostrach's similarity solution

Momentum and energy are transformed through the introduction of the similarity variable η and stream function Ψ shown in Equation A.5.

$$\eta = \frac{y}{z}\left(\frac{\mathrm{Gr}_{z,\Delta T}}{4}\right)^{1/4} \tag{A.5a}$$

$$\Psi = F(\eta)\left[4v\left(\frac{\mathrm{Gr}_{z,\Delta T}}{4}\right)^{1/4}\right] \tag{A.5b}$$

The resulting transformed equations are given in Equation A.6 for both momentum and energy:

$$F''' + 3FF'' - 2F'^2 + T^* = 0 \tag{A.6a}$$

$$T^{*''} + 3\mathrm{Pr}FT^{*'} = 0 \tag{A.6b}$$

where T^* is computed as $T - T_\infty / T_w - T_\infty$. The transformed equations for momentum and energy are higher order differentials and coupled together. Boundary conditions at $\eta = 0$ are given as; $F'(0) = F(0) = 0$, $T^*(0) = 1$ and those at $\eta = \infty$ are given as; $F'(\infty) = T^*(\infty) = 0$.

To compute the solution, initial values at $\eta = 0$ for $F''(0)$, which is the velocity gradient at the wall and $T^{*'}(0)$, which is the wall temperature gradient need to be obtained. This is done by firstly reducing the higher order differential equations (Equation A.6) into a system of first order differential equations, this process yields five first order differential equations with three coming from momentum and two from the energy equation. This system is solved using the explicit Runge-Kutta method. Since this is an initial value problem, the values for $F''(0)$ and $T^{*'}(0)$ which satisfy the given boundary conditions at $\eta = \infty$ need to be obtained. This is done by supplying the initial guess values and then iteratively solving until the successively updated approximate initial guess values satisfy the boundary conditions at $\eta = \infty$. To quickly check, if the solver is implemented correctly one can compare the predicted values against those from Ostrach's solution. At Pr = 1, Ostrach's values are 0.642 and -0.5667 for F'' and $T^{*,'}$, respectively[13]. Setting Pr = 1, solutions from the implemented solver return similar values (identical to the third decimal place). The computed initial values are then used as boundary conditions and the system is again solved.

A.5 Sparrow and Gregg similarity solution

The similarity variable (η), radius of curvature effect (ξ) and the stream function (Ψ) are written as follows for the case of a slender cylinder[131]:

$$\eta = \mathrm{Gr}_{R,\Delta T}^{1/4} \frac{R^{-7/4}}{2^{3/2}} \frac{\left(r^2 - R^2\right)}{z^{1/4}} \tag{A.7a}$$

$$\xi = \mathrm{Gr}_{R,\Delta T}^{-1/4} \frac{2^{3/2}}{R^{1/4}} z^{1/4} \tag{A.7b}$$

$$F(\eta, \xi) = \mathrm{Gr}_{R,\Delta T}^{-3/4} \frac{2^{3/2}}{\upsilon R^{3/4}} \frac{\Psi}{z^{1/4}} \tag{A.7c}$$

where R is the rod radius and z is the axial coordinate. The governing equations for momentum and energy are then transformed into[131]:

$$\xi \left(\frac{\partial F}{\partial \eta} \frac{\partial^2 F}{\partial \xi \partial \eta} - \frac{\partial F}{\partial \xi} \frac{\partial^2 F}{\partial \eta^2} \right) - F \frac{\partial^2 F}{\partial \eta^2} = \xi^2 \frac{\partial}{\partial \eta} \left[(1 + \eta \xi) \frac{\partial^2 F}{\partial \eta^2} \right] + \xi^4 T^* \tag{A.8a}$$

$$\xi \left(\frac{\partial T^*}{\partial \xi} \frac{\partial F}{\partial \eta} - \frac{\partial T^*}{\partial \eta} \frac{\partial F}{\partial \xi} \right) - F \frac{\partial T^*}{\partial \eta} = \frac{\xi^2}{\mathrm{Pr}} \frac{\partial}{\partial \eta} \left[(1 + \eta \xi) \frac{\partial T^*}{\partial \eta} \right] \tag{A.8b}$$

In comparison to the similarity solution for a flat plate, the variables are now also a function of the radius of curvature $\left(F\left(\eta, \xi\right) \text{ and } T^*\left(\eta, \xi\right)\right)$. These variables are equivalent to the series expansions shown in Equation A.9. The first term in the series expansion is essentially the flat plate solution by Ostrach[13].

$$F(\eta, \xi) = \xi^2 \left[F_0\left(\eta\right) + \xi F_1\left(\eta\right) + \xi^2 F_2\left(\eta\right) + \cdots \right] \tag{A.9a}$$

$$T^*(\eta, \xi) = T_0^*\left(\eta\right) + \xi T_1^*\left(\eta\right) + \xi^2 T_2^*\left(\eta\right) + \cdots \tag{A.9b}$$

As shown by Popiel[131] and more in-depth by Goodrich[158], the series expansion can be substituted into the momentum and energy equation, yielding a set of coupled differential equations, with the higher order series expansion terms dependent on the lower order terms. Herein, the series expansion is considered up to the second order term. The resulting system of equations are solved in a similar manner to that described for the flat plate solution. Initial values at $\eta = 0$ for F_n'', and $T_n^{*\prime}$ need to be obtained. This is done by iteratively solving the system of equations until the boundary conditions at $\eta = \infty$ are satisfied. To check the implementation of the solver, the obtained initial values are compared against those published by Goodrich[158] for a Prandtl number of 1.

A.6 Mirror profile approach

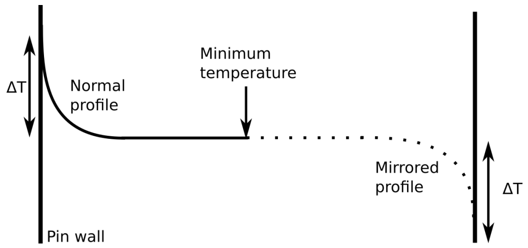

Figure A5: Illustration of the mirror profile approach used to relate computed Nusselt values to rectangular cavities.

Appendix B

B.1 Temporal convergence of turbulent kinetic energy profiles

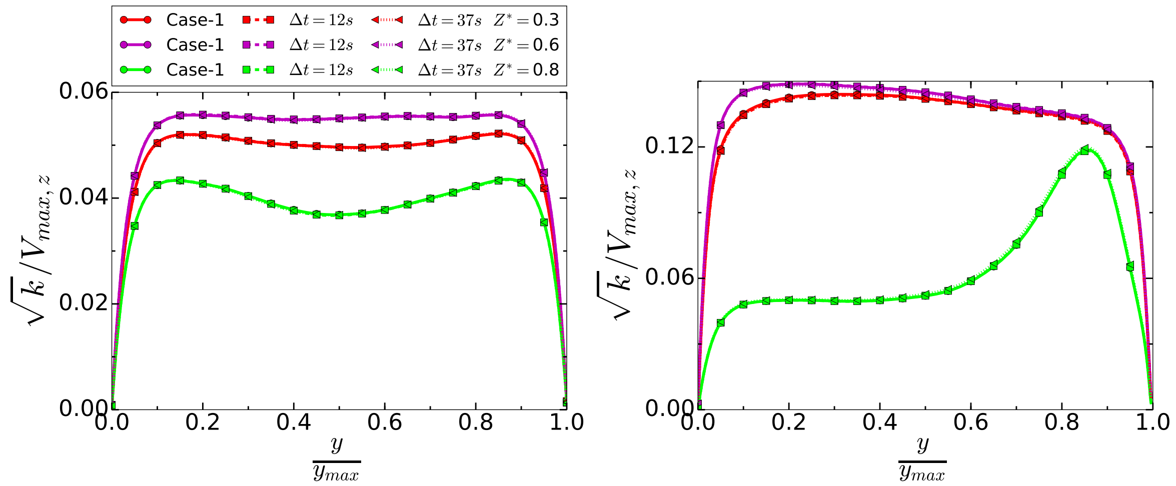

(a) Line_1

(b) Line_5

Figure B1: Turbulent kinetic energy plotted at different times for Line_1 and Line_5 (Extraction locations are given in Figure 5.1).

B.2 LES mesh quality indicator - Tall bundle

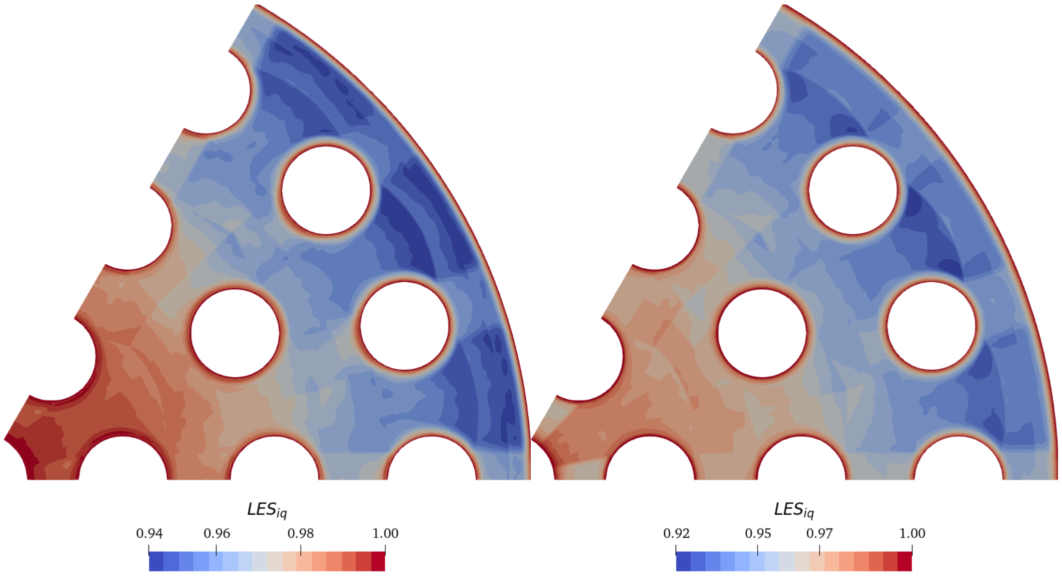

(a) $Z^* = 0.01$ (b) $Z^* = 0.25$

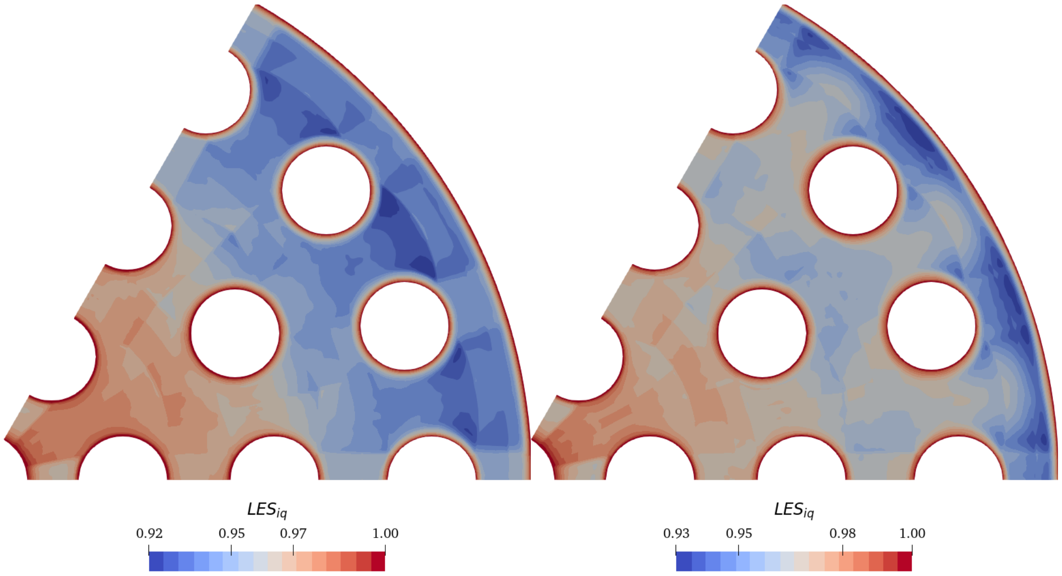

(c) $Z^* = 0.5$ (d) $Z^* = 0.75$

Figure B2: Contours of the LES_IQ parameter at varying heights and taken from the highest heating case. The scalebar is reset at each axial location to maximise the variation. LES is considered to be good if the values obtained are LES_IQ > 0.8.

B.3 Containment similarity solution

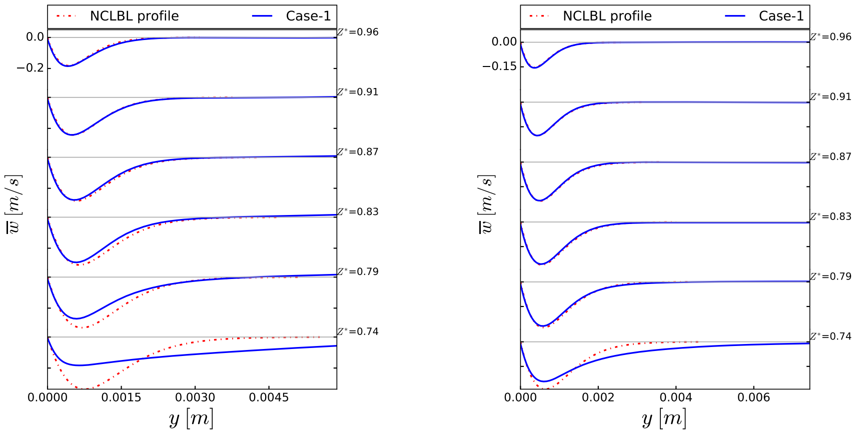

(a) Line_5 (b) Line_6

Figure B3: Velocity comparison of LES simulation data against the similarity solution by Ostrach[13] for Line_5 and Line_6. The containment surface is now located at $y/y_{max} = 0$. The top region from $Z^* = 0.96$ to $Z^* = 0.74$ is extracted

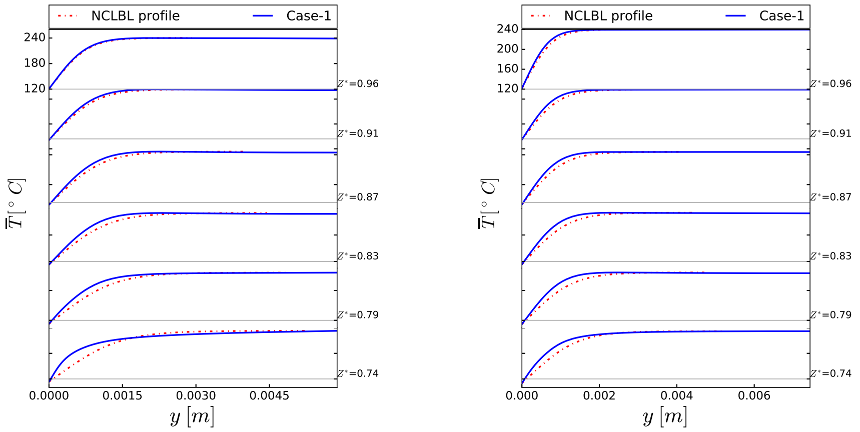

(a) Line_5 (b) Line_6

Figure B4: Temperature comparison of LES simulation data against the similarity solution by Ostrach[13] for Line_5 and Line_6. The containment surface is now located at $y/y_{max} = 0$. The top region from $Z^* = 0.96$ to $Z^* = 0.74$ is extracted.

B.4 Rod similarity solution

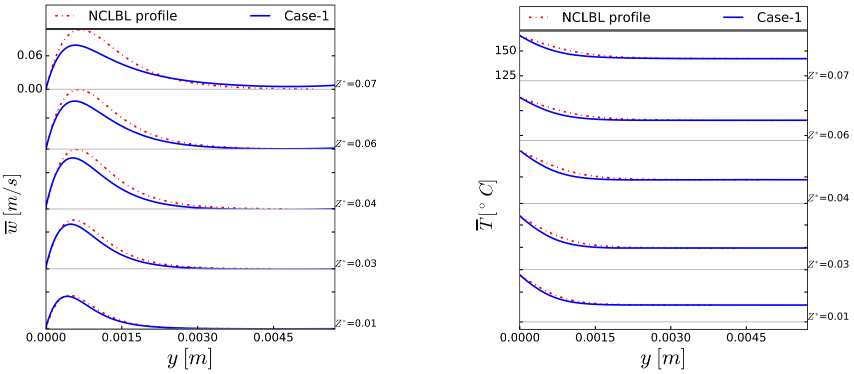

(a) Line_1 - Velocity (b) Line_1 - Temperature

Figure B5: Temperature and Velocity comparison of LES simulation data against the slender cylinder similarity solution for Line_1. Data is extracted for the bottom region from $Z^* = 0.01$ to $Z^* = 0.07$.

Appendix C

C.1 Trupp and Azad validation study

For this validation exercise, a triangular array with a P/D ratio of 1.35 was selected and flow was specified at a Reynolds number of 59 880. Figure C1 shows a sketch of the geometry. The domain was simulated using periodicity, with the top and bottom faces forming the periodic pair. Rod walls are prescribed as smooth, with a no-slip wall boundary condition. Surfaces adjoining the rod walls are given a symmetric boundary condition.

Data used for the validation comparison is extracted along the line Y shown in the figure and compared against experimental data. Simulations have been carried out to Table C.1 shows the configuration of meshes and y^+ values.

Dimensionless values shown in the figures are defined as follows: $k^+ = k/u^{*2}$, $uv^+ = uv/u^{*2}$, $U = u_a/u_b$, where u^* is friction velocity calculated using the cross-section averaged wall shear stress, uv is turbulent shear stress, u_b is the bulk velocity

Table C.1: Configuration of meshes used for the triangular array validation study.

Mesh	No cells	Boundary mesh	Core mesh	y^+ values
M-TA-1	710	HEXA	PRISM	11.14
M-TA-2	1590	HEXA	PRISM	11.67
M-TA-3	4224	HEXA	PRISM	11.18
M-TA-4	6612	HEXA	PRISM	11.94
M-TET	16555	PRISM	TETRA	12.17

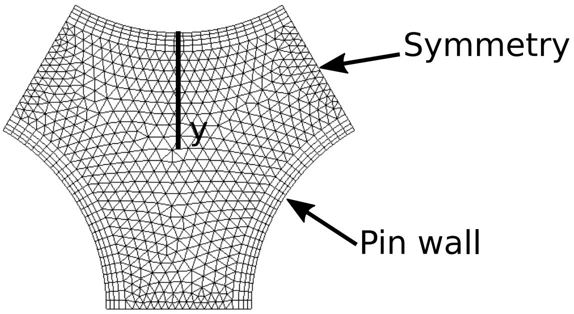

Figure C1: Slice of prismatic grid(M-TA-3)

and u_a is the streamwise velocity. Figure C2 shows a mesh dependence study based on the normalised velocity and turbulent shear stress. In this mesh dependence study, all the meshes compared used a prismatic grid, and comparisons were limited to high Reynolds number turbulence models. It can be noted meshes M-TA-3 and M-TA-4 return identical profiles for both quantities. Interestingly, mesh M-TA-1 predicts a discontinuous velocity profile, along with a turbulent shear stress profile with non-uniformities, perhaps as a result of discretization errors. The study further shows that grid independence is achieved much sooner for velocity than for turbulent shear stress. It can be concluded mesh M-TA-3 is sufficiently independent of the grid, the cross-sectional resolution of mesh M-TA-3 is shown in Figure C1.

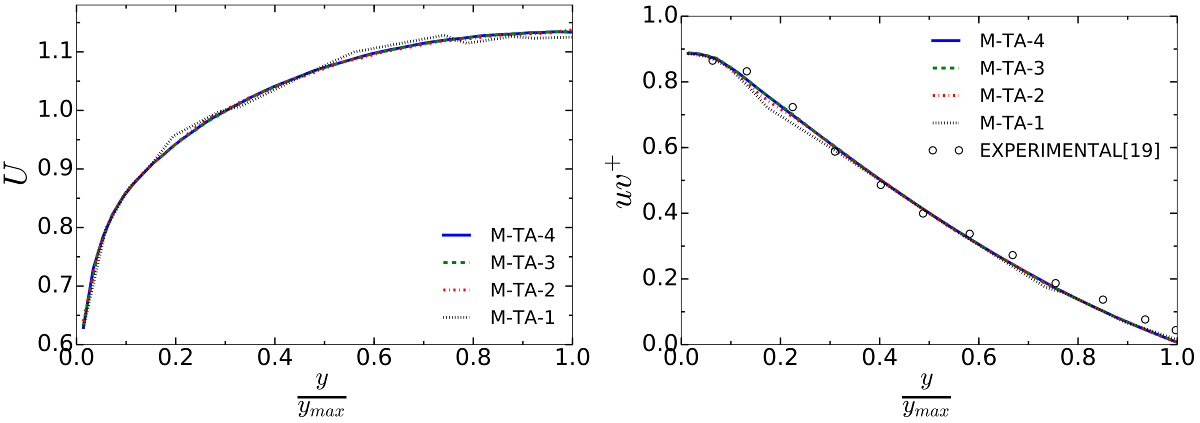

(a) (b)

Figure C2: Mesh dependence study (a) Velocity (b) turbulent shearstress

Experience suggests that an unstructured grid based on a tetrahedral mesh needs a density approximately four times greater than that of a structured mesh, and hence an unstructured mesh of four times that of mesh M-TA-3 is built and used (The tetrahedral mesh are given as M-TET in Table C.1). It should be noted for the tetrahedral mesh there is a single extruded layer at either end of the periodic pair. The extruded layer is required to provide orthogonal cells at the periodic pair upon which a source term is applied to drive the flow.

Figure C3(a) shows the predicted turbulent kinetic energy from the three turbulence models and the respective grid types. Overall, all simulations have achieved reasonably good agreement with the experiment. Small differences with respect to grid type are observed near the wall and as the grid transitions from the prism layer to the tetrahedral layer. This is evidenced in the slightly different slopes within this region ($y/y_{max} \approx 0.2$). With regards to turbulence model performance, the RSM model predicted results somewhat closer to experimental while the eddy viscosity models over-predict turbulent kinetic energy levels. For eddy viscosity models, the most important parameter is uv which is mostly dependent on the eddy viscosity. Figure C3(b) shows, turbulent shear stress levels predicted are the same within the bulk region and there are some differences between the results of the various models near the wall. Eddy viscosity models show a marginal over prediction of uv^+ near $y/y_{max} = 0.1$.

Finally, in Figure C3(c) the dimensionless axial velocity profiles show slight differences between the respective turbulence models and identical profiles concerning the respective mesh types.

C.2 Mesh dependence for ***WheatSheafed*** bundle

To assess, the mesh independence of the damaged section, the mesh was coarsened by relaxing the restriction on the maximum element area on the rod walls as well as increasing the growth rate (the rate at which tetrahedral cells increase in size from the boundary). Thus only the damaged section is altered and the recycling domain is kept constant thereby resulting in a coarse damaged section of density 15.27 million cells. The mesh configurations used in this dependence study are shown in Table C.2.

Figure C4 shows the comparison for the normalised turbulent kinetic energy obtained from the Reynolds stress model. The normalisation for turbulent kinetic energy k^* is defined as k/u_b^2. The RSM model is used to assess mesh independence as it is most susceptible to changes in mesh density. Profiles are obtained from Line_1 (see Figure 7.1(c)), at several axial locations. The results are shown to be mesh independent.

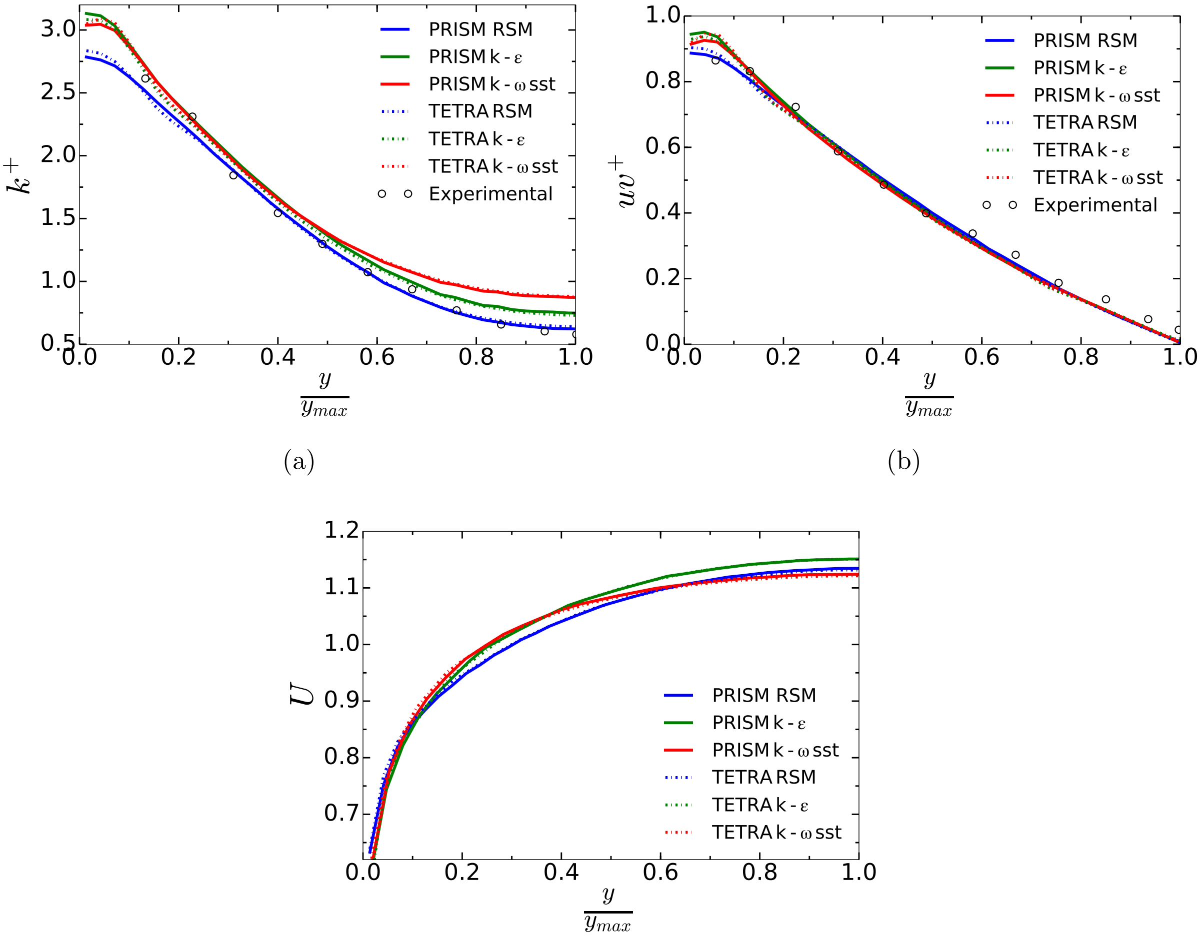

(a)

(b)

(c)

Figure C3: Study of mesh type and performance of turbulence model (a) Turbulent kinetic energy (b) Turbulent shear stress (c) Velocity

A comparison of predicted results obtained from the two turbulence models is given by comparing profiles obtained along Line_1. Figure C5 shows the normalised profiles for temperature, axial velocity, and uv. The two turbulence models predict similar trends for all quantities. For the temperature profiles (see Figure C5(a)), it is interesting to note that initially at the lower axial locations L = 0.25 and 0.5, the differences are relatively small with the maximum difference occurring near rod_1. At L = 0.75 and 1.0, the maximum difference occurs near rod_5, which is now a recirculation zone (further description given later). Furthermore, this difference is appreciably larger than that observed at the lower axial locations. The near-wall cell temperature values at $y/y_{max} = 0$ for L = 0.75 and 1.0 differ by 1.64 °C and 1.55 °C. Calculating the percentage difference as a function of maximum fluid temperature, the resulting temperature

Table C.2: Configuration of meshes used for the triangular array validation study.

Mesh	No cells (10^6)	Boundary mesh	Core mesh	y^+ values
M-1	15.27	PRISM	TETRA	22.87
M-2	21.5	PRISM	TETRA	22.8

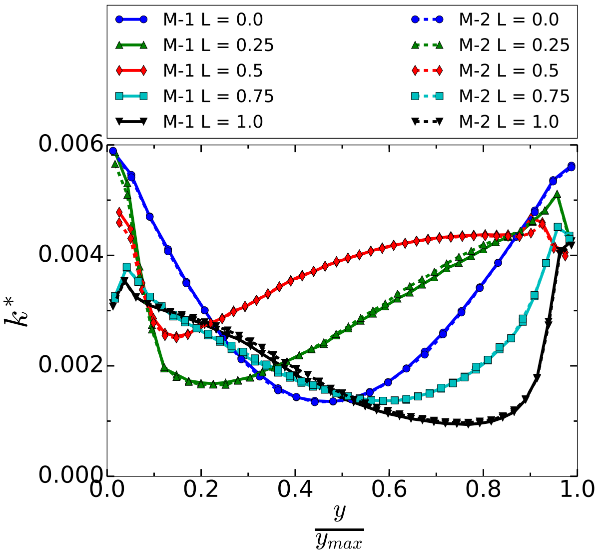

Figure C4: Mesh dependence study across Line_1

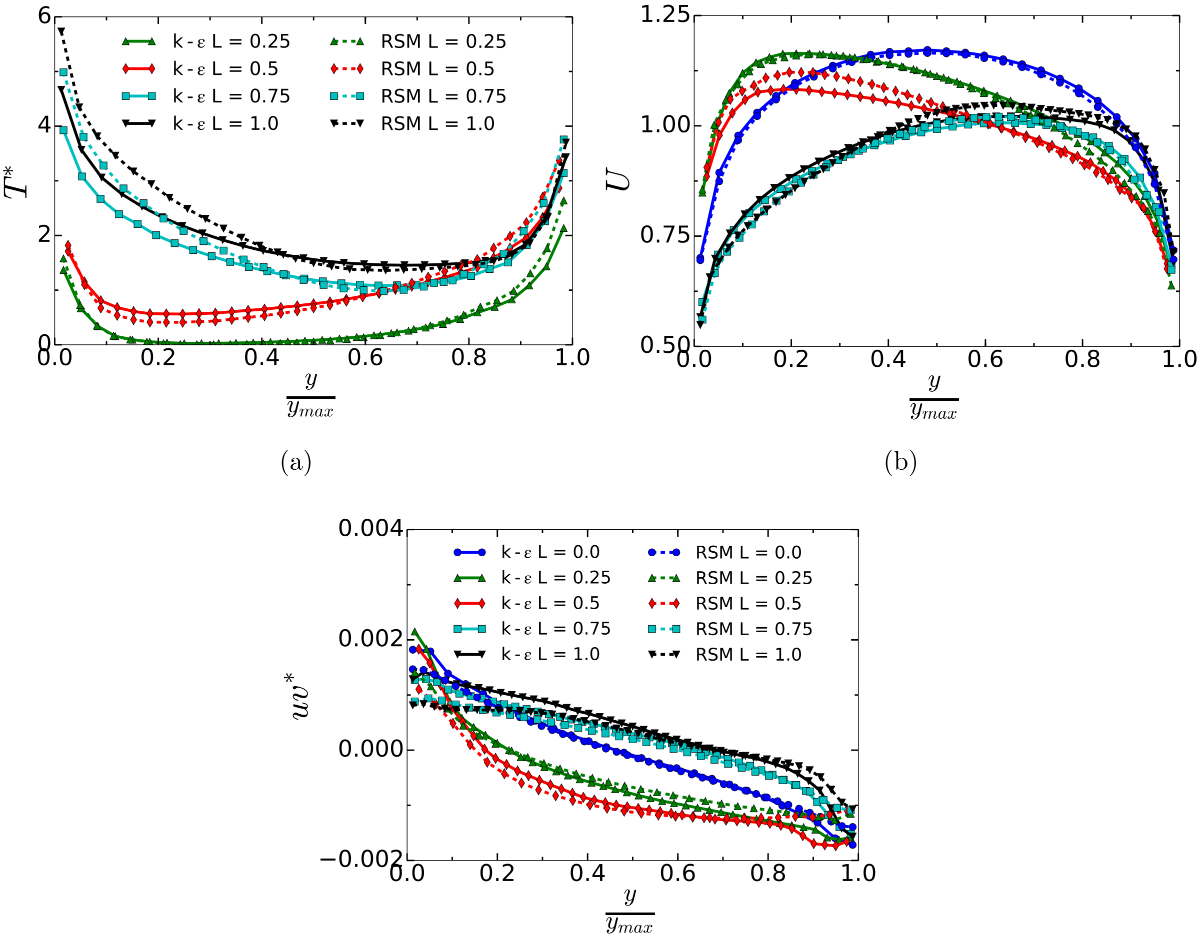

(a)

(b)

(c)

Figure C5: Comparison between of predictions between $k - \epsilon$ and RSM turbulence models. Distributions along Line_1 of (a) temperature, (b) velocity and (c) turbulent shear stress. (b) and (c) share the same legend.

difference is ≈18 % and ≈17 %, respectively.

For the normalised velocity, the two models return near-identical profiles at the inlet into the damaged section L = 0.0. At higher axial locations some differences occur near the recirculation zones and/or the rod wall. Taking the profile at L = 0.5 and calculating the percentage difference along the profile, the maximum is found to be 3.7 %. Turbulent shear stress profiles show that there is a good agreement between the turbulence models. This is particularly true on the rod surfaces and local regions where the coolant is pushed against the surface. In the recirculation zones, there is an increased difference.

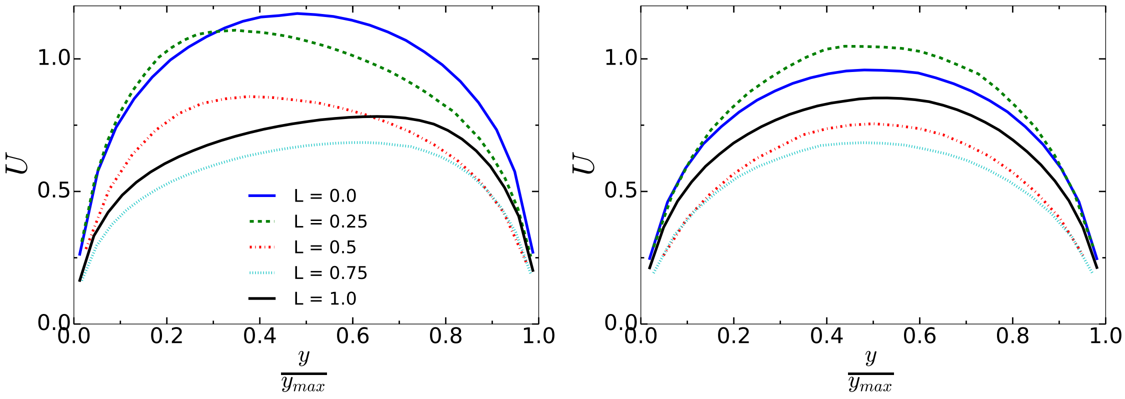

(a) (b)

Figure C6: Profiles of normalised axial velocity for rough rods along (a) Line_1, (b) Line_2

C.3 Effect of rod-roughness

Table C.3: Pressure drop comparison

Reynolds number	Correlation (Pa)	Predicted (Pa)	% difference
60 000	109.072	109.67	0.551
100 000	304.40	305.99	0.522
150 000	687.50	690.04	0.369
200 000	1225.471	1228.10	0.214

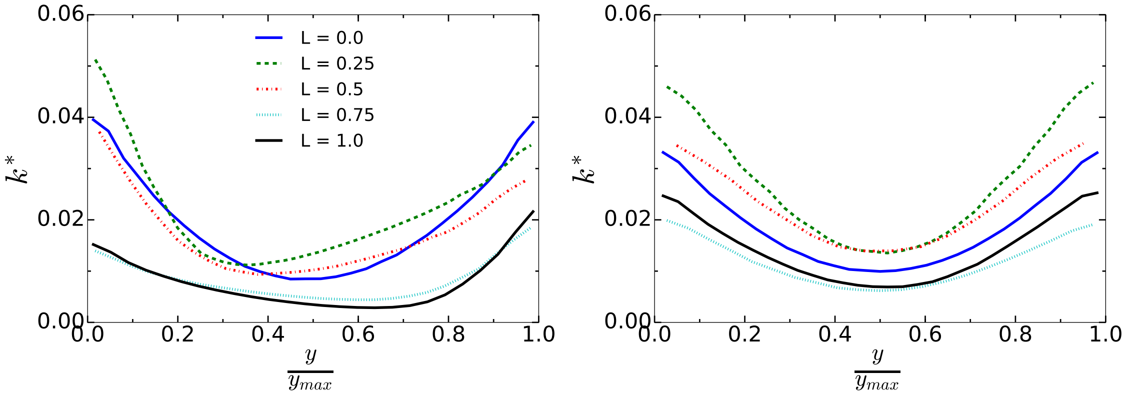

(a)

(b)

Figure C7: Profiles of normalised kinetic energy along (a) Line_1, (b) Line_2

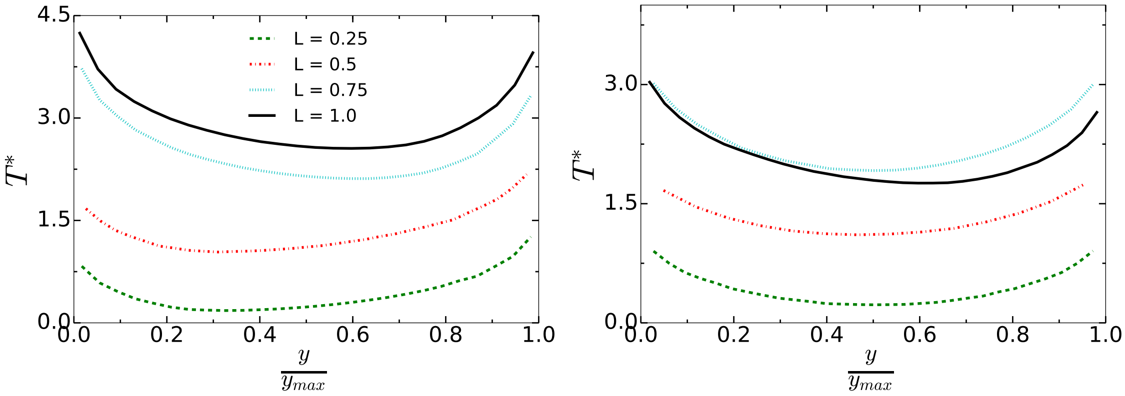

(a)

(b)

Figure C8: Profiles of normalised temperature along (a) Line_1, (b) Line_2

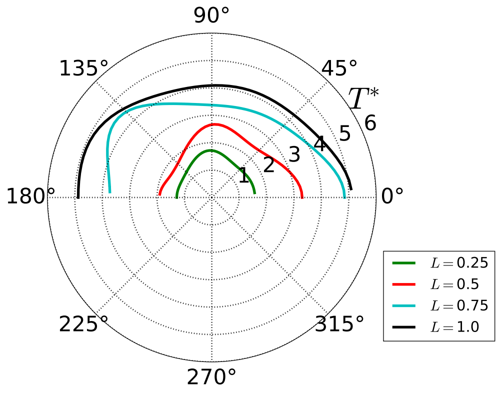

Figure C9: Circumferential variation of rod temperature for rod 1. The black arrow at 180° is oriented to the rod bundle center

Appendix D

D.1 Modelling of the *Overlapped* bundle

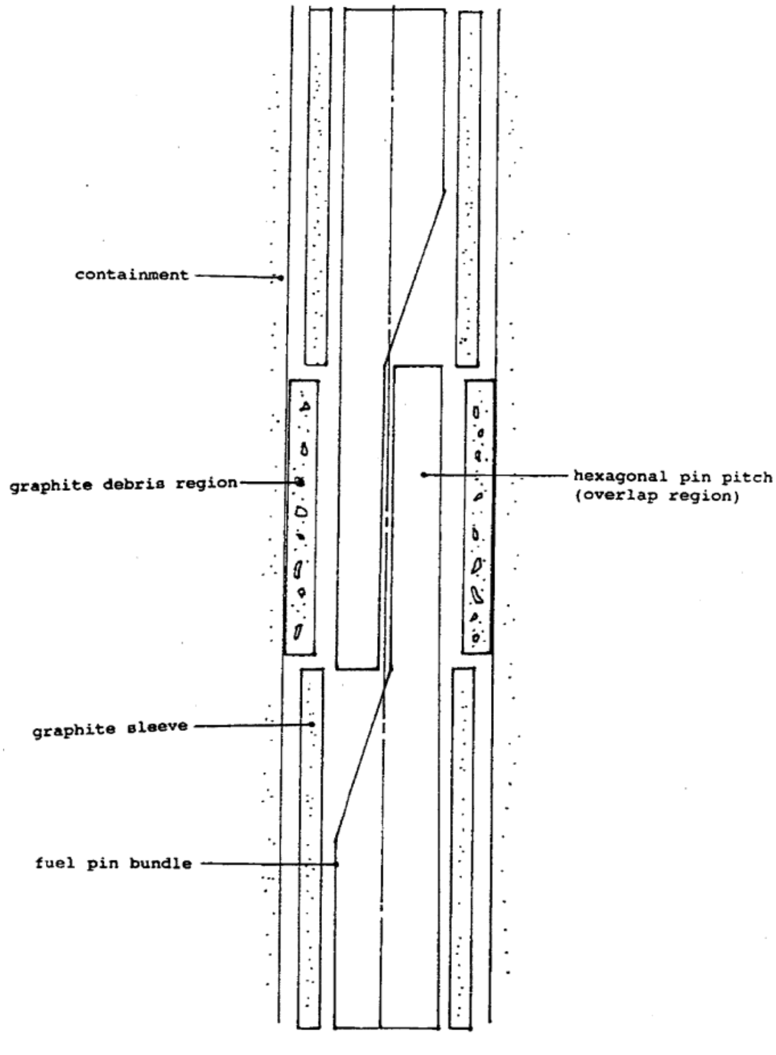

Figure D1: Sketch of *Overlapped* bundle as modelled in *CoolFuel* [17]

D.1.1 Dimensioned diagram of the *Overlapped* assembly

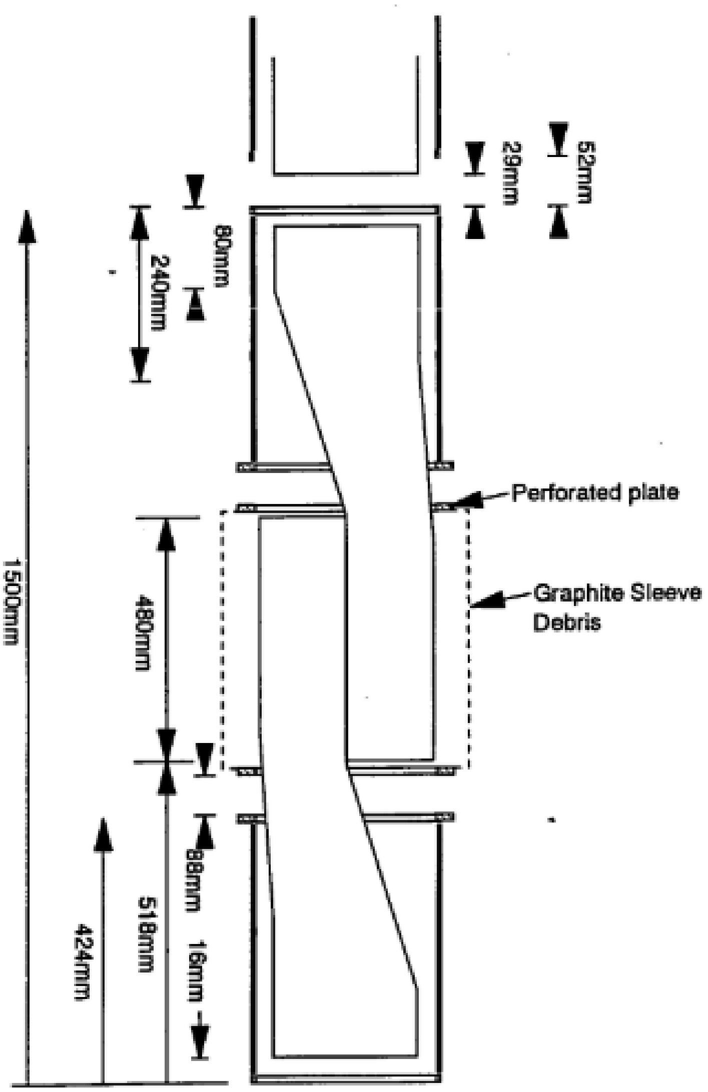

Figure D2: Dimensioned experimental assembly diagram [18]

D.1.2 Transducer readout vs calibrated power plot

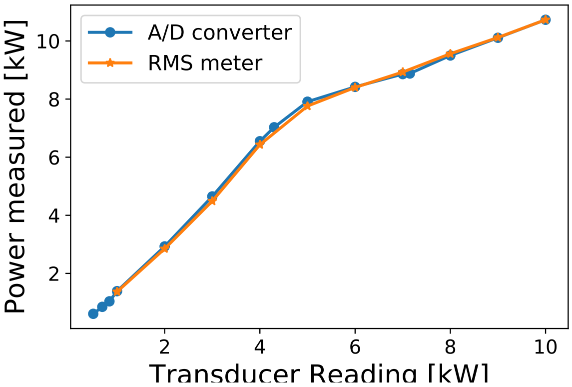

Figure D3: Comparison of transducer reading against the calibrated true power[18]

D.2 Modelling parameter sensitivity study for natural circulation conditions

Initial runs have been conducted to investigate the influence correlation sensitivity parameters have on the computed solution. Table D.1 below outlines the sensitivity parameters investigated with the results then presented in Tables D.2 and D.3 for build OLB2C3 at 40 bar and 5 bar pressure respectively.

The filtering mesh used in this sensitivity study is fixed with eight azimuthal divisions, six radial divisions inside the graphite sleeve and 4 radial divisions from the sleeve interior wall to the containment wall. In the axial direction, ten filter divisions are specified for the undamaged bundles and fifteen divisions per pin segment are specified for the *Overlapped* bundle. The solid pins have sixteen circumferential divisions.

An initial computation using the base setup, run OLB2C3S-1 in Table D.2, overpredicted the peak cladding temperatures at the overlap site, which is located in bundle 1 for build OLB2C3. Peak cladding temperatures for the remaining bundles were underpredicted along with the mean debris temperatures. Scaling, the pin axial heat transfer coefficient by a value of 0.5 increases the cladding temperatures, which is to be expected. As can be seen for run OLB2C3S-2, the peak cladding temperatures for all bundles are overpredicted, but the mean graphite temperatures are still underpredicted. At the overlap site the peak cladding temperature increases by 30 °C, while the temperature increase at debris region is by 3 °C. Even though the pin cladding temperatures have appreciably increased, the slight increase in the graphite temperatures is perhaps a reflection of the strong role natural convection plays in cooling the graphite debris. The heat transfer coefficient at the interior debris surface is then scaled down by 0.5. This results in an increase of the mean debris temperature by about 6 °C, although it remains underpredicted in comparison to the experimental result. The sensitivity parameter also affects the peak cladding temperature at the overlap site, which is further increased from the base result. Likely due to the heat loss through the surrounding interior debris surface being further restricted, which in turn increases the local bulk temperature at this site. Bundle 2 and bundle 3 show a marginal increase in temperature compared to those listed in OLB2C3S-2. In run

Table D.1: Table of sensitivity parameters investigated for the *Overlapped* geometry natural convection study

Sensitivity parameter	Possible values of parameter	Short summary
Graphite debris conductivity	*FOXDROP* model; +/− 20 %	The default conductivity model in *FREEDOM* is the *FOXDROP* model. The effect of graphite conductivity variation is investigated.
Annulus buoyancy resistance correction	TRUE or FALSE	Effect of buoyancy correction to the resistance correlation for the annulus is assessed. *Feat CoolFuel*[15] recommends that the correction be deactivated, while *CoolFuel* 3-D kept the feature activated.
Interior debris surface heat transfer coefficient	Multiplier; 0.6 - 1	An uncertainty exists with regards to the heat transfer coefficient at the interior surface of the graphite debris region. Currently, the graphite sleeve outer wall correlation is used, for lack of a better approximation, based on the assumption that at this surface there is likely to be enhanced heat transfer effects.
In-pore heat transfer coefficient	Multiplier; 0.1 - 1	The heat transfer coefficient at the graphite debris pores is approximated using the correlation contained in Amhalhel and Furmański[145]. This correlation assumes spherical particles and for forced convection conditions. An additional uncertainty also arises due to calculation of the in-pore heat transfer area.
Fuel pin cross flow resistance	1 - 2	The effect of a resistance multiplier to the cross flow correlations is investigated
Fuel pin axial resistance	1 - 2	The effect of an axial resistance multiplier to the correlations is investigated
Fuel pin heat transfer	0.7 - 1	The effect of a multiplier on the heat transfer correlation is investigated
Fuel pin emissivity	0.7 or 0.4	The appropriate pin bundle emissivity for bare fuel claddings (without carbonaceous deposits) is 0.4. The pin emissivity used in the *CoolFuel* run is not stated. It is inferred the default emissivity value (0.7) was used.

Table D.2: Table containing results of the sensitivity study. All the sensitivity studies have been carried out for Build-2 at 40 bar pressure

		Maximum Temperature(°C)			Mean Temperature(°C)
Casename	Parameter values	Elem-1	Elem-2	Elem-3	Debris
Experimental data	-	284.9	292.5	324.1	161.8
OLB2C3S-1	Initial run	300.8	269.6	309.2	149
OLB2C3S-2	Pin axial heat transfer multiplier - 0.5	330.8	300	339.3	152
OLB2C3S-3	Pin axial heat transfer multiplier - 0.5 Interior debris surface multiplier - 0.5	326.8	301.3	340	155
OLB2C3S-4	Pin axial heat transfer multiplier - 0.5 Interior debris surface multiplier - 0.5 Emissivity value - 0.4	332.1	304.2	341	151
OLB2C3S-ABC-1	Activate annulus buoyancy correction for resistance	300.1	282	326.5	149
OLB2C3S-ABC-2	Activate annulus buoyancy correction for resistance Pin axial friction factor multiplier - 1.5	317.24	290.6	337.76	147
OLB2C3S-ABC-3	Activate annulus buoyancy correction for resistance Pin axial friction factor multiplier - 2	328.5	297.3	346.6	147
OLB2C3S-ABC-4	Activate annulus buoyancy correction for resistance Pin cross flow friction factor multiplier - 2	301.6	282.4	326.5	149

OLB2C3S-ABC-5	Activate annulus buoyancy correction for resistance In-pore debris multiplier - 0.4	299	279	325	140
OLB2C3S-ABC-6	Activate annulus buoyancy correction for resistance In-pore debris multiplier - 1.0	289.7	277.7	322	132
OLB2C3S-ABC-7	Activate annulus buoyancy correction for resistance Graphite debris thermal conductivity multiplier - 0.8	300.3	281.6	326.2	149
OLB2C3S-ABC-8	Activate annulus buoyancy correction for resistance Graphite debris thermal conductivity multiplier - 1.2	300.3	281.5	326	142
OLB2C3S-ABC-9	Activate annulus buoyancy correction for resistance Emissivity value - 0.4	303.6	282	328	142

Table D.3: Table containing results of the sensitivity study. All the sensitivity studies have been carried out for Build-2 at 5 bar pressure

Casename	Parameter values	°C			
		Elem-1	Elem-2	Elem-3	Debris mean
	Experimental data	721.1	477.3	543	291
OLB2C3S-5bar-1	Initial run. Pin axial heat transfer multiplier - 0.5	652	530	568	320
OLB2C3S-5bar-2	Pin axial heat transfer multiplier - 0.5 Emissivity value - 0.4	692	549	588	300

OLB2C3S-3, the pin emissivity is reduced to a value of 0.4. As a result at the overlap site, the pin cladding temperatures are appreciably increased but for the other bundles, the temperature increase is rather moderate. At the overlap site, the pin gaps are at their narrowest thus leading to lower computed porosity. This then leads to lower computed flows and Nusselt numbers thereby enhancing the influence of radiation on the pin bundle, at this location. With regards to the graphite debris, a reduction in temperature is shown. As the debris surface gains heat from radiation and a reduction in pin emissivity naturally reduces the heat received.

In the *CoolFuel* models, the annulus buoyancy correction was used. A series of sensitivity runs denoted by OLB2C3S-ABC-* have been conducted with this parameter activated. The base setup is rerun and now denoted by OLB2C3S-ABC-1. Results show the peak cladding temperature is still underpredicted at bundle 2 although it has increased. At bundle 1 there is hardly any variation but for bundle 3, the cladding temperature is now overpredicted. The mean debris temperatures remained the same. The annulus buoyancy correction increases the resistance in the annulus. This has the net effect of lowering the convective flow through the bundle. At the top of the bundle, the effect on the cladding temperature is more pronounced as the buoyancy force in the annulus is at its largest. This is due to the larger temperature difference between the containment wall and flowing gas. The following can be noted from the additional sensitivities conducted; Scaling the pin axial friction factor increases the peak cladding temperature at all drop locations but leads to a slight decrease in graphite temperature. Further increases in pin axial friction factor do not lead to a further decrease in the debris temperature. Doubling the pin cross flow resistance leads to a slight increase in cladding temperatures but does not affect the graphite temperature. In contrast, increasing the in-pore heat transfer coefficient for the graphite debris region is shown to lead to lower peak graphite and cladding temperatures. An increase in the in-pore heat transfer would make the graphite debris a more effective sink in the fluid domain leading to lower gas temperatures. Graphite thermal conductivity values were then decreased by 20 %. This alteration yielded unchanged temperatures from run OLB2C3S-ABC-1. Increasing, the graphite thermal conductivity values by 20 %, led to lower peak graphite temperatures but the cladding temperatures were not affected. Finally, the pin cladding emissivity was decreased to 0.4. This alteration leads to a slight increase in cladding temperatures but as can be seen, the graphite temperatures are noticeably lower, this has been observed before in the earlier runs with the annulus buoyancy correction deactivated.

Two additional sensitivity runs were conducted for the build OLB2C3 at 5 bar pressure, Table D.3 shows the results. The overall trends shown in this short sensitivity study are consistent with those observed for the high pressure runs. Although it can be observed that the effect of emissivity on the cladding temperatures is magnified, but this to be expected as at lower pressures radiation becomes the dominant heat transfer mechanism.

Sensitivity parameters defined for all natural circulation cases

The sensitivity parameter values used in the current validation study are given in Table D.4 for completeness. Except for the emissivity value which should evaluated depending on the case study under consideration, safety case studies for natural convection use these predefined sensitivity parameters.

Table D.4: Table of sensitivity parameters used in the Overlapped study. Barring the emissivity (which is case dependent), these parameters are recommended for buoyancy influenced flows.

Sensitivity parameter	Value used
Graphite debris conductivity	*FOXDROP* model (no bias)
Annulus buoyancy resistance correction	FALSE
Interior debris surface heat transfer coefficient	0.6
In-pore heat transfer coefficient	0.1
Fuel pin crossflow resistance	1
Fuel pin axial resistance	1
Fuel pin heat transfer	0.7
Fuel pin emissivity	0.4

D.3 Examples of solid and fluid meshes used in validation study

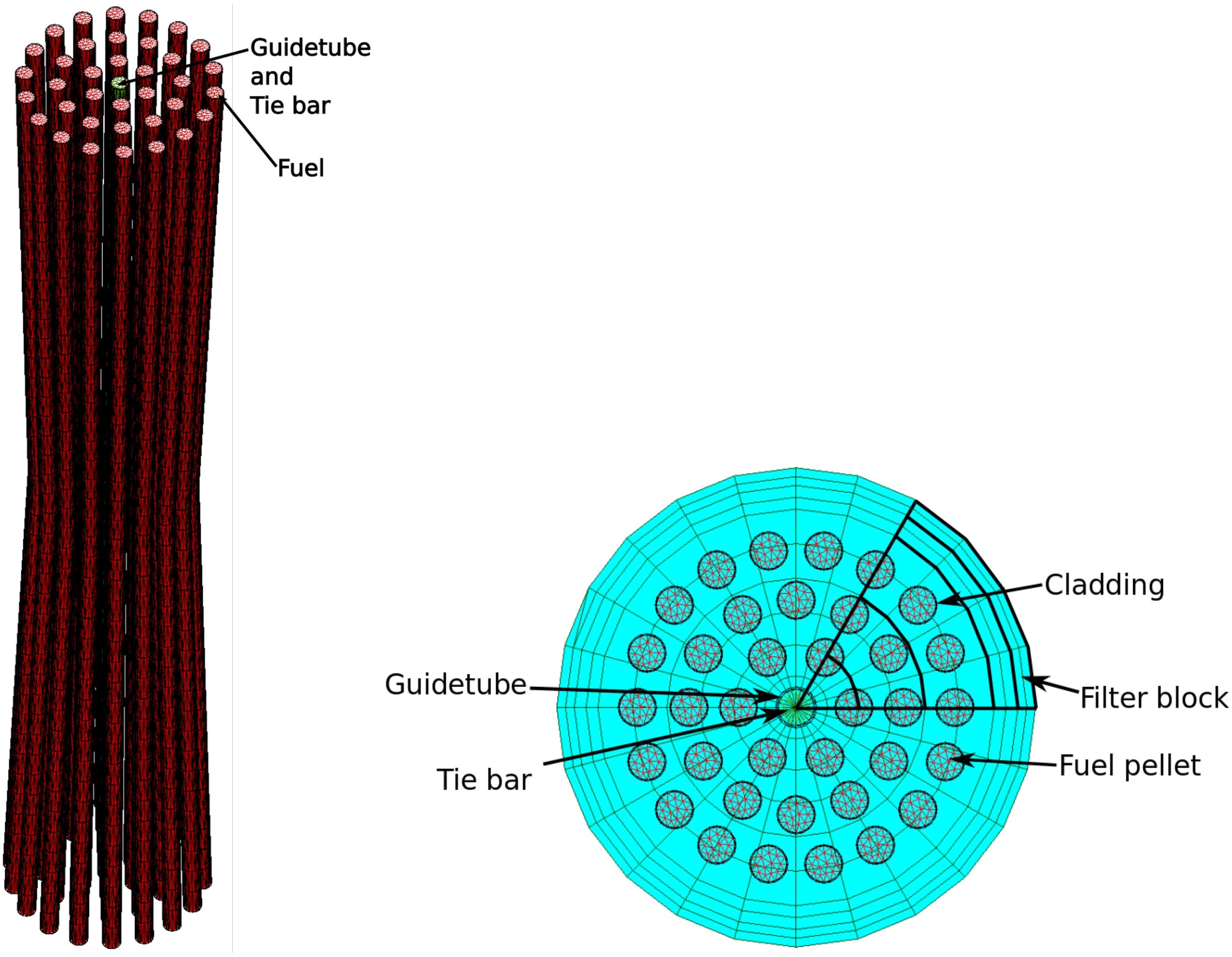

(a) Conduction mesh

(b) Cross-section fluid and solid calculation meshes

Figure D4: Solid and fluid mesh example: *WheatSheaf* bundle with 6 azimuthal and 5 radial divisions. (a) Conduction mesh and (b) Cross-section of solid and fluid mesh at mid-height.

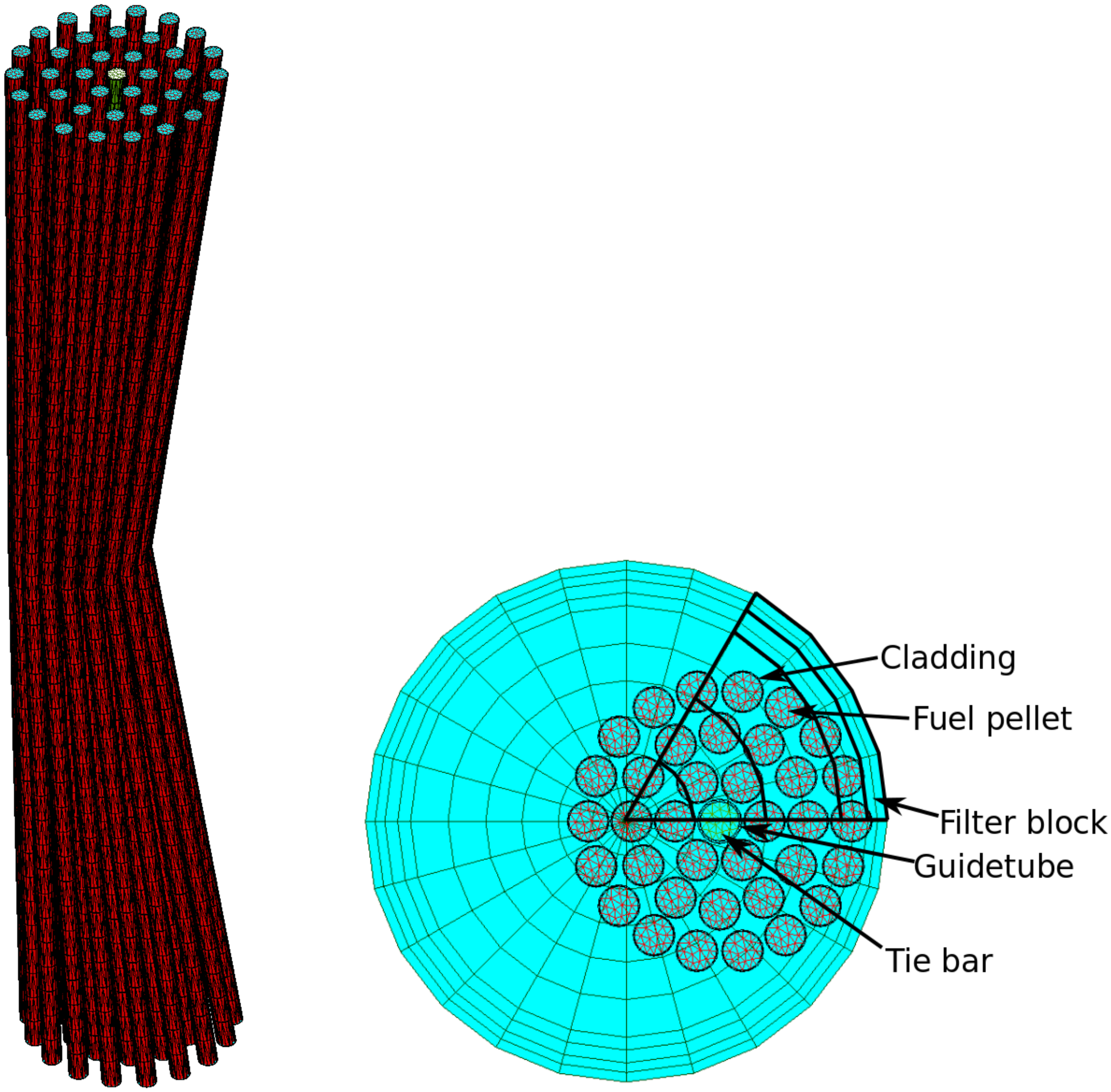

(a) Conduction mesh

(b) Cross-section fluid and solid calculation meshes

Figure D5: Solid and fluid mesh example: *ZigZag* fluid mesh with 6 azimuthal and 5 radial divisions. (a) Conduction mesh and (b) Cross-section of solid and fluid mesh at mid-height.

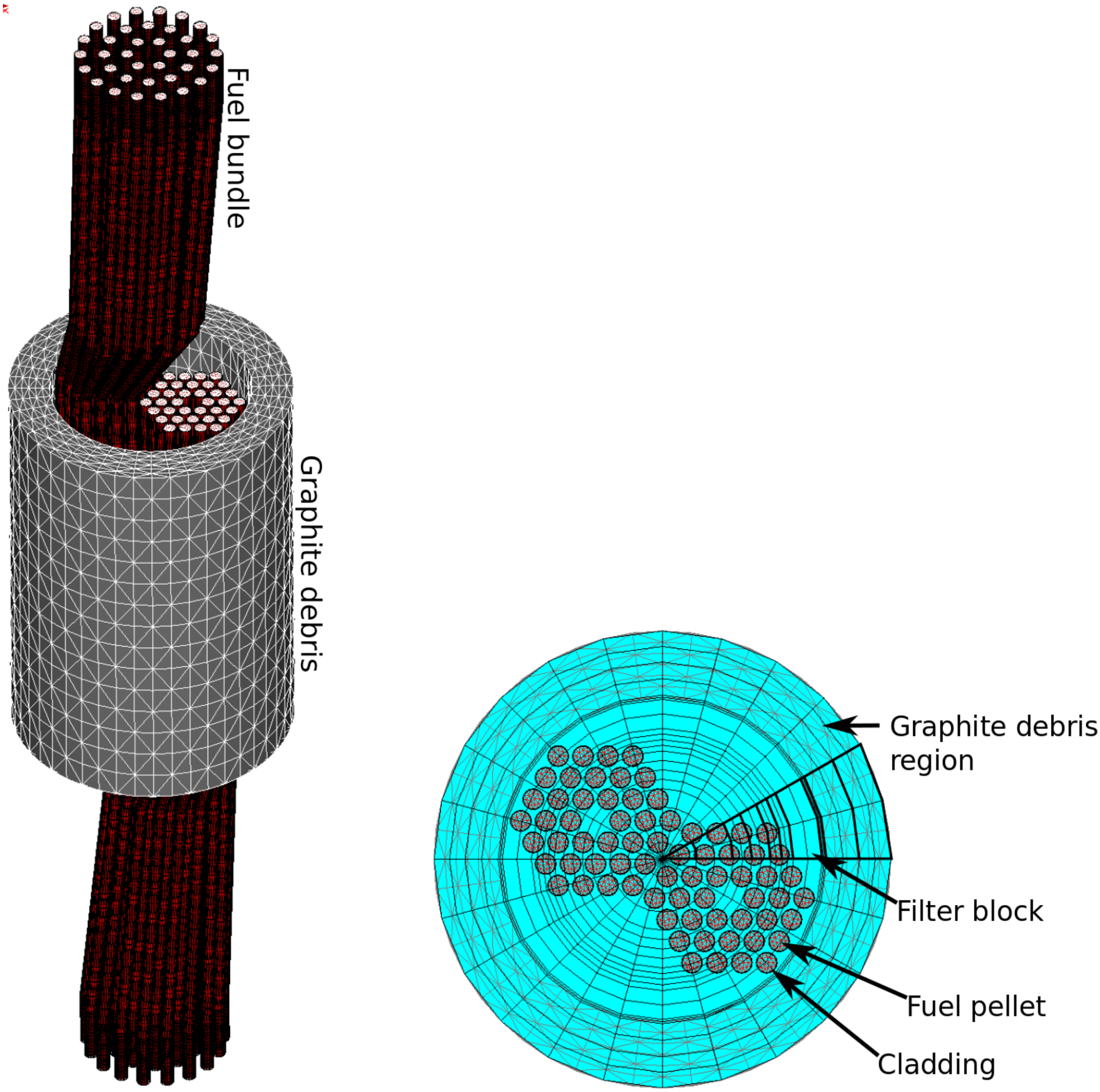

(a) Conduction mesh

(b) Cross-section fluid and solid calculation meshes

Figure D6: Solid and fluid mesh example: *Overlapped* fluid mesh with 12 azimuthal and 10 radial divisions. (a) Conduction mesh (missing guide tube and short intact sleeves at either end of bundle) and (b) Cross-section of solid and fluid mesh at mid-height.

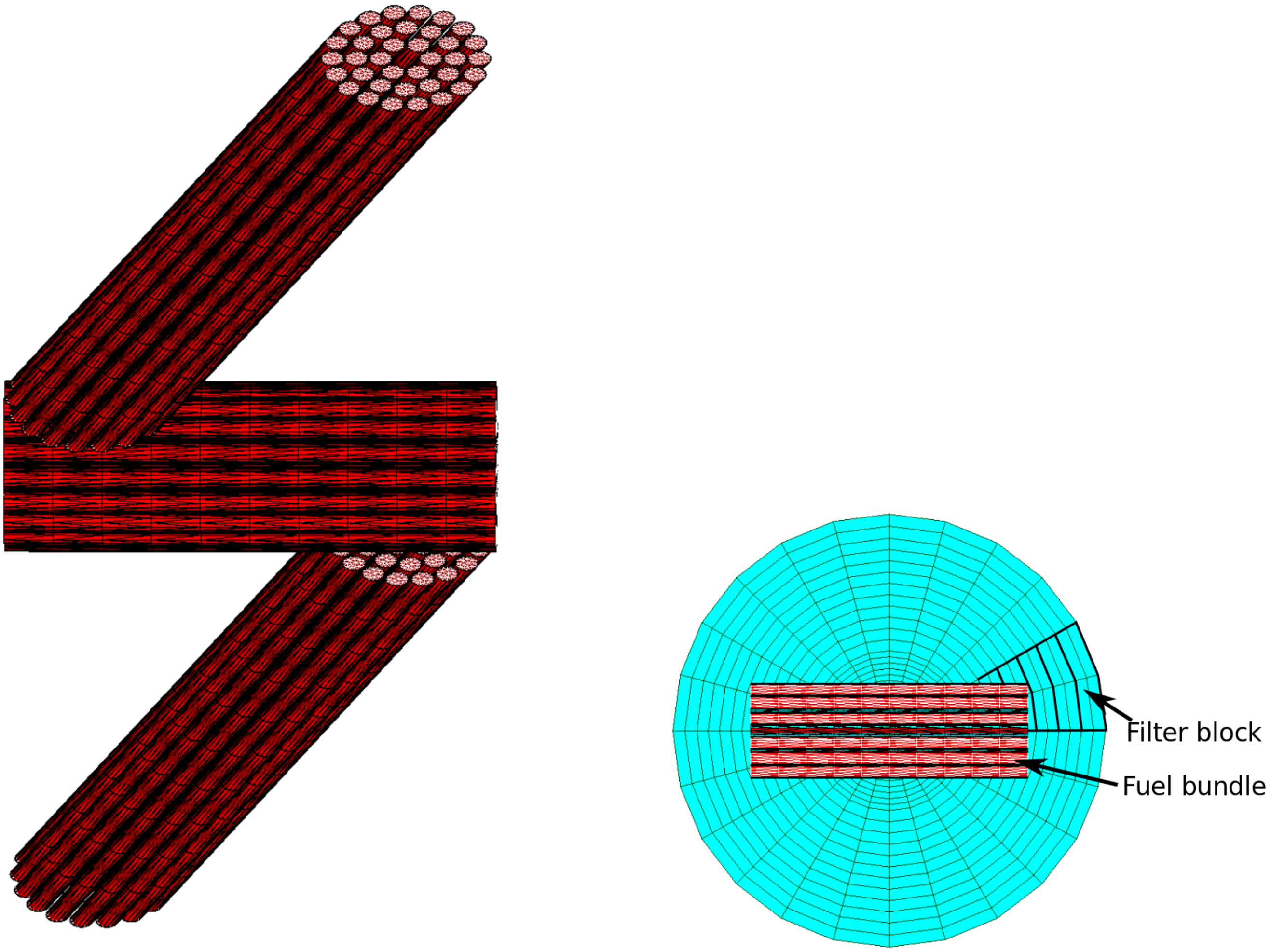

(a) Conduction mesh (b) Cross-section fluid and solid calculation meshes

Figure D7: Solid and fluid mesh example: *C_buckled* fluid mesh with 12 azimuthal and 11 radial divisions. (a) Conduction mesh (missing guide tube) and (b) Cross-section of solid and fluid mesh at mid-height.

D.3.1 Validation sensitivity runs

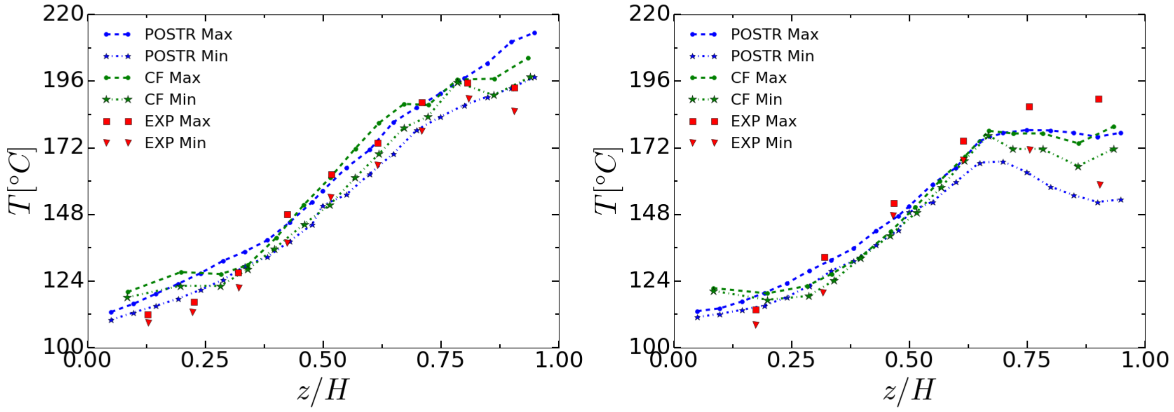

(a) Rod-rank 1 (b) Rod-rank 2

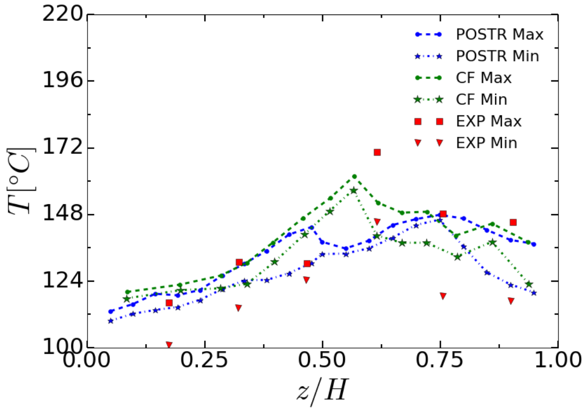

(c) Rod-rank 3

Figure D8: Sensitivity run: *WheatSheaf* bundle with 6 azimuthal, 5 radial and 20 axial divisions

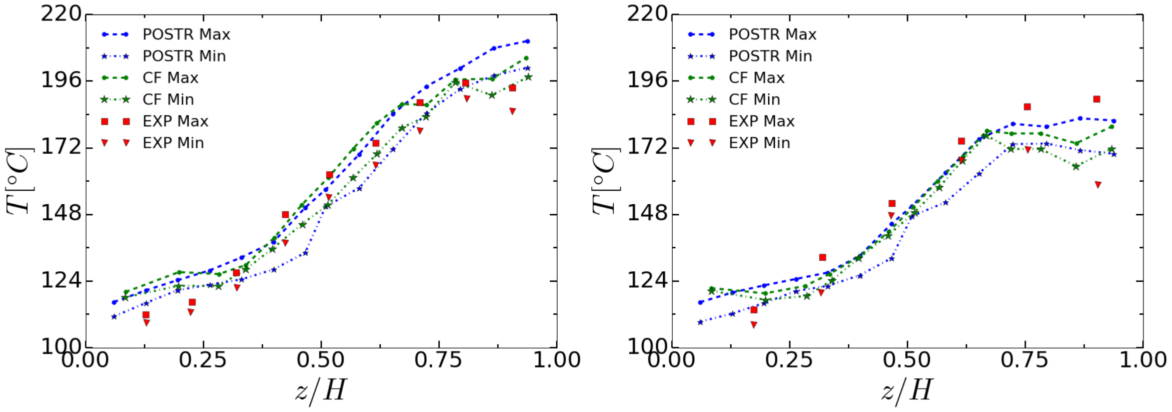

(a) Rod-rank 1

(b) Rod-rank 2

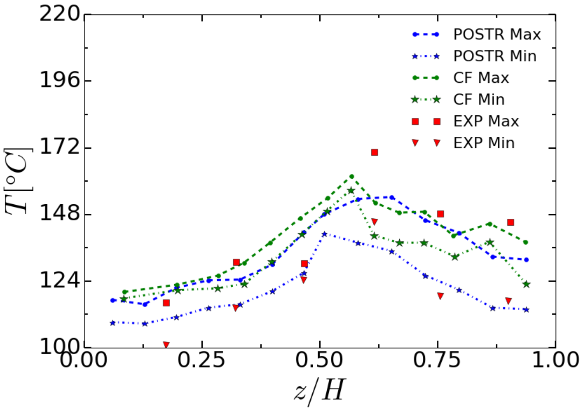

(c) Rod-rank 3

Figure D9: Sensitivity run: *WheatSheaf* bundle with 6 azimuthal, 10 radial and 14 axial divisions

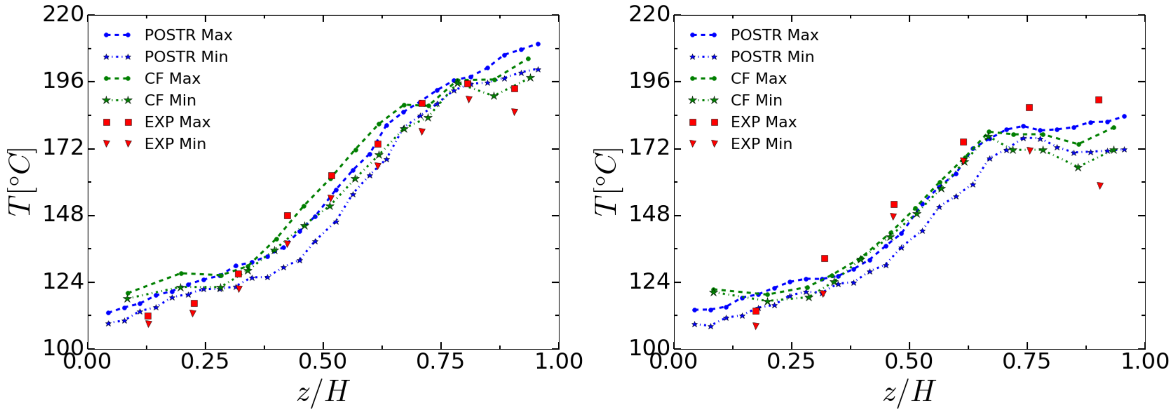

(a) Rod-rank 1 (b) Rod-rank 2

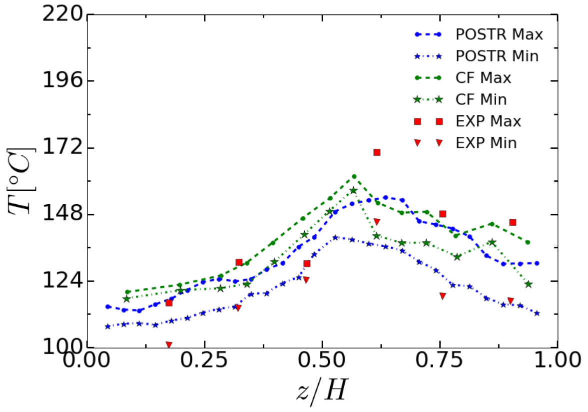

(c) Rod-rank 3

Figure D10: Sensitivity run: *WheatSheaf* bundle with 6 azimuthal, 10 radial and 28 axial divisions

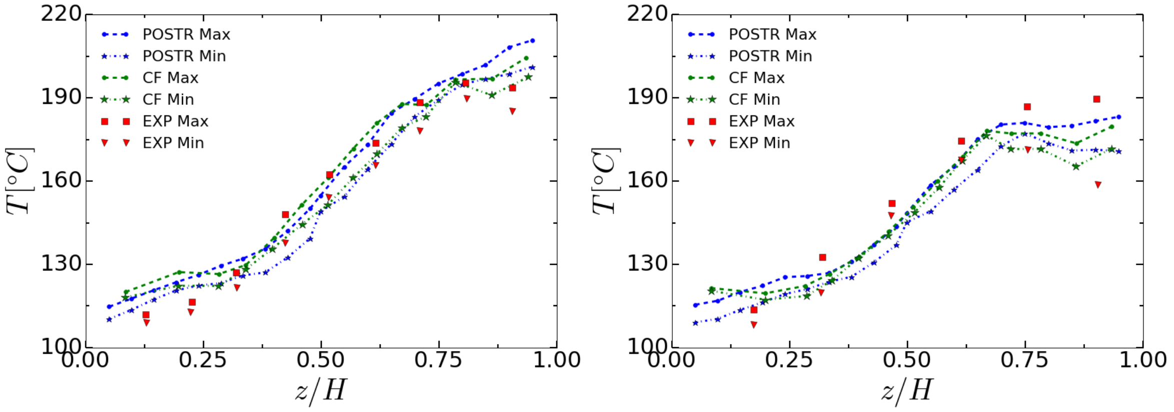

(a) Rod-rank 1

(b) Rod-rank 2

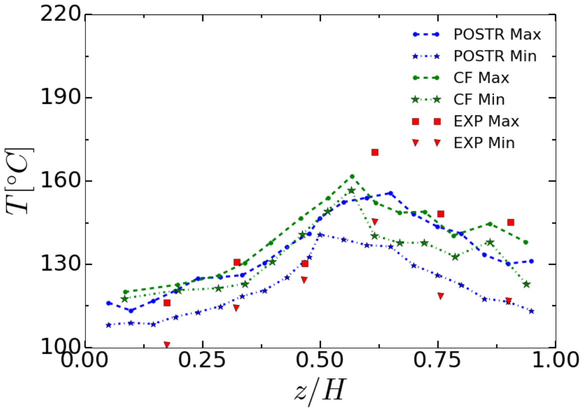

(c) Rod-rank 3

Figure D11: Sensitivity run: *WheatSheaf* bundle with 12 azimuthal, 10 radial and 20 axial divisions

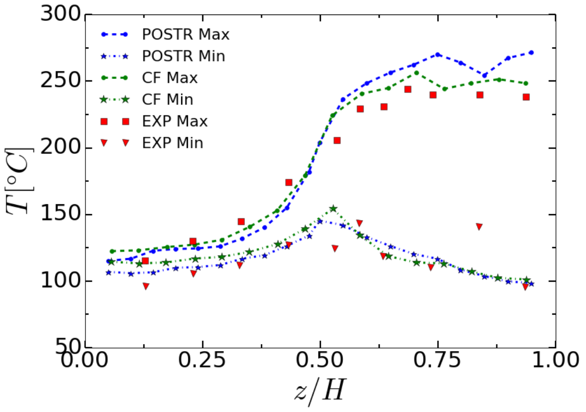

Figure D12: Sensitivity run: *ZigZag* bundle with 12 azimuthal, 10 radial and 20 axial divisions

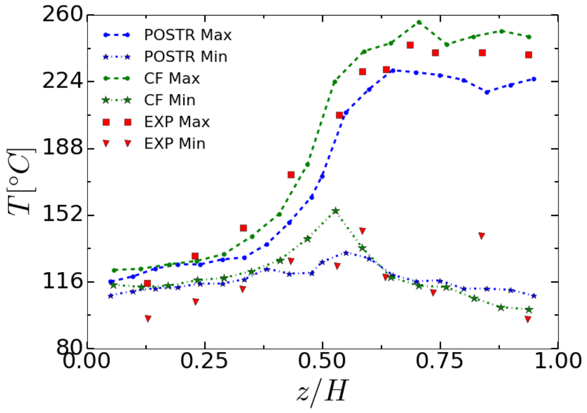

Figure D13: Sensitivity run: *ZigZag* bundle with 6 azimuthal, 5 radial and 20 axial divisions

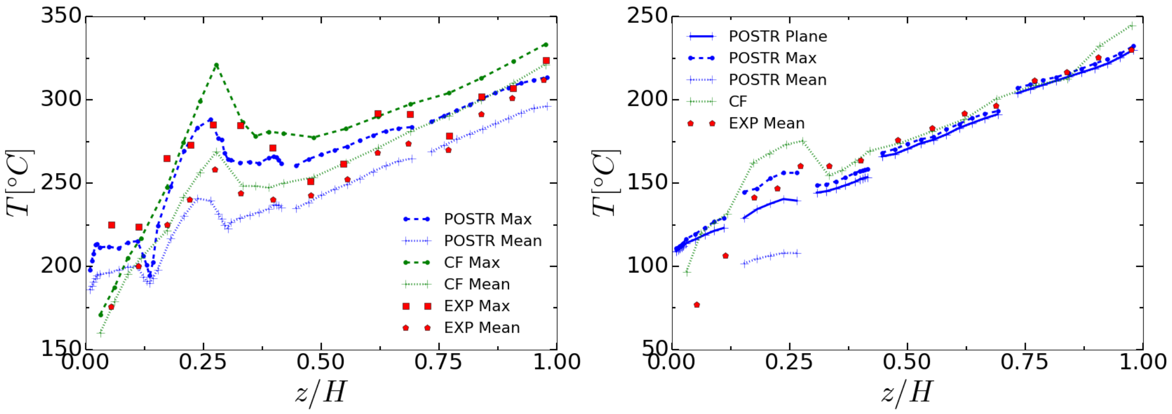

(a) Fuel temperatures

(b) Graphite temperatures

Figure D14: Sensitivity run: *Overlapped* bundle build OLB2C3 with 6 azimuthal divisions

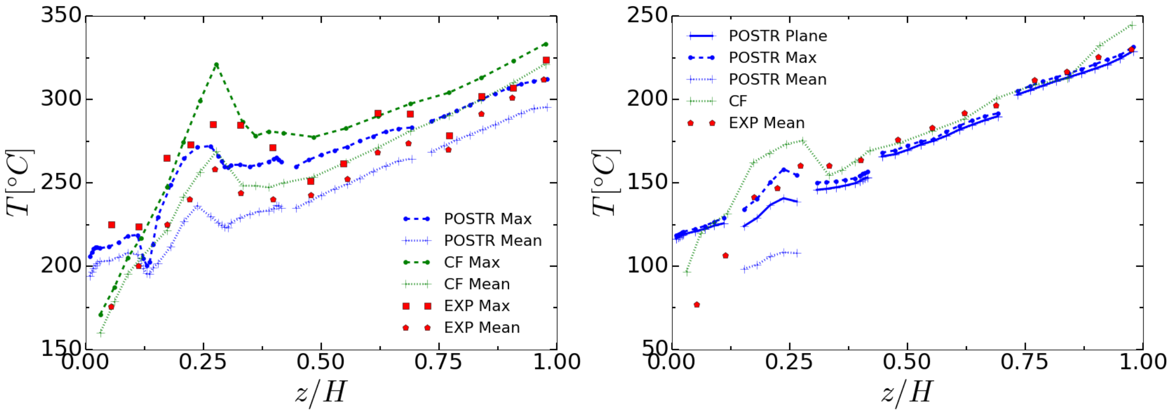

(a) Fuel temperatures

(b) Graphite temperatures

Figure D15: Sensitivity run: *Overlapped* bundle build OLB2C3 with 5 Axial divisions